UNIVERSITY OF WEST ATTICA
ΠΑΝΕΠΙΣΤΗΜΙΟ ΔΥΤΙΚΗΣ ΑΤΤΙΚΗΣ

On topological properties of materials: Topological insulators, Weyl and Dirac semimetals

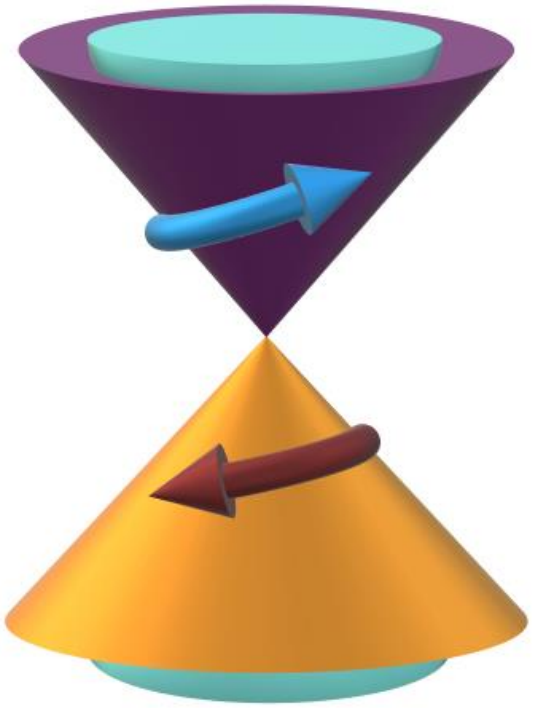

Doctoral Dissertation

Sotirios Fragkos

Supervisor:
Yerassimos Panayiotatos
Professor, University of West Attica

Athens, February 2023

ΠΑΝΕΠΙΣΤΗΜΙΟ ΔΥΤΙΚΗΣ ΑΤΤΙΚΗΣ

ΣΧΟΛΗ ΜΗΧΑΝΙΚΩΝ

ΤΜΗΜΑ ΜΗΧΑΝΟΛΟΓΩΝ ΜΗΧΑΝΙΚΩΝ

Μέλη Τριμελούς Συμβουλευτικής Επιτροπής συμπεριλαμβανομένου και του Επιβλέποντα

Α/Α	ΟΝΟΜΑ ΕΠΩΝΥΜΟ	ΒΑΘΜΙΔΑ/ΙΔΙΟΤΗΤΑ/ΤΜΗΜΑ	ΨΗΦΙΑΚΗ ΥΠΟΓΡΑΦΗ
1	ΠΑΝΑΓΙΩΤΑΤΟΣ ΓΕΡΑΣΙΜΟΣ	Καθηγητής, Τμήμα Μηχανολόγων Μηχανικών, ΠΑΔΑ. (επιβλέπων)	Gerasimos Panagiotatos Digitally signed by Gerasimos Panagiotatos Date: 2023.02.14 10:34:04 +02'00'
2	ΔΗΜΟΥΛΑΣ ΑΘΑΝΑΣΙΟΣ	Ερευνητής Α' βαθμίδας, ΕΚΕΦΕ Δημόκριτος.	ATHANASIOS DIMOULAS Digitally signed by ATHANASIOS DIMOULAS Date: 2023.02.16 09:53:27 +02'00'
3	ΧΡΟΝΑΙΟΣ ΑΛΕΞΑΝΔΡΟΣ	Καθηγητής, Τμήμα Ηλεκτρολόγων Μηχανικών και Μηχανικών Υπολογιστών, Πανεπιστήμιο Θεσσαλίας.	ALEXANDROS CHRONAIOS 15.02.2023 13:48

Μέλη Επταμελούς Εξεταστικής Επιτροπής

Α/Α	ΟΝΟΜΑ ΕΠΩΝΥΜΟ	ΒΑΘΜΙΔΑ/ΙΔΙΟΤΗΤΑ/ΤΜΗΜΑ/ΣΧΟΛΗ/ΠΑΝΕΠΙΣΤΗΜΙΟ
4	ΓΑΛΑΤΑ ΣΩΤΗΡΙΑ	Επίκουρη Καθηγήτρια, Τμήμα Ηλεκτρολόγων και Ηλεκτρονικών Μηχανικών, ΠΑΔΑ.
5	ΓΙΑΝΝΑΚΟΠΟΥΛΟΣ ΚΩΝΣΤΑΝΤΙΝΟΣ	Ερευνητής Γ' βαθμίδας, ΕΚΕΦΕ Δημόκριτος.
6	ΣΑΡΑΦΙΔΗΣ ΧΑΡΑΛΑΜΠΟΣ	Επίκουρος Καθηγητής, Τμήμα Φυσικής, ΑΠΘ.
7	ΨΥΛΛΑΚΗ ΠΑΝΔΩΡΑ	Καθηγήτρια, Τμήμα Μηχανολόγων Μηχανικών, ΠΑΔΑ.

Η έγκριση της διδακτορικής διατριβής από το Τμήμα Μηχανολόγων Μηχανικών του Πανεπιστημίου Δυτικής Αττικής δεν υποδηλοί αποδοχή των γνωμών του συγγραφέα
(Ν. 5343/32, Άρθρο 202).

ΔΗΛΩΣΗ ΣΥΓΓΡΑΦΕΑ ΔΙΔΑΚΤΟΡΙΚΗΣ ΔΙΑΤΡΙΒΗΣ

Ο κάτωθι υπογεγραμμένος Σωτήριος Φράγκος, του Αναστασίου, υποψήφιος διδάκτορας του Τμήματος Μηχανολόγων Μηχανικών της Σχολής Μηχανικών του Πανεπιστημίου Δυτικής Αττικής, δηλώνω ότι:

«Είμαι συγγραφέας και δικαιούχος των πνευματικών δικαιωμάτων επί της διατριβής και δεν προσβάλλω τα πνευματικά δικαιώματα τρίτων. Για τη συγγραφή της διδακτορικής μου διατριβής δεν χρησιμοποίησα ολόκληρο ή μέρος έργου άλλου δημιουργού ή τις ιδέες και αντιλήψεις άλλου δημιουργού χωρίς να γίνεται αναφορά στην πηγή προέλευσης (βιβλίο, άρθρο από εφημερίδα ή περιοδικό, ιστοσελίδα κ.λπ.). Επίσης, βεβαιώνω ότι αυτή η εργασία έχει συγγραφεί από μένα αποκλειστικά και αποτελεί προϊόν πνευματικής ιδιοκτησίας τόσο δικής μου, όσο και του Ιδρύματος.

Παράβαση της ανωτέρω ακαδημαϊκής μου ευθύνης αποτελεί ουσιώδη λόγο για την ανάκληση του διδακτορικού διπλώματος μου».

Ο Δηλών

SOTIRIOS FRAGKOS

Digitally signed by SOTIRIOS FRAGKOS
Date: 2023.02.14 10:20:35 +02'00'

On topological properties of materials: Topological insulators, Weyl and Dirac semimetals

Department of Mechanical Engineering

Doctoral Dissertation

Sotirios Fragkos

Mechanical Engineer

Supervisory board:

1. Yerassimos Panayiotatos, Prof. UniWA
2. Athanasios Dimoulas, Res. Dir. NCSRD
3. Alexander Chroneos, Prof. UTH

Seven-member committee:

1. Y. Panayiotatos, Prof. UniWA
2. A. Dimoulas, Res. Dir. NCSRD
3. A. Chroneos, Prof. UTH
4. S. Galata, Assist. Prof. UniWA
5. K. Giannakopoulos, Res. NCSRD
6. C. Sarafidis, Assist. Prof. AUTh
7. P. Psyllaki, Prof. UniWA

Athens, February 2023

Abstract

Topological materials are materials whose properties remain invariant under continuous transformations. Topological insulators are insulating in bulk and conducting at surface. In another class of topological materials, the material is a semimetal where their valence and conduction bands touch at, or near the Fermi level. Depending on whether the bands are non or doubly-degenerate, a topological material is called topological Weyl or Dirac semimetal, respectively. Standard topological materials possess three-dimensional crystal structures that are often formed as bulk crystals. However, the research has been focused lately on two-dimensional van der Waals topological materials due to their unique quantum electronic properties and their reduced dimensionality.

This doctoral dissertation aims on presenting theoretical and experimental results that contribute to the research on two-dimensional van der Waals topological materials. Firstly, we fabricated epitaxial $(SnBi_2Te_4)_n(Bi_2Te_3)_m$ natural van der Waals superlattices. The existence of topological surface states is confirmed by using first-principles calculations in combination with in-situ and synchrotron angle-resolved photoemission spectroscopy. Their presence is also correlated with appearance of the weak antilocalization effect observed with magnetotransport measurements.

In addition, we report on the crucial orthorhombic non-centrosymmetric Weyl semimetal T_d-phase direct room-temperature observation in epitaxial three monolayers $MoTe_2$ films generated layer by layer on InAs substrates via molecular beam epitaxy. The lattice constants of our epitaxial orthorhombic phase are found to be significantly greater than the experimental values from bulk T_d-phase of $MoTe_2$ that were previously published. In this study, we claim that the stabilization of the T_d-phase at room temperature in epitaxial thin films is significantly influenced by the expanded lattice parameters, as well as the energy position of the Weyl points.

Moreover, the family of group IV transition metal ditellurides is studied with theoretical calculations, where $HfTe_2$ and $ZrTe_2$ are classified as type-I and type-II topological Dirac semimetals, respectively. In addition, a new type-III phase is

proposed, which is achieved through a topological phase transition, by alloying the two materials in combination with in-plane strain. This strain may be used to alternate between the two types of Dirac semimetals. We successfully fabricated the desired alloy by using molecular beam epitaxy, and performed angle-resolved photoemission spectroscopy, where the topological Dirac semimetal behavior is displayed.

Finally, theoretical results of the WTe_2, and to a lesser extend $MoTe_2$, in a van der Waals heterostructure with the $CrTe_2$ two-dimensional ferromagnet are presented. WTe_2 and $MoTe_2$ are topological Weyl semimetals in large thicknesses and two-dimensional topological insulators down to the single layer, holding great opportunities on spintronic applications. Our findings suggest that an interfacial Dzyaloshinskii-Moriya interaction strong enough to create Néel-type skyrmion lattice is produced whose dynamics are tested under external magnetic fields and temperature. This study also shows that the generation and annihilation of magnetic skyrmions in the $CrTe_2/WTe_2$ van der Waals heterostructure can be achieved and that the motion of the magnetic skyrmions can be controlled by ultra-low spin-polarized currents.

Περίληψη

Τα τοπολογικά υλικά είναι υλικά των οποίων οι ιδιότητες παραμένουν αμετάβλητες υπό συνεχείς μετασχηματισμούς. Οι τοπολογικοί μονωτές είναι μονωτές εσωτερικά και αγώγιμοι στην επιφάνεια. Σε μια άλλη κατηγορία τοπολογικών υλικών, το υλικό είναι ημιμέταλλο όπου οι ζώνες σθένους και αγωγιμότητάς τους τέμνονται πάνω ή κοντά στο επίπεδο Fermi. Ανάλογα με το αν οι ζώνες είναι μη ή διπλά εκφυλισμένες, ένα τοπολογικό υλικό ονομάζεται τοπολογικό ημιμέταλλο Weyl ή Dirac, αντίστοιχα. Τα τυπικά τοπολογικά υλικά διαθέτουν τρισδιάστατες κρυσταλλικές δομές που συχνά σχηματίζονται ως πολυστρωματικοί κρύσταλλοι. Ωστόσο, η έρευνα έχει επικεντρωθεί τελευταία σε δισδιάστατα τοπολογικά υλικά van der Waals λόγω των μοναδικών κβαντικών ηλεκτρονικών ιδιοτήτων τους και της μειωμένης τους διάστασης.

Η παρούσα διδακτορική διατριβή στοχεύει στην παρουσίαση θεωρητικών και πειραματικών αποτελεσμάτων που συμβάλλουν στην έρευνα πάνω στα δισδιάστατα τοπολογικά υλικά. Πρώτον, κατασκευάσαμε επιταξιακά φυσικές υπερδομές van der Waals $(SnBi_2Te_4)_n(Bi_2Te_3)_m$. Η ύπαρξη τοπολογικών επιφανειακών καταστάσεων επιβεβαιώνεται με τη χρήση υπολογισμών πρώτων αρχών σε συνδυασμό με τη γωνιακός εξαρτώμενη φασματοσκοπία φωτοεκπομπής in-situ και σύγχροτρον. Η παρουσία τους συσχετίζεται επίσης με την εμφάνιση του φαινομένου ασθενούς αντιεντοπισμού που παρατηρείται με τις μετρήσεις μαγνητομεταφοράς.

Επιπλέον, αναφέρουμε την άμεση παρατήρηση της κρίσιμης ορθορομβικής μη κεντροσυμμετρικής ημιμεταλλικής φάσης Weyl T_d σε θερμοκρασία δωματίου, σε επιταξιακά υμένια $MoTe_2$ τριών μονοστρωμάτων, που δημιουργούνται στρώμα προς στρώμα σε υποστρώματα InAs μέσω επιταξίας με μοριακές δέσμες. Οι πλεγματικές σταθερές της επιταξιακής ορθορομβικής μας φάσης βρέθηκαν να είναι σημαντικά μεγαλύτερες από τις πειραματικές τιμές από των πολυστρωματικών κρυστάλλων φάσης T_d του $MoTe_2$ που δημοσιεύθηκαν προηγουμένως. Σε αυτή τη μελέτη, υποστηρίζουμε ότι η σταθεροποίηση της φάσης T_d σε θερμοκρασία δωματίου σε επιταξιακές λεπτές μεμβράνες επηρεάζεται σημαντικά από τις παραμέτρους του διογκωμένου πλέγματος, καθώς και η ενεργειακή θέση των σημείων Weyl.

Επιπλέον, η οικογένεια των μεταβατικών μετάλλων διτελλουριδίων της ομάδας IV μελετάται με θεωρητικούς υπολογισμούς, όπου τα $HfTe_2$ και $ZrTe_2$ ταξινομούνται ως τοπολογικά ημιμέταλλα Dirac τύπου-I και τύπου-II, αντίστοιχα. Επιπρόσθετα, προτείνεται μια νέα φάση τύπου-III, η οποία επιτυγχάνεται μέσω μιας τοπολογικής μετάβασης φάσης, με κράμα των δύο υλικών σε συνδυασμό με την εφαρμογή ενδοεπίπεδων τάσεων. Αυτή η τάση μπορεί να χρησιμοποιηθεί για την εναλλαγή μεταξύ των δύο τύπων ημιμετάλλων Dirac. Κατασκευάσαμε με επιτυχία το επιθυμητό κράμα χρησιμοποιώντας επιταξία με μοριακές δέσμες και πραγματοποιήσαμε γωνιακός εξαρτώμενη φασματοσκοπία φωτοεκπομπής, όπου παρατηρήθηκε η τοπολογική ημιμεταλλική συμπεριφορά Dirac.

Τέλος, παρουσιάζονται θεωρητικά αποτελέσματα του WTe_2, και σε μικρότερο βαθμό του $MoTe_2$, σε μια ετεροδομή van der Waals με τον δισδιάστατο σιδηρομαγνήτη $CrTe_2$. Το WTe_2 και το $MoTe_2$ είναι τοπολογικά ημιμέταλλα Weyl σε μεγάλα πάχη και δισδιάστατοι τοπολογικοί μονωτές σε πάχος ενός μονοστρώματος, και είναι πολλά υποσχόμενα για εφαρμογές στη σπιντρονική. Τα ευρήματά μας υποδηλώνουν ότι παράγεται μία διεπιφανειακή αλληλεπίδραση Dzyaloshinskii-Moriya αρκετά ισχυρή ώστε να δημιουργήσει πλέγμα σκυρμιονίων τύπου Néel του οποίου η δυναμική ελέγχεται υπό εξωτερικά μαγνητικά πεδία και τη θερμοκρασία. Αυτή η μελέτη δείχνει επίσης ότι η δημιουργία και η εξάλειψη των σκυρμιονίων στην ετεροδομή $CrTe_2/WTe_2$ μπορεί να επιτευχθεί και ότι η κίνηση των σκυρμιονίων μπορεί να επιτευχθεί με εξαιρετικά χαμηλά πολωμένα ρεύματα σπιν.

Introduction

In this doctoral dissertation, I aim to present theoretical and experimental results that contribute to the more than ten years of research on topological materials. Ever since this new class of materials was first created —a discovery that helped win the Nobel Prize in Physics in 2016— researchers have been intrigued by the possibilities for electronics applications. However, the research has been focused lately on two-dimensional van der Waals topological materials due to their unique quantum electronic properties and their reduced dimensionality.

The Introduction in Chapter 1 is focused around the progress that has been made so far in the field of two-dimensional topological materials. At first, the three main categories of topological materials are described, namely the topological insulators, Weyl and Dirac semimetals. Secondly, the origin and regulation of various properties are reviewed, involving electronic and transport properties. Lastly, some device applications of two-dimensional van der Waals topological materials are presented, including memories and spintronic devices.

In Chapter 2, a short description of the main theoretical and experimental methods used during this research will be given, which is separated in two parts. Firstly, the theoretical methods are described, including density functional theory, Wannier functions, tight-binding model and atomistic spin simulations. Secondly the experimental techniques for material growth and characterization are introduced, including molecular beam epitaxy, reflection high energy electron diffraction, photoelectron spectroscopies and scanning tunneling microscopy.

In Chapter 3, the research on epitaxial $(SnBi_2Te_4)_n(Bi_2Te_3)_m$ natural van der Waals superlattices will be presented, where the existence of topological surface states is confirmed and correlate them with magnetotransport observations using first-principles calculations in combination with in-situ and synchrotron ARPES. While the topological surface states overlap with bulk conduction band states at the Fermi energy, it is shown that by increasing the Sn concentration, the influence of BCB states is reduced and becomes minimum for $SnBi_2Te_4$.

In Chapter 4, the direct observation at room temperature of the non-centrosymmetric orthorhombic topological Weyl semimetal phase in epitaxial thin films of $MoTe_2$ grown by molecular beam epitaxy is reported. First-principles calculations predict eight type-II Weyl nodes which are located below (but near) the Fermi energy making them accessible to charge

transport and creating the prospect for practical applications exploiting the non-trivial topological properties.

In Chapter 5, the family of group IV transition metal ditellurides is studied, where $HfTe_2$ and $ZrTe_2$ are classified as type-I and type-II Dirac semimetals, respectively, by using first principles calculations. In addition, a new $Hf_xZr_{1-x}Te_2$ type-III state is proposed, achieved through a topological phase transition by alloying the two materials in combination with in-plane strain. The linearly dispersive Dirac cone of the type-III state is also observed by in-situ angle-resolved photoemission spectroscopy.

Chapter 6 presents theoretical results of the WTe_2 (and to a lesser extent, $MoTe_2$) two-dimensional van der Waals topological material in a heterostructure with the $CrTe_2$ two-dimensional ferromagnet. The findings suggest that an interfacial Dzyaloshinskii-Moriya interaction strong enough to form magnetic skyrmions is produced whose properties are test under external stimuli. This study shows that generation and annihilation of skyrmions in the $CrTe_2/WTe_2$ vdW heterostructure can be achieved and that the motion of the skyrmions can be manipulated by ultra-low spin-polarized currents.

Finally, in Chapter 7 a summary of conclusions of all the above research is presented and feature research is proposed.

Acknowledgments

Firstly, I would like to thank my supervisor Dr. Yerassimos Panayiotatos, Professor at the Department of Mechanical Engineering of the University of West Attica, who guided and encouraged me all these years, throughout the duration of both my BSc and Ph.D. I also thank him for giving me access to ARIS of GRNET High-Performance Computing Services to perform my theoretical calculations. Most importantly, I thank him for the general interest he showed in me, as his advices were not limited only to the framework of my Ph.D.

I give many special thanks to my co-advisor Dr. Athanasios Dimoulas, Research Director of the Epitaxy and Surface Science Laboratory of N.C.S.R. "Demokritos", for the opportunity he gave me to work in an internationally recognized laboratory, the fruitful discussions, and his guidance during my Ph.D. I also want to thank him for the financial support he gave me from the European Union H2020 SKYTOP project (Grant No. 824123), for dealing with topics outside the focus of Ph.D. In addition, I would like to thank my second co-advisor Dr. Alexander Chroneos, Professor at the University of Thessaly, for our constructive discussions.

Moreover, I would like to thank the Energy Sector of the Department of Mechanical Engineering of the University of West Attica for granting me the Ph.D. title.

I would also like to thank all the collaborators I had throughout these years. I sincerely thank Dr. José Marquez-Velasco for teaching me the basic principles of density functional theory (DFT) calculations. The postdoctoral fellows Dr. Polychronis Tsipas Dr. Evangelia Xenogiannopoulou, Dr. Stefanos Chaitoglou, and Dr. Dimitra Tsoutsou for our collaboration in the epitaxial growth of the materials used in this work and their characterization with X-ray spectroscopy (XPS), angle-resolved photoemission spectroscopy (ARPES) and scanning tunneling microscopy (STM). In addition, I would like to thank Evgenia Symeonidou and Dr. Panagiotis Pappas for our collaboration in performing and discussing the theoretical calculations.

I thank all the above and the rest of my collaborators, Dr. Christina Zacharaki, Nikitas Siannas, Dr. Nicholas Kelaidis, Akylas Lintzeris, Elli Georgopoulou-Kotsaki, Dr.

Alexandros El Sachat and Dr. Ikaros Hauge[+], for the cooperation we had, their invaluable moral support and the perfect environment we created.

For the experiments performed at SOLEIL Synchrotron radiation facility in Paris, I would like to thank Dr. Laëtitia Baringthon and Dr. Patrick Le Fèvre for our exceptional collaboration and their accommodation during our beam time. For the STEM results (Figures 3.5-3.8 and 4.5, 4.6) provided for this work I want to thank Dr. Praveen Kumar, Dr Carlos Alvarez and Dr. Hanako Okuno from CEA-Grenoble. For the XRD data (Figure 3.2) I would like to thank Dr. Aristide Lemaitre and Dr. Gilles Patriarche from University Paris-Saclay. For synchrotron XRD data (Figure 4.6) I also thank Dr. Roberto Sant and Dr. Gilles Renaud for University of Grenoble. For the magnetotransport measurements data (Figure 3.17) I want to thank Dr. Nicolas Reyren and Dr. Jean-Marie George from CNRS-Thales in Paris.

For providing free public access to the open-source codes *Wannier90*, *WannierTools*, and *Spirit*, I would like to thank A. Mostofi (Imperial College London), QuanSheng Wu (EPFL), and Gideon P. Müller (RWTH Aachen), respectively.

And final but most important, I thank my family who made me the person I am, my crazy beloved friends for the countless memories we share together, and my partner Natalia for all the beautiful moments and support she gave me all these years.

Publications in scientific peer-reviewed journals and conference presentations related to the present thesis:

Publications

[1] S. Fragkos, P. Pappas, E. Symeonidou, Y. Panayiotatos and A. Dimoulas, Magnetic skyrmion manipulation in $CrTe_2/WTe_2$ 2D van der Waals heterostructure, *Appl. Phys. Lett.* 120, 182402 (2022).

[2] E. Rongione, S. Fragkos, L. Baringthon, J. Hawecker, E. Xenogiannopoulou, P. Tsipas, C. Song, M. Mičica, J. Mangeney, J. Tignon, T. Boulier, N. Reyren, R. Lebrun, J.-M. George, P. Le Fèvre, S. Dhillon, A. Dimoulas and H. Jaffrès, Ultrafast Spin-Charge Conversion at $SnBi_2Te_4$/Co Topological Insulator Interfaces Probed by Terahertz Emission Spectroscopy, *Adv. Opt. Mater.* 10, 2102061 (2022).

[3] S. Fragkos, P. Tsipas, E. Xenogiannopoulou, Y. Panayiotatos and A. Dimoulas, *Type-III Dirac fermions in $Hf_xZr_{1-x}Te_2$ topological semimetal candidate*, *J. Appl. Phys.* 129, 075104 (2021).

[4] S. Fragkos, L. Baringthon, P. Tsipas, E. Xenogiannopoulou, P. Le Fèvre, P. Kumar, H. Okuno, N. Reyren, A. Lemaitre, G. Patriarche, J.-M. George and A. Dimoulas, *Topological surface states in epitaxial $(SnBi_2Te_4)_n(Bi_2Te_3)_m$ natural van der Waals superlattices, Phys. Rev. Materials* 5, 014203 (2021).

Conferences

[1] S. Fragkos, P. Tsipas, E. Xenogiannopoulou, Y. Panayiotatos and A. Dimoulas, Type-I, II and III topological Dirac semimetals in 1T transition metal ditelluride family, 35th *Panhellenic Conference on Solid State Physics and Materials Science*, Virtual, 26-29 September 2021. Oral presentation

[2] S. Fragkos, P. Tsipas, E. Xenogiannopoulou, Y. Panayiotatos and A. Dimoulas, Type-I, II and III topological Dirac semimetals in group IV 2D transition metal ditelluride family, *EUROMAT 2021*, Virtual, 13-17 September 2021. Oral presentation

[3] S. Fragkos, P. Tsipas, D. Tsoutsou, E. Xenogiannopoulou, R. Sant, C. Alvarez, G. Renaud, H. Okuno, Y. Panayiotatos and A. Dimoulas, Epitaxial $HfTe_2$, $ZrTe_2$ and type-III Dirac fermions in $Hf_xZr_{1-x}Te_2$ topological semimetal candidate, *APS March Meeting*, Virtual, 15-19 March 2021. Oral presentation

Table of Contents

Table of Figures

List of Abbreviations

AFM	Antiferromagnetic
ARPES	Angle-resolved photoemission spectroscopy
BZ	Brillouin zone
CBM	Conduction band minimum
CCD	Charge coupled device
DFT	Density functional theory
DMI	Dzyaloshinskii-Moriya interaction
DP	Dirac point
DSM	Dirac semimetal
EDC	Energy distribution curves
FM	Ferromagnetic
FWHM	Full width at half maximum
GGA	Generalized gradient approximation
GIXD	Grazing incidence X-ray diffraction
GMR	Giant magnetoresistance
HAADF	High-angle annular dark field
HK	Hohenberg-Kohn
HLN	Hikami-Larkin-Nagaoka
HM	Heavy metals
HRSTEM	High-resolution transmission electron microscopy
KS	Kohn-Sham
LDA	Local density approximation
LDOS	Local density of states
LLG	Landau-Lifshitz-Gilbert
LMR	Linear magnetoresistance
MBE	Molecular beam epitaxy
MCP	Multi-channel plate
MDC	Momentum distribution curves
MLWF	Maximally localized Wannier functions
MR	Magnetoresistance
MRAM	Magnetic random-access memory
MTJ	Magnetic tunnel junction

NMR	Negative magnetoresistance
PAW	Projector augmented waves
PBE	Perdew-Burke-Ernzerhof
PRAM	Parallel random-access memory
QAHE	Quantum anomalous Hall effect
QHE	Quantum Hall effect
QL	Quintuple layer
RHEED	Reflection high-energy electron diffraction
RRAM	Resistive random-access memory
SL	Septuple layer
SOC	Spin-orbit coupling
SOT	Spin-orbit torque
STEM	Scanning transmission electron microscopy
STM	Scanning tunneling microscopy
STS	Scanning tunneling spectroscopy
TB	Tight-binding
TEM	Transmission electron microscopy
TI	Topological insulator
TM	Topological material
TMD	Transition metal dichalcogenides
TMR	Tunneling magnetoresistance
TRAM	Topological-switching random-access memory
TSM	Topological semimetal
TSS	Topological surface state
UPS	Ultraviolet photoelectron spectroscopy
VASP	Vienna ab-initio simulation package
vdW	van der Waals
WAL	Weak antilocalization
WL	Weal localization
WSM	Weyl semimetal
XPS	X-ray spectroscopy
XRD	X-ray diffraction

1. Introduction to topological materials

It's been nearly ten years since the topological surface states were first detected in HgTe quantum wells experimentally [1.1] and seven years since the nomination of D. J. Thouless, F. D. Haldane and J. M. Kosterlitz with Nobel Prize in Physics, whose theoretical work established the role of topology in understanding exotic forms of matter. The term *topology* derives from a mathematical notion that was used to define an object's invariant property under continuous deformation. Topologically protected band structures give topological materials (TMs) their insensitive properties to impurities, defects, and deformations [1.2]. It is important to note that current theoretical researches suggest that approximately 25% of known materials are TMs [1.3-1.5], demonstrating the enormous potential and the wide research field. Reducing a system's dimension is more likely to result in new physical phenomena than it is in the case of bulk TMs, such as outstanding electrical and magnetic properties [1.6-1.12], and topological phase transitions [1.13-1.15]. This is because enhanced quantum effects and higher correlations typically occur in the 2D limit.

In atomically thin van der Waals (vdW) topological materials, where intralayer coupling plays a crucial role and many 2D vdW TMs exhibit unique electronic properties due to their reduced dimensionality, the fascinating nature of 2D systems is particularly obvious [1.15-1.19]. In addition, isolated 2D vdW TMs with atomically thin thicknesses can be put together in precisely determined way to form heterostructures [1.20]. These stackings of 2D TMs vdW heterostructures typically possess atomically abrupt interfaces between layers, which significantly enhances the 2D electronic systems and enables scientists to investigate proximity effect [1.21-1.24] and numerous unique quantum interface phenomena, like the fascinating and recently discovered twistronics based on graphene [1.25-1.28]. In 2D TMs vdW heterostructures, the transport of entropy, charge, and energy in the 2D limit will be impacted by the correlation interaction between electron, spin and phonon [1.29-1.33]. Therefore, it is anticipated that 2D TMs vdW heterostructures will display more novel physical characteristics, device applications, and controllable and optimized performance.

This Ph.D. thesis focuses on the three main types of 2D vdW TMs, including topological insulators (TIs), Weyl semimetals (WSMs), and Dirac semimetals (DSMs).

TIs are the first kind of materials with non-trivial topological properties that are insulating in the bulk but they have metallic character at surfaces. Their topological surface states (TSS), with their spin locked to the orbital momentum, are protected by time-reversal symmetry and created from the band inversion induced by the strong spin-orbit coupling (SOC) of the heavy atoms (Fig. 1.1) [1.34].

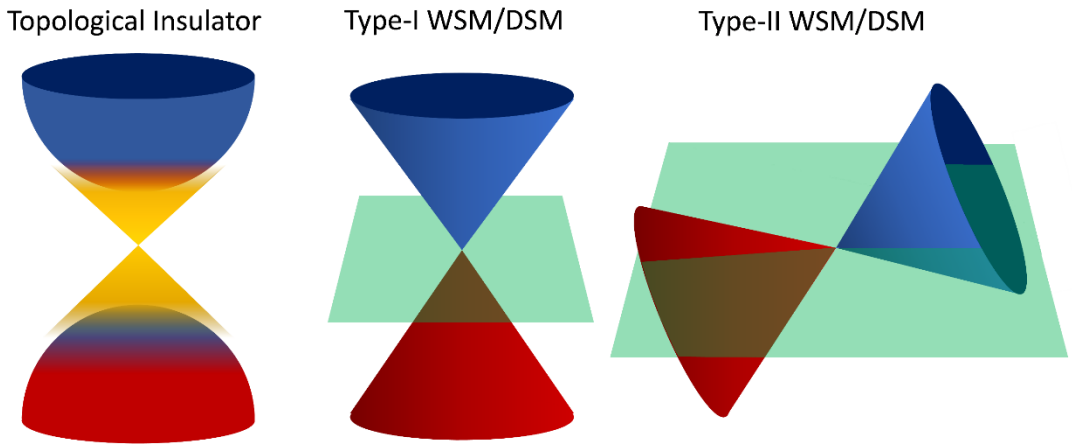

Figure 1.1. Schematic of the band structure for TI, type-I WSM/DSM and type-II WSM/DSM. The topological surface states of the TI are indicated with yellow color. The green planes are Fermi surfaces.

The first discovered vdW TIs are Bi_2Se_3, Bi_2Te_3, Sb_2Te_3 [1.35-1.37], whose physical properties, like temperature-insensitive giant and linear magnetoresistance [1.38], quantum oscillations [39], quantum Hall effect (QHE) [1.40] anomalous photoelectric effect [1.41], enhanced thermoelectric performance [1.42], and topological phase transition [1.13, 1.14], have been extensively studied. Additionally, a number of their multicomponent alloys with tunable band structures, including $Bi_2(Te_{1-x}Se_x)_3$ [1.43], $(Bi_{1-x}Sb_x)_2(Te_{1-y}Se_y)_3$ [1.44], $(Bi_{1-x}Sb_x)_2Se_3$ [1.45], and $(Bi_{1-x}Sb_x)_2Te_3$ [1.46] have also been systematically studied, with tunable band structures, and a series of tunable properties [1.47-1.51] and device performance [1.52-1.54] based on their 2D morphology. Additionally, the effects of dimensionality reduction will significantly alter the electronic band structure of 2D vdW TMs, leading to a topological phase transition that produces 2D vdW TIs. Monolayers of T_d-$MoTe_2$, T_d-WTe_2, and $ZrTe_5$ are great examples [1.15, 1.55, 1.56], and experimental studies on the physical properties and device applications are reported [1.6, 1.7, 1.22, 1.57]. Recently, $MnBi_2Te_4$ [1.19] and Cr/V-doped $(Bi_xSb_{1-x})_2Te_3$ [1.9], have been experimentally identified as 2D vdW TIs with inherent magnetism. In these magnetic vdW TIs, long-

range magnetism breaks time-reversal symmetry which gives rise to the quantum anomalous Hall effect (QAHE) [1.9, 1.19]. The fields of electronics, spintronics, thermoelectrics, electrochemistry, and optoelectronics are the present emphasis of 2D vdW TI applications. Exotic particles contained in 2D TIs have the potential for many future uses. For instance, Majorana modes based topological quantum computing [1.58], spin-orbit torque (SOT) magnetic devices [1.59] and electrically-driven magnetic-memory based on *k*-space magnetic monopoles [1.60] or skyrmions [1.61].

In topological semimetals (TSMs), including WSMs [1.62] and DSMs [1.63], the valence and conduction energy bands cross each other at (or close to) the Fermi level (E_F) (Fig. 1.1). TSMs can be classified into type-I where the E_F crosses the top or bottom Dirac cone, while in type-II TSMs the E_F crosses both the top and bottom Dirac cones (Fig. 1.1). For WSMs, the energy bands are described by the Weyl equation, and possess linear dispersion around the Weyl point, which is attributed to the massless nature of the carriers [1.64]. Weyl points in the *k*-space are chiral and are protected by time-reversal symmetry. T_d-WTe_2 [1.65] and T_d-$MoTe_2$ [1.66], are examples of traditional vdW WSMs. They are all categorized as type-II WSM, which is made possible by breaking the type-I WSM's Lorentz invariance [1.67]. The 2D vdW WSMs T_d-WTe_2 and T_d-$MoTe_2$ have a wide range of tunable physical properties, including gate/magnetic field tuned superconductivity [1.68, 1.69], anisotropic photoresponse [1.70], giant magnetoresistance (GMR) [1.71, 1.72], quantum oscillations [1.65], robust room temperature ferroelectric-switching [1.12], robust spin-polarization [1.73], and ultrafast spin-relaxation [1.74]. These materials have a wide range of potential applications in memories [1.75, 1.76] and spintronics [1.77-1.79].

When two Weyl nodes with opposing chirality coincide at the same *k*-point, the Dirac points of DSMs emerge. The Dirac point is hence quadruply degenerate. The DSMs are protected by both time-reversal and crystal (rotational) symmetries in contrast to the WSM. The following 2D materials have been classified as type-II DSMs: $PtSe_2$ [1.80], $PtTe_2$ [1.81], $PdTe_2$ [1.82], $NiTe_2$ [1.83], $ZrTe_2$ [1.84], $ZrTe_5$ [1.85] and $HfTe_5$ [1.86]. These 2D vdW DSMs, do not only display special characteristics that are either the same as or different from those of graphene, but they also support the miniaturization and low-energy consumption of electronic devices and offer additional exotic applications based on Weyl or Dirac fermions in the future, such as high fault-tolerant

quantum computing and high-frequency transistor. An overview of all the above-mentioned applications and properties based on TIs and TSMs is shown in Fig. 1.2.

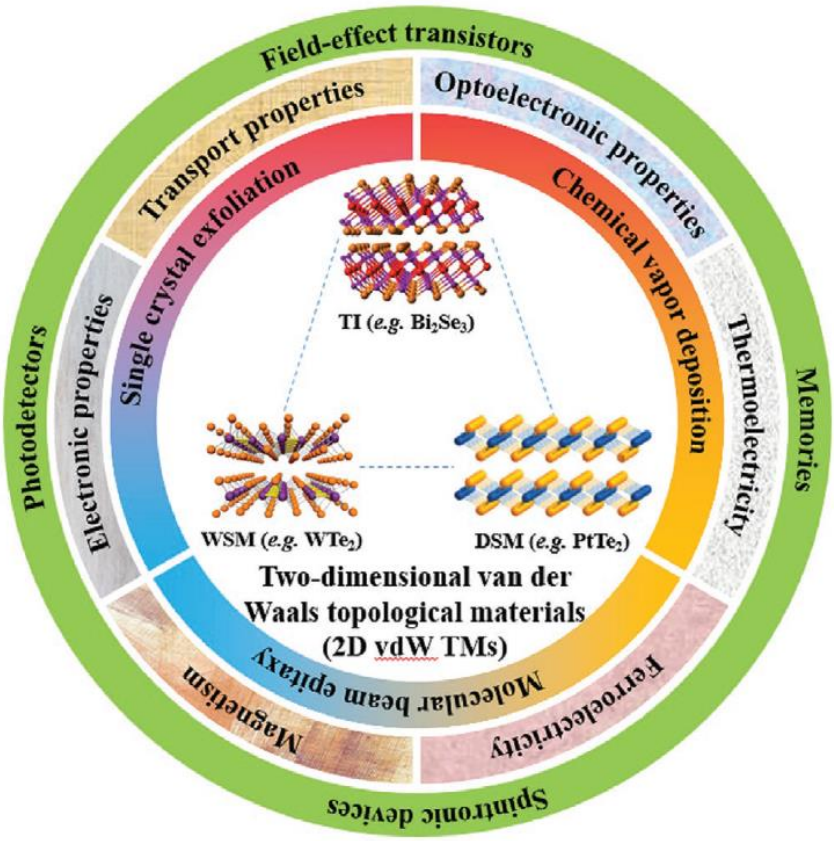

Figure 1.2. Overview framework based on 2D vdW TMs [1.87].

In addition to current experimental research, theoretical calculations and modeling are powerful when it comes to the quest for new 2D TMs [1.88, 1.89], while they have also proven to be indispensable tools for the deeper understanding of the underlying physics, particularly the quantum effects of 2D crystals, as compared to bulk materials [1.90-1.94]. These days, a range of computation and simulation techniques are available to conveniently demonstrate the dimensionality-driven band structure evolution (or topological phase transition) in vdW TMs with controlled thickness, which is difficult to observe in experiments. Even though their bulk counterparts are 3D TIs, the vdW TIs Bi_2Se_3, Bi_2Te_3, and Sb_2Te_3's *GW* calculations show that they have different topological phases in their same-thickness 2D structure [1.90]. For instance, 2 QL Sb_2Te_3 and 2 QL Bi_2Te_3 exhibit a topologically trivial band structure and a non-trivial quantum spin-Hall phase, respectively. In addition, Zhang et al. [1.94] discovered the alternating transition between topologically trivial and non-trivial band structure in both

2D Bi_2Se_3 and Bi_2Te_3 with decreasing thickness from 20 to 1 QL using first-principles calculations. Furthermore, theoretical simulations demonstrate that the bulk counterparts of the antiferromagnetic vdW materials $MnBi_2Te_4$ and $MnSb_2Te_4$ all have TI states while changing their band structure and magnetism in few-layer 2D structures [1.91]. The axion insulator phase and the QAHE are theoretically anticipated to be realized in the monolayer $MnBi_2Te_4$ ferromagnet, which is a topologically trivial and displays the alternating transition between ferrimagnetism and antiferromagnetism for odd and even number of layers, respectively [1.93]. Dimensional effects impact not just the properties of TIs but also the properties of TSMs. T_d-WTe_2 shows nonmonotonically thickness-dependent thermal conductivity from bulk to few-layer 2D structure, whereas $MoTe_2$ exhibits band structure evolution from semimetalic to semiconducting [1.92]. According to theoretical calculations, these characteristics are caused by, respectively, changing phonon dispersions in 2D WTe_2 and rising interband SOC in 2D $MoTe_2$. Additionally, Yao et al. [1.95] theorized the existence of the topological phase transition from a WSM to a 2D TI in $TaIrTe_4$ when its thickness is reduced down to the single layer, and also in WSMs WTe_2 and $MoTe_2$.

The discussion below, will focus on some properties of 2D vdW TMs, including the electronic and transport properties, which are also studied in the materials of this dissertation (Chapters 3-6). In addition, the potential challenges and advantages of 2D vdW TMs in two types of microelectronic-related devices, such as memory and spintronic devices will be discussed.

1.1. Properties

Symmetry protected topological states of TMs, are highly robust against material impurities, defects and disorder, and can be manipulated by quantum regulations and topological phase transitions. The band structure evolution brought on by the 2D quantum confinement effect causes 2D vdW TMs to exhibit some noticeable alterations in properties when compared to the bulk equivalent [1.13-1.15]. Additionally, it is possible to realize a variety of unusual physical phenomena and comprehend their causes by carefully controlling and optimizing the properties of vdW TMs using magnetic fields [1.69], electric fields [1.6, 1.7, 1.9, 1.51, 1.71], light [1.41], proximity effect [1.21-1.23], etc. The discussion will be focused on the electrical and transport properties of 2D vdW TMs.

1.1.1. Electronic Properties

When compared to their bulk counterparts, 2D vdW TMs have shown unique physical characteristics in the 2D limit, such as massless Dirac fermions in monolayer graphene with unique QHE and high carrier mobility [1.96, 1.97]. Understanding 2D vdW TMs' distinctive physical properties and potential applications essentially depends on characterizing their electronic properties. To acquire electronic properties from 2D vdW TMs, angle resolved photoemission spectroscopy (ARPES) technique can be performed, which although requires high-quality materials with clean, vast and extremely homogeneous single crystal domains. This section, is focused on the topological electronic states and topological phase transitions of vdW TMs.

1.1.1.1. Topological Electronic States

ARPES is a band structure imaging method that uses the photoelectric effect to gather data on the momentum and binding energy of materials in *k*-space. In Chapter 2.2.3, the ARPES approach is covered in more detail. In high-quality 2D Bi_2Te_3 thin films, Xue et al. [1.98] in 2010 directly demonstrated the massless Dirac TSS and the lack of bulk conduction bands at the E_F (Fig. 1.3a). Other TIs including Bi_2Se_3 and Sb_2Te_3 have been shown to have comparable band structures [1.99]. These findings show that spin-polarized Dirac fermions, unique gapless electronic states, linear dispersion with locked spin-momentum, are present in the TSS. Within the 2D limit, vdW TSMs also support topological electronic states aside from TIs. Both 1 and 3 layers of $ZrTe_2$ thin films showed a Dirac-like cone, according to Tsipas et al. [1.84] (Fig. 1.3b). This characteristic shows that the massless Dirac fermions, which can be seen of as having properties similar to graphene (for example, a Fermi velocity 60% of graphene), are still present in the DSM $ZrTe_2$ in the 2D limit. Fermi arcs, which are topologically protected surface states, are another feature of 2D type-II WSMs. Anisotropic chiral transport properties and other unique quantum phenomena appear as a result of the bulk band's significant tilt near the Weyl point [1.71, 1.100-1.102]. For instance, the band number of 2D WTe_2 decreases when the thickness is reduced from 5 to 2 layers (Fig. 1.3c) [1.103]. In parallel, the hole-like band dispersions around the Fermi level change as they move below the Fermi level, indicating the transition from semimetal to insulator by opening a small bandgap (Fig. 1.3d). It is significant to note that monolayer WTe_2 transforms into an intrinsic 2D TI with gapless edge states in the bulk

band gap at temperatures lower than 100 K, as directly demonstrated by scanning tunneling spectroscopy (STS) spectra (Fig. 1.3e) [1.104]. As the gate voltage changes from a negative to a positive value, the applied electric-field changes the E_F and the bulk band gap of WTe_2 monolayer continues to increase (Fig. 1.3e). As a result, 2D few-layer WTe_2 already demonstrates a variety of tunable electronic characteristics, opening the door to tunable properties and potential applications [1.6, 1.22, 1.105-1.107].

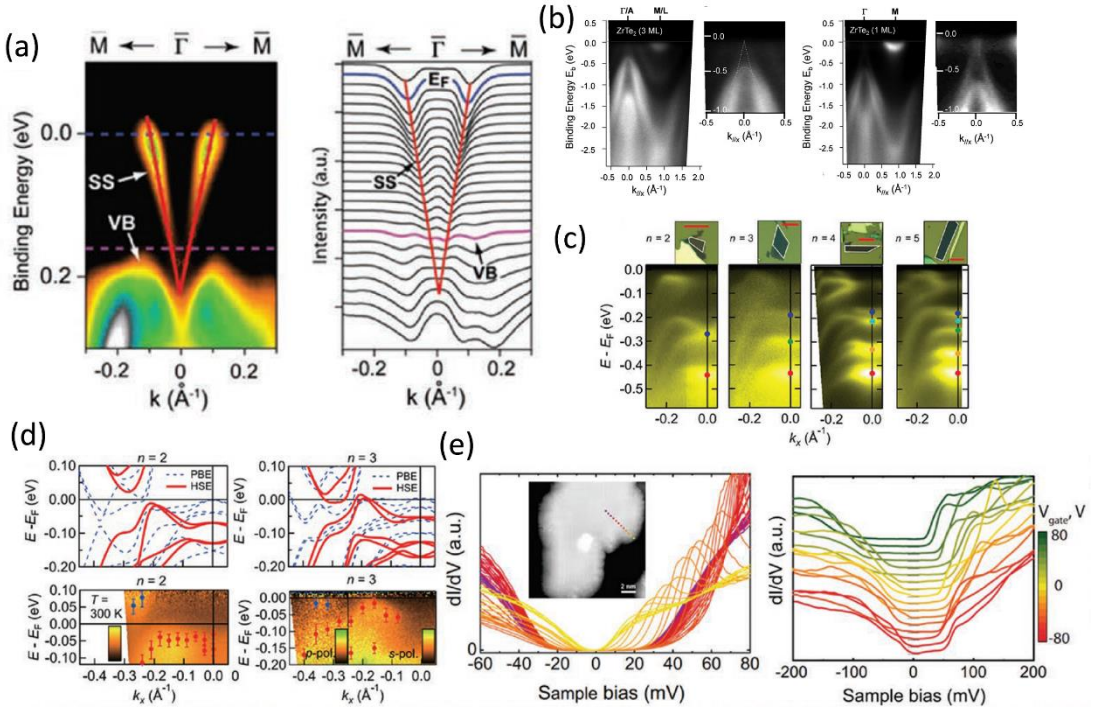

Figure 1.3. (a) Electronic band structure of 80 nm Bi_2Te_3 obtained by ARPES and the corresponding momentum distribution curves [1.98]. (b) Band structure of 1 and 3 $ZrTe_2$ monolayers [1.84]. (c) Optical images and the corresponding energy bands of 2-5 WTe_2 layers [1.103]. (d) ARPES and density theoreticaly obtained band structures of 2-3 layers WTe_2. (e) STS spectra of WTe_2 monolayer [1.104].

1.1.1.2. Topological Phase Transition

Topological phase transitions are special phase transitions that do not involve symmetry breaking. The topological phase transition in 2D vdW TMs can be influenced by a variety of variables, including thickness [1.13, 1.14, 1.16, 1.57], dopant concentration [1.108, 1.109], disorder [1.110], and magnetic field [1.111]. Due to the tunable thicknesses and pronounced effects of the 2D quantum confinement on the chemical potential of the electronic band structure, thickness or dopant concentration-induced topological phase transitions in the vdW TMs are quite common. When the

thickness is reduced to the 2D limit, some 2D vdW TMs experience a topological phase transition [1.14, 1.19, 1.98, 1.112, 1.113]. Theoretically, a 2D Bi_2Se_3 thin film undergoes a thickness-driven topological phase transition from a 2D trivial insulator to a 2D quantum spin Hall state to a 3D TI with increased thickness (Fig. 1.4a) [1.14]. In fact, the ARPES measurements show that when the thickness of 2D Bi_2Se_3 thin films increases from 2QL to 8QL, the band dispersions noticeably change (Fig. 1.4b). In 8QL Bi_2Se_3 thin film, the Dirac linear dispersion is observed, which is similar to the bulk counterpart. The band hybridization in-between the top and bottom TSS of TIs like Bi_2Se_3 and Bi_2Te_3 is responsible for the formation of a topologically trivial insulating state [1.99]. The Dirac semimetal-to-normal metal transition of 2D $PtTe_2$ occurs when the thickness is below 4-6 layers (Fig. 1.4c) [1.112], which is comparable to the Dirac semimetal-to-semiconductor transition of 2D $PtSe_2$ when the thickness is below 2.5 nm [1.113]. While the topological nature of WSM T_d-WTe_2 is still present in the 2D limit, a topological phase transition from WSM to TI takes place. Conducting edge states have been directly seen in monolayer T_d-WTe_2 in 2019 utilizing microwave impedance microscopy measurement, in accordance with the typical TI characteristic [1.16, 1.95]. Many 2D vdW TMs have the intriguing and important property of thickness-driven topological phase transitions. When the thickness of a vdW TM is reduced to a critical level, these phase transitions have a significant impact on the transport properties and future device applications. Examples include the use of $PtSe_2$ ultrathin semiconductor in (opto)electronic devices [1.113] and the dramatically enhanced resistance of T_d-WTe_2 in monolayer [1.114]. Other approaches for inducing the topological phase transition include doping and disorder. The topological surface states of the 2D $(Bi_{1-x}In_x)_2Se_3$ thin film gradually converge into the bulk states as the SOC decreases by adding In [1.108, 1.109]. By adjusting the thickness and In concentrations, three distinct phases, including topological-metal, trivial-metal, and trivial-insulator, can transform into one another (Fig. 1.4d). Furthermore, Brahlek et al. [1.110] investigated in a 2D Bi_2Se_3 thin film the robustness of topological properties with different levels of disorder and discovered that the high disorder breaks the topological invariant, forcing the film into the insulating trivial state. As a result of the disrupted crystalline order in long-range and the insulating nature, respectively, ARPES and STS results are absent in high disorder circumstances. In conclusion, the topological phase transition is a key tool for realizing and controlling unusual topological quantum states, such as the

quantum spin Hall state and the QAH state, and for advancing knowledge of the band structure evolution impact on topological features.

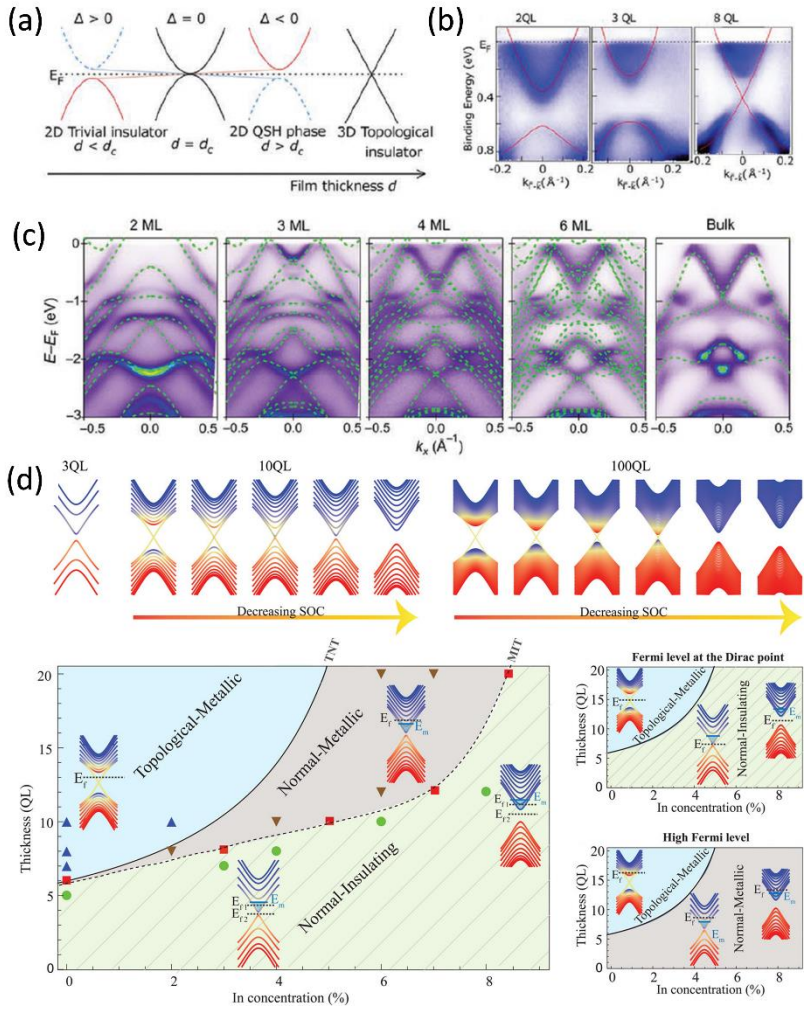

Figure 1.4. (a) Schematic illustration of the thickness dependence of topological phase transition in Bi_2Se_3 and (b) ARPES spectra of Bi_2Se_3 at different thicknesses [1.14]. (c) Thickness dependence of $PtTe_2$ band structure [1.112]. (d) Topological phase diagram of $(Bi_{1-x}In_x)_2Se_3$ for different thicknesses and In concentration [1.109].

1.1.2. Transport Properties

The TSS in TIs come from locked spin-momentum of electrons, which allows them to move freely in the TSS without being scattered [1.115]. Additionally, bulk valence and conduction bands of TSMs have similar linear dispersion to the TSS of TIs. The transport characteristics of nanodevices typically indicate these stable, novel electronic states in 2D TMs, which can influence the mobility of electrons in a material [1.34]. The E_F and carrier density control of vdW TMs have recently been the focus of numerous attempts, including doping, [1.116], and field-effect gating [1.6, 1.47, 1.71]. Particularly, 2D vdW TMs frequently display unusual transport properties, including

giant magnetoresistances [1.38, 1.71, 1.72, 1.117], quantum oscillation [1.39, 1.65, 1.116], QHE [1.40, 1.49], weak localization (WL), and weak antilocalization (WAL) [1.8, 1.21, 1.47, 1.118, 1.119]. Understanding these transport processes is crucial to comprehending the nature of vdW TMs. The emergence and control of magnetoresistance, WL and WAL will be discussed in this section, which are also investigated on the materials studied in Chapter 3 of this work.

1.1.2.1. Magnetoresistance

Linear magnetoresistance (LMR) was first observed in Bi by Kapitza in 1928 [1.120]. The LMR effect has been reported in numerous vdW TMs and is widely used in magnetic sensors, hard drives and magnetic storage [1.38, 1.117, 1.121, 1.122]. Investigations into the physical origins of LMR in TMs are currently ongoing, however the quantum model [1.123] or classical model [1.124] best explain its behavior. In a low electron-concentration system, such as vdW TMs with zero bandgaps and linear dispersion, the LMR is predicted to occur when the lowest Landau level is occupied. In various 2D vdW TMs, including Bi_2Se_3 nanosheet [1.117] and Bi_2Te_3 nanosheet [1.39], the giant LMR has been reported (Fig. 1.5a).

When electron and hole carriers are transported simultaneously in some TSMs, the magnetic field will undergo electron-hole resonance, which will result in the development of giant MR (GMR) (Fig. 1.5b) [1.125, 1.126]. For instance, the GMR observed in the electrostatic top-gated 2D WTe_2 nanosheet is proven to have originated from the electron-hole compensation process [1.71]. In 2D $MoTe_2$ nanosheet [1.72] and $ZrTe_5$ thin flake [1.127], similar behavior and physical origins have also been discovered. However, this GMR effect in vdW TSMs often decreases with lower thickness due to the hole-electron balance and the reduction in carrier density and when the thickness is reduced. In vdW WSMs with doping oxidized surface, it is shown that the loss of mobility is still another component that contributes to the suppression of MR [1.126].

Except from the positive MR in perpendicularly applied magnetic fields, a negative MR (NMR) has been shown in 2D $ZrTe_5$ nanosheet (Fig. 1.5c) [1.127], $ZrTe_2$ thin film [1.128], $HfTe_5$ nanosheet [1.129], and Bi_2Se_3 nanosheet [1.130] by applying a parallel external magnetic field. The NMR effect arises due to the chiral anomaly which originates from nontrivial Berry curvature [1.127]. In general, it's critical to

comprehend the causes of and control mechanisms over the MR in 2D vdW TMs, which is mostly related to the intrinsic topological band structure, mobility and carrier density.

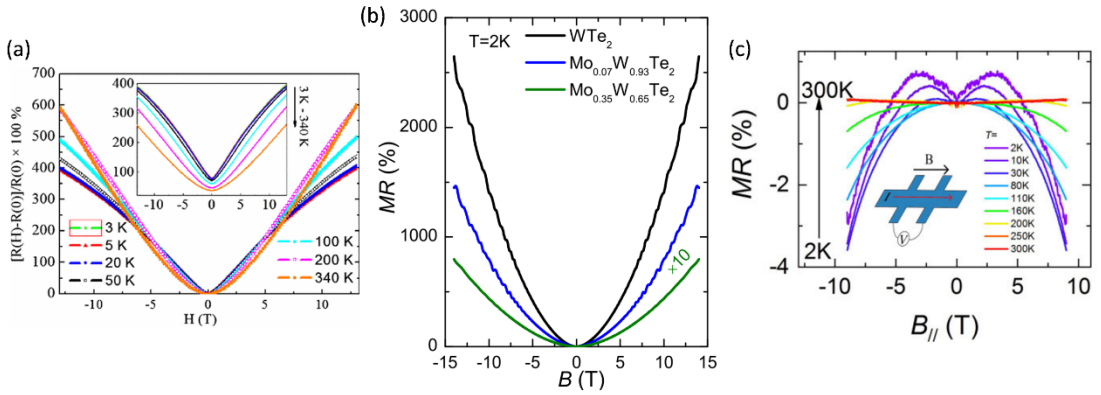

Figure 1.5. (a) LMR curves of Bi_2Te_3 at various temperatures [38]. GMR measurements in $Mo_xW_{1-x}Te_2$ for different Mo concentrations [1.126]. (c) NMR effect in 2D $ZrTe_5$ under parallel applied magnetic field [1.127].

1.1.2.2. Weak Localization and Antilocalization effects

When the temperature rises, the WL, which results from coherently backscattered conduction electrons which constructively interfere, will disrupt [1.131]. Additionally, Weyl or Dirac fermions in TMs with linear Dirac dispersion relations and spin-orbit interaction induce a nontrivial Berry phase in *k*-space and result in interference cancellation [1.132]. Due to its connection to the non-trivial Berry phase in the strong spin-orbit interaction of TM systems, this quantum impact lowers the possibility of backscattering, thus emerging the WAL effect, which might also be present at high temperatures [1.133]. In general, the phase coherence length l_φ and coefficient a, which are used to assess the type of localization, are extracted in order to investigate the evolution and origin of WL and WAL. The 2D quantum confinement effect will drive the transition from a 3D to a 2D WAL, which depends on the relative thickness of the TMs and between l_φ (Fig. 1.6a) [1.134]. WL and WAL have so far been observed in a large number of 2D vdW TMs [1.8, 1.50, 1.118, 1.119, 1.135]. The strong downward resistance dip is a typical transport property of WAL, which can occasionally only occur in a perpendicular magnetic field ($B \perp I$) (Fig. 1.6b) or occasionally exists in both a parallel magnetic field (B||I) and a perpendicular magnetic field ($B \perp I$) (Fig. 1.6c). The former implies the WAL's typical 2D character, which results from strong SOC systems [1.8].

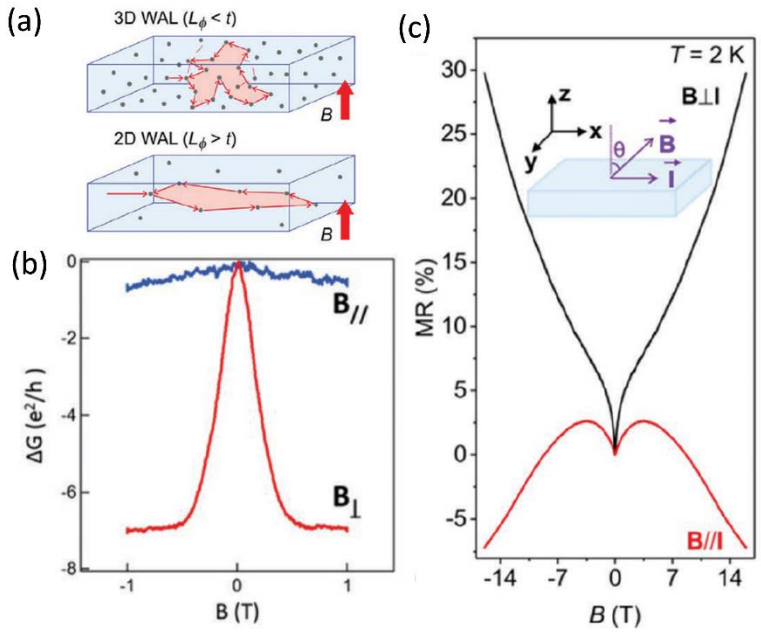

Figure 1.6. (a) Schematic of 2D and 3D WAL [134]. (b) ΔG magnetoconductance for a 2D T_d-$MoTe_2$ for perpendicular and parallel magnetic fields [1.8]. (c) MR for a 2D $BiSbTeSe_2$ under perpendicular and parallel magnetic fields [1.50].

The latter suggests that topological surface states and bulk states jointly contribute to WAL, and it is crucial to quantitatively describe the contributions of surface states and bulk states. Hikami-Larkin-Nagaoka (HLN) theory [1.136] and anisotropic magnetoconductance [1.50] are two methods that could be used to extract the contribution of topological surface states. In addition, it has been demonstrated that changing the temperature [1.102, 1.137], magnetic field [1.138], and gate voltage [1.51] may achieve the crossover between WL and WAL in 2D vdW TMs. Additionally, 2D vdW TMs like $(Bi_{0.57}Sb_{0.43})_2Te_3$ [1.51] and WTe_2 [1.139] have shown a gate-tunable transition between WAL and WL. These reports were all examined using HLN theory, and the variations of the phase coherence length are attributed to gate voltages. The ambipolar control between WAL and WL is achieved, for instance, by a few-layer WTe_2 exhibiting a highly adjustable strong SOC [1.139]. These findings suggest that the WL and WAL can be studied on vdW TMs, which typically have an element with a large atomic number and consequently strong spin-orbit interaction.

1.2. Device applications

Due to their tunable thickness, topological stability of electronic band structure and physical properties in general, vdW TMs have a wide range of possible device applications. In addition to advancing our understanding of the novel state of

matter and band structure, studies and fabrication of cutting-edge vdW TMs devices also support the development of next-generation 2D topological electronics with low-power and high-speed. This section will focus on two types of applications closely related to the modern industry of microelectronics, including memories and spintronic devices.

1.2.1. Memories

The need for data storage with non-volatility, high-density, high-speed, radiation resistance and low-power consumption can be achieved by non-volatile memories. Due to their significant downscaling potential, ease of stacking, large spin-orbit torque (SOT) efficiency, strong SOC, strain, and electric-field driven phase transition, vdW TMs-based memories display unique and powerful device capabilities [1.75, 1.76, 1.140, 1.141]. Magnetic random-access memory (MRAM), resistive random-access memory (RRAM), and topological switching random-access memory (TRAM) are the three types of recently developed vdW TMs-based memories. The SOT-MRAM based on 2D vdW TIs demonstrate greater efficiency with higher read and write speeds due to the strong SOT on contiguous magnetization produced by the spin-momentum locking TSS [1.142, 1.143]. Wu et al. in 2021 [1.144] successfully incorporated 10 nm $(Bi,Sb)_2Te_3$ layer in magnetic tunnel junction (MTJ) (Fig. 1.7a). The outstanding performance of this SOT-MRAM advanced prototype device was demonstrated by the enormous room temperature tunneling MR (TMR) ratio and extremely low switching current density. High SOT efficiency is crucial for improving SOT-MRAM performance. Above room-temperature SOT efficiency up to 1.59 is predicted in this TI-based MTJ by shifting the critical switching magnetic field. Future logical conversion and data storage applications for SOT-MRAM based on 2D vdW TIs will be very promising due to its one order of magnitude larger SOT efficiency than the conventional heavy metals.

RRAM is a type of memory in which conductive channels form and break in the material to control the device's high and low resistance. Due to their conducting TSS and multiphase transition, respectively, vdW TMs like 2D TIs and 2D $MoTe_2$ are appropriate for building RRAM [1.75, 1.76, 1.145]. Up to this point, RRAM based on vdW TMs have been reported in Sb_2Te_3 [1.146], Bi_2Se_3 [1.145], and $MoTe_2$ [1.75]. Along with the vdW TIs, the 2D $MoTe_2$ nanosheet exhibits a large room-temperature

on/off current ratio up to 106 and 107 in nanosecond to sub-nanosecond switching RRAM with its electric field and strain tunable phase transitions from semiconducting 2H phase to semimetalic T_d phase, respectively [1.75, 1.76]. These findings point to the enormous potential of vdW TMs for applications involving photo-regulated, nanosecond/sub-nanosecond switching, and non-volatile RRAM (Fig. 1.7b). By building the GeTe/Sb_2Te_3 superlattice (Fig. 1.7c), a new type of memory, namely TRAM, was created that does not involve melting during the reset process [1.87]. Charge injection is used to power 2D GeTe/Sb_2Te_3-superlattice-based TRAM as compared to Joule-heat in $Ge_2Sb_2Te_5$-based parallel RAM (PRAM). Moreover, the high-low resistances of TRAM often only involve short-range atomic migration, in contrast to the PRAM transition from the crystalline to the amorphous state. This characteristic guarantees that TRAM's critical switching voltage (0.6 V) is lower than PRAM's (1 V).

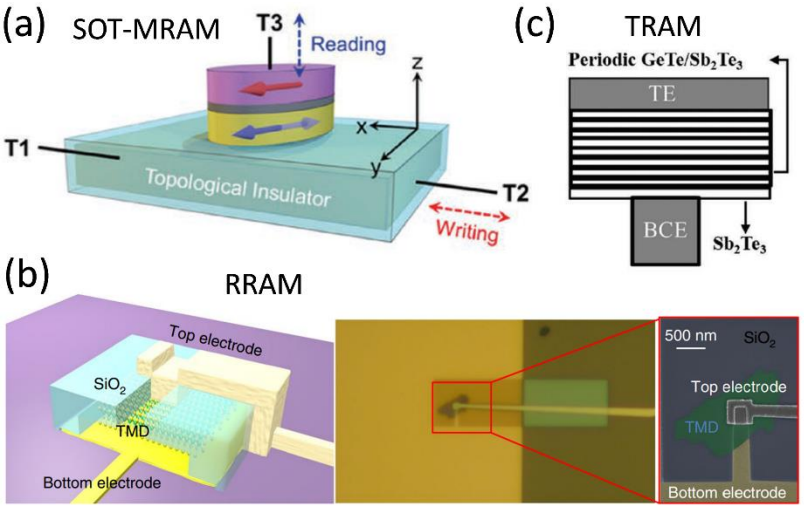

Figure 1.7. (a) Schematic illustration of a TI-based SOT-MRAM [1.141]. (b) Schematic diagram of a vertical $MoTe_2$-based RRAM device and optical and SEM images showing of the fabricated device [1.75]. (c) Schematic of the 2D GeTe/Sb_2Te_3 TRAM cell, where the BCE and TE are the bottom and top electrodes, respectively [1.87].

Currently, 2D vdW TMs-based TRAM need additional theoretical and practical research. Overall, despite the 2D vdW TMs-based memory's great potential in next-generation spintronics and electronics, there is still much work to be done in terms of conceptual design, the process of preparing devices (such as creating high-quality device interfaces, developing new device structures, and integrating processes), and understanding internal mechanisms.

1.2.2. Spintronic devices

Spintronic devices based on 2D vdW TMs combine electron spin and topology, advancing and deepening spintronics research. The spin-valve device [1.54, 1.147], spin dynamics [1.73, 1.74, 1.148, 1.149], and low-power current-driven magnetization switching [1.77-1.79, 1.150] are also essential for next-generation low-power spintronic devices, such as SOT-MTJs, aside from the vdW TI-based memories that were covered in the previous section.

For multifunctional spintronics, current control is more viable than voltage control. When a current flows on the surface of a TI, spin-momentum locking, a key property of the nontrivial TSS in TIs, causes an in-plane spin-polarized current which is perpendicular to the current direction [1.147]. A 2D vdW TI-based spin-valve device, such as a 2D $BiSbTeSe_2$-based spin-valve device with NiFe electrodes (Fig. 1.8a) [1.54] or a 2D Bi_2Se_3-based spin-valve device with Ni electrodes [1.147], is based on the current-induced spin-polarization of the 2D vdW TI surface and the changes in the relative magnetization orientations of the ferromagnetic electrode. Therefore, such a spin-valve effect is accomplished between one spin-polarized ferromagnetic electrode and the current-driven spin polarization of the TSS (Fig. 1.8b). The pumped spin current is enhanced by the strong SOC in the 2D vdW TI layer and is mostly transformed into a DC-voltage signal by the inverse spin Hall effect of the TI. For instance, a 2D Bi_2Se_3-based spin pump device (Fig. 1.8c) is composed of a 2D Bi_2Se_3 thin film, a magnet made of CoFeB, and a top protective layer made of MgO that serves to isolate oxygen from the coplanar waveguide [1.151].

Due to their robust SOC, topologically protected band structure, high charge-to-spin conversion efficiencies, and strong intrinsic spin-Hall effect, many 2D vdW TMs, including Bi_2Se_3 [1.152], $(Bi_{1-x}Sb_x)_2Te_3$ [1.150], T_d-$MoTe_2$ [1.79], and T_d-WTe_2 [1.77, 1.78], have demonstrated current-driven magnetization switching. Yang et al. [1.78] proposed the 2D WTe_2/NiFe thin film heterostructure with room temperature low-power SOT induced magnetization switching and an easy axis for with out-of-plane magnetization. Importantly, under a small in-plane current pulse, the SOT generation in WTe_2 thin film can efficiently reverse the magnetic moments of the NiFe, a current which is two orders of magnitude smaller than that of devices using heavy metals. Additionally, the study of 2D ferromagnetism and vdW-integrated spintronics

has been advanced due to recently found 2D vdW ferromagnets [1.153]. Therefore, 2D TMs/ferromagnet vdW heterostructures like $ZrTe_2/CrTe_2$ [1.154], WTe_2/Fe_3GeTe_2 [1.155, 1.156], and $(Bi_{1-x}Sb_x)_2Te_3/Fe_3GeTe_2$ [1.150] are likewise capable of current-induced magnetization switching, and they exhibit critical current densities that are typically similar to those of heavy metal/ferromagnet heterostructures. However, due to the low T_c of these 2D ferromagnets, they can be used only at low temperatures for current-driven magnetization switching. For current-driven magnetization switching devices, the critical switching current density and operating temperature are the most crucial performance factors. These findings show the electric magnetization-switching due to charge-to-spin in a vdW TM/ferromagnet heterostructure and open the door to current-driven, low-power magnetization control using spintronics built on 2D vdW TM.

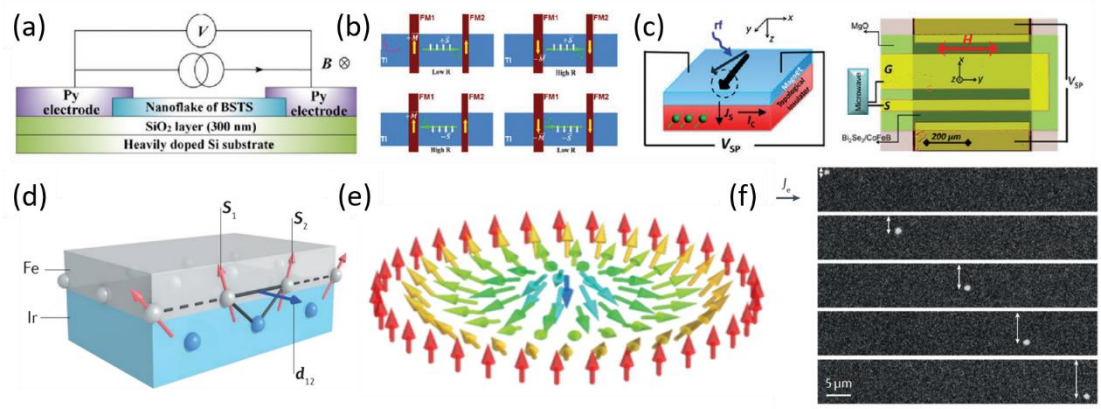

Figure 1.8. (a) Schematic illustration of the $BiSbTeSe_2$-based spin-valve device [1.54]. (b) The spin-dependent transportation process for 2D TIs-based spin-valve devices are shown schematically [1.147]. (c) Schematic illustration and the optical image of the 2D Bi_2Se_3 spin pumping device [1.151]. (d,e) Schematic picture of the DMI and of a Neel-type skyrmion [1.61]. (f) Current-induced skyrmion manipulation images obtained by Kerr microscopy [1.61].

In addition to current-driven magnetization switching in 2D vdW TM/ferromagnet heterostructures, the Dzyaloshinskii–Moriya interaction (DMI) arises (Fig. 1.8d) , due to the strong SOC and broken inversion symmetry at the interface [1.61, 1.157]. DMI has been recognized as a key ingredient in the creation, stabilization, and manipulation of magnetic skyrmions (Fig. 1.8e). The possibility of incorporating topology into electronic devices for communications and information storage provided by magnetic skyrmions may be particularly appealing. Skyrmion racetrack memories, skyrmionic logic devices, and skyrmion radio frequency devices are the most promising applications [1.61, 1.157]. The research of magnetic skyrmions is being pushed towards

the 2D limit, combining 2D vdW TMs, due to their strong SOC, with 2D magnets. In mechanically exfoliated heterostructures of Fe_3GeTe_2 with WTe_2, Néel-type skyrmions have been observed [1.158]. Additionally, heterostructures with TIs and compounds related to Cr_xTe_y have been extensively investigated [1.159-1.161], where the topological Hall effect (which is caused by electrons scattered on skyrmions) has been observed. The next target in these systems is the skyrmion motion driven by the electric currents and SOT (Fig. 1.8f) [1.61, 1.157]. Due the spin-momentum locking in the TSS, and strong SOC these systems are expected to manipulate skyrmions with lower power compared to the usual heavy metals, thus making them very promising for spintronic applications.

References

[1.1] M. König, S. Wiedmann, C. Brüne, A. Roth, H. Buhmann, L. W. Molenkamp, X.-L. Qi, and S.-C. Zhang, Science **318**, 766 (2007).

[1.2] X.-L. Qi and S.-C. Zhang, Physics Today **63**, 33-38 (2010).

[1.3] M. G. Vergniory, L. Elcoro, C. Felser, N. Regnault, B. A. Bernevig, and Z. Wang, Nature **566**, 480 (2019).

[1.4] F. Tang, H. C. Po, A. Vishwanath, and X. Wan, Nature **566**, 486-489 (2019).

[1.5] T. Zhang, Y. Jiang, Z. Song, H. Huang, Y. He, Z. Fang, H. Weng, and C. Fang, Nature **566**, 475 (2019).

[1.6] V. Fatemi, S. Wu, Y. Cao, L. Bretheau, Q. D. Gibson, K. Watanabe, T. Taniguchi, R. J. Cava, and P. Jarillo-Herrero, Science **362**, 926 (2018).

[1.7] D. A. Rhodes, A. Jindal, N. F. Q. Yuan, Y. Jung, A. Antony, H. Wang, B. Kim, Y.-C. Chiu, T. Taniguchi, K. Watanabe, K. Barkmak, L. Balicas, C. R. Dean, X. Qian, L. Fu, A. Pasupathy, and J. Hone, Nano Lett. **21**, 2505 (2021).

[1.8] C. H. Naylor, W. M. Parkin, J. Ping, Z. Gao, Y. R. Zhou, Y. Kim, F. Streller, R. W. Carpick, A. M. Rappe, M. Drndic, J. M. Kikkawa, and A. T. C. Johnson, Nano Lett. **16**, 4297 (2016).

[1.9] C.-Z. Chang, J. Zhang, X. Feng, J. Shen, Z. Zhang, M. Guo, K. Li, Y. Ou, P. Wei, L.-L. Wang, Z.-Q. Ji, Y. Feng, S. Ji, X. Chen, J. Jia, X. Dai, Z. Fang, S.-C. Zhang, K. He, Y. Wang, L. Lu, X.-C. Ma, and Q.-K. Xue, Science **340**, 167 (2013).

[1.10] C. Liu, Y. Wang, H. Li, Y. Wu, Y. Li, J. Li, K. He, Y. Xu, J. Zhang, and Y. Wang, Nat. Mater. **19**, 522 (2020).

[1.11] Z. Fei, W. Zhao, T. A. Palomaki, B. Sun, M. K. Miller, Z. Zhao, J. Yan, X. Xu, and D. H. Cobden, Nature **560**, 336 (2018).

[1.12] S. Yuan, X. Luo, H. L. Chan, C. Xiao, Y. Dai, M. Xie, and J. Hao, Nat. Commun. **10**, 1775 (2019).

[1.13] S. Xu, Y. Han, X. Chen, Z. Wu, L. Wang, T. Han, W. Ye, H. Lu, G. Long, Y. Wu, J. Lin, Y. Cai, K. M. Ho, Y. He, and N. Wang, Nano Lett. **15**, 2645 (2015).

[1.14] Y. Sakamoto, T. Hirahara, H. Miyazaki, S.-i. Kimura, and S. Hasegawa, Phys. Rev. B **81**, 165432 (2010).

[1.15] S. Tang, C. Zhang, D. Wong, Z. Pedramrazi, H.-Z. Tsai, C. Jia, B. Moritz, M. Claassen, H. Ryu, S. Kahn, J. Jiang H. Yan, M. Hashimoto, D. Lu, R. G. Moore, C.-C. Hwang, C. Hwang, Z. Hussain, Y. Chen, M. M. Ugeda, Z. Liu, X. Xie, T. P. Devereaux, M. F. Crommie, S.-K. Mo, and Z.-X. Shen, Nat. Phys. **13**, 683 (2017).

[1.16] Y. Shi, J. Kahn, B. Niu, Z. Fei, B. Sun, X. Cai, B. A. Francisco, D. Wu, Z.-X. Shen, X. Xu, D. H. Cobden, and Y.-T. Cui, Sci. Adv. **5**, eaat8799, (2019).

[1.17] A. F. Young, J. D. Sanchez-Yamagishi, B. Hunt, S. H. Choi, K. Watanabe, T. Taniguchi, R. C. Ashoori, and P. Jarillo-Herrero, Nature **505**, 528 (2014).

[1.18] S. Liu, M. X. Wang, C. Chen, X. Xu, J. Jiang, L. X. Yang, Y. Y. Lv, J. Zhou, Y. B. Chen, S. H. Yao, M. H. Lu, Y. F. Chen, C. Felser, B. H. Yan, Z. K. Liu, and Y. L. Chen, APL Mater. **6**, 121111 (2018).

[1.19] Y. Deng, Y. Yu, M. Z. Shi, Z. Guo, Z. Xu, J. Wang, X.-H. Chen, and Y. Zhang, Science **367**, 895 (2020).

[1.20] A. K. Geim and I. V. Grigorieva, Nature **499**, 419 (2013).

[1.21] Q. Li, C. He, Y. Wang, E. Liu, M. Wang, Y. Wang, J. Zeng, Z. Ma, T. Cao, C. Yi, N. Wang, K. Watanabe, T. Taniguchi, L. Shao, Y. Shi, X. Chen, S.-J. Liang, Q.-H. Wang, and F. Miao, Nano Lett. **18**, 7962 (2018).

[1.22] W. Zhao, Z. Fei, T. Song, H. K. Choi, T. Palomaki, B. Sun,P. Malinowski, M. A. McGuire, J.-H. Chu, X. Xu, and D. H. Cobden, Nat. Mater. **19**, 503 (2020).
[1.23] R. Watanabe, R. Yoshimi, M. Kawamura, M. Mogi, A. Tsukazaki, X. Z. Yu, K. Nakajima, K. S. Takahashi, M. Kawasaki, and Y. Tokura, Appl. Phys. Lett. **115**, 102403 (2019).
[1.24] P. Zareapour, A. Hayat, S. Y. F. Zhao, M. Kreshchuk, A. Jain, D. C. Kwok, N. Lee, S.-W. Cheong, Z. Xu, A. Yang, G. D. Gu, S. Jia, R. J. Cava, and K. S. Burch, Nat. Commun. **3**, 1056 (2012).
[1.25] A. L. Sharpe, E. J. Fox, A. W. Barnard, J. Finney, K. Watanabe, T. Taniguchi, M. A. Kastner, D. Goldhaber-Gordon, Science **365**, 605 (2019).
[1.26] A. Kerelsky, L. J. McGilly, D. M. Kennes, L. Xian, M. Yankowitz, S. Chen, K. Watanabe, T. Taniguchi, J. Hone, C. Dean, A. Rubio, and A. N. Pasupathy, Nature **572**, 95 (2019).
[1.27] Z. Hao, A. M. Zimmerman, P. Ledwith, E. Khalaf, D. H. Najafabadi, K. Watanabe, T. Tanigucho, A. Vishwanath, and P. Kim, Science **371**, 1133 (2021).
[1.28] S. Turkel, J. Swann, Z. Zhu, M. Christos, K. Watanabe, T. Taniguchi, S. Sachdev, M. S. Scheurer, E. Kaxiras, C. R. Dean, A. N. Pasupathy, Science **376**, 193 (2022).
[1.29] D. Khokhriakov, A. W. Cummings, K. Song, M. Vila, B. Karpiak, A. Dankert, S. Roche, S. P. Dash, Sci. Adv. **4**, eaat9349 (2018).
[1.30] L. Kou, S.-C. Wu, C. Felser, T. Frauenheim, C. Chen, and B. Yan, ACS Nano 8, 10448 (2014).
[1.31] Y. Cho, J. H. Kang, L. Liang, M. Taylor, X. Kong, S. Ghosh, F. Kargar, C. Hu, A. A. Balandin, A. A. Puretzky, N. Ni, and C. W. Wong, Phys. Rev. Res. **4**, 013108 (2022).
[1.32] H. Oka and M. Koshino, Phys. Rev. B **104**, 035306 (2021).
[1.33] B. Hunt, J. D. Sanchez-Yamagishi, A. F. Young, M. Yankowitz, B. J. LeRoy, K. Watanabe, T. Taniguchi, P. Moon, M. Koshino, P. Jarillo-Herrero, and R. C. Ashoori, Science **340**, 1427 (2013).
[1.34] P. Liu, J. R. Williams, and J. J. Cha, Nat. Rev. Mater. **4**, 479 (2019).
[1.35] Y. L. Chen, J. G. Analytis, J.-H. Chu, Z. K. Liu, S.-K. Mo, X. L. Qi, H. J. Zhang, D. H. Lu, X. Dai, Z. Fang, S. C. Zhang, I. R. Fisher, Z. Hussain, and Z.-X. Shen, Science **325**, 178 (2009).
[1.36] Y. Xia, D. Qian, D. Hsieh, L. Wray, A. Pal, H. Lin, A. Bansil, D. Grauer, Y. S. Hor, R. J. Cava, and M. Z. Hasan, Nat. Phys. **5**, 398 (2009).
[1.37] D. Hsieh, Y. Xia, D. Qian, L. Wray, F. Meier, J. H. Dil, J. Osterwalder, L. Patthey, A. V. Fedorov, H. Lin, A. Bansil, D. Grauer, Y. S. Hor, R. J. Cava, and M. Z. Hasan, Phys. Rev. Lett. **103**, 146401 (2009).
[1.38] X. Wang, Y. Du, S. Dou, and C. Zhang, Phys. Rev. Lett. **108**, 266806 (2012).
[1.39] C. Weyrich, T. Merzenich, J. Kampmeier, I. E. Batov, G. Mussler, J. Schubert, D. Grützmacher, and T. Schäpers, Appl. Phys. Lett. **110**, 092104 (2017).
[1.40] N. Koirala, M. Brahlek, M. Salehi, L. Wu, J. Dai, J. Waugh, T. Nummy, M.-G. Han, J. Moon, Y. Zhu, D. Dessau, W. Wu, N. P. Armitage, and S. Oh, Nano Lett. **15**, 8245 (2015).
[1.41] H. Zhang, J. Yao, J. Shao, H. Li, S. Li, D. Bao, C. Wang, G. Yang, Sci. Rep. **4**, 5876 (2014).
[1.42] A. Soni, Z. Yanyuan, Y. Ligen, M. K. K. Aik, M. S. Dresselhaus, and Q. Xiong, Nano Lett. **12**, 1203 (2012).

[1.43] C. Chen, Z. Xie, Y. Feng, H. Yi, A. Liang, S. He, D. Mou, J. He, Y. Peng, X. Liu, Y. Liu, L. Zhao, G. Liu, X. Dong, J. Zhang, L. Yu, X. Wang, Q. Peng, Z. Wang, S. Zhang, F. Yang, C. Chen, Z. Xu, and X. J. Zhou, Sci. Rep. **3**, 2411, (2013).
[1.44] T. Arakane, T. Sato, S. Souma, K. Kosaka, K. Nakayama, M. Komatsu, T. Takahashi, Z. Ren, K. Segawa, and Y, Ando, Nat. Commun. **3**, 636 (2012).
[1.45] Y. Satake, J. Shiogai, D. Takane, K. Yamada, K. Fujiwara, S. Souma, T. Sato, T Takahashi, and A. Tsukazaki, J. P. Cond. Matt. **30**, 085501 (2018).
[1.46] J. Zhang, C.-Z. Chang, Z. Zhang, J. Wen, X. Feng, K. Li, M. Liu, K. He, L. Wang, X. Chen, Q.-K. Xue, X. Ma, and Y. Wang, Nat. Commun. **2**, 574 (2011).
[1.47] J. J. Cha, M. Claassen, D. Kong, S. S. Hong, K. J. Koski, X.-L. Qi, Y. Cui, Nano Lett. **12**, 4355 (2012).
[1.48] R. Yoshimi, A. Tsukazaki, Y. Kozuka, J. Falson, K. S. Takahashi, J. G. Checkelsky, N. Nagaosa, M. Kawasaki, and Y. Tokura, Nat. Commun. **6**, 6627 (2015).
[1.49] Y. Xu, I. Miotkowski, C. Liu, J. Tian, H. Nam, N. Alidoust, J. Hu, C.-K. Shih, M. Z. Hasan, and Y. P. Chen, Nat. Phys. **10**, 956 (2014).
[1.50] H. Li, H.-W. Wang, Y. Li, H. Zhang, S. Zhang, X.-C. Pan, B. Jia, F. Song, and J. Wang, Nano Lett. **19**, 2450 (2019).
[1.51] M. Lang, L. He, X. Kou, P. Upadhyaya, Y. Fan, H. Chu, Y. Jiang, J. H. Bardarson, W. Jiang, E. S. Choi, Y. Wang, N.-C. Yeh, J. Moore, and K. L. Wang, Nano Lett. **13**, 48 (2013).
[1.52] Y. Satake, J. Shiogai, K. Fujiwara, and A. Tsukazaki, Phys. Rev. B 98, 125415 (2018).
[1.53] W. S. Whitney, V. W. Brar, Y. Ou, Y. Shao, A. R. Davoyan, D. N. Basov, K. He, Q.-K. Xue, and H. A. Atwater, Nano Lett. **17**, 255 (2017).
[1.54] M. Zhang, X. Wang, S. Zhang, Y. Gao, Z. Yu, X. Zhang, M. Gao, F. Song, J. Du, X. Wang, L. He, Y. Xu, and R. Zhang, IEEE Electr. Dev. Lett. **37**, 1231 (2016).
[1.55] X.-B. Li, W.-K. Huang, Y.-Y. Lv, K.-W. Zhang, C.-L. Yang, B.-B. Zhang, Y. B. Chen, S.-H. Yao, J. Zhou, M.-H. Lu, L. Sheng, S.-C. Li, J.-F. Jia, Q.-K. Xue, Y.-F. Chen, and D.-Y. Xing, Phys. Rev. Lett. **116**, 176803 (2016).
[1.56] X. Qian, J. Liu, L. Fu, and J. Li, Science **346**, 1344 (2014).
[1.57] Z. Fei, T. Palomaki, S. Wu, W. Zhao, X. Cai, B. Sun, P. Nguyen, J. Finney, X. Xu, and D. H. Cobden, Nat. Phys. **13**, 677 (2017).
[1.58] C. Nayak, S. H. Simon, A. Stern, M. Freedman, and S. Das Sarma, Rev. Mod. Phys. **80**, 1083 (2008).
[1.59] R. R. Y. Wang, and H. Yang, J. Phys. D: Appl. Phys. **51**, 273002 (2018).
[1.60] X.-L. Qi, R. Li, J. Zang, and S.-C. Zhang, Science **323**, 1184 (2009).
[1.61] C. Back, V. Cros, H. Ebert, K. Everschor-Sitte, A. Fert, M. Garst, T. Ma, S. Mankovsky, T. L. Monchesky, M. Mostovoy, N. Nagaosa, S. S. P. Parkin, C. Pfleiderer, N. Reyren, A. Rosch, Y. Taguchi, Y. Tokura,10, K. von Bergmann. and J. Zang, J. Phys. D Appl. Phys. **53**, 363001 (2020).
[1.62] B. Yan and C. Felser, Annu. Rev. Condens. Matter Phys. **8**, 337 (2017).
[1.63] T. O. Wehling, A. M. Black-Schaffer, and A. V. Balatsky, Adv. Phys. **63**, 1 (2014).
[1.64] P. A. M. Dirac and R. H. Fowler, "The quantum theory of the electron," Proceedings of the Royal Society of London. Series A, Containing Papers of a Mathematical and Physical Character, vol. 117, pp. 610-624 (1928).

[1.65] P. Li, Y. Wen, X. He, Q. Zhang, C. Xia, Z.-M. Yu, S. A. Yang, Z. Zhu, H. N. Alshareef, and X.-X. Zhang, Nat. Commun. **8**, 2150 (2017).
[1.66] K. Deng, G. Wan, P. Deng, K. Zhang, S. Ding, E. Wang, M. Yan, H. Huang, H. Zhang, Z. Xu, J. Denlinger, A. Fedorov, H. Yang, W. Duan, H. Yao, Y. Wu, S. Fan, H. Zhang, X. Chen, and S.Zhou, Nat. Phys. **12**, 1105 (2016).
[1.67] A. A. Soluyanov, D. Gresch, Z. Wang, Q. Wu, M. Troyer, X. Dai, B. A. Bernevig, Nature **527**, 495 (2015).
[1.68] Y. Gan, C.-W. Cho, A. Li, J. Lyu, X. Du, J.-S. Wen, L.-Y. Zhang, Chin. Phys. B **28**, 117401 (2019).
[1.69] T. Asaba, Y. Wang, G. Li, Z. Xiang, C. Tinsman, L. Chen, S. Zhou, S. Zhao, D. Laleyan, Y. Li, Z. Mi, and Lu Li, Sci. Rep. **8**, 6520 (2018).
[1.70] J. Lai, X. Liu, J. Ma, Q. Wang, K. Zhang, X. Ren, Y. Liu, Q. Gu, X. Zhuo, W. Lu, Y. Wu, Y. Li, J. Feng, S. Zhou, J.-H. Chen, and D. Sun, Adv. Mater. **30**, 1707152 (2018).
[1.71] Y. Wang, L. Wang, X. Liu, H. Wu, P. Wang, D. Yan, B. Cheng, Y. Shi, K. Watanabe, T. Taniguchi, S.-J. Liang, and F. Miao, Nano Lett. **19**, 3969 (2019).
[1.72] S. Zhong, A. Tiwari, G. Nichols, F. Chen, X. Luo, Y. Sun, A. W. Tsen, Phys. Rev B **97**, 241409 (2018).
[1.73] M. Chen, K. Lee, J. Li, L. Cheng, Q. Wang, K. Cai, E. E. M. Chia, H. Chang, and H. Yang, ACS Nano **14**, 3539 (2020).
[1.74] Q. Wang, J. Li, J. Besbas, C.-H. Hsu, K. Cai, L. Yang, Shuai Cheng, Yang Wu, Wenfeng Zhang, Kaiyou Wang, Tay-Rong Chang, Hsin Lin, Haixin Chang, Hyunsoo Yang, Adv. Sci. **5**, 1700912 (2018).
[1.75] F. Zhang, H. Zhang, S. Krylyuk, C. A. Milligan, Y. Zhu, D. Y. Zemlyanov, L. A. Bendersky, B. P. Burton, A. V. Davydov, and J. Appenzeller, Nat. Mater. **18**, 55 (2019).
[1.76] W. Hou, A. Azizimanesh, A. Sewaket, T. Peña, C. Watson, M. Liu, H. Askari, and S. M. Wu, Nat. Nanotechnol. **14**, 668 (2019).
[1.77] S. Shi, S. Liang, Z. Zhu, K. Cai, S. D. Pollard, Y. Wang, J. Wang, Q. Wang, P. He, J. Yu, G. Eda, G. Liang, and H. Yang, Nat. Nanotechnol. **14**, 945 (2019).
[1.78] S. Shi, J. Li, C.-H. Hsu, K. Lee, Y. Wang, L. Yang, J. Wang, Q. Wang, H. Wu, W. Zhang, G. Eda, G. Liang, H. Chang, H. Yang, Adv. Quant. Technol. **4**, 2100038 (2021).
[1.79] S. Liang, S. Shi, C.-H. Hsu, K. Cai, Y. Wang, P. He, Y. Wu, V. M. Pereira, H. Yang, Adv. Mater. **32**, 2002799 (2020).
[1.80] K. Zhang, M. Yan, H. Zhang, H. Huang, M. Arita, Z. Sun, W. Duan, Y. Wu, and S. Zhou, Phys. Rev. B **96**, 125102 (2017).
[1.81] M. Yan, H. Huang, K. Zhang, E. Wang, W. Yao, K. Deng, G. Wan, H. Zhang, M. Arita, H. Yang, Z.Sun, H. Yao, Y. Wu, S. Fan, W. Duan, and S. Zhou, Nat. Commun. **8**, 257 (2017).
[1.82] H.-J. Noh, J. Jeong, E.-J. Cho, K. Kim, B. I. Min, and B.-G. Park, Phys. Rev. Lett. **119**, 016401 (2017).
[1.83] B. Ghosh, D. Mondal, C.-N. Kuo, C. S. Lue, J. Nayak, J. Fujii, I. Vobornik, A. Politano, and A. Agarwa, Phys. Rev. B **100**, 195134 (2019).
[1.84] P. Tsipas, D. Tsoutsou, S. Fragkos, R. Sant, C. Alvarez, H. Okuno, G. Renaud, R. Alcotte, T. Baron, and A. Dimoulas, ACS Nano **12**, 1696, (2018).
[1.85] G. Zheng, J. Lu, X. Zhu, W. Ning, Y. Han, H. Zhang, J. Zhang, C. Xi, J. Yang, H. Du, K. Yang, Y. Zhang, and M. Tian, Phys. Rev. B **93**, 115414 (2016).
[1.86] S. Singh, N. Kumar, S. Roychowdhury, C. Shekhar, and C. Felser, J. Phys. Condens. Matt. **34**, 225802 (2022).

[1.87] G. Zhang, H. Wu, L. Zhang, L. Yang, Y. Xie, F. Guo, H. Li, B. Tao, G. Wang, W. Zhang, H. Chang, Small **18**, 2204380 (2022).
[1.88] K. Choudhary, K. F. Garrity, A. C. E. Reid, B. DeCost, A. J. Biacchi, A. R. Hight Walker, Npj Comput. Mater. **6**, 173 (2020).
[1.89] T. Olsen, E. Andersen, T. Okugawa, D. Torelli, T. Deilmann, and K. S. Thygesen, Phys. Rev. Mater. **3**, 024005 (2019).
[1.90] T. Förster, P. Krüger, and M. Rohlfing, Phys. Rev. B **93**, 205442 (2016).
[1.91] P. Li, J. Yu, Y. Wang, and W. Luo, Phys. Rev. B **103**, 155118 (2021).
[1.92] C. Wu, C. Liu, Y. Tao, Y. Zhang, and Y. Chen, Phys. Lett. A **384**, 126751 (2020).
[1.93] M. M. Otrokov, I. P. Rusinov, M. Blanco-Rey, M. Hoffmann, A. Y. Vyazovskaya, S. V. Eremeev, A. Ernst, P. M. Echenique, A. Arnau, and E. V. Chulkov, Phys. Rev. Lett. **122**, 107202 (2019).
[1.94] C.-X. Liu, H. Zhang, B. Yan, X.-L. Qi, T. Frauenheim, X. Dai, Z. Fang, and S.-C. Zhang, Phys. Rev. B **81**, 041307 (2010).
[1.95] X. Dong, M. Wang, D. Yan, X. Peng, J. Li, W. Xiao, Q. Wang, J. Han, J. Ma, Y. Shi, and Y. Yao, ACS Nano **13**, 9571, (2019).
[1.96] K. S. Novoselov, A. K. Geim, S. V. Morozov, D. Jiang, M. I. Katsnelson, I. V. Grigorieva, S. V. Dubonos, and A. A. Firsov, Nature **438**, 197 (2005).
[1.97] K. S. Novoselov, A. K. Geim, S. V. Morozov, D. Jiang, Y. Zhang, S. V. Dubonos, I. V. Grigorieva, and A. A. Firsov, Science **306**, 666 (2004).
[1.98] Y.-Y. Li, G. Wang, X.-G. Zhu, M.-H. Liu, C. Ye, X. Chen, Adv. Mater. **22**, 4002 (2010).
[1.99] Y. Zhang, K. He, C.-Z. Chang, C.-L. Song, L.-L. Wang, X. Chen, J.-F. Jia, Z. Fang, X. Dai, W.-Y. Shan, S.-Q. Shen, Q. Niu, X.-L. Qi, S.-C. Zhang, X.-C. Ma, and Q.-K. Xue, Nat. Phys. **6**, 584 (2010).
[1.100] Y. Wang, E. Liu, H. Liu, Y. Pan, L. Zhang, J. Zeng, Y. Fu, M. Wang, K. Xu, Z. Huang, Z. Wang, H.-Z. Lu, D. Xing, B. Wang, X. Wan, and F. Miao, Nat. Commun. **7**, 13142 (2016).
[1.101] W. Zhou, J. Chen, H. Gao, T. Hu, S. Ruan, A. Stroppa, and W. Ren, Adv. Mater. 31, 1804629 (2019).
[1.102] X. Zhang, J. M. Woods, J. J. Cha, and X. Shi, Phys. Rev.B **102**, 115161 (2020).
[1.103] M. Sakano, Y. Tanaka, S. Masubuchi, S. Okazaki, T. Nomoto, A. Oshima, K. Watanabe, T. Taniguchi, R. Arita, T. Sasagawa, T. Machida, and K. Ishizaka, Phys. Rev. Res. **4**, 023247 (2022).
[1.104] Y. Maximenko, Y. Chang, G. Chen, M. R. Hirsbrunner, W. Swiech, T. L. Hughes, Npj Quant. Mater. **7**, 29 (2022).
[1.105] S.-Y. Xu, Q. Ma, H. Shen, V. Fatemi, S. Wu, T.-R. Chang, Guoqing Chang, A. M. M. Valdivia, C.-K. Chan, Nat. Phys. **14**, 900 (2018).
[1.106] E. Sajadi, T. Palomaki, Z. Fei, W. Zhao, P. Bement, C. Olsen, S. Luescher, X. Xu, J. A. Folk, D. H. cobden, Science **362**, 922 (2018).
[1.107] F. Lüpke, D. Waters, S. C. de la Barrera, M. Widom, D. G. Mandrus, J. Yan, R. M. Feenstra, and B. M. Hunt, Nat. Phys. **16**, 526 (2020).
[1.108] L. Wu, M. Brahlek, R. Valdés Aguilar, A. V. Stier, C. M. Morris, Y. Lubashevsky, L. S. Bilbro, N. Bansal, S. Oh, and N. P. Armitage, Nat. Phys. **9**, 410 (2013).
[1.109] M. Salehi, H. Shapourian, N. Koirala, M. J. Brahlek, J. Moon, and S. Oh, Nano Lett. **16**, 5528 (2016).
[1.110] M. Brahlek, N. Koirala, M. Salehi, J. Moon, W. Zhang, H. Li, X. Zhou, M.-G. Han, L. Wu, T. Emge, H.-D. Lee, C. Xu, S. J. Rhee, T. Gustafsson, N. P.

Armitage, Y. Zhu, D. S. Dessau, W.Wu, and S. Oh, Phys. Rev. B **94**, 165104 (2016).
[1.111] Y. Satake, J. Shiogai, G. P. Mazur, S. Kimura, S. Awaji, K. Fujiwara, T. Nojima, K. Nomura, S. Souma, T. Sato, T. Dietl, and A. Tsukazaki, Phys. Rev. Mater. **4**, 044202 (2020).
[1.112] K. Deng, M. Yan, C.-P. Yu, J. Li, X. Zhou, K. Zhang, Y. Zhao, K. Miyamoto. T. Okuda, W. Duan Y. Wu, X. Zhong, and S. Zhou, Sci. Bull. **64**, 1044 (2019).
[1.113] A. Ciarrocchi, A. Avsar, D. Ovchinnikov, and A. Kis, Nat. Commun. 9, 919 (2018).
[1.114] Z.-Y. Jia, Y.-H. Song, X.-B. Li, K. Ran, P. Lu, H.-J. Zheng, X.-Y. Zhu, Z.-Q. Shi, J. Sun, J. Wen, D. Xing, and S.-C. Li, Phys. Rev. B **96**, 041108 (2017).
[1.115] D. Culcer, A. Cem Keser, Y. Li, and G. Tkachov, 2D Mater. **7**, 022007 (2020).
[1.116] L. Zhang, T. Helm, H. Lin, F. Fan, C. Le, Y. Sun, A. Markou, and C. Felser, Adv. Mater. **33**, 2102107 (2021).
[1.117] B. F. Gao, P. Gehring, M. Burghard, and K. Kern, Appl. Phys. Lett. **100**, 212402 (2012).
[1.118] L. Wang, I. Gutiérrez-Lezama, C. Barreteau, N. Ubrig, E. Giannini, and A. F. Morpurgo, Nat. Commun. **6**, 8892 (2015).
[1.119] J. Wang, A. M. DaSilva, C.-Z. Chang, K. He, J. K. Jain, N. Samarth, X.-C. Ma, Q.-K. Xue, and M. H. W. Chan, Phys. Rev. B **83**, 245438 (2011).
[1.120] P. Kapitza and E. Rutherford, Proceedings of the Royal Society of London. Series A, Containing Papers of a Mathematical and Physical Character, vol. **119**, pp. 358-443, 1928.
[1.121] W. J. Wang, K. H. Gao, Q. L. Li, and Z.-Q. Li, Appl.Phys. Lett. **111**, 232105 (2017).
[1.122] S. Gu, K. Fan, Y. Yang, H. Wang, Y. Li, F. Qu, G. Liu, Z.-A. Li, Z. Wang, Y. Yao, J. Li, L. Lu, and F. Yang, Phys. Rev. B **104**, 115203 (2021).
[1.123] A. A. Abrikosov, J. Phys. A: Math. Gen. **36**, 9119 (2003).
[1.124] M. M. Parish and P. B. Littlewood, Phys. Rev. B **72**, 094417 (2005).
[1.125] M. Udagawa and E. J. Bergholtz, Phys. Rev. Lett. **117,** 086401 (2016).
[1.126] D. Fu, X. Pan, Z. Bai, F. Fei, G. A. Umana-Membreno, H. Song, X. Wang, B. Wang, and F. Song, Nanotechnology **29**, 135705 (2018).
[1.127] Z. Xie, X. Wei, X. Qiang, Y. Zhang, S. Yan, S. Cao, C. Tian, P. Wang, L. Zhang, G. D. Gu, H. Lu, and J.-H. Chen, Phys. Rev. B **104**, 125439 (2021).
[1.128] H. Wang, C. H. Chan, C. H. Suen, S. P. Lau, and J.-Y. Dai, ACS Nano **13**, 6008 (2019).
[1.129] P. Wang, T. Hou, F. Tang, P. Wang, Y. Han, Y. Ren, H. Zeng, L. Zhang, and Z. Qiao, Chin. Phys. Lett. **38**, 017201 (2021).
[1.130] H. Zhang, H. Li, H. Wang, G. Cheng, H. He, and J. Wang, Appl. Phys. Lett. **113**, 113503 (2018).
[1.131] G. Bergmann, Sol. State Commun. **42**, 815 (1982).
[1.132] S.-Q. S. Hai-Zhou Lu, Chin. Phys. B, **25** 117202 (2016).
[1.133] L. Fu and C. L. Kane, Phys. Rev. B **76**, 045302 (2007).
[1.134] Y. Nakazawa, M. Uchida, S. Nishihaya, M. Ohno, S. Sato, and M. Kawasaki, Phys. Rev. B **103**, 045109 (2021).
[1.135] J. J. Cha, D. Kong, S.-S. Hong, J. G. Analytis, K. Lai, and Y. Cui, Nano Lett. **12**, 1107 (2012).
[1.136] S. Hikami, A. I. Larkin, and Y. Nagaoka, Progr. Theoret. Phys. **63**, 707 (1980).
[1.137] H. B. Zhang, H. L. Yu, D. H. Bao, S. W. Li, C. X. Wang, and G. W. Yang, Phys.Rev. B **86**, 075102 (2012).

[1.138] Z. Wang, L. Wei, M. Li, Z. Zhang, and X. P. A. Gao, Phys. Status Solidi B **255**, 1800272 (2018).
[1.139] E. Zhang, R. Chen, C. Huang, J. Yu, K. Zhang, W. Wang, S. Liu, J. Ling, X. Wan, H.-Z. Lu, and F. Xiu, Nano Lett. **17**, 878 (2017).
[1.140] A. R. Mellnik, J. S. Lee, A. Richardella, J. L. Grab, P. J. Mintun, M. H. Fischer, A. Vaezi, A. Manchon, E.-A. Kim, N. Samarth, and D. C. Ralph, Nature **511**, 449 (2014).
[1.141] H. Wu, A. Chen, P. Zhang, H. He, J. Nance, C. Guo, J. Sasaki, T. Shirokura, P. N. Hai, B. Fang, S. A. Razavi, K. Wong, Nat. Commun. **12**, 6251 (2021).
[1.142] X. Che, Q. Pan, B. Vareskic, J. Zou, L. Pan, P. Zhang, G. Yin, H. Wu, Q. Shao, P. Deng, and K. L. Wang, Adv. Mater. **32**, 1907661 (2020).
[1.143] H. Xue, W. Lv, D. Wu, J. Cai, Z. Ji, Y. Zhang, J. Phys. Chem. Lett. **12**, 2394 (2021).
[1.144] H. Wu, Y. Xu, P. Deng, Q. Pan, S. A. Razavi, K. Wong, L. Huang, B. Dai, Q. Shao, G. Yu, X. Han, Adv. Mater. **31**, 1901681 (2019).
[1.145] B. Das, P. K. Sarkar, N. S. Das, S. Sarkar, and K. K. Chattopadhyay, J. Appl. Phys. **124**, 124503 (2018).
[1.146] H. Bryja, J. W. Gerlach, A. Prager, M. Ehrhardt, B. Rauschenbach, and A. Lotnyk, 2D Mater. **8**, 045027 (2021).
[1.147] J. Tian, I. Childres, H. Cao, T. Shen, I. Miotkowski, and Y. P. Chen, Solid State Commun. **191**, 1 (2014).
[1.148] M. Jamali, J. S. Lee, J. S. Jeong, F. Mahfouzi, Y. Lv, Z. Zhao, B. N. Nikolic, K. A. Mkhoyan, N. Samarth, and J.-P. Wang, Nano Lett. **15**, 7126 (2015).
[1.149] F. Mahfouzi, N. Nagaosa, and B. K. Nikolić, Phys. Rev. B **90**, 115432 (2014).
[1.150] R. Fujimura, R. Yoshimi, M. Mogi, A. Tsukazaki, M. Kawamura, K. S. Takahashi, M. Kawasaki, and Y. Tokura, Appl. Phys. Lett. **119**, 032402 (2021).
[1.151] E. Saitoh, M. Ueda, H. Miyajima, and G. Tatara, Appl. Phys. Lett. **88**, 182509 (2006).
[1.152] Y. Wang, D. Zhu, Y. Wu, Y. Yang, J. Yu, R. Ramaswamy, R. Mishra, S. Shi, M. Elyasi, K.-L. Teo, Y. Wu, H. Yang, Nat. Commun. **8**, 1364 (2017).
[1.153] C. Gong and X. Zhang, Science **363**, eaav4450 (2019).
[1.154] Y. Ou, W. Yanez, R. Xiao, M. Stanley, S. Ghosh, B. Zheng, W. Jiang, Y.-S. Huang, T. Pillsbury, A. Richardella, C. Liu, Nat. Commun. **13**, 2972 (2022).
[1.155] I. Shin, W. J. Cho, E.-S. An, S. Park, H.-W. Jeong, S. Jang, W. J. Baek, S. Y. Park, D.-H. Yang, J. H. Seo, G.-Y. Kim, Adv. Mater. **34**, 2101730 (2022).
[1.156] I. H. Kao, R. Muzzio, H. Zhang, M. Zhu, J. Gobbo, S. Yuan, D. Weber, R. Rao, J. Li, H. H. Edgar, J. E. Goldberger, J. Yan, Nat. Mater. **21**, 1029 (2022).
[1.157] A. Fert, N. Reyren, and V. Cros, Nat. Rev. Mater. **2**, 17031 (2017).
[1.158] Y. Wu, S. Zhang, J. Zhang, W. Wang, Y. L. Zhu, J. Hu, G. Yin, K. Wong, C. Fang, C. Wan, X. Han, Q. Shao, T. Taniguchi, Nat. Commun. **11**, 3860 (2020).
[1.159] J. Chen, L. Wang, M. Zhang, L. Zhou, R. Zhang, L. Jin, Nano Lett. **19**, 6144 (2019).
[1.160] L. Zhou, J. Chen, X. Chen, B. Xi, Y. Qiu, J. Zhang, ACS Appl. Mater. Interf. **12**, 25135 (2020).
[1.161] X. Zhang, S. C. Ambhire, Q. Lu, W. Niu, J. Cook, J. S. Jiang, ACS Nano **15**, 15710 (2021).

2. Theoretical and experimental methods

2.1. Theoretical methods

2.1.1. Density functional theory

The behavior of electrons in the vast environment of other electrons, nuclei, electromagnetic fields, and other fundamental forces can be used to explain a variety of natural phenomena that are of interest to material scientists. One of the most crucial issues in condensed matter is hence the search for a solution to the many-body problem.

The properties of the electrons are accurately described by the many-body Hamiltonian of the Schrödinger equation

$$\hat{H} \cdot \Psi\left(\{\vec{R_I}, \vec{r_i}\}\right) = E \cdot \Psi\left(\{\vec{R_I}, \vec{r_i}\}\right) \tag{2.1}$$

where *I*,*i* are the nuclei and electron positions. The Hamiltonian associated with this system of *N* nuclei and *n* electrons is

$$\hat{H} = -\frac{1}{2}\sum_i \nabla_i^2 - \frac{1}{2}\sum_I \nabla_I^2 - \sum_{I,i} \frac{Z_I}{\left|\vec{R_I} - \vec{r_i}\right|} + \sum_{I \neq J} \frac{Z_I \cdot Z_J}{\left|\vec{R_I} - \vec{R_J}\right|} + \sum_{i \neq j} \frac{1}{\left|\vec{r_i} - \vec{r_j}\right|} \tag{2.2}$$

the first two terms represent the kinetic energy of electrons and nuclei, the next three terms describe the Coulomb interaction between nuclei-electrons, nuclei-nuclei and electrons-electrons respectively.

In a first approximation, Eq. (2.2) can be simplified if one takes into account the huge mass difference between nuclei and electrons. In the Born-Oppenheimer approach [2.1] the nuclei are considered stationary so the second term of Eq. (2.2) can be neglected. Moreover, the fourth term in Eq. (2.2) is essentially a constant and the corresponding term in the Hamiltonian can be omitted, leading to the electronic Hamiltonian

$$\hat{H} = -\frac{1}{2}\sum_i \nabla_i^2 - \sum_{I,i} \frac{Z_I}{\left|\vec{R_I} - \vec{r_i}\right|} + \sum_{i \neq j} \frac{1}{\left|\vec{r_i} - \vec{r_j}\right|} = \hat{T} + \hat{V}_{ext} + \hat{V}_{ee} \tag{2.3}$$

Even with these approximations this equation is not solvable due to the large number of variables (3N variables describe the wavefunction Ψ for N electrons) and the fact that the interaction between electrons makes Eq. (2.3) non-separable.

The first attempt to approach the problem was done by Hartree in 1927 with the wavefunction of the system being expressed as a product of single particle states that each satisfy the Schrödinger equation in the mean field created by the remaining

electrons. In 1930 Fock and Slater approximated the wave function of the system as a Slater determinant to account for the fermionic nature of electrons with their antisymmetric wave function behavior leading to an improvement of the Hartree method, the Hartree-Fock approximation [2.2, 2.3].

At the same time, a completely different approach was adopted in 1927 by Thomas [2.4] with the development of the Thomas-Fermi model [2.5]. Based on calculations for a uniform electron gas they expressed the energy of an electron system as a function of its density. This was the first consideration where the central quantity in the calculations was no longer the wavefunctions of the electrons, but their density. More details on the above models can be found in the bibliographic references [2.6-2.8]. In the next paragraphs we will briefly present the density functional theory (DFT), the most widespread method for electronic structure calculations in solid state physics that was the basis of the theoretical calculations in this work.

A publication by Hohenberg and Kohn (HK) in 1964 [2.9] laid the foundations of DFT. The central quantity is no longer the electron wavefunctions that require 3N variables but the electron density, drastically reducing the number of variables to describe the system to three. The first HK theorem states that an external potential $V_{ext}(\vec{r})$ is a unique function $n(\vec{r})$ of the density. Therefore, from the moment that the external potential determines the Hamiltonian of the system, it follows that its energy will also be a uniquely defined functional of it. With the help of the Eq. (2.3) we can therefore describe the energy of the system as

$$E[n(\vec{r})] = F[n(\vec{r})] + \int n(\vec{r}) \cdot V_{ext}(\vec{r}) d\vec{r} \tag{2.4}$$

where $F[n(\vec{r})] = T[n(\vec{r})] + E_{ee}[n(\vec{r})]$.

The second HK theorem states that the energy of the system in its ground state is given by the Eq. (2.4) if and only if the density corresponds to the actual density of the ground state. Therefore, if one substitutes a random density, provided it satisfies the relation $\int n(\vec{r}) d\vec{r} = N$, one will find an upper bound of the actual energy in the ground state. Thus, the ground state energy is determined by the relation

$$E_o = min\left\{F[n(\vec{r})] + \int n(\vec{r}) \cdot V_{ext}(\vec{r}) d\vec{r}\right\} \tag{2.5}$$

A year later, Kohn and Sham (KS) [2.10] published a method for determining the ground state energy via Eq. (2.5). The central idea of the method is to replace the system of interacting bodies of density *n(r)* in potential $V_{ext}(r)$ with a system of non-interacting bodies of the same density and potential $V_{eff}(r)$ as we will see below. The global functional was expressed in the form

$$F[n(\vec{r})] = T_s[n(\vec{r})] + \frac{1}{2}\int \frac{n(\vec{r})\cdot n(\vec{r}')}{|\vec{r}-\vec{r}'|} d\vec{r}' + E_{xc}[n(\vec{r})] \tag{2.6}$$

where the first term represents the kinetic energy of a system of non-interacting electrons and can be expressed as

$$T_s[n(\vec{r})] = -\frac{1}{2}\sum_{i=1}^{N} \langle \Psi_i | \nabla^2 | \Psi_i \rangle \tag{2.7}$$

where Ψ_i are the orbitals of the non-interacting system so that $n(\vec{r}) = \sum_{i=1}^{N} |\Psi_i|^2$.

The second term in Eq. (2.6) is the Coulomb interaction (or Hartree term) and the third contains corrections due to exchange and correlation interactions of a system of interacting electrons of density *n(r)*. Thus, the function of the energy will have the form

$$\begin{aligned} E[n(\vec{r})] = T_s[n(\vec{r})] + \frac{1}{2}\int \frac{n(\vec{r})\cdot n(\vec{r}')}{|\vec{r}-\vec{r}'|} d\vec{r}' + E_{xc}[n(\vec{r})] \\ + \int n(\vec{r})\cdot V_{ext}(\vec{r}) d\vec{r} \end{aligned} \tag{2.8}$$

The ground state energy is obtained from the following Euler-Lagrange equation by introducing the variable μ to satisfy the condition $n(\vec{r}) = \sum_{i=1}^{N} |\Psi_i|^2$

$$\frac{\delta T_s[n(\vec{r})]}{\delta n(\vec{r})} + \int \frac{n(\vec{r}')}{|\vec{r}-\vec{r}'|} dr' + V_{ext}(\vec{r}) + \frac{\delta E_{xc}[n(\vec{r})]}{\delta n(\vec{r})} = \mu \tag{2.9}$$

Therefore, if we consider as effective potential

$$V_{eff}(\vec{r}) = \int \frac{n(\vec{r}')}{|\vec{r}-\vec{r}'|} d\vec{r}' + V_{ext}(\vec{r}) + \frac{\delta E_{xc}[n(\vec{r})]}{\delta n(\vec{r})} \tag{2.10}$$

then the system of non-interacting electrons moving in the effective potential $V_{eff}(r)$ will satisfy the one-particle Schrödinger equation

$$\left(-\frac{1}{2}\nabla_i^2 + V_{eff}(\vec{r})\right)\Psi_i(\vec{r}) = \varepsilon_i \Psi_i(\vec{r}) \tag{2.11}$$

The energy, density and other properties of the ground state of the above system can be determined from the self-consistent solution of Eq. (2.11) with the condition $n(\vec{r}) = \sum_{i=1}^{N} |\Psi_i|^2$.

The Kohn-Sham system of equations gives an accurate description of the ground state of the system of interacting electrons provided we know exactly the exchange-correlation potential $V_{xc} = \frac{\delta E_{xc}[n(\vec{r})]}{\delta n(\vec{r})}$. Unfortunately, to date such a relation has not been found, so the approach to reality through DFT essentially depends on how well we approximate the V_{xc} potential.

The most simplified approximation of $E_{xc}[n(\vec{r})]$ is the local density approximation (LDA) method, where the $E_{xc}[n(\vec{r})]$ value is approached by

$$E_{xc}^{LDA}[n(\vec{r})] = \int n(\vec{r}) \cdot \varepsilon_{xc}\big(n(\vec{r})\big) d\vec{r} \tag{2.12}$$

Where $\varepsilon_{xc}\big(n(\vec{r})\big)$ is the exchange-correlation energy per electron of a homogeneous electron gas with density $n(\vec{r})$. An improvement of the LDA approach is the GGA (generalized gradient approximation) approach where $E_{xc}[n(\vec{r})]$ is approximated as a function of the density and its slope

$$E_{xc}^{GGA}[n(\vec{r})] = \int n(\vec{r}) \cdot \varepsilon_{xc}\big(n(\vec{r})\big) d\vec{r} + \int F_{xc}[n(\vec{r}), \nabla n(\vec{r})] d\vec{r} \tag{2.13}$$

The Vienna Ab-initio Simulation Package (VASP) software package [11, 12] was used for DFT calculations. The implementation of the VASP code uses as a basis for the development of the basic quantities (orbitals, charge density and other physical quantities) plane waves and ultrasoft pseudopotentials or projector augmented waves (PAW) type potentials for ion and valence electron interactions.

2.1.2. Wannier functions and tight-binding method

2.1.2.1. Wannier functions

The orthonormal orbitals developed by Gregory Wannier in 1937 lie in the same Hilbert space as the eigenfunctions of the Kohn-Sham Hamiltonian. The need to be able to explain the electronic structure of a solid in terms of localized orthonormal orbitals, similar to how one characterizes molecular states in quantum chemistry in terms of atomic orbitals, was the driving force for the development of such an alternate set.

In order to convince oneself that such a set exists, we follow Wannier [2.13] and consider a free electron, in a periodic solid. Using Bloch's Theorem, we see that the eigenfunctions $\Psi_{nk}(r)$ can be written as

$$\Psi_{nk}(r) = u_n e^{ik\cdot r} \tag{2.14}$$

where u_n has the periodicity of the one-particle effective Hamiltonian. Let's concentrate on just one electronic band, *n*. Our understanding of Fourier analysis is used to provide the intuition for creating a collection of "localized" functions. In fact, we "understand" that a function's Fourier transform typically demonstrates a considerable degree of localization when a function is truly delocalized in space (like a Bloch function). Consequently, we intuitively define a group of functions that depend on $\vec{R}$, as

$$w_{nR} = \frac{1}{\sqrt{N}} \sum_{k\in BZ} \Psi_{nk}(r) e^{-ik\cdot R} \tag{2.15}$$

where BZ denotes the Brillouin zone. Though the concept of employing a Fourier transform to create a set of localized Wannier functions from a set of delocalized Bloch functions is simple, the Bloch function phases still contain some arbitrariness that prevents the Wannier functions from being unique. In fact, if the set of Bloch functions is transformed in the manner described below

$$\Psi_{nk}(r) \rightarrow e^{iu_{nk}} \Psi_{nk}(r) \tag{2.16}$$

the KS Hamiltonians are then left unchanged, where $|\Psi_{nk}\rangle$ becomes $e^{iu_{nk}}|\Psi_{nk}\rangle$, and $\langle\Psi_{nk}|$ becomes $\langle\Psi_{nk}|e^{iu_{nk}}$. As a result, this new set of Bloch functions accurately describes the system's physics. The set of Wannier functions is noticeably modified if one multiplies each Bloch function by a different phase factor. Up until very recently [2.14], this indeterminacy was a significant barrier to the widespread use of Wannier functions in solid state physics. In the section that follows, we'll see how to use the phase indeterminacy of the Bloch functions to our advantage in order to get around the non-uniqueness problem.

Given the mathematical invariance of the energy functional under a general unitary transformation of the occupied Bloch functions and the phase indeterminacy of Bloch functions, let us suggest the most general transformation:

For the discrete case

$$|w_{nR}\rangle = \frac{1}{\sqrt{N}} \sum_{k \in BZ} \left[\sum_{m} U_{mn}^{k} |\Psi_{mk}\rangle \right] e^{-ikR} \tag{2.17a}$$

For the continuous case

$$|w_{nR}\rangle = \frac{1}{\sqrt{N}} \frac{V}{(2\pi)^d} \int dk \left[\sum_{m} U_{mn}^{k} |\Psi_{mk}\rangle \right] e^{-ikR} \tag{2.17b}$$

It is simple to demonstrate that the Wannier functions as specified are orthonormal if the Bloch functions are normalized over the entire supercell (volume *V*) based on the unitarity of the *k*-dependent matrices U_{mn}^{k} and the orthonormality of the Bloch basis

$$\langle w_{nR} | w_{n'R'} \rangle = \int dr \, w_{nR}^{*}(r) w_{n'R'}^{*}(r) = \delta_{nn'} \delta_{RR'} \tag{2.18}$$

The inverse relation is given by

$$|\Psi_{nk}\rangle = \frac{1}{\sqrt{N}} \sum_{R} \left[\sum_{m} (U_{mn}^{k})^{-1} |\Psi_{mR}\rangle \right] e^{ikR} \tag{2.19}$$

where *R* runs over all the elementary unit cells inside the supercell. It is possible to think of Eq. 2.17 as a two-step procedure. We define a completely new set of Bloch functions through in the first step

$$|\Phi_{nk}\rangle = \sum_{m} U_{mn}^{k} |\Psi_{mk}\rangle \tag{2.20a}$$

and we Fourier transform in the second step

$$|w_{nR}\rangle = \frac{1}{\sqrt{N}} \sum_{k \in BZ} |\Phi_{nk}\rangle e^{ikR} \tag{2.20b}$$

We can completely arbitrarily select the *k*-dependent matrices, resulting in a unique set of Wannier functions for each set of matrices. Following Marzari and Vanderbilt [2.14], we will identify the unique set of *k*-dependent matrices for which Wannier functions are maximally localized in order to establish a special set of Wannier functions. The set of Wannier functions will minimize the sum of their mean square spread, which is defined as

$$\Omega = \sum_{n} [\langle r^2 \rangle_n - \langle r \rangle_n^2] = \sum_{n} [\langle w_{n0} | r^2 | w_{n0} \rangle - \langle w_{n0} | r | w_{n0} \rangle^2] \tag{2.21}$$

Where Ω is defined as the spread functional. Eq. 2.20 provide the necessary matrix elements for the position operator in the Wannier function basis for a given

transformation (i.e., given U_{mn}^{k} matrices) in terms of the periodic part of the Bloch functions [2.15]

$$\langle r\rangle_n = i\sum_{k\in BZ}\langle u_{nk}|\nabla_k|u_{nk}\rangle = i\frac{V}{(2\pi)^d}\int dk\,\langle u_{nk}|\nabla_k|u_{nk}\rangle$$
$$\langle r\rangle_n = -\sum_{k\in BZ}\langle u_{nk}|\nabla_k^2|u_{nk}\rangle = -\frac{V}{(2\pi)^d}\int dk\,\langle u_{nk}|\nabla_k^2|u_{nk}\rangle \quad (2.22)$$

Maximally localized Wannier functions (MLWF) are the Wannier functions that reduce the spread functional in Eq. 2.21. Typically, the procedure to calculate the MLWFs involves two steps. First, a given number of initial Bloch functions ($M \times N$ if M is the number of bands computed for each k vector in the BZ and N is the number of k such vectors) are taken, and then an optimally smooth sub-manifold of $M \times N$ Bloch functions is extracted (where $M' \leq M$). This process is known as the disentanglement procedure. Metallic systems for which there is no energy gap separating the occupied manifold of Bloch functions from the unoccupied manifold can be dealt with via the disentanglement technique. Beginning with the ideal sub-manifold of Bloch states, the second step, often referred to as the wannierization procedure, determines the set of k-dependent matrices that minimizes the spread functional. The process is iterative and employs both conjugate-gradient and steepest descent techniques [2.16]. A detailed description of both disentanglement and wannierization procedures amongst other information can be found in reference [2.17]. The tight binding method, which we shall discuss in the following section, uses Wannier functions as local orbitals. These functions are created from the output of DFT calculations.

2.1.2.2. Tight-binding method

Tight-binding (TB) method is a semi-empirical approach in which by projecting the Hamiltonian of the system onto a series of local orbitals it is possible to study electronic structures of solid-state systems. Constructing TB models can be done with several ways, such as MLWFs [2.17] and Slater–Koster method [2.18]. MLWF [2.17] is the most common method when someone is interested in performing real materials simulations. MLWF is implemented in Wannier90 software [2.16], which acquires interfaces with many first-principles software packages like VASP. Consequently, MLWF TB models can be computed automatically from DFT calculations combined with Wannier90 [2.16].

In different TB methods, the basis functions could be mutually orthogonal or non-orthogonal. Nevertheless, WannierTools package [2.19], which is used in this work as a tool to calculate topological properties of materials, is capable of dealing with the TB models only with orthogonal basis functions. Fortunately, this restriction is satisfied by the Wannier functions for the MLWF TB technique. The general orthogonal TB methods are briefly introduced in this section. Refs [2.17, 2.20] contain instructions on how to build MLWF TB models.

Let i be the atoms, μ the orbitals, m l the combination of iμ, R the lattice vectors in 3D crystal, and τ_i the position of atoms in a home unit cell. The local orbital for the i'th atom centered at $R + \tau_i$ can be described as

$$\varphi_{Rm} \equiv \varphi_m(r - R) \equiv \varphi_{i\mu}(r - R - \tau_I) \tag{2.23}$$

The orthogonality of orbitals requires $\langle \varphi_{Rm} | \varphi_{R'n} \rangle = \delta_{RR'}\delta_{mn}$. The TB parameters of the Hamiltonian that acquire the translational symmetry due to Bloch's theorem can be calculated through

$$H_{mn}(R) = \langle \varphi_{0m} | \hat{H} | \varphi_{Rm} \rangle \tag{2.24}$$

Once we obtain the TB Hamiltonian $H_{mn}(R)$, the Hamiltonian in k-space can be acquired by a Fourier transformation [2.17]. There are two conventions for Fourier transformations. One is

$$H_{mn}(k) = \sum_R e^{ik\cdot R} H_{mn}(R) \tag{2.25}$$

The other one is

$$H_{mn}(k) = \sum_R e^{ik\cdot(R+\tau_m-\tau_n)} H_{mn}(R) \tag{2.26}$$

The eigenvalues for these two conventions can be shown to be the same, but the eigenvectors are different. Eq. (2.25) first convention's eigenvectors are comparable to Bloch wave functions $\Psi_{nk}(r)$. The eigenvectors of the second convention Eq. (2.26) are analogous to the periodic part of the Bloch wave functions $u_{nk}(r) = \Psi_n e^{-ik\cdot r}$, which is of great importance in Berry phase and Berry curvature or the Wannier centers calculations. Therefore, the second convention is used in WannierTools. More information regarding the methods and capabilities of

WannierTools to calculate topological properties of materials, can be found in the primary publication [2.19].

2.1.3. Atomistic spin simulations

In the search for innovative materials with ideal or target properties, functionalities, and performance, multiscale material simulations have become one of the most effective and common tools. Simulations are used to reduce the design continuum for devices, to create novel materials with less effort, to replace tests that seem impractical, to analyze past experiments and propose new ones. They can also shed light on the underlying physics on timescales ranging from femtoseconds to decades and from Ångström to millimeters. Multiscale simulations [2.21] are crucial for the conception and development of the next-generation data devices [2.22] in this context, where spintronics is a particularly active field. This includes nontrivial magnetic textures like solitons with a time dilemma of 16 orders of magnitude between recording and saving information, as well as nanoscale magnetic objects like domain barriers. The simulation method is very helpful since it connects the necessary characteristics to the choice of magnetic materials and their advancement, opening up a wide range of potential applications [2.23].

To compute atom interactions and several other features, ab initio techniques, such as DFT, are frequently used since quantum mechanics is the key to understanding magnetism at its core. Due to their computational cost, such calculations can currently only be utilized to simulate time-dependent dynamics on timescales relevant for spintronics and magnetic structures in crystals with length scales in the order of 1 nm. Ab initio techniques can be used to extract parameters for more approximate, atomistic spin models, like Heisenberg spin-lattice Hamiltonians.

In order to extend simulations of magnetization dynamics across the duration of nanoseconds for systems with hundreds of nanometers, precise information about the electronic structure is integrated out to effective parameters characterizing the interaction between pairs of classical spins. The well-known micromagnetic approximation [2.24], which is based on the assumption of a continuous magnetization vector field, defined at any point of the magnetic sample, is the third level of the multiscale spintronics approach and is valid when changes in the magnetization are significantly larger in space than the underlying atomic lattice. The atomistic spin-

lattice model, on the other hand, accounts for the length scale between a few and many tens of nanometers, which is becoming increasingly essential from a technological standpoint.

In this case, we employed *Spirit* [2.25], a general-purpose, open-source, i.e., publicly accessible, framework for atomistic spin simulations. The time- and space-dependent evolution of magnetization can be simulated using a variety of computational techniques. The simulation of magnetic properties of materials and the temporal behavior of devices described by the Landau-Lifshitz-Gilbert (LLG) dynamics are definitely revolutionized by this software.

In *Spirit* is implemented the following atomically resolved Heisenberg Hamiltonian

$$H = -\sum_i m_i B \cdot n_i - \sum_i \sum_j K_i \left(\hat{K}_j \cdot n_i\right)^2 - \sum_{\langle ij \rangle} J_{ij} n_i \cdot n_j - \sum_{\langle ij \rangle} D_{ij} \cdot \left(n_i \times n_j\right) \tag{2.27}$$

the spin direction at each lattice site *i* is denoted by n_i, the magnetic moment is $m_i = \mu_i n_i$, B is the applied magnetic field, K the magnetic anisotropy constant, J_{ij} the magnetic exchange coupling constant and D_{ij} the Dzyaloshinskii-Moriya interaction (DMI).

The spin dynamics are described by the LLG equation [2.26, 2.27]

$$\frac{\partial n_i}{\partial t} = -\frac{\gamma}{(1+a^2)\mu_i} n_i \times B_i^{eff} - \frac{\gamma a}{(1+a^2)\mu_i} n_i \times \left(n_i \times B_i^{eff}\right) - \frac{\gamma a}{(1+a^2)\mu_B} u n_i \times (\hat{j}_e \cdot \nabla_r) n_i + \frac{\gamma}{(1+a^2)\mu_B} u n_i \times [n_i \times (\hat{j}_e \cdot \nabla_r) n_i] \tag{2.28}$$

Where each term corresponds to (a) precession, (b) damping, (c) precession-like current-induced spin torque, and (d) damping-like current-induced spin torque, $\alpha = 0.05$ is the damping parameter, γ is the electron gyrometric ratio, the effective field $B_i^{eff} = -\partial H / \partial n_i$ and u is spin torque defined as

$$u = j_e P \hbar \mu_B / (2 e M_s) \tag{2.29}$$

with j_e the spin-polarized current density, e the electron charge, ħ is Planck's reduced constant, P is the current polarization and M_s the magnetization saturation. The effective field including a stochastic thermal field $B_i^{eff} \rightarrow B_i^{eff} + B_i^{th}$ is given by

$$B_i^{th}(t) = \sqrt{2D_i}\eta_i(t) = \sqrt{2ak_BT\frac{\mu_i}{\gamma}}\eta_i(t) \tag{2.30}$$

where η_i is white noise.

2.2. Experimental Methods

2.2.1. Molecular beam epitaxy

Molecular Beam Epitaxy (MBE) is the most ideal method for developing ultrathin films. Initially the method was invented for the development of high-purity semiconductors, but in the following years it was used for many applications in the broad field of studying surfaces [2.28, 2.29].

Development in an MBE system requires ultrahigh vacuum, with pressures lower than 10^{-9} mbar in order to avoid impurities in the sample being developed. To reach such low pressures requires the cooperation of different types of pumps that are activated in different pressure ranges. Initially a mechanical pump reduces the pressure in the chamber to ~10^{-3} mbar and then in cooperation with a turbo pump the pressure in the chamber can reach a pressure range of ~10^{-6}-10^{-7} mbar. In the final stage, a cryopump can reach and maintain the pressure at values of ~10^{-10} mbar. Fig. 2.1 shows the MBE system that is located in the Epitaxy and Surface Science Lab of the Institute of Nanoscience and Nanotechnology of the N.C.S.R. "Demokritos", which was used for the growth and characterization of all the structures presented in this work.

The architecture of the MBE chamber is constructed in such a way that the beams of atoms or molecules produced by the various sublimation methods are guided to the surface of a crystalline substrate, e.g., Si, InAs, AlN, etc. The possibility of scattering of the bonds on their way to the substrate is very small due to the ultra-high vacuum conditions that prevail. The particles then interact on or before they reach the substrate, which is kept at a temperature suitable for creating the desired structure. The MBE system also has the ability to rotate the substrate during element deposition to ensure better coating uniformity.

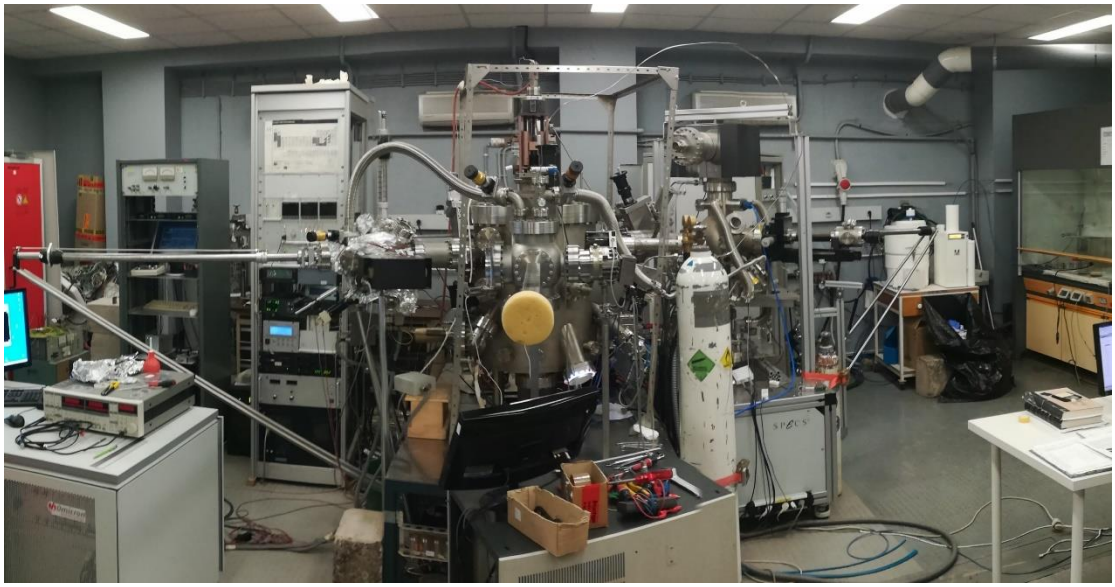

Figure 2.1. Panoramic view of the MBE system located in the Epitaxy and Surface Science Lab of the Institute of Nanoscience and Nanotechnology of the N.C.S.R. "Demokritos"

At such low pressures, the growth is determined by kinetic processes at the surface. To achieve the desired growth of epitaxial structures, the deposition rate of atoms on the surface of the substrate is usually low. The material evaporation is done by various methods that depend on their melting temperature. One method of evaporation is to heat the material in a Knudsen cell with the material placed in a suitable crucible, in which we usually place the chalcogenides. Refractory materials, such as transition metals, are sublimated by bombarding them with electrons fired from an electron gun. The deposition rate of the materials is accurately determined using quartz crystals connected to a deposition rate monitor. The structural characterization of the surface, i.e., whether the material is crystalline, polycrystalline or amorphous, is done using the technique of reflection high energy electron diffraction (RHEED).

The system has three Knudsen cells in which, as mentioned above, the material is placed in suitable crucibles. There are various materials from which the crucibles are made, so that the evaporation needs of a wide variety of materials can be met. The temperature of the cell can be increased up to 2000 °C in order to evaporate the material, while its recording is done using a thermocouple. Due to the high temperature development in the cells during operation, water is passed through the gasket to keep the gasket temperature low. The flow of atoms resulting from the evaporation of the material can be interrupted by means of a magnetic shutter which is controlled by a main control unit [2.30].

In addition, the system is also equipped with two electron guns for co-evaporation of transition metals. The electron guns have three (one) slots for placing materials and a filament. Electrons produced as a high voltage is applied to the filament, pass through a controlled electromagnetic field, which is created by a strong magnet and a capacitor. By properly adjusting the properties of this field, we can precisely determine the trajectory of the electrons in order to guide them onto the material to be evaporated. The movement from one cell to another is done through a mechanical axis and the flow of atoms resulting from the sublimation of the material can again be interrupted through a magnetic shutter [2.30].

2.2.2. Reflection high energy electron diffraction

The RHEED method is the most widespread study technique [2.31] of the surfaces in an MBE chamber, i.e., it is used for quality control but also for monitoring the growth of the film. In the RHEED method high energy electrons, about 10-100 keV, are incident on the sample surface at angles of about 1°-5° and the diffracted electron beams are incident and observed on a fluorescent screen, as we see in Fig. 2.2 for a typical setup. The technique is extremely surface-selective, as the electrons are diffracted only in a few atomic levels, due to the small angle of incidence of the electrons despite their high energy. The basic principles of the RHEED technique are described below.

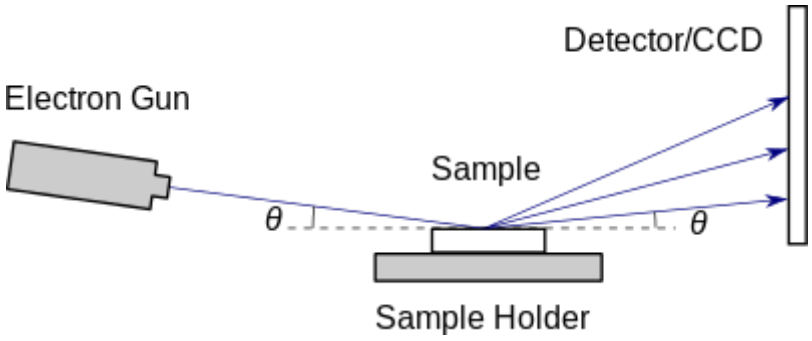

Figure 2.2. Geometry of a typical RHEED set-up [2.32].

Using the kinematic approach, where we assume that the electrons are elastically scattered and only the incident beam can be diffracted (Fig. 2.3), we can calculate the position of appearance of the amplifying contribution points. In order to be a reinforcing contribution between two electrons scattered from two points that are separated by a distance *R*, should hold [2.32]

$$R\cos\theta + R\cos\theta' = \vec{R}\cdot\hat{n} - \vec{R}\cdot\hat{n'} = m\cdot\lambda \qquad (2.31)$$

From the Eq. (2.31) and with the help of Figure 2.3 it follows that

$$\vec{R}\left(\vec{k} - \vec{k'}\right) = 2 \cdot \pi \cdot m \tag{2.32}$$

The Eq. (2.32), also known as the Laue condition, defines that in order to have an amplifying contribution the difference of the wave vectors of the incident and scattered beam should be equal to a vector of the inverse lattice. The geometric construction that will help us find the directions where the Laue condition is satisfied, is called the Ewald sphere.

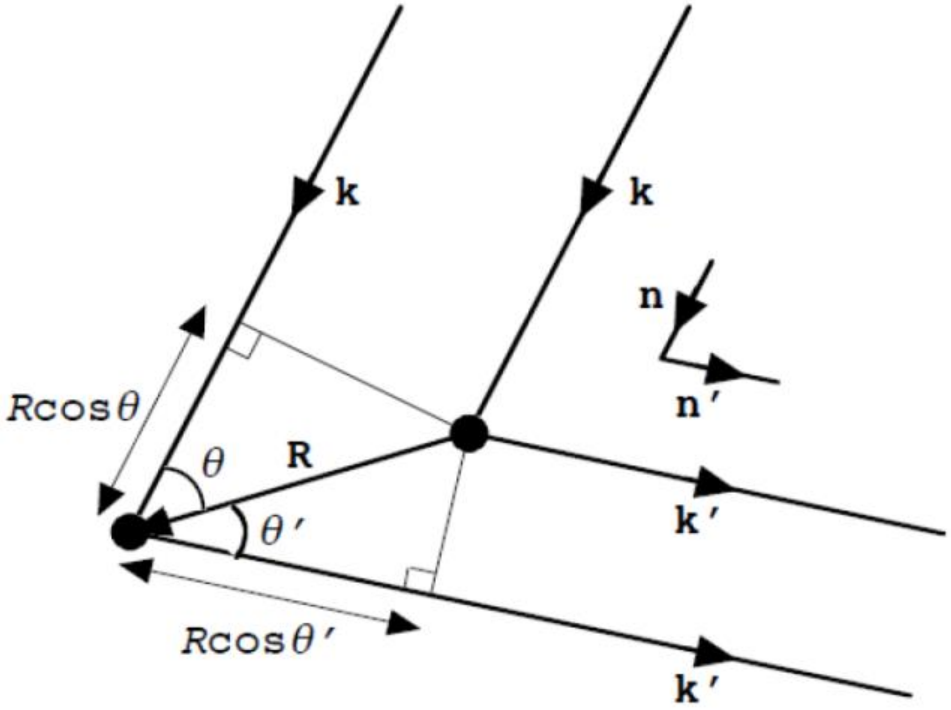

Figure 2.3. Difference in the path traveled between two rays scattered from two points at a distance R [2.32].

The Ewald sphere has a radius equal to the wavevector of the electrons, and the intersection of this sphere with the inverse lattice points determines the wavevectors that will lead to an amplifying contribution.

The inverse space of a surface consists of a two-dimensional grid with bars of infinite length perpendicular to the points of the inverse grid. The intersection of the Ewald sphere with the bars of the inverse space gives us the wave vectors of the scattered electrons that satisfy the Laue condition, as we see in Fig. 2.4.

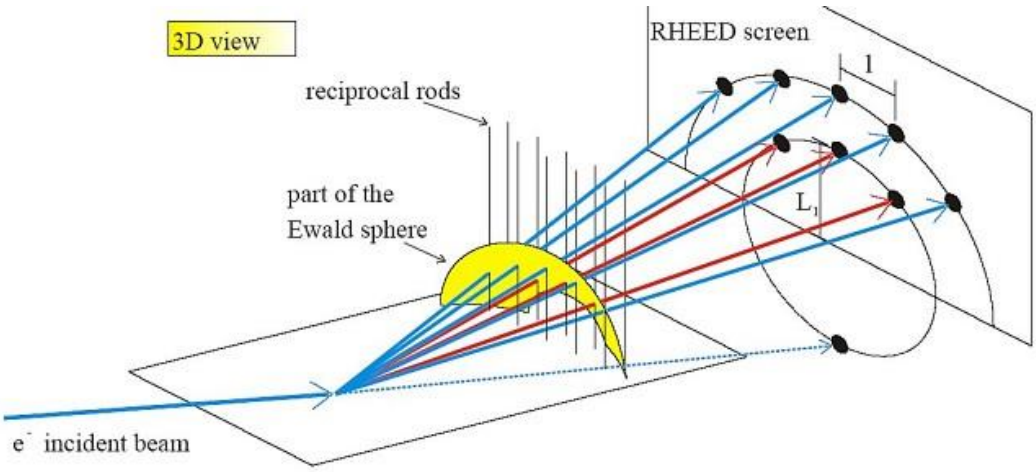

Figure 2.4. 3D view of inverse space and the Ewald sphere [2.33].

Ideally the interference image we would see from an ideally flat surface would be a set of well-defined points. But in reality, because the surface usually has imperfections, the beam of incident electrons is not monoenergetic, and furthermore because there is a small angular dispersion, we observe lines corresponding to a section of a small piece of a rod in the inverse space of the Ewald sphere.

2.2.3. Photoelectron spectroscopy

Photoelectron spectroscopy refers to techniques that exploit the photoelectric effect [2.34] to study the electronic structure of materials. The most widespread applications of this technique are X-ray photoelectron spectroscopy (XPS) which is used for the chemical analysis of surfaces by obtaining information about the elements that make up a material but also about the chemical bonds that create them together, and the ultraviolet photoelectron spectroscopy (UPS) technique used to extract information from the energy valence bands of a material. The UPS technique is usually applied to record the band structure of a material with the angle-resolved photoemission spectroscopy (APRES) method.

In Fig. 2.5 we see the basic operating principle of photoelectron spectroscopy. By throwing photons of a certain energy on a surface we can extract photoelectrons whose kinetic energy we measure using an electron analyzer. A necessary condition for the extraction of photoelectrons is that the excitation energy hv be greater than the output work Φ of the material [2.32]. The kinetic energy measured by the photoelectron analyzer allows us to determine the binding energy of an electron through the relationship:

$$E_B = h \cdot \nu - E_{KIN} - \Phi \tag{2.33}$$

In the simplified model of non-interacting electrons, the photoelectronic distribution represents the density of electronic states determined with the help of relation (2.33). Electrons corresponding to bound orbitals can be excited with the help of soft χ-rays and are found at binding energies from a few tens to thousands of eV below the Fermi level, while electrons originating from the valence band usually have energies of a few eV and can be excited using infrared light of photon energy of a few tens of eV.

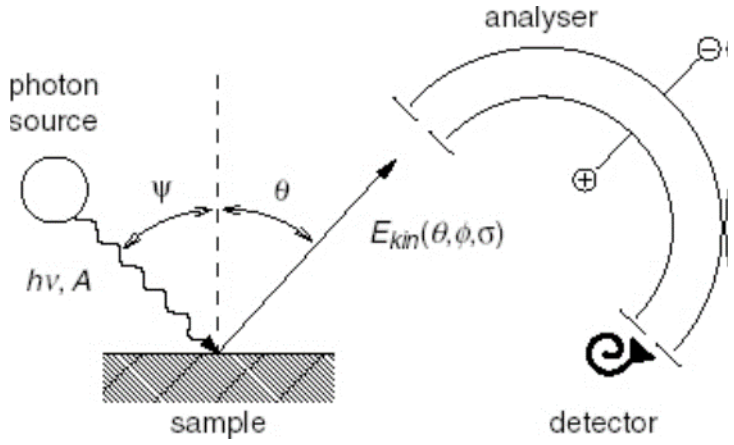

Figure 2.5. Basic principle of a photoelectron spectroscopy measurement [2.35].

To understand the photoemission process we divide it into three separate steps [2.29, 2.36]. These steps are, (a) the excitation of the photoelectron to an unoccupied energy state of the energy bands of the material, (b) the transport of the electron to the surface, and (c) the refraction at the surface and exit of the electron into the void.

In the first step the transition probability of the electron from the initial state Ψ_i to the final state Ψ_f is given by Fermi's rule through the relation

$$P_{i\to f} = \frac{2\pi}{\hbar}\left|\langle\Psi_f|H_{h\nu}|\Psi_i\rangle\right|^2 \delta\left(E_f - E_i - h\nu\right) \tag{2.34}$$

where the quantity in Dirac's δ function ensures conservation of energy, that is, the electron will transition from one state to another only if the difference between the two energy states (E_f–E_i) is equal to the photon's energy ($h\nu$). The transition probability is calculated if one considers the photon-electron interaction as a perturbation in the framework of change theory. The disturbance in the system can be written as

$$H_{h\nu} = \frac{e}{m_e c} A \cdot \hat{p} \tag{2.35}$$

with A the electromagnetic field and p the momentum operator for the electron.

In the second step the electron should reach the surface without being scattered. If N_i is the number of photoelectrons that will be excited, those that will reach the surface without being scattered will be

$$N = N_i \cdot e^{\frac{d}{\lambda}} \tag{2.36}$$

Where d is the distance from the crystal/vacuum surface and λ is the mean free path of the electron.

In the third step the electrons that reach the surface are refracted by the surface potential, at least at an angle θ to the surface. This process can be represented by Bloch states inside the crystal and plane waves in the energy vacuum [2.35]

$$E_{KIN}^{vac} = \frac{\hbar^2}{2m} k_{vac}^2 \tag{2.37}$$

Resolving the electron wave vector into a perpendicular and a parallel component will apply to the two components

$$\left|k_{||}\right| = \left|k_{||}^{vac}\right| = \frac{1}{\hbar}\sqrt{2 \cdot m \cdot E_{KIN}} \sin\theta \tag{2.38}$$

$$\left|k_{\perp}^{vac}\right| = \frac{1}{\hbar}\sqrt{2 \cdot m \cdot E_{KIN}} \cos\theta \tag{2.39}$$

The symmetry of the surface preserves the parallel wave vector of momentum, this is the basic quantity we measure in the ARPES method that we will present next and it is the method we use to measure the energy bands of materials. In contrast, translation symmetry breaking perpendicular to the surface does not preserve the vertical wave vector. By enforcing the principle of energy conservation, we find that

$$\left|k_{\perp}\right| = \frac{1}{\hbar}\sqrt{2 \cdot m \cdot (E_{KIN} \cos\theta + V_o)} \tag{2.40}$$

Where V_0 is the inner potential.

2.2.3.1. X-ray photoelectron spectroscopy

In X-ray photoelectron spectroscopy, soft X-rays (1000-1500 eV) are used to excite bound levels and measure their electron binding energy through relation (2.33). The measured binding energies are characteristic of each species of atom and the intensity of the signal is proportional to the number of atoms in the region from which the photoelectrons originate. XPS is an ideal method for determining the elements that make up the sample. The peaks in an XPS spectrum mainly belong to two categories.

Firstly, the peaks that originate from bound atomic states and have a fixed binding energy and secondly the Auger peaks where their binding energy changes with the change of excitation energy.

Finally, we can get information about the bonds between atoms from the displacements of the characteristic peaks of a material. The state of oxidation or any other reaction of an atom affects the binding energy of its bound electrons, or the peaks of the spectrum and give us information about the bonds that have been created in a sample.

2.2.3.2. Angle-resolved photoemission spectroscopy

The angle-resolved photoemission spectroscopy (ARPES) technique is the most basic technique for recording the structure of the electron energy bands in a solid. Fig. 2.6 shows a simple representation of the method we follow to record an ARPES spectrum.

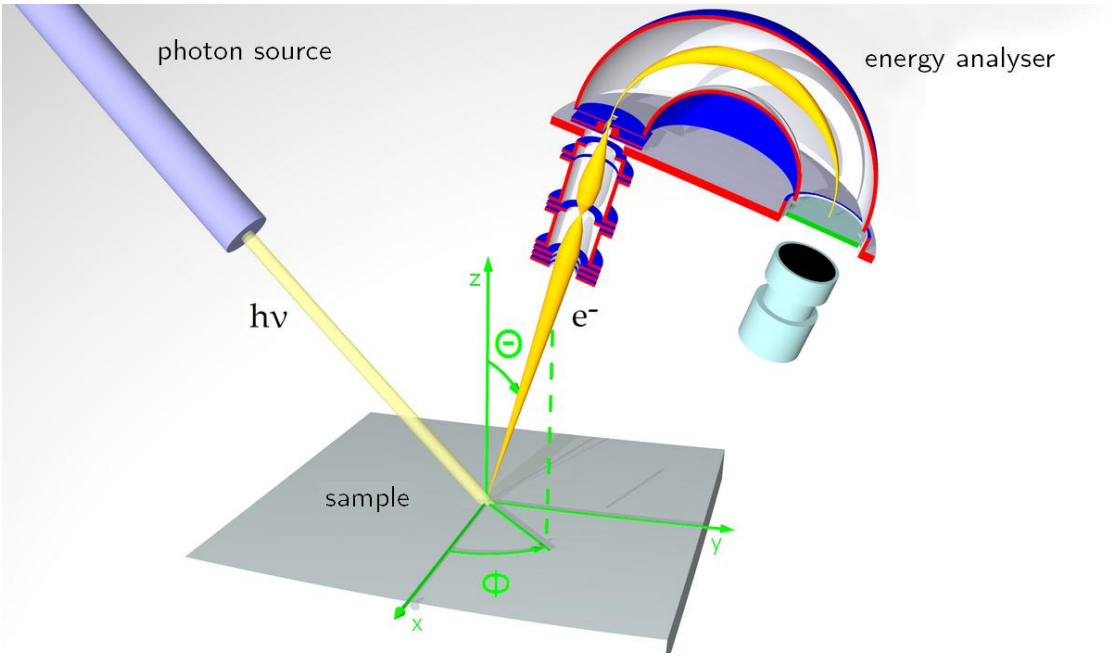

Figure 2.6. Basic working principle of the ARPES method, photoelectrons exiting the sample at a certain angle pass through the electron analyzer and are measured by the detector [2.37].

By bombarding a surface with photons of energy in the range of 20-100 eV, the electrons exiting the material are measured and their kinetic energy is determined according to relation (2.33). Knowing the angle formed by the sample with the analyte, the parallel wave vector of the photoelectron can be determined through relation (2.38). By collecting measurements for a range of angles we can determine the scattering of electrons in the solid, i.e., represent the structure of the energy bands.

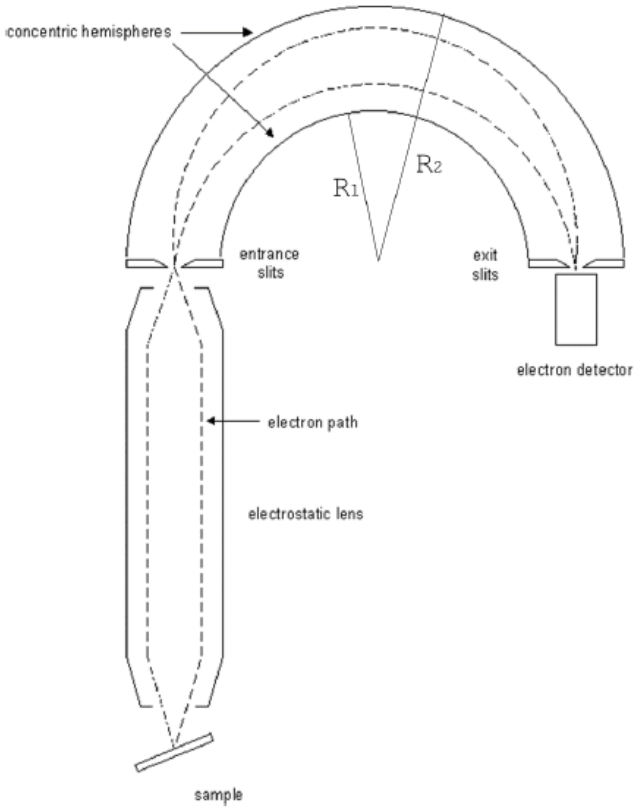

Figure 2.7. Schematic illustration of a hemispherical electron analyzer [2.29].

The measurement of the kinetic energy of the electrons is done with the help of an electron analyzer which is also the most important instrument for the measurements of the structure of the energy bands. In Fig. 2.7 we see a schematic illustration of a hemispherical electron analyzer, the most common type of analyzer found in a photoelectron spectroscopy setup. Electrons escaping the sample pass through an array of electromagnetic lenses and, after being slowed down, are focused into the entrance slit. The two hemispheres with radii R_1 and R_2 are at a fixed potential difference ΔV so that only electrons that pass the input slit with a certain kinetic energy will pass and eventually reach the output slit to be measured by the detector. The value of energy is determined by the relationship

$$\mathrm{E_{pass}} = \frac{e \cdot \Delta V}{\frac{R_1}{R_2} - \frac{R_2}{R_1}} \tag{2.41}$$

while the energy resolution is equal to

$$\Delta E_\alpha = E_{pass} \frac{2 \cdot \mathrm{w}}{R_1 + R_2} + \frac{a^2}{2} \tag{2.42}$$

where w is the width of the entrance slit and α is the acceptance angle set by the electromagnetic lens array. By varying the deceleration potential in the electromagnetic lens system, the value of the E_{pass} energy changes and electrons for different kinetic energies can be counted.

In most modern arrangements the detector consists of a two-dimensional Multi-Channel Plate (MCP) which acts as a two-dimensional electron multiplier. The electrons after their multiplication end up on a fluorescent screen and the emitted signal is recorded by a Charged Coupled Device (CCD) camera. Measurements with this type of detector record the kinetic energy of the electrons over a range of energies giving an image of a piece of inverse space instead of a single *k*-point that conventional detector measure.

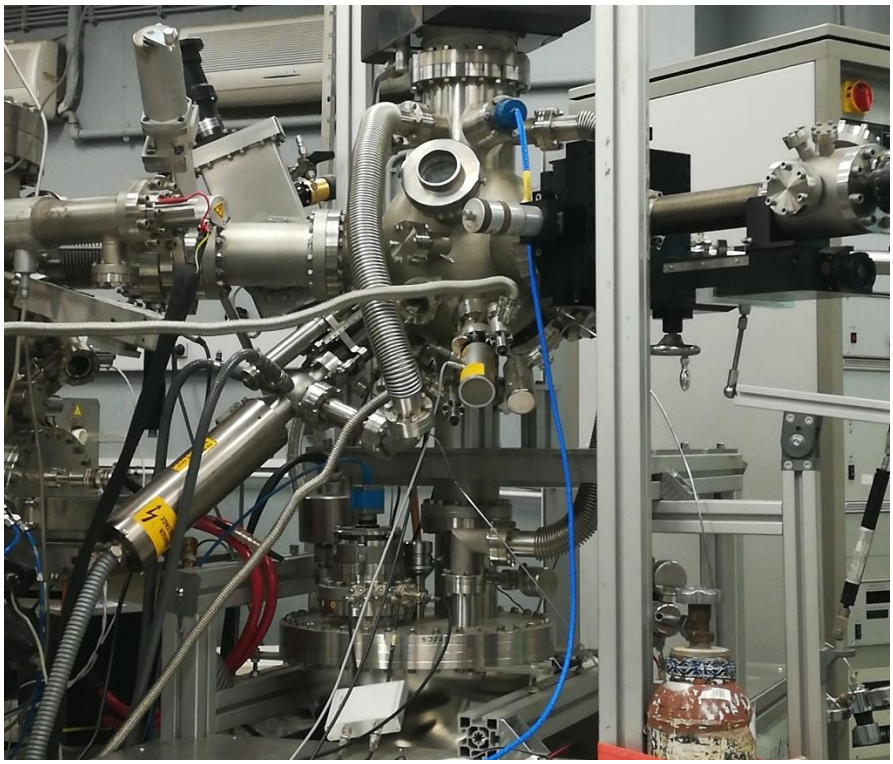

Figure 2.8. The UPS/ARPES and XPS chamber of the Epitaxy and Surface Science Laboratory at N.C.S.R. "Demokritos".

At the Epitaxy and Surface Science Lab of the N.C.S.R. "Demokritos", ARPES measurements are made in the same chamber as X-ray Photoelectron Spectroscopy (Fig. 2.8). The ARPES system has a 100 mm radius hemispherical electron analyzer (PHOIBOS 100 from SPECS) and a CCD detector. A He gas discharge lamp (UV 10/35 from SPECS company) with a photon energy (He-I) equal to 21.22 eV was used as the main photon source. For additional measurements, Ne (Ne-I) and Ar (Ar-I) gas with photon energies equal to 16.67 and 11.62 eV respectively can be used.

2.2.4. Scanning tunneling microscopy

Scanning tunneling microscopy (STM) was invented in the early 1980s [2.38] and borrowed elements from existing measuring systems such as the surveyor. Fig. 2.9 shows a schematic representation of the microscope. The metal spike approaches the sample surface at distances of the order of nm. A potential difference of the order of 10 mV – 2 V is applied between the sample and the tip. This results in an electron flow of the order of 100 pA – 10 nA from the surface to the tip or vice versa, depending on the voltage bias.

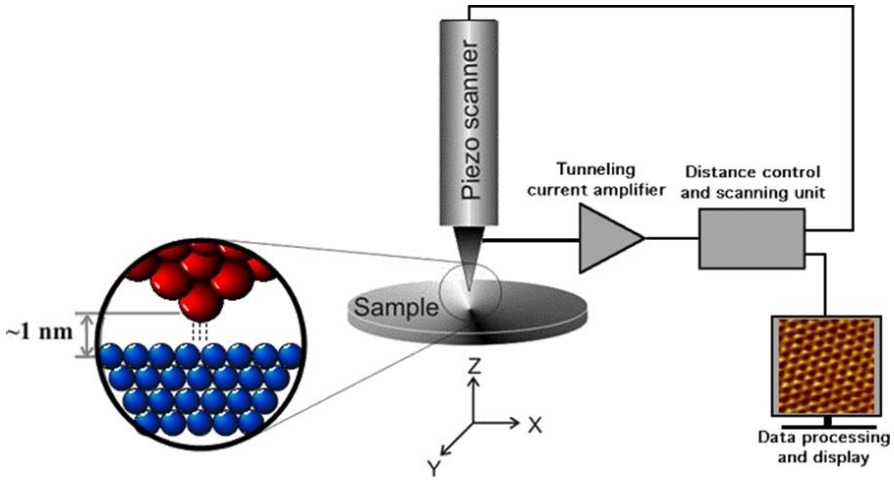

Figure 2.9. Schematic representation of a typical experimental set-up for STM [2.39].

The scanning electron microscope has two operating options [2.39]: (a) Scan under conditions of fixed vertical pin position - display only via current variation and (b) Surface scanning under constant current conditions - imaging via variation of vertical tip position and micro-fluctuations of current

The most common and safest mode of operation is the second. In this mode the position of the pin along the *zz*' axis is properly adjusted so that the current selected by the user remains constant. The tip is not in resistive contact with the sample and the current results only from electrons that have tunneled from the sample to the tip or vice versa.

The stylus moves in the *xy* plane and scans the surface of the sample. During this process, the current exhibits small fluctuations which are recorded and the position of the spike on the *zz'* axis is actively adjusted to keep the current as constant as possible. These two processes (small current variation and *zz*' tip position) are translated into an image by superimposing them on the xy coordinates of the scanned surface and depict the topography of the sample. The movement in the xy plane as well as the vertical

position of the tip are controlled through an external computer system which is connected to the experimental setup. It is worth mentioning that the characterization of surfaces with STM can be carried out in various environmental conditions of pressure and temperature even in the atmosphere. However, the quality and cleanliness of the surface as well as the sharpness of the tip are decisive factors in the experimental process for good imaging of the sample, especially at atomic scales.

The basic operating principle of the STM is the quantum tunneling effect. The phenomenon can be described through the time-independent Schrödinger equation

$$-\frac{\hbar^2}{2m}\frac{\partial^2 \Psi_n(z)}{\partial z^2} + U(z)\Psi_n(z) = E\Psi_n(z) \tag{2.43}$$

where $\hbar$ is Planck's reduced constant, z is the position in the reference direction, m is the mass of the electron, E the energy of the electron, and U the height of the potential barrier. Reference direction is the zz' axis perpendicular to the xy plane, where the electron flow and the potential barrier between the sample and the tip appear. The wavefunction of the electron has the form

$$\Psi_n(z) = \Psi_n(0)e^{\pm ikz} \tag{2.44a}$$

$$k = \sqrt{\frac{2m(E-U(z)}{\hbar}} \tag{2.44b}$$

However, within a potential barrier the wave function is decreasing and becomes

$$\Psi_n(z) = \Psi_n(0)e^{\pm kz} \tag{2.45a}$$

$$k = \sqrt{\frac{2m(U-E)}{\hbar}} \tag{2.45b}$$

This allows us to calculate the current that will flow between the sample and the pin

$$I = A\sum_{E_f-eV}^{E_f} |\Psi_n(0)|^2 e^{-2kW} \tag{2.46}$$

Where A is a constant, V the applied voltage, W the width of the potential barrier and E_f the Fermi level. However, the local density of states (LDOS) at a distance ε from the Fermi level is given as

$$\rho_s(z, E_f) = \frac{1}{\varepsilon} \sum_{E_f-\varepsilon}^{E_f} |\Psi_n(z)|^2 \tag{2.47}$$

and the tunneling current for z = 0 at the sample surface can be expressed as

$$I = AV\rho_s(0, E_f)e^{-2kW} \tag{2.48}$$

Equation 2.48 gives the current flowing between sample and pin (in the present view from sample to pin) and highlights three main factors: (a) The current has an ohmic relationship with the applied voltage, (b) it depends exponentially on the distance W between the tip and the sample and, (c) it depends on the LDOS, which is crucial for depicting the topography of the sample, especially at the individual level.

References

[2.1] M. Born and R. Oppenheimer, Annalen der Physik **389**, 457 (1927).
[2.2] D. R. Hartree, Math. Proc. Camb. Philos. Soc. **24**, 89 (2008).
[2.3] V. Fock, Zeitschrift für Physik **61**, 126 (1930).
[2.4] L. H. Thomas, Math. Proc. Camb. Philos. Soc. **23**, 542 (1927).
[2.5] N. H. March, Adv. Phys. 6, 1 (1957).
[2.6] E. Kaxiras, Atomic and Electronic Structure of Solids. Cambridge: Cambridge University Press, 2003.
[2.7] R. M. Martin, Electronic Structure: Basic Theory and Practical Methods. Cambridge: Cambridge University Press, 2004.
[2.8] J. Kohanoff, Electronic Structure Calculations for Solids and Molecules: Theory and Computational Methods. Cambridge: Cambridge University Press, 2006.
[2.9] P. Hohenberg and W. Kohn, Phys. Rev. **136**, B864 (1964).
[2.10] W. Kohn and L. J. Sham, Phys. Rev. **140**, A1133 (1965).
[2.11] G. Kresse and J. Furthmüller, Comput. Mater. Sci. **6**, 15 (1996).
[2.12] G. Kresse and J. Furthmüller, Phys. Rev. B **54**, 11169 (1996).
[2.13] G. H. Wannier, Phys. Rev. **52**, 191 (1937).
[2.14] N. Marzari and D. Vanderbilt, Phys. Rev. B **56**, 12847 (1997).
[2.15] E. I. Blount, "Formalisms of Band Theory," in Solid State Physics. vol. 13, F. Seitz and D. Turnbull, Eds., ed: Academic Press, 1962, pp. 305-373.
[2.16] A. A. Mostofi, J. R. Yates, Y.-S. Lee, I. Souza, D. Vanderbilt, and N. Marzari, Comput. Phys. Commun. **178**, 685 (2008).
[2.17] N. Marzari, A. A. Mostofi, J. R. Yates, I. Souza, and D. Vanderbilt, Rev. Mod. Phys. **84**, 1419 (2012).
[2.18] J. C. Slater and G. F. Koster, Phys. Rev. **94**, 1498 (1954).
[2.19] Q. Wu, S. Zhang, H.-F. Song, M. Troyer, and A. A. Soluyanov, Comput. Phys. Commun. **224**, 405 (2018).
[2.20] A. A. Mostofi, J. R. Yates, G. Pizzi, Y.-S. Lee, I. Souza, D. Vanderbilt, and N. Marzari, Comput. Phys. Commun. **185**, 2309 (2014).
[2.21] M. Hoffmann, B. Zimmermann, G. P. Müller, D. Schürhoff, N. S. Kiselev, C. Melcher, and S. Blügel, Nat. Commun. **8**, 308 (2017).
[2.22] I. Žutić, J. Fabian, and S. Das Sarma, Rev. Mod. Phys. **76**, 323 (2004).
[2.23] S. D. Bader, Rev. Mod. Phys. **78**, 1 (2006).
[2.24] W. F. Brown, Micromagnetics. New York, London: Interscience Publishers, 1963.
[2.25] G. P. Müller, M. Hoffmann, C. Dißelkamp, D. Schürhoff, S. Mavros, M. Sallermann, N. S. Kiselev, H. Jónsson, and S. Blügel, Phys. Rev. B **99**, 224414 (2019).
[2.26] L. Landau and E. Lifshitz, in Perspectives in Theoretical Physics, L. P. Pitaevski, Ed., ed Amsterdam: Pergamon, 1992, pp. 51-65.
[2.27] T. L. Gilbert, IEEE Trans. Magn. **40**, 3443 (2004).
[2.28] R. F. C. Farrow, Molecular beam epitaxy: applications to key materials. New Jersey: Moyes publications, 1995.
[2.29] E. Golias, "Doctorate thesis," School of Applied Mathematics and Physical Science, National Technical University of Athens, Athens, 2013.
[2.30] A. Dimoulas, and Y. Panayiotatos, "Notes on the Molecular Beam Epitaxy Lab," School of Applied Mathematics and Physical Science, National Technical University of Athens, Athens, 2008.

[2.31] W. Braun, Applied RHEED: reflection high-energy electron diffraction during crystal growth vol. 154: Springer Science & Business Media, 1999.
[2.32] N. Ashcroft and N. Mermin, "Solid state physics; thomson learning, inc," Stamford, CT, 1976.
[2.33] B. Landgraf, "Structural, magnetic and electrical investigation of Iron-based III/V-semiconductor hybrid structures," 2014.
[2.34] A. B. Arons and M. B. Peppard, "Einstein's Proposal of the Photon Concept—a Translation of the Annalen der Physik Paper of 1905," American Journal of Physics, vol. 33, pp. 367-374, 1965.
[2.35] F. Reinert and S. Hüfner, "Photoemission spectroscopy—from early days to recent applications," New Journal of Physics, vol. 7, pp. 97-97, 2005/04/29 2005.
[2.36] J. Márquez-Velasco, "Doctoral dissertation," School of Applied Mathematics and Physical Science, National Technical University of Athens, Athens, 2016.
[2.37] https://commons.wikimedia.org/wiki/File:PES3.jpg, "Principle of Angle Resolved Photoelectron Spectroscopy," ed. Wikipedia, 2009.
[2.38] G. Binnig and H. Rohrer, "Scanning tunneling microscopy- from birth to adolescence," Reviews of Modern Physics, vol. 59, pp. 615-625, 07/01/ 1987.
[2.39] S. Aminalragia-Giamin i, "Doctoral dissertation," Physics department, National and Kapodistrian University of Athens, Athens, 2017.

3. Topological surface states in epitaxial $(SnBi_2Te_4)_n(Bi_2Te_3)_m$ natural van der Waals superlattices

3.1. Introduction

Topological surface states (TSS) in three-dimensional (3D) topological insulators (TI) have their spin locked to the orbital momentum due to strong spin-orbit coupling (SOC), which results in high charge to spin conversion efficiency [3.1, 3.2] via the Edelstein effect [3.3]. They may therefore be excellent replacements for heavy metals (Pt, Ta, etc.) in spin orbit torque (SOT) magnetic devices, among other uses [3.2]. The parasitic contribution from the bulk conduction band (BCB) restricts the usage of conventional 3D TIs, such as the layered Bi_2Se_3 and Bi_2Te_3, for practical applications. The surface topological features can be tailored to promote the TSS contribution in the electrical transport by combining with other substances. As an illustration, it has been demonstrated [3.4] that doping Bi_2Te_3 with 0.9% Sn causes the Fermi level to fall inside the bulk energy gap, crossing only the TSS and obviating the need for BCB contribution. The TSS and bulk electrical band structure in alloys with Sn-rich compositions [3.5] or compounds with more Sn at stoichiometric compositions, such as the Bi-rich $SnBi_2Te_4$, $SnBi_4Te_7$, etc., have not been experimentally thoroughly explored. Intriguingly, the parent SnTe is also a topological crystalline insulator [3.6], opening the possibility that TSS can be created over the full range of Sn composition x (0-1). The Sn-Bi-Te mixed compound is anticipated to take the shape of a natural van der Waals heterostructure of the general form $(SnBi_2Te_4)_n(Bi_2Te_3)_m$ where n layers of $SnBi_2Te_4$ alternate with m layers of Bi_2Te_3 based on prior research on comparable compounds $PbBi_2Te_4$, $PbBi_4Te_7$, $GeBi_4Te_7$, and $MnBi_2Te_4$ [3.7-3.11]. In the first member of the series, $SnBi_2Te_4$ (n = 1, m = 0), SnTe takes up the middle position at the septuplet layer when it mixes with Bi_2Te_3, whereas in the second member of the series, $SnBi_4Te_7$ (n = 1, m = 1), one $SnBi_2Te_4$ septuplet alternates with one Bi_2Te_3 quintuple to form a natural van der Waals superlattice. One $SnBi_4Te_7$ septuplet alternates with two or more Bi_2Te_3 quintuples in higher order members of the series, such as $SnBi_6Te_{10}$, (n = 1, m = 2), to construct natural van der Waals superlattices [3.5]. The Fermi level is located in the gap, and theoretical analyses of the various series members have demonstrated that they are all TIs [3.5, 3.12]. $SnBi_2Te_4$, the first member of the series, has already been synthesized in bulk form (nanoplates) [3.13], and a weak

antilocalization (WAL) effect has been detected in magnetotransport studies, which has been linked to TSS that may be mixed in with bulk contributions. Furthermore, it has been demonstrated [3.13] that the bulk $SnBi_2Te_4$ departs from ideality due to a cation exchange and the presence of both Sn and Bi in the septuplet's middle row, with Sn predominating. Regarding the electronic band structure and the presence of TSS in any member of the series, there are no experimental data available. To prove a significant contribution of TSS to electrical conduction, essential for SOT devices and spintronics, direct observation of the TSS by ARPES and their association with magnetotransport are needed. Furthermore, all previous research has focused on equilibrated bulk material growth [3.13–3.16]. The natural van der Waals superlattice structure and their topological properties could be tailored with the help of epitaxial thin films grown by out-of-equilibrium methods like molecular beam epitaxy (MBE). This would pave the way for scalable large area growth of composite TI/magnetic layer devices.

In this work [3.17], we report on four distinct TI compounds and alloys, namely Bi_2Te_3, $SnBi_4Te_7$, $SnBi_2Te_4$, and $Sn_{1-x}Bi_xTe$, produced via molecular beam epitaxy on InAs(111)/Si(111) substrates, as well as their structure and electrical properties, particularly those related to the TSS. High-resolution scanning transmission electron microscopy (STEM) analysis of the layered structure reveals layer stacking in the form of a natural van der Waals superlattice. We confirm the existence of TSS and correlate it with magnetotransport observations using first-principles calculations in combination with in-situ and synchrotron ARPES. We then shift the Fermi level's position with regard to the TSS and the BCB by adjusting the Bi/Sn ratio while having it monitored by ARPES. This allows us to pinpoint the Sn composition at which the TSS contribution is greatest in relation to the BCB.

3.2. Results

3.2.1. Epitaxial growth and natural van der Waals superlattice

Four of the eight samples that were grown on InAs(111) substrates with various Bi/Sn ratios were carefully examined (Table I). The chemically cleaned InAs(111)/Si(111) substrates were prepared in a 5N HF solution in isopropyl alcohol for 5 min to etch (remore) the surface oxide and then washed in isopropyl alcohol for 30 seconds to prevent the substrate from reoxidizing. To obtain a clean and flat InAs(111) (In-terminated) surface, an annealing step at 400° C in UHV is then performed, as shown

by RHEED. A 2 × 2 reconstruction in RHEED pattern attributable to In surface vacancies shows that appropriate, mild Ar+ sputtering (E ≈ 1.5 keV, p ≈ 2×10^{-5} mbar, t ≈ 30 s) was used to create a clean surface before the annealing process [3.18]. The films are developed in a UHV MBE (DCA Instruments) vertical chamber under Te-rich conditions. The system's base pressure is 5×10^{-10} mbar. Bi and Te (99.999%) are vaporized in Knudsen cells, and Sn is vaporized in an e-beam evaporator. The nominal ratio derived from the evaporation rates is confirmed by X-ray photoelectron spectroscopy (XPS) using sensitivity factors from the literature (Fig. 3.1). The rate of Sn deposition in comparison to Bi determines the composition of Sn. Te is provided under over-pressurized conditions where the growth rate ratio Te/M (M=Bi, Sn) is less than 15. Under these conditions, surplus Te with a low sticking coefficient is desorbed while Te is integrated into the material to produce the desired stoichiometric compounds. The ratios and thicknesses of the other four samples were defined by X-ray diffraction (XRD) (Fig. 3.2).

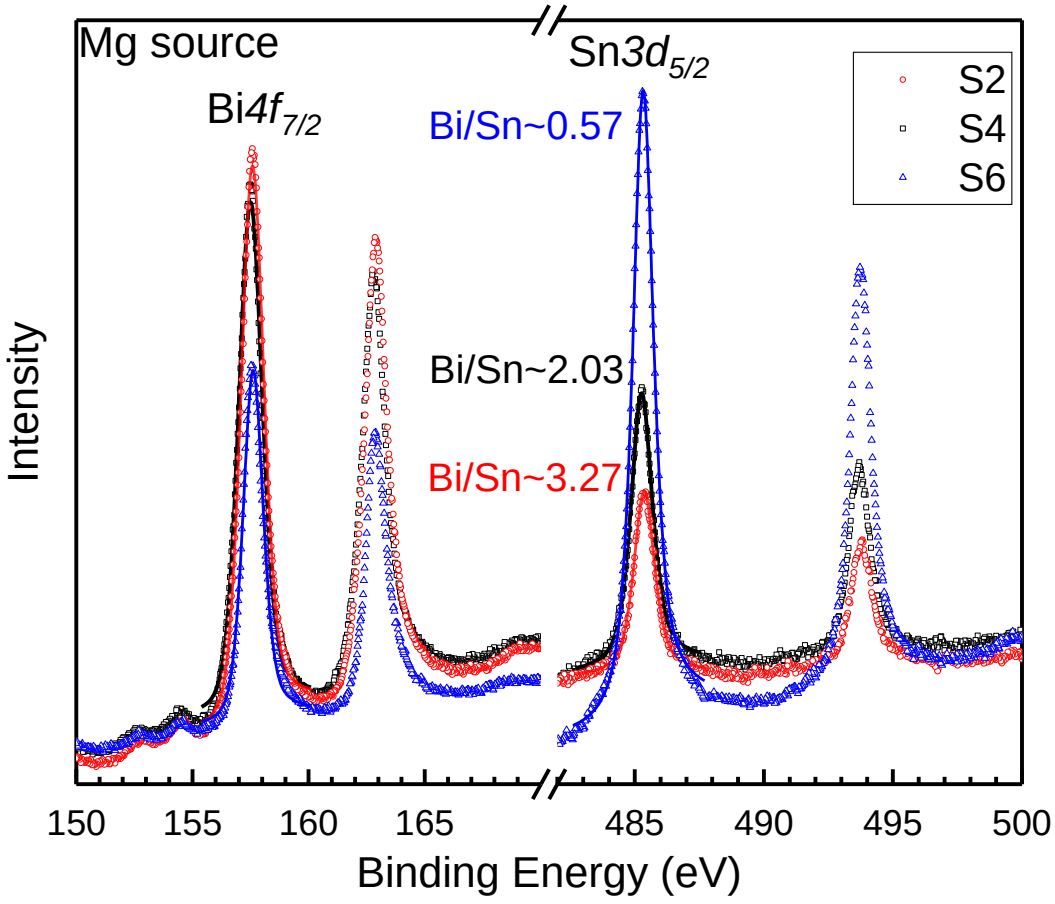

Figure 3.1. Bi_{4f} and Sn_{3d} peak XPS spectra of samples S2, S4 and S6 on InAs(111) substrates at room temperature. Sample S1 is not shown since Sn is absent. The solid line is a fitting of the experimental data used to calculate the Bi/Sn ratio.

The samples grown on InAs(111) substrates (samples S1, S2, S4, and S6, Table I) are examined by in situ X-ray photoelectron spectroscopy (XPS) using Mg-K_a & Al-Ka radiations (1253.6 eV & 1486.6 eV respectively) from the SPECS XR50 source, with a take-off angle of 52° (Fig. 3.1). The binding energies of the $Bi4f_{7/2}$ and $Sn3d_{5/2}$ core levels for the three samples (S2, S4 and S6, Table I) are around 157.6 eV and 485.3 eV, respectively, suggesting the Bi-Te and Sn-Te bonds. With the help of the peak areas and the area sensitivity factors of 4.25 and 4.3 for the $Bi4f_{7/2}$ and $Sn3d_{5/2}$ peaks, respectively, the [Bi]/[Sn] ratios for each sample were calculated. The [Bi]/[Sn] ratios of S2, S4 and S6 is 3.27, 2.03, and 0.57, respectively.

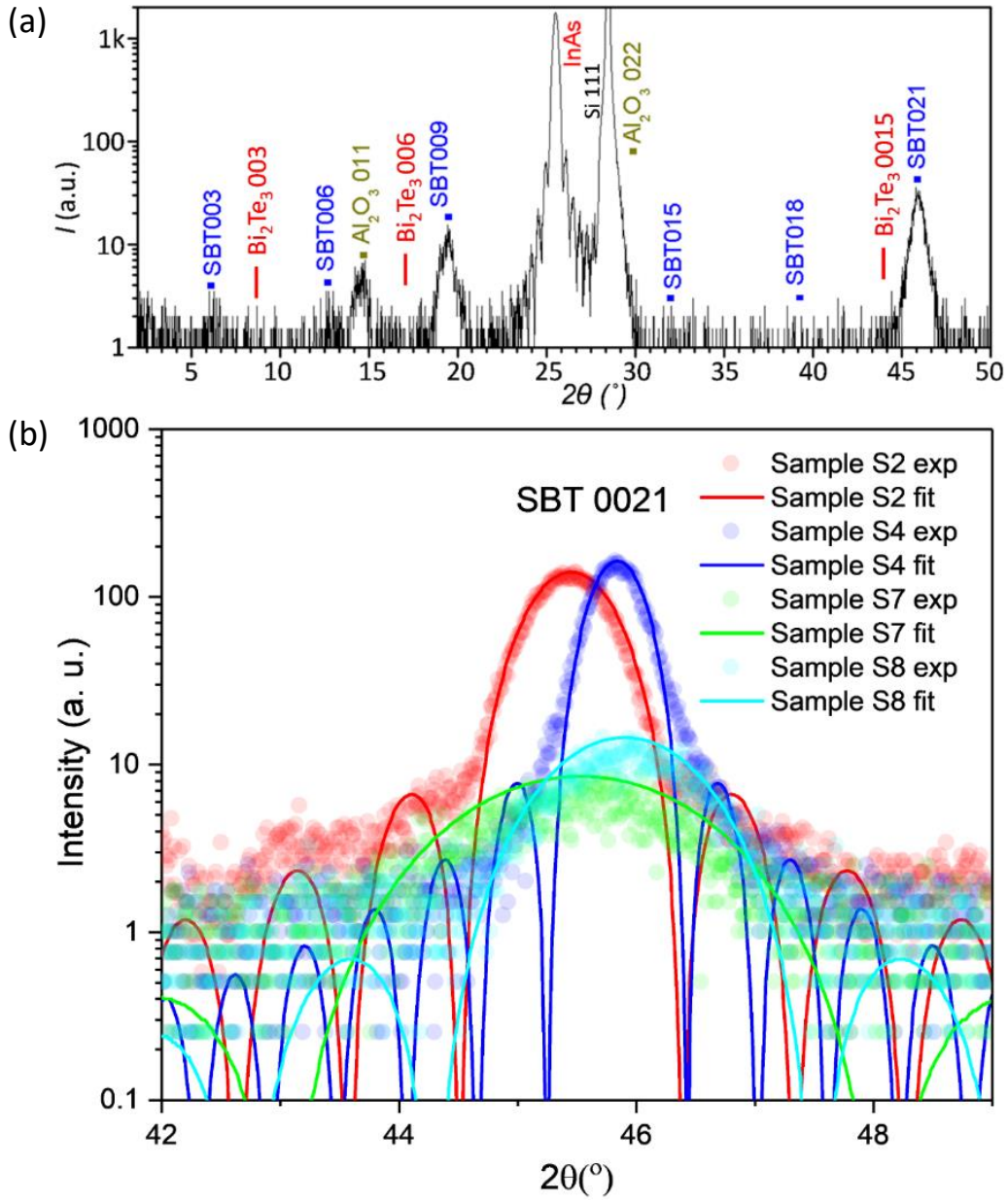

Figure 3.2. (a) XRD spectra of epitaxially grown $SnBi_2Te_4$ on InAs(111) substrate. (b) The (0021) diffraction peak of S2, S4, S7 and S8 samples.

X-ray diffraction was performed with a laboratory diffractometer (Bruker D8) with a Cu K_α source. Over the whole area of the epitaxial film, XRD measurements (Fig. 3.2a) support the septuplet structure of $SnBi_2Te_4$ formed on InAs(111) substrate. The diffraction spots' produced *d* spacings and the spacing of a $SnBi_2Te_4$ compound are in agreement. It is noteworthy that no contribution from quintuple layers similar to Bi_2Te_3 is present, indicating a pure phase of the 7-layer $SnBi_2Te_4$ structure. By analysing the diffraction peak (0021) of XRD spectra in Fig 3.2b for the S2, S4, S7 and S8 samples, their thicknesses are estimated to be 10.2 (±0.99), 16.2 (±0.99), 3.8 (±0.99) and 5.9 (±0.99) nm, respectively.

Table I. Samples grown by MBE for various thicknesses determined by HRTEM and XRD, and Their Bi/Sn ratios estimated by in-situ XPS.

Sample	Thickness *d* (nm)	Bi/Sn ratio
S1	~20 (HRTEM)	-
S2	10.2 (XRD)	3.27
S3	~22 (HRTEM)	3.21
S4	16.2 (XRD)	2.03
S5	~22 (HRTEM)	1.98
S6	~10 (HRTEM)	0.57
S7	3.8 (XRD)	3.05
S8	5.9 (XRD)	1.80

In this work, epitaxial InAs(111) on Si(111) substrates with significant technological implications are used. The InAs substrates provide an excellent template for chalcogenide epitaxial growth. Because they saturate dangling bonds without interacting with the substrate, the chalcogen atoms (Se, Te) are frequently utilized for the passivation of GaAs and related compounds, including InAs, prior to MBE growth.

Chalcogenides like $ZrTe_2$ and $MoTe_2$ [3.19, 3.20] are consequently 2D materials that create clean, sharp interfaces with outstanding epitaxial order.

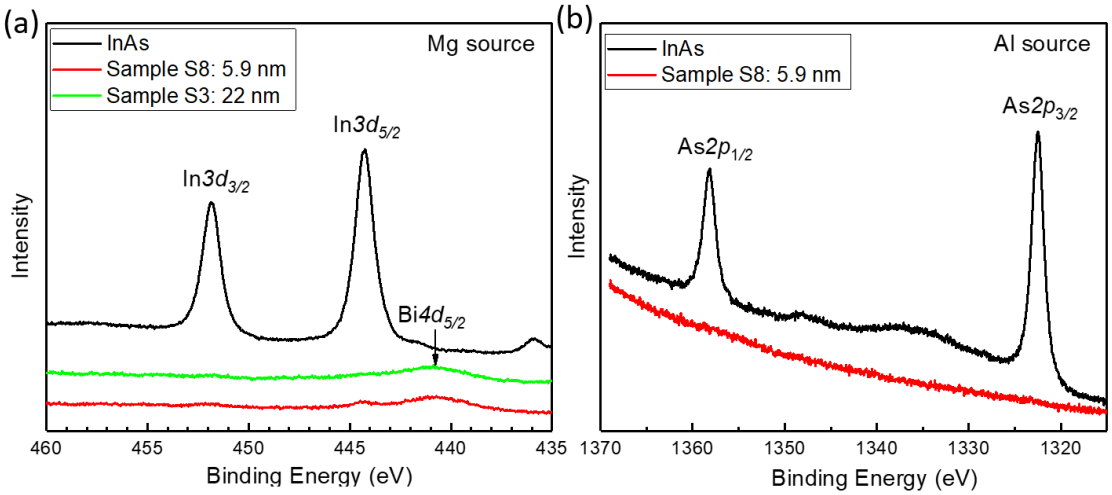

Figure 3.3. XPS spectra of: a) In_{3d} region of bare InAs(111) substrate and samples S8 and S3 on InAs(111). B) As_{2p} region of bare InAs(111) substrate and samples S8 on InAs(111).

This substrate is favorable for the epitaxial growth of Bi_2Te_3 and Sn-containing compounds due to the nearly lattice matching condition between the InAs and Bi_2Te_3. For the purpose of ensuring that neither In nor As are segregated from the substrate into the epitaxial films during the growth, In*3d* and As*2p* peaks for bare InAs(111) and samples S3 and S8 were thoroughly examined using XPS (Fig. 3.3). The InAs used in this experiment has a thickness of 35 nm. The In_{3d} and As_{2p} detailed XPS regions for the bare InAs(111) substrate, as well as for the epitaxial samples S3 and S8, are shown in Fig. 3.3. Neither In nor As are segregated from the substrate into the epitaxial films throughout the growth, as seen by the lack of peaks in samples S3 and S8.

The 2×2 reconstruction pattern of the reflection high-energy electron-diffraction (RHEED) in Fig. 3.4 shows that substrates are treated (see Methods section) to obtain a clean InAs(111) surface prior to development. Additionally, RHEED shows a good in-plane alignment along high symmetry crystallographic dimensions between the layers and the substrate. The excellent matching of the streak positions suggests that the lattice constants of all compounds are quite comparable. The latter have a propensity to enlarge as the Sn concentration rises. A nearly lattice matching condition between the layers and the substrate is also indicated by RHEED. The relative values of Bi_2Te_3, $SnBi_2Te_4$, $SnBi_4Te_7$, and $Sn_{0.64}Bi_{0.36}Te$ are predicted to be 4.343 Å, 4.392 Å, 4.403 Å, and 4.475 Å using the in-plane lattice constant a = 4.284 Å of InAs as a reference.

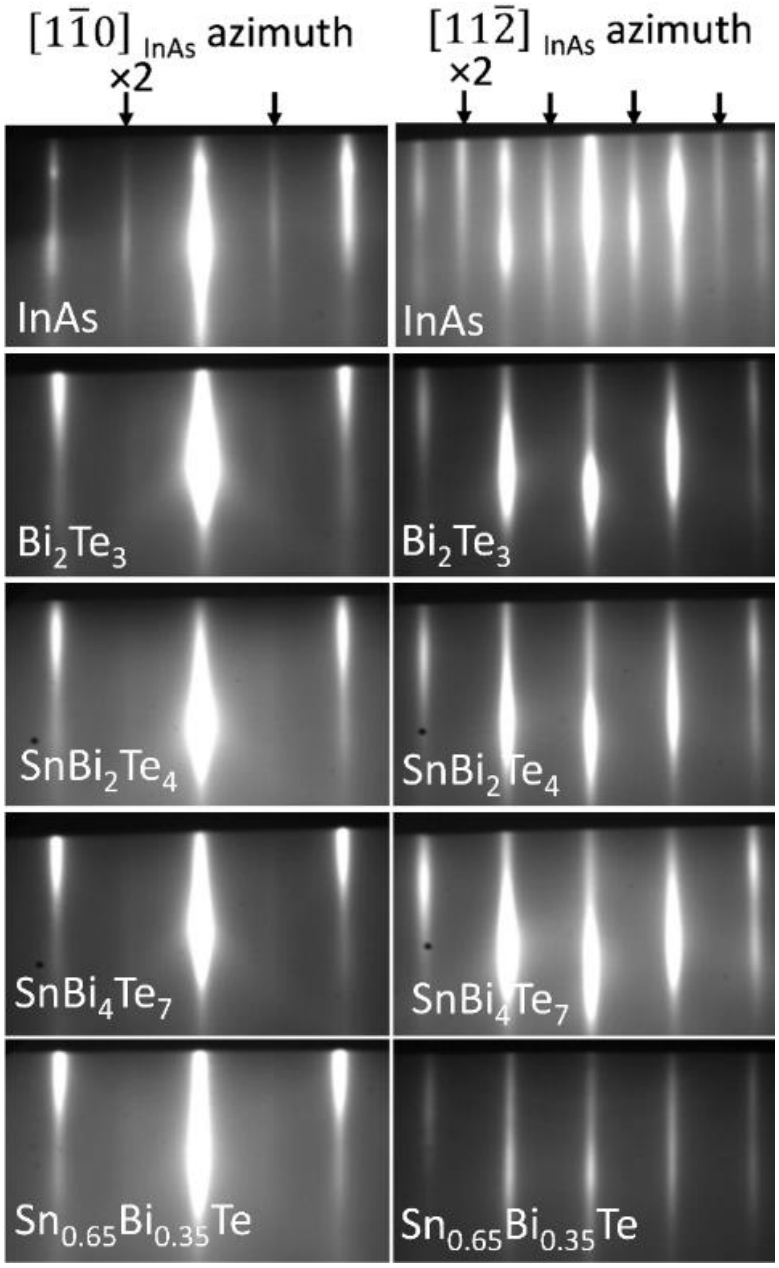

Figure 3.4. RHEED patterns of InAs(111) substrate and Sn-Bi-Te films along the InAs[1$\bar{1}$0] and [11$\bar{2}$] azimuths.

Cross-sectional high-resolution scanning transmission electron microscopy is used to study the microstructure. Figs. 3.5 and 3.6 provide the data for $SnBi_2Te_4$ and Bi_2Te_3, respectively, while $SnBi_4Te_7$ and $Sn_{0.64}Bi_{0.36}Te$ images are displayed in Figs. 3.7 and 3.8, respectively. STEM measurements have been performed utilizing 200 keV of Cs-corrected Themis (Thermo Fisher). Using a convergence semiangle of 20 mrad and collecting scattering greater than 55 mrad, HAADF-STEM pictures were obtained. The Cross-Beam 750 (ZEISS) was used to prepare STEM specimens using the FIB lift-out procedure at 30 kV, followed by cleaning at 5 kV. Other samples were measured using

an aberration-corrected FEI TITAN 200 Themis microscope that was running in the STEM mode at 200 keV, 70 pA, with a probe size of 0.09 nm at the full width at half maximum. The probe's half-angle for convergence was 17.6 mrad, while the HAADF-inner STEM's and outer half-angles for detection were 69 and 200 mrad, respectively. 2048 × 2048 pixels were used for all micrographs. The overall acquisition duration was 41 seconds, with an 8-second dwell period. The sample was processed using focused ion beam (FIB) ion milling and thinning to produce lamellae for STEM viewing. A carbon coating was applied to the sample surface before FIB ion milling in order to shield it from the platinum mask that would later be deposited during the procedure. A FEI SCIOS dual-beam FIB-SEM was used to perform ion milling and thinning. Final polishing was done at 5 keV after the initial etching was done at 30 keV. The silicon substrate's <110> zone axis was used to prepare the lamellae.

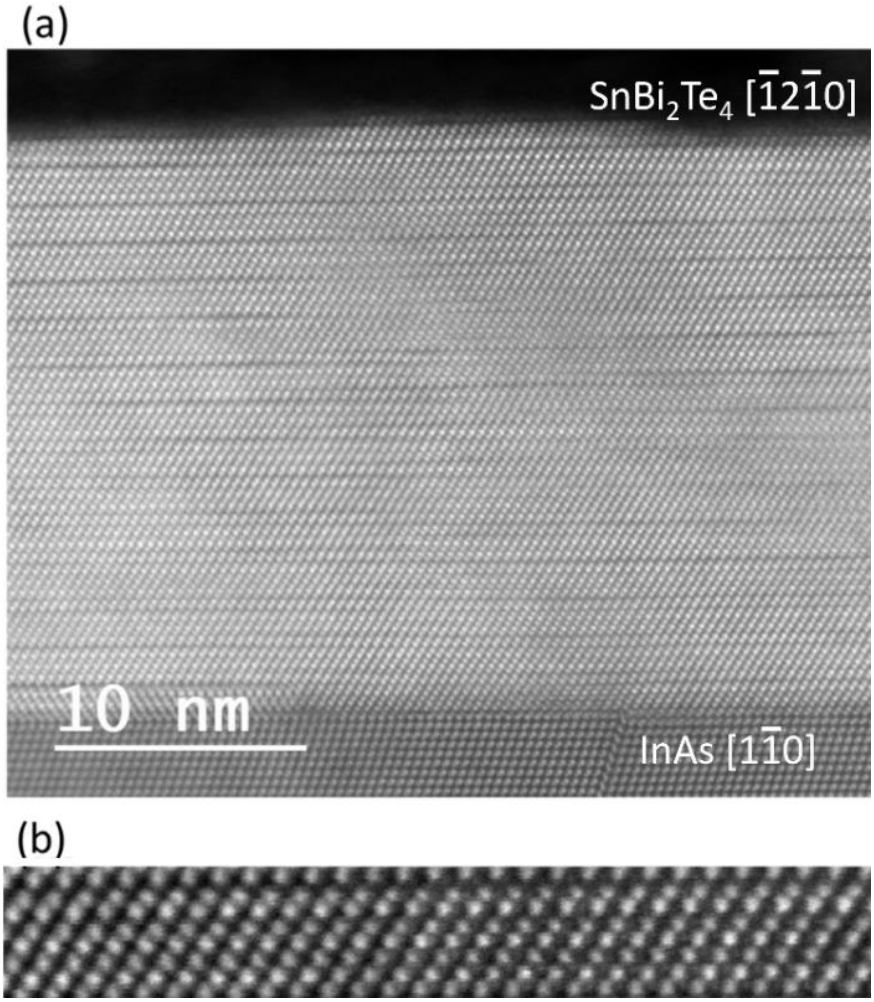

Figure 3.5. (a) High resolution cross-sectional STEM image of layered $SnBi_2Te_4$ (sample S5). (b) Detailed image of one SL showing a 7-row arrangement of the form Te-MII-Te-MI-Te-MII-Te. The MI and MII metal positions are mostly occupied by Sn and Bi, respectively.

The layered structure of $SnBi_2Te_4$ (Fig. 3.5a) exhibits a small van der Waals gap (Sample S5). Each layer in Fig. 3.5(b) is a septuplet with seven atom rows, four of which are occupied by Te atoms and the remaining by the metal atoms Bi and Sn.

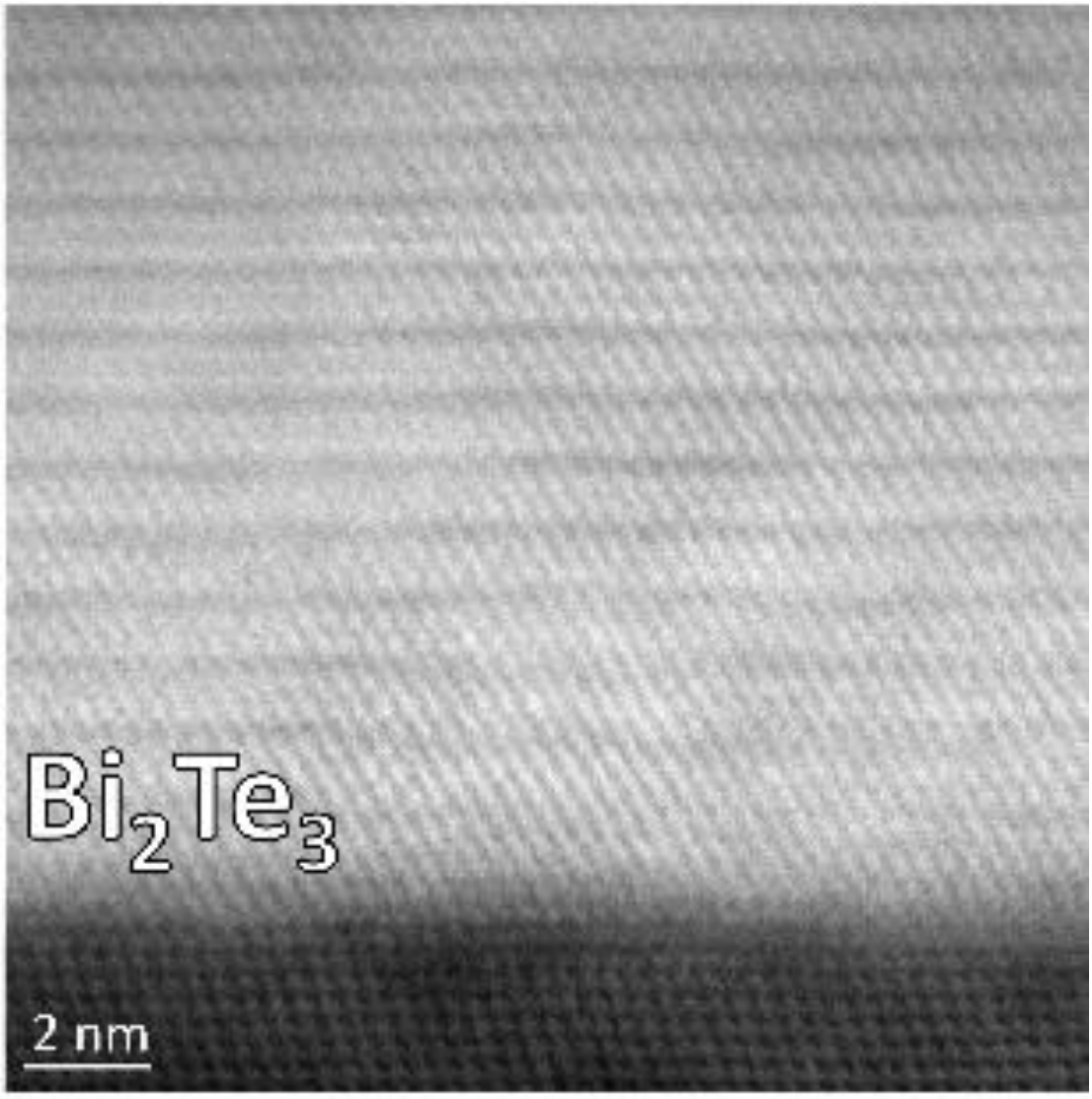

Figure 3.6. STEM image of Bi_2Te_3 on InAs(111) substrate, indicating a quintuplet vdW structure.

The septuplet structure (Fig. 3.5b) differs significantly from the parent Bi_2Te_3 quintuple structure (Fig. 3.6). STEM was used to observe sample S1's crystal structure. In contrast to the septuplet structure of the $SnBi_2Te_4$ exhibited in Fig. 3.5, the STEM picture of Fig. 3.6 depicts a layered structure made up of quintuplets of the type Te-Bi-Te-Bi-Te (Bi_2Te_3), separated by vdW gaps.

Additionally, X-ray diffraction (Fig. 3.2) confirms the septuplet structure by revealing a pure phase of the 7-layer structure over the whole film region with no contributions

from other phases (e.g., quintuple Bi_2Te_3-like phase). A tendency to produce an ordered alloy, with Sn preferably occupying the middle row, is shown by the septuplet arrangement. It should be noted that, as shown in Fig. 3.6, the substrate surface roughness affects the film microstructure. As a result, the quintuplets appear to be slightly out of parallel with one another.

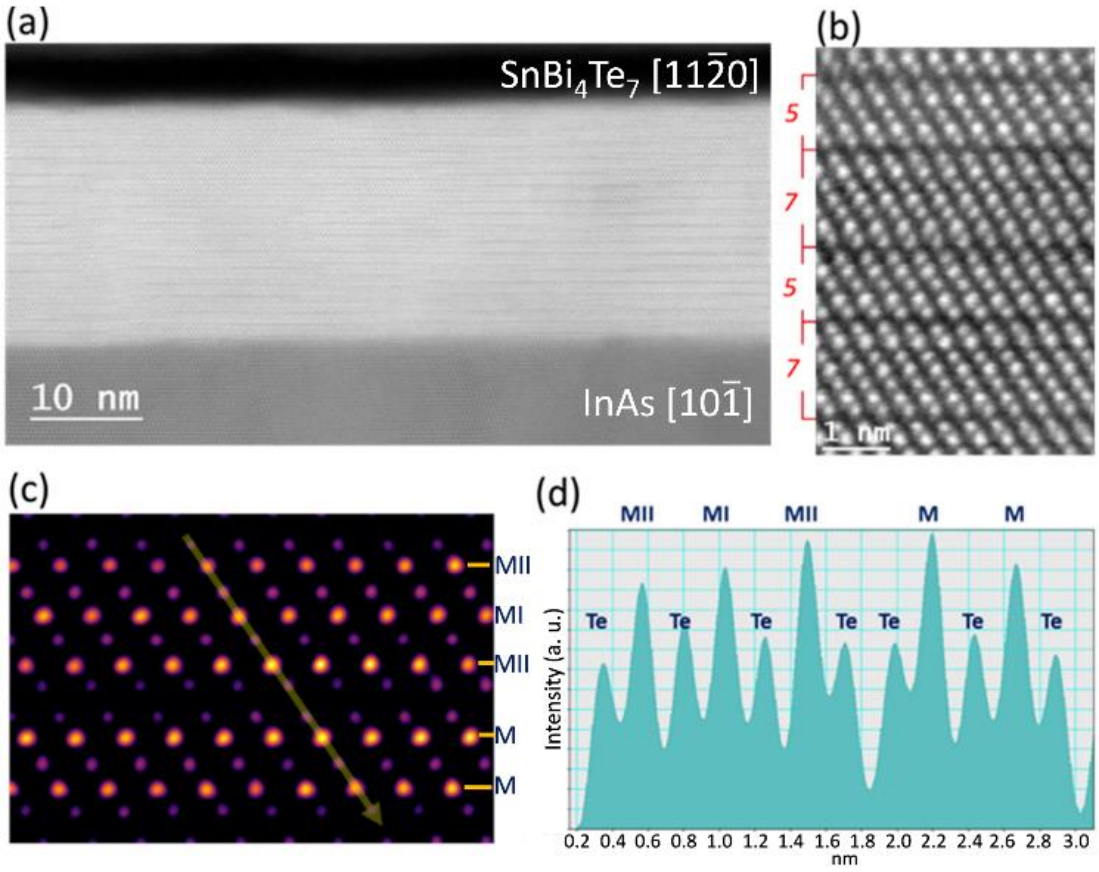

Figure 3.7. (a) High resolution cross-sectional image of $SnBi_4Te_7$ (Sample S3). (b) HR-STEM shows alternating QL and SL layers forming a natural vdW superlattice, with a vdW gap separating each layer. (c) HAADF image and (d) the intensity line profile along a yellow line in (c) showing the possibility of exchange between Sn and Bi atoms in the middle row of the SL.

However, as will be detailed below with reference to Fig. 3.7, which shows the Bi-rich $SnBi_4Te_7$, deviation from this ideal arrangement occurs. $SnBi_4Te_7$ adopts a natural van der Waals superlattice structure to accommodate the excess Bi, where septuplets (SL) of $SnBi_2Te_4$ alternate with quintuples (QL) of Bi_2Te_3 (Fig. 3.7a,b) (Sample S3). Although it is not maintained across the entire film thickness, the sequence occurs quite frequently. For instance, the first three layers of the film seen in Fig. 3.7 have an SL/SL/SL stacking, which is followed by a QL/SL/SL configuration. The bottom part of the film, close to the interface, then exhibits a tendency to produce an almost perfect

alternating SL/QL structure. The $SnBi_2Te_4$ septuplet layer deviates from the model structure, according to which Sn occupies ideally the middle row, denoted MI, and Bi occupies the rows MII (Fig. 3.7d), as shown by an examination of the intensity of the high-angle annular dark field image (Fig. 3.7c). The centre row's intensity in the model layout should be low, even lower than the Te rows' intensity. The metal locations MI and MII are occupied by both Sn and Bi atoms, indicating that there is a large exchange between Bi and Sn, as seen by the high intensity of the middle row (Fig. 3.7b). It should be emphasized that the bulk-grown $SnBi_2Te_4$ nanoplates also experience an exchange of Sn and Bi [3.13].

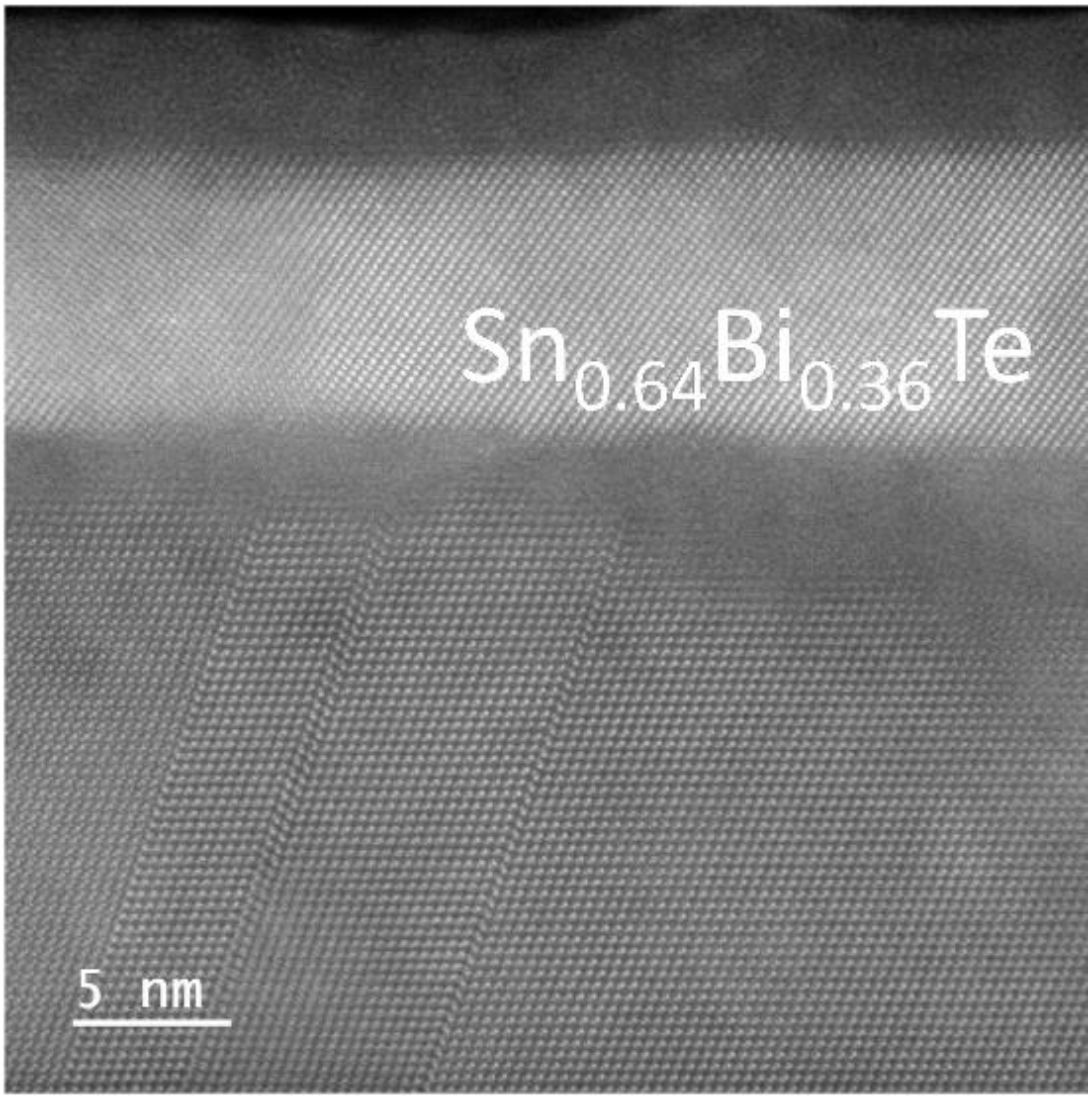

Figure 3.8. STEM image of the $Sn_{0.64}Bi_{0.36}Te$ alloy, adopting a three-dimensional cubic crystal structure on InAs(111) substrate.

The Sn-rich alloy acquires a three-dimensional cubic structure (Fig. 3.8) rather than a layered one, remarkably similar to the parent SnTe compound, when Sn content rises

above the $SnBi_2Te_4$ composition (Sample S6, Table I) [3.21-3.23]. While likewise produced on InAs(111) substrates, the $Sn_{0.64}Bi_{0.36}Te$ alloy (sample S6, Table I) adopts a three-dimensional cubic crystal structure (Fig. 3.8) rather of a layered one, which is remarkably similar to the parent SnTe compound. The thickness is estimated to be around 10 nm. The amorphization caused during focused ion beam (FIB) specimen preparation is what is responsible for the amorphous layer at the interface between the $Sn_{0.64}Bi_{0.36}Te$ and InAs.

3.2.2. First-principles calculations

Since the parent Bi_2Te_3 and SnTe TIs are well-researched materials [3.21–3.24], ab-initio calculations are focused on $SnBi_4Te_7$ and $SnBi_2Te_4$. The DFT calculations were performed using the Vienna Ab initio Simulation Package (VASP) [3.25, 3.26] and projector augmented waves [3.27]. The generalized gradient approximation with Perdew-Burke-Ernzerhof [3.28] parameterization was used as exchange correlation functional. The kinetic cut-off energy was set at 500 eV, employing a $9 \times 9 \times 9$ *k*-mesh using the Monkhorst-Pack scheme [3.29]. The ionic positions were fully optimized by applying conjugate gradient, using a force threshold of 10^{-3} eV·Å^{-1}. The MLWFs are fitted based on *s* and *p* orbitals of Sn, Bi and Te atoms using the *Wannier90* code [3.30] and the $\mathbb{Z}_2$ and the projected BZ calculations were carried out by the *WannierTools* software [3.31]. Spin-orbit coupling was included in band structure calculations.

By calculating the $\mathbb{Z}_2$ topological invariants in the $k_z = 0$ and $k_z = \pi$ planes (see Methods section), it is possible to determine the topological nature of $SnBi_4Te_7$ and $SnBi_2Te_4$ materials. $\mathbb{Z}_2$ is equal to one for the $k_z = 0$ plane and zero for the $k_z = \pi$ plane. As a result, there is a band order inversion, which causes a non-trivial band gap and the emergence of surface states. Employing corresponding software available from the Bilbao Crystallographic server [3.32, 3.33] to calculate the irreducible representations, where the materials are categorized as strong TIs, meaning that the TSS, for both materials, are protected by time-reversal symmetry, further confirms the band inversion between $\bar{\mathbf{\Gamma}}_9$ and $\bar{\mathbf{\Gamma}}_8$. No band-inversion is predicted in the M and L time-reversal invariant momentum points.

A global band gap of ~0.1 eV can be seen in the electronic band structure (Fig. 3.9a) of $SnBi_4Te_7$ (trigonal space group $P\bar{3}m1$) determined by DFT along the KΓL and HAL directions of the Brillouin zone (BZ) (Fig. 3.9b). Depending on whether the surface is

SL or QL terminated, two alternative TSS are revealed by the projected BZ calculation (Fig. 3.9c). The majority of the material is centrosymmetric, but thin films with an even number of layers (SL/QL, SL/QL/SL/QL, etc.) lack inversion symmetry, and their bands around the Fermi level are split, representing the two distinct TSS at the top and bottom surfaces (Fig. 3.9d). This holds the potential to be intriguing because it leads to (near) energy degeneracies at the Fermi level, which may significantly affect the spin Hall conductivity of this substance. It should be noted that the film-substrate interaction already separates the Dirac cones of the top and bottom surfaces for any actual system due to the violation of inversion symmetry.

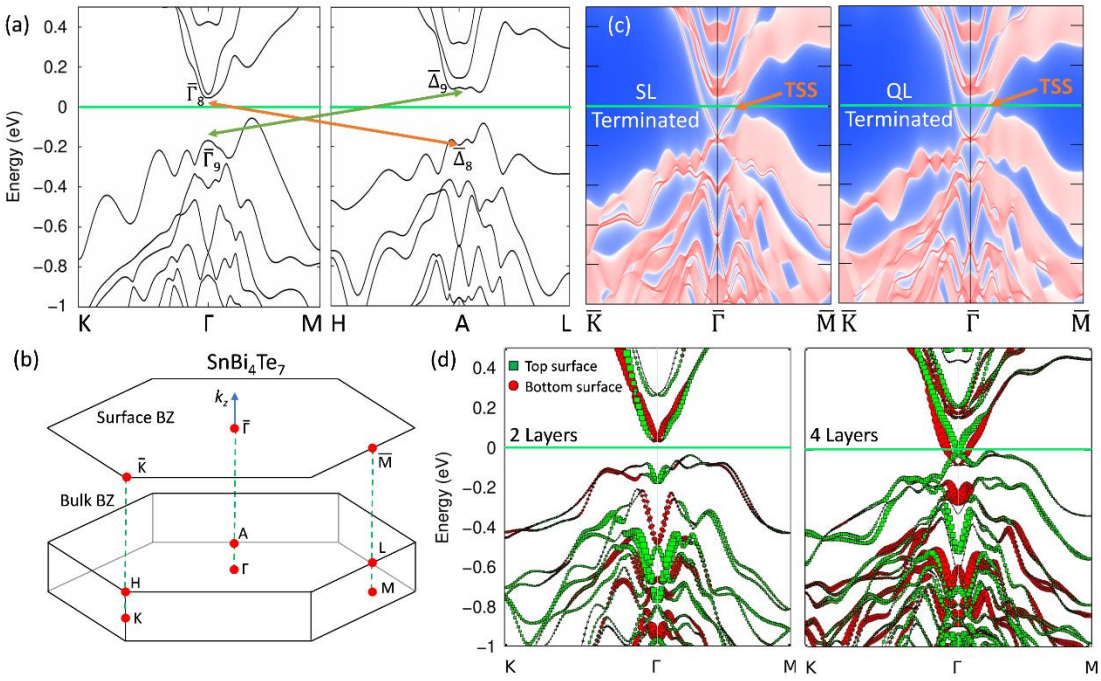

Figure 3.9. (a) The calculated electronic band structure by DFT of bulk $SnBi_4Te_7$ along the KΓL, HAL high-symmetry directions indicating the band inversion (orange and green lines). (b) The first Brillouin zone, (c) the projected Brillouin zone along the $\bar{K}\bar{\Gamma}\bar{M}$ direction of the two different (SL or QL) terminations and (d) the band structures of the 2 and 4 layers with broken-inversion symmetry. The red and green filed-symbols correspond to the atomic orbitals of the bottom and top surfaces, respectively.

$SnBi_2Te_4$ crystallizes in a rhombohedral structure with space group $R\bar{3}m$, just like its parent compound Bi_2Te_3. A band gap of 0.1–0.2 eV is observed in the predicted band structures of bulk $SnBi_2Te_4$ along the KΓL and KZX directions of the BZ (Fig. 3.10a) are shown in Fig. 3.10b. A tiny overlap between the valence and conduction bands can be observed by calculating the BZ's projection along the $\bar{K}\bar{\Gamma}\bar{M}$ direction (Fig. 3.10c), but it diminishes with thinner thicknesses, as shown in Fig. 3.10d.

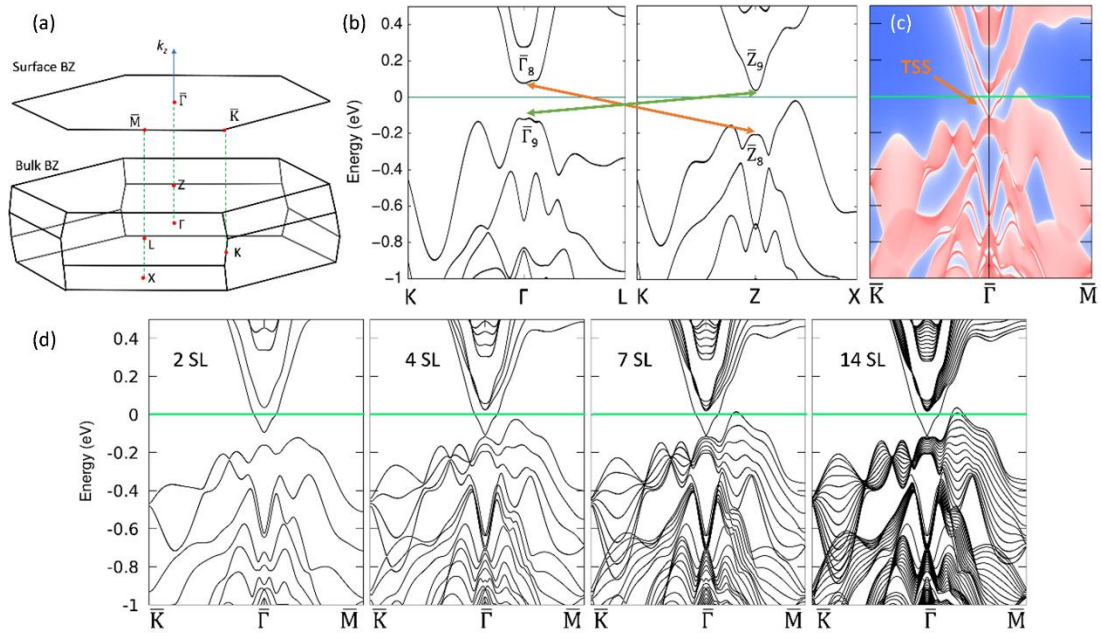

Figure 3.10. (a) The Brillouin zone of $SnBi_2Te_4$. (b) The theoretically calculated band structure of bulk $SnBi_2Te_4$ along the KΓL, KZX and showing the band inversion (green and orange lines), (c) the Brillouin zone projection along the $\bar{K}\bar{\Gamma}\bar{M}$ direction and (d) the band structures of 2, 4, 7 and 14 SL.

3.2.3. Topological surface states imaging by ARPES

A systematic investigation of the band structure as a function of Sn composition is performed, at 15 K using synchrotron ARPES with variable photon energy and at room temperature using *in-situ* ARPES with He I excitation at 21.22 eV. After the Te capping was removed from specially prepared samples, measurements were made at the SOLEIL-Synchrotron facility "CASSIOPEE" using horizontally polarized light and varying photon energies between 19 and 80 eV to track the electronic band dispersion along the k_z axis. The measurements were made at a temperature of 15 K with a polar angle step of 0.2° and an energy resolution of 15 meV. Typically, the k_z scan periodicity is used to calculate the inner potential's V_0 value. There is no evident periodicity in the scan in this case because we are working with a surface state. Therefore, we employed a different methodology [3.34] to estimate V_0 from $V_0=|E_0|+\Phi$ where E_0 corresponds to the energy of the bottom of the valence band referenced to Fermi level and Φ, the material work function. By combining our ARPES and our DFT calculations we estimate E_0 = 3.5 eV at $k_{||}$ = 0 Å^{-1} and from UPS we estimate Φ = 5 eV, so V_0 = 8.5 eV. Then, k_z as a function of photon energy $h\nu$ for perpendicular emission (i.e., $k_{||}$ = 0 Å^{-1}),

is obtained as in Ref. [3.34] from $k_z = \sqrt{\frac{2m}{\hbar^2}(E_k + V_0)}$, where m is the effective mass of electrons inside the solid and E_k is the kinetic energy of the emitted electrons, which satisfies $E_k = h\nu - \Phi - E_B$, where E_B is the electron binding energy.

A 100 mm hemispherical electron analyser with a 2D CCD detector (SPECS) was used to do the in-situ ARPES measurements at ambient temperature without compromising the vacuum. Photoelectrons are excited using the resonance line of the He I atom (21.22 eV). With a polar angle step of 1°, the system's energy resolution is better than 40 meV.

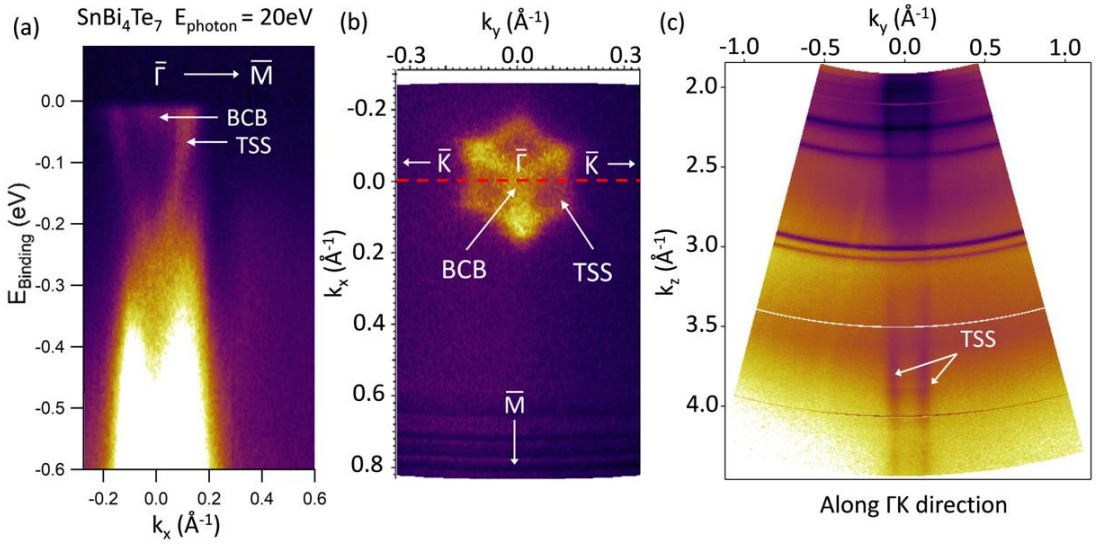

Figure 3.11. (a) ARPES spectra of $SnBi_4Te_7$ for E_{photon} =20 eV along $\bar{\Gamma}\bar{M}$ direction and (b) the Fermi surface. (c) The photon k_z-k_y energy dependent Fermi surface map at the Fermi level (k_y parallel to $\bar{\Gamma}\bar{K}$). The traces of the TSS are recorded at the k_y values at which the red dashed line in (b) intersects the surface state. BCB denote the bulk conduction band states.

Two distinct states are typically seen coexisting at the Fermi surface close to the BZ's center (Fig. 3.11a). The BCB is considered to be responsible for one of these triangular-shaped states since it possesses the trigonal symmetry of the bulk material (Fig. 3.11b). The hexagonal symmetry of the BCB, which is attributable to a surface band, clearly distinguishes it from the other state. The latter band's surface nature is further supported by ARPES since it isn't affected by the photon excitation energy. This is shown in Fig. 3.6c, where the k_z-k_y (parallel to ΓZ and ΓK plane) Fermi surface map at E_F is produced by scanning with photon energy from 19 to 80 eV for an inner potential V_0 = 8.5 eV with horizontal polarization (see details in Methods section) and recording the photoelectron intensity for all k_y momenta along ΓK. The hexagonal feature is a surface

state, as evidenced by the map's appearance of two almost parallel lines that are independent of photon energy.

The resonances of the Bi*5d*, Sn*4d*, and Te*4d* core levels are responsible for the horizontal intensities found around k_z ~2.5 $Å^{-1}$ and k_z ~3.0 $Å^{-1}$, respectively. Additionally, no bulk band dispersion is shown in the k_z-k_y Fermi surface map because, as seen in the contour plot in Fig. 3.11b, the contribution of bulk states is much more evident at the hexagonal feature's corners along the direction than it is at the BZ center and along the ΓK direction. It can be seen that the hexagonally formed surface band inside the bulk band gap is actually a topological surface state by direct comparison with the DFT computations (Figs. 3.9c and 3.10c). According to the DFT predictions, the Fermi level does not cross the valence band in the case of $SnBi_4Te_7$. However, for all sample thicknesses examined from 11 SL down to 2 SL, ARPES does not support the DFT prediction that the valence band maxima (Fig. 3.10c) disperse above the Fermi level in the case of $SnBi_2Te_4$. It is believed that the well-known underestimate of the band gap in the LDA and GGA-PBE functionals is the cause of the difference between theory and experiment [3.35].

It should be noted that since the surface of the material is not completely flat, it is impossible to determine the top surface of $SnBi_4Te_7$ with ARPES. On the sample, some regions are terminated with Bi_2Te_3, while other nearby regions are terminated with $SnBi_2Te_4$. Even in the ideal scenario of a flat surface, it would have been challenging to directly compare with DFT since the ARPES resolution is insufficient to distinguish between the two terminations and the differences between the two terminations predicted by theory (Fig. 3.9d) is extremely small.

The Fermi surface plots at various photon energies (Fig. 3.12) show the bulk states dispersion more clearly since the bulk conduction bands change in size and intensity as a function of photon energy. The Fermi surface plots for thin $SnBi_4Te_7$ and thick and thin $SnBi_2Te_4$ films (samples S7, S4, and S8, respectively) at various photon energies show the dispersion of the bulk states, and Fig. 3.12 shows how the trigonal-shaped BCBs located near the Γ point change in shape and intensity as the photon energy changes. The hexagonal TSS, on the other hand, shows no notable alteration, pointing to its two-dimensional character.

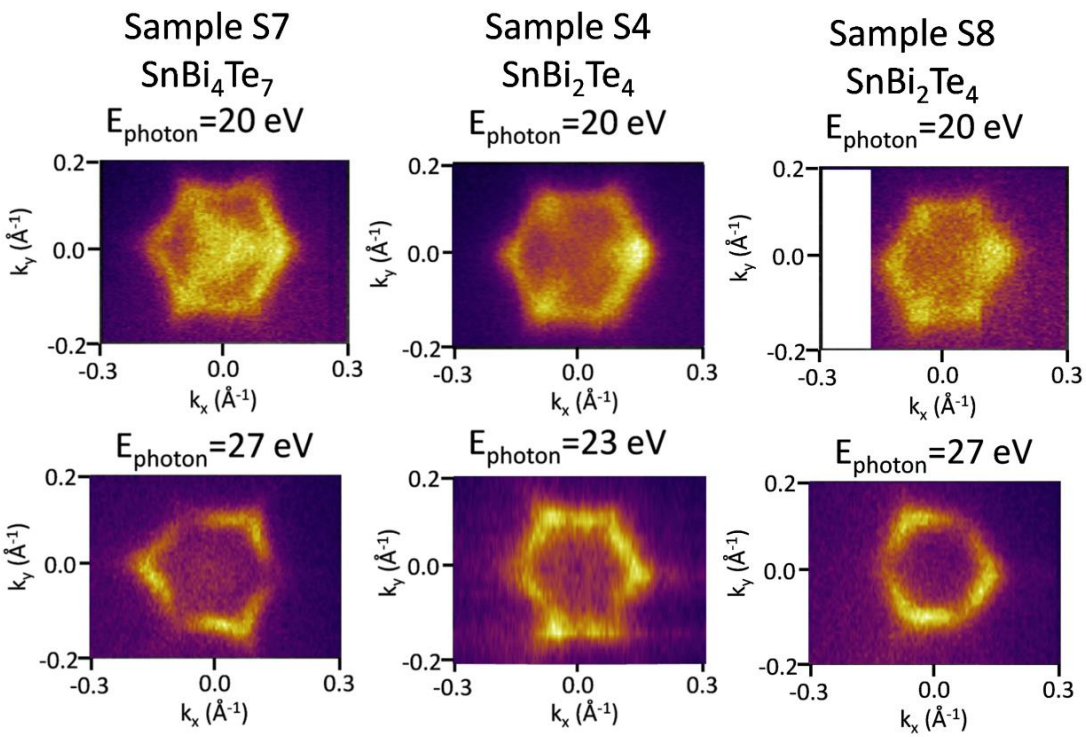

Figure 3.12. The Fermi surfaces of samples S7, S4 and S8 at different photon energies.

According to Fig. 3.13, the form and intensity of TSS and BCB energy dispersions are not dependent on thickness but rather appear to be related to the Sn concentration in Bi-rich compounds. The thin $SnBi_4Te_7$ and $SnBi_2Te_4$ samples' ARPES spectra in Fig. 3.13 are compared with the corresponding thick samples shown in Figs. 3.14b,c. Similar TSS and BCB characteristics exist in the thin $SnBi_4Te_7$ in Fig. 3.13a and the thick $SnBi_4Te_7$ in Fig. 3.14b. In more detail, the TSS and BCB intensities at the Fermi surface are almost the same in the two samples, and the energy positions of the DP and the BCB minimum are approximately at the same energy relative to the Fermi level. The thin $SnBi_2Te_4$ (Fig. 3.13b) and thick $SnBi_2Te_4$ (Fig. 3.13c) exhibit comparable TSS dispersion patterns, but the BCB at the Fermi surface is hardly perceptible in either sample. In short, there is little or no dependence of the electronic band structure on the film thickness.

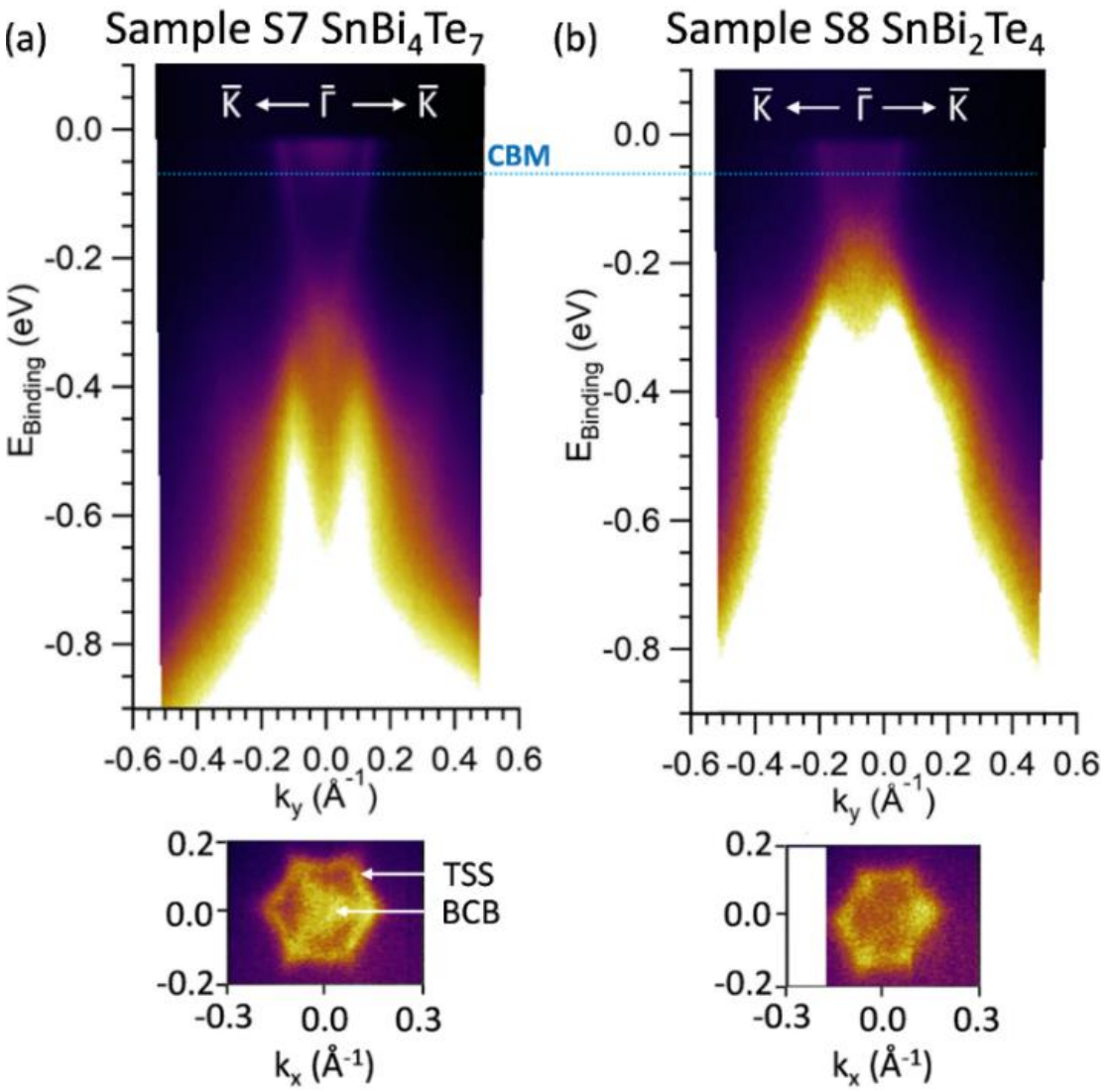

Figure 3.13. ARPES spectra of thinner (a) $SnBi_4Te_7$ and (b) $SnBi_2Te_4$ samples (S7 and S8, respectively) and their Fermi surface plots. The conduction band minimum is indicated with horizontal blue dotted line.

More particularly, in $SnBi_2Te_4$ compared to $SnBi_4Te_7$ and Bi_2Te_3, the BCB is less obvious, or more precisely, less severe (Fig. 3.14). As Sn composition rises, the conduction band minimum (CBM) changes to a higher energy, narrowly passing the Fermi level for the $SnBi_2Te_4$ compound which has the highest Sn concentration. The same pattern can be seen in the Fermi surface plots of Fig. 3.14, where the intensity of the trigonal-shaped BCB drops as Sn concentration rises and hardly appears in the $SnBi_2Te_4$ compound, where the TSS predominates at the Fermi surface.

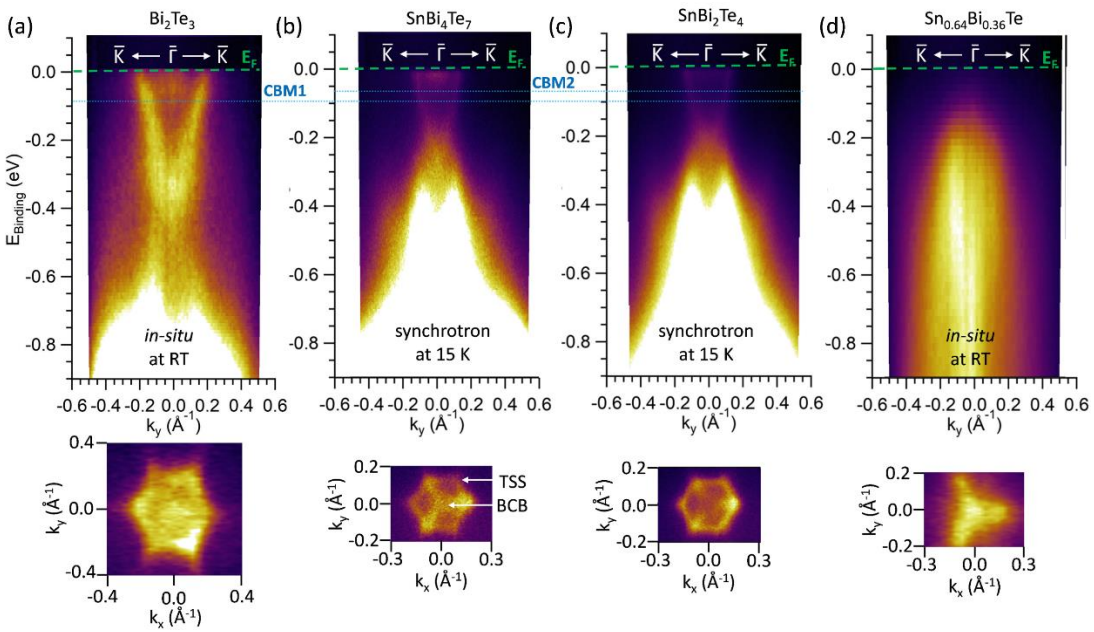

Figure 3.14. (a-d) Band dispersions measurements by ARPES and their k_x-k_y Fermi surfaces for the four samples with varying Sn concentrations recorded along $\bar{K}\bar{\Gamma}\bar{K}$. The shifting of the conduction band minimum (CBM) is indicated with blue horizontal dotted lines. BCB and TSS in (b) indicate the bulk conduction band and topological surface states, respectively.

The 2D electron density of the TSS is calculated from ARPES measurements at the Fermi surface using Luttinger's theory [3.36-3.38] as follows: $n_{2D} = A_F/(4\pi^2)$, where A_F is the area in momentum space of the closed orbit at the Fermi level that can be approximately represented by a hexagon (Fig. 3.11 and 3.14). The electron densities are found to be n_{2D}=1.37 (±0.2)×10^{13} cm^{-2} for $SnBi_2Te_4$ and n_{2D}=1.40 (±0.25)×10^{13} cm^{-2} for $SnBi_4Te_7$. These values were obtained by taking into account the non-degenerate spin polarized TSS band at the top surface.

The hexagonal symmetry of the TSS in the $Sn_{0.64}Bi_{0.36}Te$ alloy vanishes as Sn is progressively increased, and as would be expected given that the sample forms a cubic 3D SnTe-like structure with a valence band maximum at Γ [3.24], the trigonally structured valence band states dominate the ARPES spectral weight. In summary, $SnBi_2Te_4$ exhibits a strong TSS at the Fermi energy with the least interference from BCB states. In order to correlate the observed TSS with transport properties, it is important to examine the magnetotransport properties of the $SnBi_2Te_4$ compound, which exhibits the largest influence from TSS (see next section). Imaging the energy and momentum distribution curves for samples S1, S2, S4, and S6 at the Fermi level and around the point, respectively, further supports this claim (Fig. 3.15).

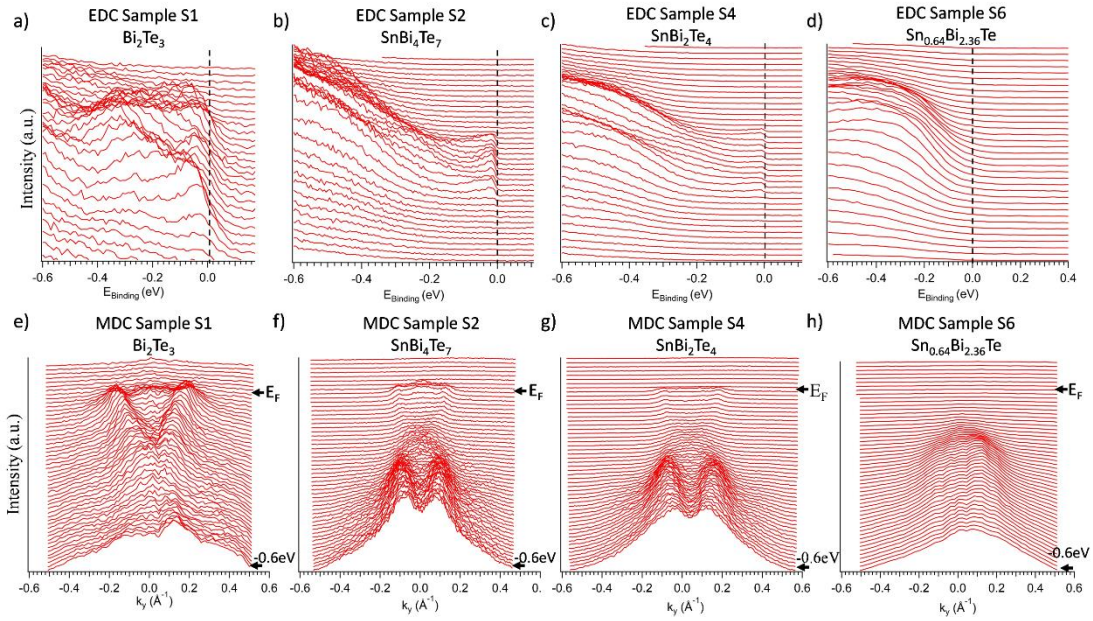

Figure 3.15. (a-d) Energy and (e-h) momentum distribution curves for samples S1, S2, S4 and S6.

In contrast to the other compounds, $SnBi_2Te_4$ exhibits a pronounced TSS at the Fermi energy with the least interference from BCB states, as can be seen from the image in Fig. 3.14 in the main text. This assertion is further supported by Fig. 3.15 depiction of the energy (EDCs) and momentum distribution curves (MDCs) for samples S1, S2, S4, and S6 at the Fermi level and, respectively, around the Γ point.

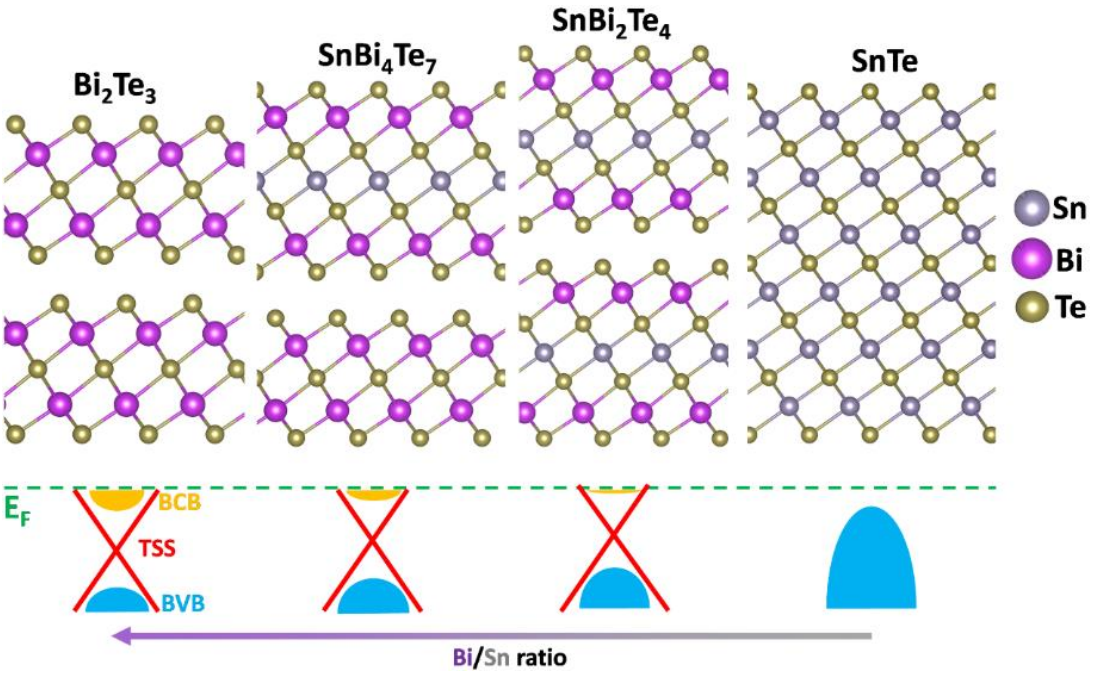

Figure 3.16. Schematic indicating the evolution of crystal and band structure as a function of Bi/Sn ratio.

Fig. 3.16 illustrates how crystal and band structure changed as a function of composition (Bi/Sn ratio). This sums up our research, which shows that by adjusting the Bi/Sn ratio, we can switch between end compounds by growing in a natural van der Waals superlattice where one $SnBi_2Te_4$ septuplet and one Bi_2Te_3 quintuple alternate. We can also adjust where the Fermi level is in relation to the TSS and the BCB.

3.2.4. Topological surface states contribution in magnetotransport

Following the ARPES experiment, MBE in-situ deposited 3 nm of Al to protect the sample. The Al then underwent a natural oxidation in air. After that, the sample was patterned in Hall bar to conduct the magnetoresistance measurement. Hall bars measuring 50 wide by 150 long are used to print samples, providing fine control over the homogeneity and direction of the current. The transverse and longitudinal resistance were measured simultaneously using nanovoltmeters and a dc current source. A superconducting coil generates the magnetic field, and the sample is put on a goniometer to change the field's direction in relation to the current one. To provide appropriate electrical contacts, lift-off of Ti(20nm)/Au(150nm) Au deposited via evaporation was used to prepare the contacts.

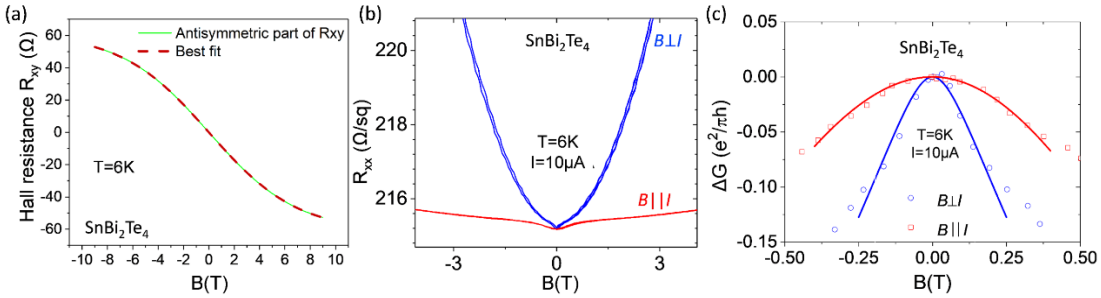

Figure 3.17. Magnetotransport measurements of $SnBi_2Te_4$ obtained at 6 K. (a) Hall resistance (R_{xy}) showing characteristic non-linear bent shape due to multi-band conduction. (b) Longitudinal resistance (R_{xx}) as a function of the out-of-plane and in-plane applied magnetic fields revealing the WAL effect. (c) Magnetoconductance ΔG normalized by $e^2/(\pi h)$ as a function of the applied magnetic field.

Fig. 3.17 shows $SnBi_2Te_4$ magnetoresistance experiments at a low temperature (6 K). Since the antisymmetric portion of the Hall resistance in Fig. 3.17a is nonlinear, at least two different types of carriers must be involved. According to the fitting, the two types of carriers are both electrons, with one having a large density attributed to the BCB n_{BCB} = -4.69 (±0.1)×10^{14} cm^{-2} and low mobility μ_{BCB} = 43.2 (±2) $cm^2\ V^{-1}{\cdot}s^{-1}$, while the other with a lower density n_{TSS} = -6.9 (±0.03)×10^{12} cm^{-2} and higher mobility μ_{TSS} = 1260 (±2) $cm^2{\cdot}V^{-1}{\cdot}s^{-1}$. With the TSS density n_{2D} = 1.37×10^{13} cm^{-2} obtained from

ARPES, the latter density, n_{TSS}, matches within a factor of 2 (see previous section). This mismatch can be attributed to band bending since the surface changed from transport measurement (Al capping) to ARPES [3.39].

We made the assumption that TSS had in-plane helical spin-orbit coupling while neglecting potential out-of-plane spin components in order to determine the carrier density from Hall resistance. As a result, the 2D TSS is responsible for the low electron density's Hall resistance. The greater electron density is thought to be a result of BCB, which can also be seen in the Fermi level ARPES data. Since there are only two unique carrier contributions in the Hall data that are attributable to TSS and BCB, it is likely that the unoxidized Al cap has no impact on magnetotransport; otherwise, a third type of carriers would have been seen, which was not the case in this case.

The magnetoresistance of $SnBi_2Te_4$ for an out-of-plane magnetic field (BI, blue curve) and an in-plane magnetic field ($B \| I$, red curve) is depicted in Fig. 3.17b. Both orientations exhibit a magnetoresistance dip at low magnetic fields ($|B|$ 0.25 T), which is a result of the large SOC in topological insulators (Fig. 3.17b) and the weak antilocalization (WAL) effect [3.40]. The formation of a comparable magnetoresistance dip in parallel magnetic field, however, suggests that a WAL effect emanating from the bulk $SnBi_2Te_4$ contributes to the conductance in addition to TSS, even if the appearance of a dip in $B \perp I$ is connected with a 2D TSS [3.40–3.42].

In Fig. 3.17c, the magnetoconductance ΔG is depicted as a function of the magnetic field and is, approximately obtained from the measured magnetoresistance by using the formula [3.43]:

$$\Delta G = \frac{1}{R(\theta, B)} - \frac{1}{R(\theta, 0)} \tag{3.1}$$

The experimental curves are fitted using Eqs. 3.2 and 3.3 for the out-of-plane and in-plane B fields, respectively:

$$\Delta G_{\perp}(B) \approx \alpha_{\perp} \frac{-e^2}{\pi h} \left[\psi\left(\frac{1}{2} + \frac{B_{\Phi}}{B}\right) - \ln\left(\frac{B_{\Phi}}{B}\right) \right] \tag{3.2}$$

$$\Delta G_{||}(B) \approx \alpha_{||} \frac{-e^2}{\pi h} \ln\left(1 + \beta \frac{ed^2}{4\hbar B_{\Phi}} B^2\right) \tag{3.3}$$

where $B_{\Phi} = \hbar/(4el_{\Phi}^2)$, ψ is the digamma function and l_{Φ} is the phase coherence length. We determine $\alpha_{\perp}$ and l_{Φ} by fitting the magnetoconductance to the Hikami-Larkin-Nagaoka (HLN) formula (Eq. 3.2) [3.44, 3.45] for the perpendicular applied magnetic field, and we then determine $\alpha_{||}$ and β ($0<\beta<1$) by fitting the magnetoconductance to

Eq. 3.3 [3.45–3.47] for the parallel magnetic field, with l_Φ ~ 52 nm coming from Eq. 3.2. This is simply an approximation since film anisotropy typically predicts that l_Φ for in-plane longitudinal transport will differ from l_Φ for transverse transport over the film thickness. Prefactors $\alpha_\perp$ and $\alpha_\parallel$ have values of -0.42 and -0.39, respectively, according to Eqs. 3.2 and 3.3. The data provided for $SnBi_2Te_4$ nanoplates produced in bulk and our findings are in good agreement [3.13].

More particularly, the MR dip is likewise evident in both *B* field orientations in Ref. [3.12], and the fitting results in α = -0.4, and l_Φ = 108.4 nm. Given that the two surfaces are connected via the bulk in the current study, the perpendicular and in-plane field measurements produce identical values of α that are extremely near to -0.5, demonstrating that the system operates as a single transport channel system. Eq. 3.3 yields a value for β = 0.24, a parameter linked to surface state penetration depth that reveals the degree of the correlation between the lower and upper TSS. The closer the parameter gets to the number 1 [3.48], the larger this correlation is.

Since electron-electron and Zeeman interaction effects are suppressed in perpendicular magnetic fields, they were disregarded in the study of perpendicular magnetoresistance data [3.43]. However, our films do not show this parabolic dependency of parallel magnetoconductance, which is thought to be introduced by these effects at low magnetic field strength [3.43, 3.49, 3.50]. This led to the conclusion that these impacts had a rather minor impact. Additionally, electron-electron interactions are predicted [3.50] for films as thin as 6 nm, which is far thinner than the 22 nm ones used in this study.

3.3. Discussion and conclusions

In this work, TEM and XRD confirm that $SnBi_2Te_4$ thin films formed on MBE create septuplet layers that are separated from one another by van der Waals gaps. The center row of the TEM pictures is primarily occupied by Sn, but there is also significant exchange with Bi, comparable to what has been seen in bulk grown $SnBi_2Te_4$ nanoplates [3.13]. The $SnBi_4Te_7$ compound, on the other hand, is ordered as a natural van der Waals superlattice where $SnBi_2Te_4$ septuplets and Bi_2Te_3 quintuples alternate. The TSS in $SnBi_2Te_4$ and $SnBi_4Te_7$, barely overlap with BCB states at the Fermi level, according to the ARPES observations. There is little to no connection between the electrical band structure close to the Fermi level and thickness. The $SnBi_2Te_4$

compound, which corresponds to films with a larger Sn concentration, has the least amount of Fermi energy overlap with the BCB states, making it more appropriate for applications that rely on the TSS electronic transport capabilities.

Magnetotransport experiments have provided more evidence for the TSS in the compound $SnBi_2Te_4$. There are two different types of carriers present, as evidenced by the non-linear Hall resistance (Fig. 3.17a) (electron-like). One of them has a concentration of 6.9×10^{12} cm^{-2}, which is only a factor of 2 smaller than the value of 1.37×10^{13} cm^{-2} estimated from ARPES for the 2D TSS and is attributed to the different band bending [3.39] brought on by the Al capping that is added after ARPES for the transport measurements. This material has the highest mobility of 1260 $cm^2\cdot V^{-1}\cdot s^{-1}$. The aforementioned information leads to the conclusion that the high mobility carriers identified by Hall measurements and the 2D TSS investigated by ARPES are well correlated.

Longitudinal magnetoresistance provides additional information. Both the $B||I$ and $B\perp I$ configurations exhibit a resistance dip at zero magnetic field B (<0.25 T), which is attributed to a weak antilocalization (WAL) effect introduced by the material's strong spin orbit coupling. Generally speaking, a bulk contribution in addition to the TSS contribution is thought to have occurred since a dip in the $B||I$ measurement appears [3.38, 3.40, 3.41].

The values of the measured prefactors can be used to draw conclusions about the various contributions. A value of α ~ -1 denotes the additive contribution of two independent 2D channels, while α ~ -0.5 denotes contribution from just one 2D channel [3.38, 3.49]. Although the parameter α is often the main focus of literature study, the value of β also provides significant information. The final indicator indicates how deeply TSS penetrate the film [3.48]. The occurrence of a high value of 1 denotes a strong coupling between the bottom and top TSS that results in the conveyance of a single 2D TSS channel. However, in our films, the observed β = 0.24 is quite low, suggesting that the two TSS contribute to magnetotransport independently, in which case we would anticipate a ~ -1. However, the measured value of a is -0.42, which is near to the average value of -0.5 for a contribution from a single 2D channel. Therefore, it can be said that the entire film with $d < l_\Phi$, which consists of two interfaces and one

bulk contribution, acts as one 2D channel with a = -0.42, just as it was previously argued for Bi_2Se_3 [3.48].

Our $SnBi_2Te_4$ films exhibit behavior that is comparable to that found in thick (50 nm) Bi_2Te_3 films [3.40, 3.41]. In particular, it should be noted that for thinner Bi_2Te_3 films (5 nm), a single contribution from 2D TSS, working as one channel, has been observed [3.40, 3.51], suggesting that thinned $SnBi_2Te_4$ down to a few nm could be a viable method to isolate a pure 2D TSS transport.

It should be noted that a WAL to WL transition can occur in a number of materials, which might result in negative magnetoresistance at higher magnetic fields because of increased disorder and a lack of topological protection [3.52, 3.53]. With a few notable exceptions [3.40, 3.41, 3.51], this transition is absent in TIs, including the $SnBi_2Te_4$ in the current work, and the behavior is instead characterized by a dip at zero field followed by a parabolic behavior at higher fields. This is seen as proof that our films have enough sufficient topological protection of TSS to prevent the transition from WAL to WL regimes.

References

[3.1] N. H. D. Khang, Y. Ueda, and P. N. Hai, Nat. Mater. **17**, 808 (2018).

[3.2] Y. Wang, R. Ramaswamy, and H. Yang, J. Phys. D: Appl. Phys. **51**, 273002 (2018).

[3.3] J.-C. Rojas-Sánchez, S. Oyarzún, Y. Fu, A. Marty, C. Vergnaud, S. Gambarelli, L. Vila, M. Jamet, Y. Ohtsubo, A. Taleb-Ibrahimi, P. Le Fèvre, F. Bertran, N. Reyren, J.-M. George, and A. Fert, Phys. Rev. Lett. **116**, 096602 (2016).

[3.4] Y. L. Chen, J. G. Analytis, J.-H. Chu, Z. K. Liu, S.-K. Mo, X. L. Qi, H. J. Zhang, D. H. Lu, X. Dai, Z. Fang, S. C. Zhang, I. R. Fisher, Z. Hussain, and Z.-X. Shen, Science **325**, 178 (2009).

[3.5] M. G. Vergniory, T. V. Menshchikova, I. V. Silkin, Yu. M. Koroteev, S. V. Eremeev, and E. V. Chulkov, Phys. Rev B **92**, 045134 (2015).

[3.6] Y. Tanaka, Z. Ren, T. Sato, K. Nakayama, S. Souma, T. Takahashi, K. Segawa, and Y. Ando, Nat. Phys. **8**, 800 (2012).

[3.7] K. Kuroda, H. Miyahara, M. Ye, S. V. Eremeev, Yu. M. Koroteev, E. E. Krasovskii, E. V. Chulkov, S. Hiramoto, C. Moriyoshi, Y. Kuroiwa, K. Miyamoto, T. Okuda, M. Arita, K. Shimada, H. Namatame, M. Taniguchi, Y. Ueda, and A. Kimura , Phys. Rev. Lett. **108**, 206803 (2012).

[3.8] S. V. Eremeev, Yu. M. Koroteev, and E. V. Chulkov, JETP Letters **92**, 161 (2010).

[3.9] D. Souchay, M. Nentwig, D. Günther, S. Keilholz, J. de Boor, A. Zeugner, A. Isaeva, M. Ruck A. U. B. Wolter, B. Büchnerde, O. Oeckler**,** J. Mater. Chem. C **7,** 9939 (2019).

[3.10] Y. Deng, Y. Yu, M. Z. Shi, Z. Guo, Z. Xu, J. Wang, X. H. Chen, and Y. Zhang, Science **367**, 895 (2020).

[3.11] S.-Y. Xu, L. A. Wray, Y. Xia, R. Shankar, A. Petersen, A. Fedorov, H. Lin, A. Bansil, Y. S. Hor, D. Grauer, R. J. Cava, M. Z. Hasan, arXiv:1007.5111, 2010. https://arxiv.org/abs/1007.5111

[3.12] M. G. Vergniory, T. V. Menshchikova, S. V. Eremeev, and E. V. Chulkov, Appl. Surf. Sci. **267**, 146 (2013).

[3.13] Y.-C. Zou, Z.-G. Chen, E. Zhang, F. Kong, Y. Lu, L. Wang, J. Drennan, Z. Wang, F. Xiu, K. Cho, and J. Zou, Nano Res. **11**, 696 (2018).

[3.14] L. Pan, J. Li, D. Berardan, and N. Dragoe, J. Solid State Chem. **225,** 168 (2015).

[3.15] R. Vilaplana, J. A. Sans, F. J. Manjón, A. Andrada-Chacón, J. Sánchez-Benítez, C. Popescu, O. Gomis, A. L .J. Pereira, B. García-Domene, P. Rodríguez-Hernández, A. Muñoz, D. Daisenberger, O. Oeckler, J. Alloys Compd **685**, 962 (2016).

[3.16] V. L. Kuznetsov, L. A. Kuznetsova, and D. M. Rowe, J. Phys. D: Appl. Phys. **34**, 700 (2001).

[3.17] S. Fragkos, L. Baringthon, P. Tsipas, E. Xenogiannopoulou, P. Le Fèvre, P. Kumar, H. Okuno, N. Reyren, A. Lemaitre, G. Patriarche, J.-M. George, and A. Dimoulas, Phys. Rev. Materials **5**, 014203 (2021).

[3.18] A. Tagushi and K. Kanisawa, Appl. Surf. Sci. **252**, 5263 (2006).

[3.19] P. Tsipas, D. Tsoutsou, S. Fragkos, R. Sant, C. Alvarez, H. Okuno, G. Renaud, R. Alcotte, T. Baron, and A. Dimoulas, ACS Nano **12**, 1696 (2018).

[3.20] P. Tsipas, S. Fragkos, D. Tsoutsou, C. Alvarez, R. Sant, G. Renaud, H. Okuno, and A. Dimoulas, Adv. Funct. Mater. **28**, 1802084 (2018).

[3.21] S.-Y. Xu, C. Liu, N. Alidoust, M. Neupane, D. Qian, I. Belopolski, J. D. Denlinger, Y. J. Wang, H. Lin, L. A. Wray, G. Landolt, B. Slomski, J. H. Dil, A. Marcinkova, E. Morosan, Q. Gibson, R. Sankar, F. C. Chou, R. J. Cava, A. Bansil & M. Z. Hasan, Nat. Commun. **3**, 1192 (2012).
[3.22] S. Fragkos, R. Sant, C. Alvarez, E. Golias, J. Marquez-Velasco, P. Tsipas, D. Tsoutsou, S. Aminalragia-Giamini, E. Xenogiannopoulou, H. Okuno, G. Renaud, O. Rader, and A. Dimoulas, Phys. Rev. Mater. **3**, 104201 (2019).
[3.23] J. Wang, N. Wang, H. Huang, and W. Duan, Chin. Phys. B **25**, 117313 (2016).
[3.24] M. Z. Hasan and C. L. Kane, Rev. Mod. Phys. 82, 3045 (2010).
[3.25] G. Kresse and J. Furthmuller, Comput. Mater. Sci. **76**, 3626. (1996).
[3.26] G. Kresse and J. Furthmüller, Phys. Rev. B **54**, 11169 (1996).
[3.27] P. E. Blöchl, Phys. Rev. B **50**, 17953 (1994).
[3.28] J. P. Perdew, K. Burke, and M. Ernzerhof, Phys. Rev. Lett. **77**, 3865 (1996).
[3.29] H. Monkhorst and J. Pack, Phys. Rev. B, **13**, 5188 (1976).
[3.30] A. A. Mostofi, J. R. Yates, Y.-S. Lee, I. Souza, D. Vanderbilta, and N. Marzari, Comput. Phys. Commun. **185**, 2309 (2014).
[3.31] Q. S. Wu, S. N. Zhang, H.-F. Song, M. Troyer, and A. A. Soluyanov, Comput. Phys. Commun. **224**, 405 (2018).
[3.32] M. G. Vergniory, L. Elcoro, C. Felser, N. Regnault, B. A. Bernevig, and Z. Wang, Nature **566**, 480 (2019).
[3.33] M. G. Vergniory, L. Elcoro, Z. Wang, J. Cano, C. Felser, M. I. Aroyo, B. A. Bernevig, and B. Bradlyn, Phys. Rev. E **96**, 023310 (2017).
[3.34] A. Damascelli, Phys. Scr. **109**, 61 (2004).
[3.35] J. P. Perdew, Int. J. Quantum Chem **28**, 497 (1985).
[3.36] M. Ben Shalom, A. Ron, A. Palevski, and Y. Dagan, Phys. Rev. Lett. **105**, 206401 (2010).
[3.37] M. Kang, B. Kim, S. H. Ryu, S. W. Jung, J. Kim, L. Moreschini, C. Jozwiak, E. Rotenberg, A. Bostwick, and K. S. Kim, Nano Lett. **17**, 1610 (2017).
[3.38] E. Lahoud, E. Maniv, M. Shaviv Petrushevsky, M. Naamneh, A. Ribak, S. Wiedmann, L. Petaccia, Z. Salman, K. B. Chashka, Y. Dagan, and A. Kanigel, Phys. Rev. B **88**, 195107 (2013).
[3.39] Q. Barbedienne, J. Varignon, N. Reyren, A. Marty, C. Vergnaud, M. Jamet, C. Gomez-Carbonell, A. Lemaître, P. Le Fèvre, F. Bertran, A. Taleb-Ibrahimi, H. Jaffrès, J.-M. George, and A. Fert, Phys. Rev. B **98**, 195445 (2018).
[3.40] H.-T. He, G. Wang, T. Zhang, I.-K. Sou, G. K. L Wong, J.-N. Wang, H.-Z. Lu, S.-Q. Shen, and F.-C. Zhang, Phys. Rev. Lett. **106**, 166805 (2011).
[3.41] S.-P. Chiu and J.-J. Lin, Phys. Rev. B **87**, 035122 (2013).
[3.42] H. Li, H.-W. Wang, Y. Li, H. Zhang, S. Zhang, X.-C. Pan, B. Jia, F. Song, and J. Wang, Nano Lett. **19**, 2450 (2019).
[3.43] H. Tang, X. Yan, Y. Xiong, K. Dou, Y. Zhao, J. Jie, X. Wang, Q. Fu, J. Yang, M. Lu, and D. Xu, npj Quantum Mater. **4**, 1 (2019).
[3.44] S. Hikami, A. I. Larkin, and Y. Nagaoka, Prog. Theor. Phys. **63**, 707 (1980).
[3.45] C. J. Lin, X. Y. He, J. Liao, X. X. Wang, V. Sacksteder IV, W. M. Yang, T. Guan, Q. M. Zhang, L. Gu, G. Y. Zhang, C. G. Zeng, X. Dai, K. H. Wu, and Y. Q. Li, Phys. Rev. B **88**, 041307(R) (2013).
[3.46] B. Al'tshuler and A. Aronov, JETP Lett. **33**, 499 (1981).
[3.47] V. Dugaev and D. Khmel'nitskii, Zh. Eksp. Teor. Fiz., **86**, 1784 (1984).

[3.48] A. Banerjee, O. Deb, K. Majhi, R. Ganesan, D. Senb, and P. S. A. Kumar, Nanoscale **9**, 6755 (2017).

[3.49] M. Liu, C.-Z. Chang, Z. Zhang, Y. Zhang, W. Ruan, K. He, L.-L. Wang, X. Chen, J.-F. Jia, S.-C. Zhang, Q.-K. Xue, X. Ma, and Y. Wang, Phys. Rev. B **83**, 165440 (2011).

[3.50] J. Wang, A. M. DaSilva, C.-Z. Chang, K. He, J. K. Jain, N. Samarth, X.-C. Ma, Q.-K. Xue, and M. H. W. Chan, Phys. Rev. B **83**, 245438 (2011).

[3.51] A. Roy, S. Guchhait, S. Sonde, R. Dey, T. Pramanik, A. Rai, H. C. P. Movva, L. Colombo, and S. K. Banerjee, Appl. Phys. Lett. **102**, 163118 (2013).

[3.52] K. Banerjee, J. Son, P. Deorani, P. Ren, L. Wang, and H. Yang, Phys. Rev. B **90**, 235427 (2014).

[3.53] H. B. Zhang, J. D. Yao, J. M. Shao, and G. W. Yang, J. Phys. D: Appl. Phys. **49** 095003 (2016).

4. Type-II Weyl semimetal phase in epitaxial $MoTe_2$ at room temperature

4.1. Introduction

Group VI (Mo, W) two-dimensional (2D) transition metal disulphide and diselenide materials are semiconductors that have received a significant deal of attention due to their wide range of possible applications [4.1-4.3]. These materials are commonly stabilized in the hexagonal 2H prismatic structure. The WTe_2 and $MoTe_2$ ditellurides are significant exceptions, as structural and electronic instability leads to a transition into a lower symmetry, deformed 1T (commonly referred to as 1T′) octahedral crystal structure with metallic or semimetalic characteristics [4.4].

At room temperature (RT), the most stable phase of WTe_2 is 1T′. However, for $MoTe_2$, the 2H phase is the most stable, with the metastable 1T phase being only a few tens of meV higher in energy [4.5]. Due to the low energy difference, 1T′ can be stabilized at RT by using bulk growth techniques [4.6-4.10] at high temperature, usually followed by a quick cooling to RT. By applying external stimuli, reversible transitions from the semiconducting to the metallic phase via a thin energy barrier may be achievable [4.5] according to the metastability of 1T′. This has already been experimentally proven at RT using strain [4.11] or electrostatic doping by a gate bias [4.12], making $MoTe_2$ a promising candidate material for the creation of practical electronic devices.

Additionally, the fascinating physical characteristics of $MoTe_2$ and WTe_2 enhance functionality and greatly broaden the variety of applications. These materials have been expected to be 2D topological insulators (or quantum spin Hall insulators) in the limit of a monolayer with a centrosymmetric structure [4.13], which has recently been experimentally confirmed in the case of WTe_2 [4.14]. As first predicted [4.15] and later confirmed [4.16] for bulk WTe_2 material, 1T′ WTe_2 adopts at RT an orthorhombic $Pmn2_1$ (T_d) structure (γ-phase) that lacks inversion symmetry to become a topological type-II Weyl semimetal. Contrarily, few layer or bulk 1T′ $MoTe_2$ is commonly found at room temperature (RT) in a centrosymmetric monoclinic $P2_1/m$ β-phase, which is thought to be a quantum spin Hall state [4.17]. At lower temperatures, typically below 250 K or 150 K, $MoTe_2$ undergoes a structural phase transition from the β-phase to the non-centrosymmetric orthorhombic (T_d) γ-phase.

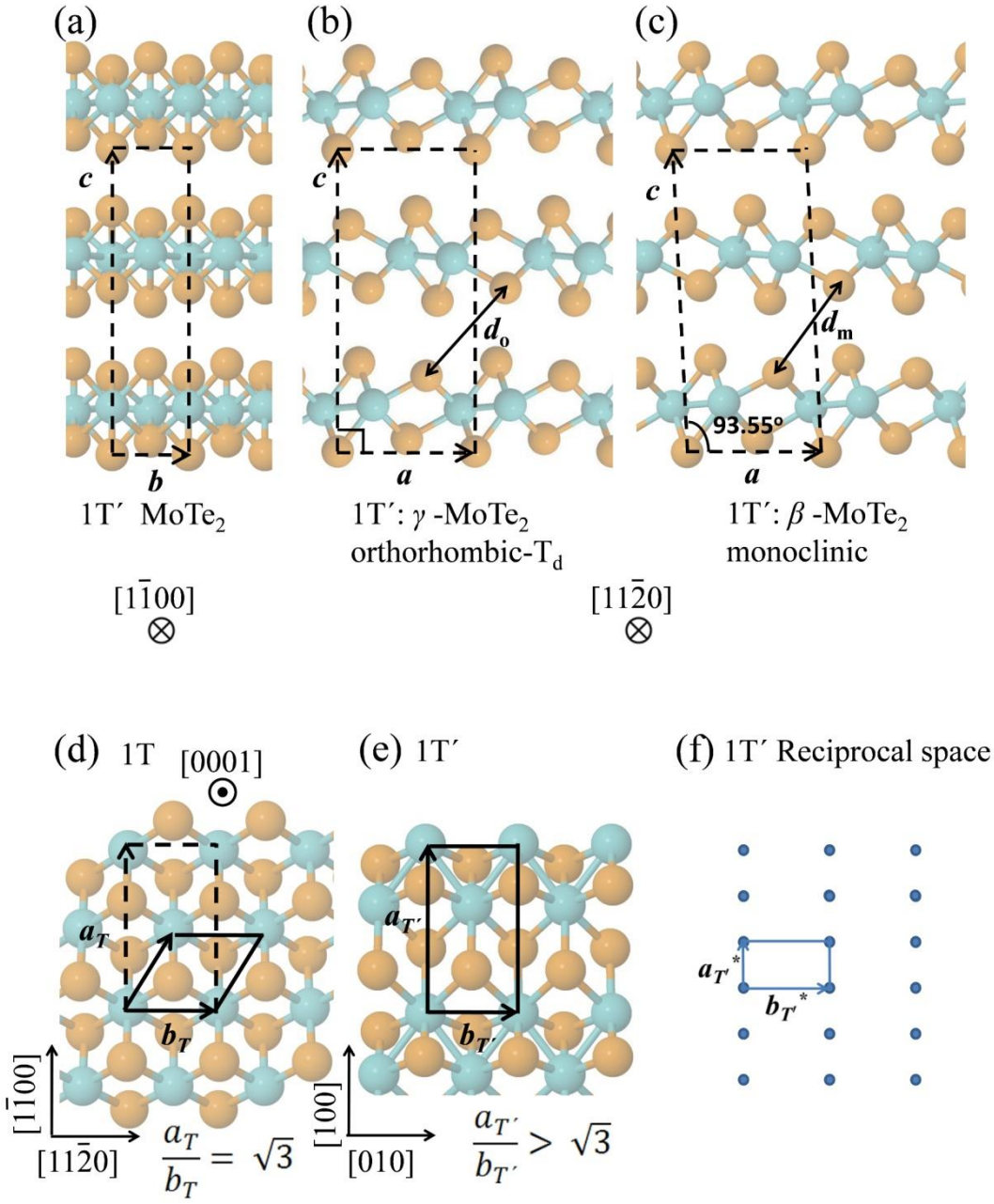

Figure 4.1. Crystal structures for the 1T′ $MoTe_2$ (a) along $[1\bar{1}00]$ direction and (b) T_d-phase along the $[11\bar{2}0]$ direction, (c) monoclinic β-phase along the $[11\bar{2}0]$ direction. (d)-(f) Top view of the direct and reciprocal lattices. Lattice constants are indicated as a, b and a^*, b^* respectively. (d) 1T, (e) 1T′, (f) 1T′reciprocal lattice. The solid lines represent the primitive unit cells. The broken line represents the non-primitive unit cell for 1T $[1\bar{1}00]$ and $[11\bar{2}0]$ of 1T correspond to [100] and [010] of the distorted (1T′) lattice, respectively.

In this case, $MoTe_2$ is predicted [4.18] to become a type-II topological Weyl semimetal (similar to γ-WTe_2), which has already been confirmed by ARPES in bulk $MoTe_2$ [4.8, 4.9, 4.19, 4.20]. The lattice parameters and the strain have a significant impact on the number of Weyl nodes, their location in k-space and energy, and the type of surface states (topological or trivial) in γ-$MoTe_2$. Theoretical values [4.21] of the lattice

parameters deviate significantly from experimental values [4.6-4.9], which also much rely on the fabrication technique. While the majority of studies discover 8 Weyl nodes [4.8, 4.9, 4.18, 4.20, 4.22] only 4 Weyl nodes are also anticipated [4.23], the lowest number ever recorded for a non-magnetic Weyl semimetal. When compared to WTe_2 [4.15, 4.16, 4.24, 4.25], $MoTe_2$ Weyl nodes [4.8, 4.9, 4.18, 4.20, 4.22] are always closer to Fermi energy (E_F), but they are always above E_F, including those in $Mo_xW_{1-x}Te_2$ [4.26, 4.27], making it difficult to observe them with ARPES and to utilize them effectively in operational electronic devices.

Controlling the lattice parameter and stabilizing the γ-phase of $MoTe_2$ at room temperature using appropriate epitaxial techniques and substrates is crucial for illuminating the electronic structure of γ-$MoTe_2$, in particular the Weyl node configuration, and for utilizing the topological properties in real-world applications. More generally, the processing of devices depends on the ability to synthetically produce $MoTe_2$ thin films on cm-scale crystalline substrates. The stacking, physical characteristics, and most stable structural phases of epitaxial thin films may differ from those formed by equilibrium bulk techniques because epitaxial processes are often non-equilibrium and affected by the substrate. While 1T′ structures can also be produced by post-growth temperature modifications, CVD-grown $MoTe_2$ thin films are often found in the RT most stable 2H structure [4.28-4.30]. Mo (W) and Te have very similar electronegativities [4.31], which makes it difficult to grow epitaxial thin films of $MoTe_2$ (and WTe_2) by MBE. The material tends to form intermetallic Mo-Mo or W-W bonds during co-evaporation of Mo (W) and Te, which does not favor the incorporation of Te in the material and results in poor Te-deficient and highly non-stoichiometric films. After adopting interrupted growth methodology to successfully produce the stable 1T′ WTe_2 by MBE on a variety of 2D substrates [4.31], a few studies [4.32–4.34] have reported the stable 2H $MoTe_2$ phase by MBE, however, the metastable 1T′ $MoTe_2$ phase remained elusive until recently, when two separate groups [4.35–4.36] revealed evidence of RT 1T′ MBE films mixed with 2H on epi-graphene/S It is unknown specifically whether they adopt the monoclinic or orthorhombic structure due to a lack of knowledge regarding the epitaxial quality and thin film structure. It is very desirable, but challenging to achieve at RT, to stabilize the Weyl semimetal phase. It has already been demonstrated using bulk single crystals that substituting W for 8% of the Mo will create the γ-phase, which is an intriguing strategy [4.37]. In thin films that have been

exfoliated from bulk materials where low dimensionality is expected to be important, indirect evidence of RT γ-$MoTe_2$ has recently been revealed [4.38]. There haven't been any reports of direct observations of the γ-$MoTe_2$ phase at RT on bulk or epitaxial material.

Here, we report on the crucial orthorhombic non-centrosymmetric Weyl semimetal γ-phase direct RT observation in epitaxial 3 ML $MoTe_2$ films generated layer by layer on InAs(111)/Si(111) substrates via MBE. Additionally, we notice an unusual triclinic layer stacking that topological analysis predicts to be trivial and without Weyl points due to the presence of centrosymmetric. The lattice constants of our epitaxial orthorhombic phase are found to be significantly greater than the experimental values from bulk γ-phase $MoTe_2$ that were previously published. In this study, we claim that the stabilization of the γ-phase at room temperature in epitaxial thin films is significantly influenced by the expanded lattice parameters, as well as the energy position of the Weyl points.

4.2. Results

4.2.1. Crystal structure and reciprocal lattice

To make data interpretation easier, a brief description of the reciprocal lattice and structure features is provided. As previously indicated, the low temperature (T < 250 K) orthorhombic (T_d) *Pmn2*$_1$ γ-phase or the RT monoclinic *P2*$_1$*/m* β-phase are the two common phases in which the 1T distorted (1T′) structure of $MoTe_2$ can be found (Fig. 4.1). Here, we utilize the following notation. Without distinguishing between orthorhombic or monoclinic stacking, 1T′ refers to the distorted 1T. While β-$MoTe_2$ refers to monoclinic stacking, T_d-$MoTe_2$ refers to orthorhombic stacking. The interatomic distance d (Fig. 4.1b,c), which increases in the orthorhombic structure relative to the monoclinic ($d_o > d_m$) due to a parallel shift of the top layer with reference to the bottom one [4.21], is a distinguishing feature of the two phases. The undistorted 1T lattice can be represented by a rectangular surface non-primitive unit cell (dashed line in Fig. 1d), which is twice as large as the hexagonal primitive unit cell (solid line), or by a primitive hexagonal unit cell (solid line), with lattice parameters a_T and b_T such that $a_T/b_T = \sqrt{3}$. The surface rectangular primitive unit cell of 1T, however, deviates from the "ideal" value of $\sqrt{3}$ by having an $a_{T'}/b_{T'} > \sqrt{3}$ value. Similar to this, the reciprocal space of 1T has a rectangular primitive unit cell with the reciprocal lattice

constant ratio $b^*_{T'}/a^*_{T'}>\sqrt{3}$. As will be detailed below, the deviation of these ratios from ideal values results in distinctive signatures in our data that make it easier to characterize the nanostructure of our films.

4.2.2. Sequential layer by layer thin film epitaxial growth and surface structure

Ex-situ chemical cleaning, in-situ thermal annealing, and, if necessary, a light Ar^+ sputtering before thermal annealing are used to prepare in-terminated InAs(111)/Si(111) substrates. This process is repeated until a 2×2 reconstruction pattern in Reflection High Energy Electron Diffraction (RHEED) (Fig. 4.2) is obtained, which indicates a clean, oxide-free surface. Layer by layer, with each layer developed in a two-step procedure, thin 1-3 ML $MoTe_2$ films are created (see Methods). First, a single layer of $MoTe_2$ is formed using the same beam-interrupted epitaxy technique as for the MBE formation of WTe_2 at a low temperature of 280 ^oC and a Te/Mo ratio of 100/1 [4.31]. Following 30 seconds of W and Te co-deposition, the growth is paused for around 60 seconds while the film is continuously exposed to Te, and then the growth is resumed by opening the Mo shutter for an additional 30 seconds. Up till 1ML of $MoTe_2$ is finished, the procedure is repeated. It is estimated that the growth rate will be 0.5ML/min. The sample is then annealed at 400°C for 30 minutes while being exposed to Te flux (0.5 /sec), improving the crystallinity and surface ordering as measured by RHEED (Fig. 4.2). $MoTe_2$ thin films can be developed sequentially, layer by layer, when the first layer is fully formed and optimized. This is accomplished by repeating the identical steps for the second and third layers.

The streaky RHEED patterns (Fig. 4.2c–f) show a homogenous, smooth $MoTe_2$ film that is rotating in phase with the substrate (Fig. 4.2a,b). The diffused background in Figure 4.2e,f shows how the top surface of the film degrades at 3 ML thickness, in contrast to 1 ML $MoTe_2$, which exhibits higher contrast and sharper diffraction streaks (Fig. 4.2c,d). The RHEED patterns are connected with the 1T′ structure's reciprocal space, and the only way to correctly understand a RHEED pattern is to take into account a superposition of domains that are rotated by 0, 60, or 120 degrees (Fig. 4.2 g,h). The hallmark of the deformed 1T′ structure is the presence of the weaker intensity streaks, which sets it apart from the hexagonal symmetry of the 2H or 1T structures, where only the greater intensity peaks are anticipated to be present.

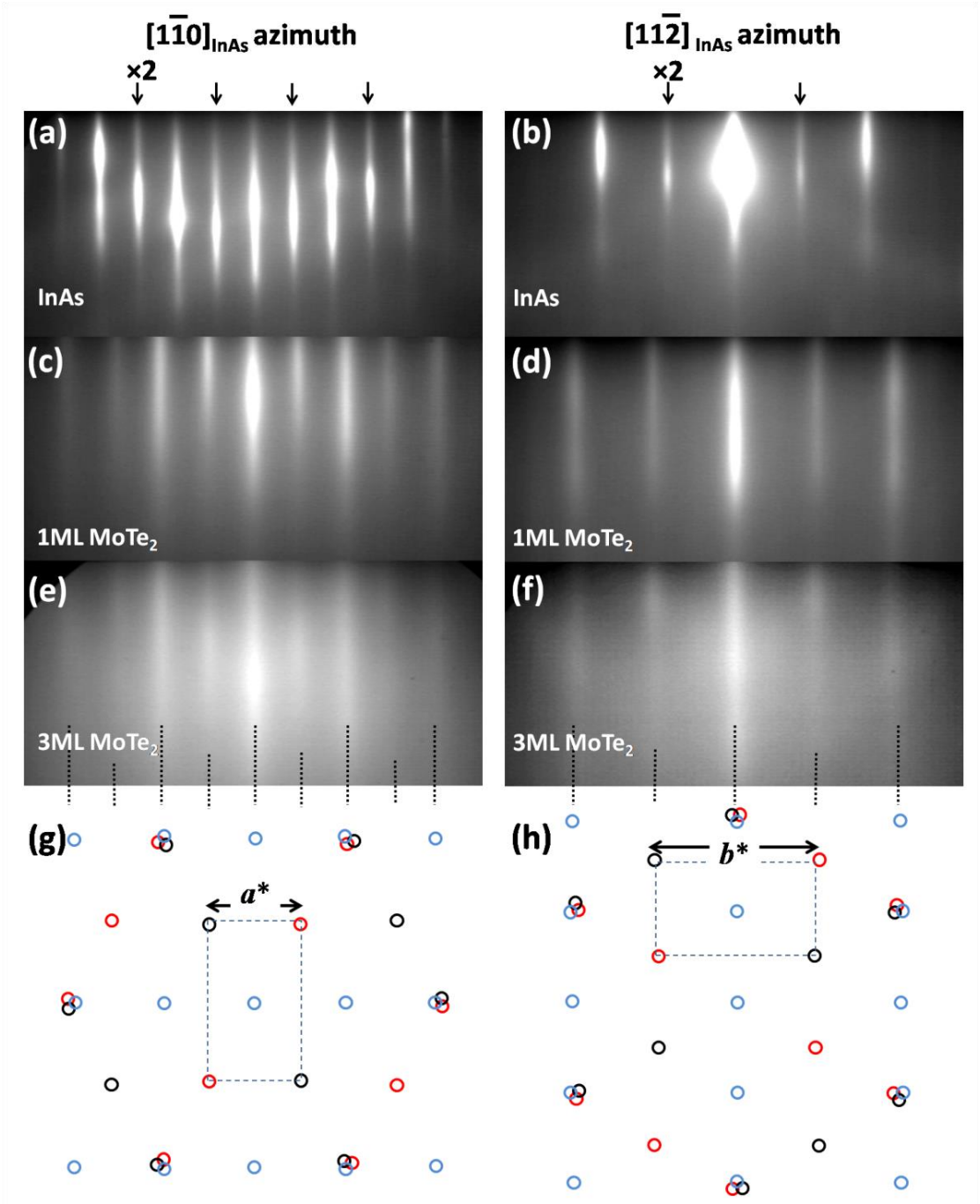

Figure 4.2. RHEED patterns from (a,b) an InAs clean surface, (c,d) a 1 ML epitaxial $MoTe_2$, (e,f) a 3 ML epitaxial $MoTe_2$. (g,h) schematic showing the superposition of reciprocal lattices from 0° (blue circles), 60° (black circles), 120° (red circles) rotated 1T′ domains. The broken line rectangles mark the primitive reciprocal unit cells and a^* and b^* are the reciprocal lattice parameters.

The reciprocal space lattice constant $a^* = 0.9849$ Å^{-1} can be directly determined from Figs. 4.2 c and e, and with the aid of calibration with the known lattice parameters of InAs, and then translated to the real space lattice constant $a=2/a^*$, which is calculated to be 6.38 Å. Likewise, the values $b^* = 1.7952$ Å^{-1} and $b=2/b^* = 3.50$ Å are found from

Figs. 4.2 d, f. More precise calculations based on synchrotron XRD data show that the parameters *a* and *b* are in a fair amount of agreement (Fig. 4.5 and related discussion in main text).

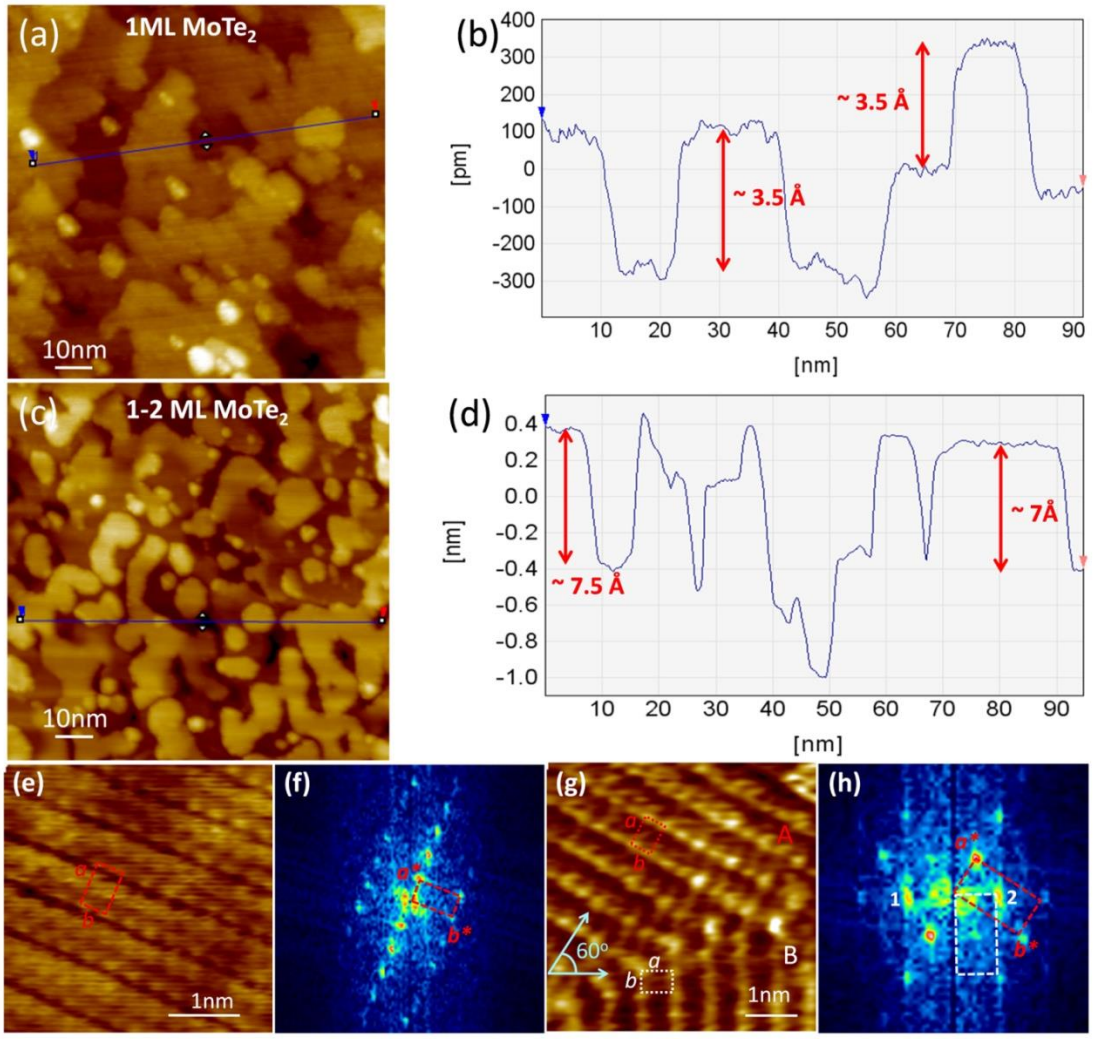

Figure 4.3. Room-temperature STM of distorted $MoTe_2$. (a,b) 1 ML $MoTe_2$ and the related line scan, indicating the influence of the InAs substrate (c,d) Surface morphology of an incomplete second $MoTe_2$ layer with the corresponding linescan indicating the thickness of the top layer, including the vdW gap. (e,f) Surface and the corresponding Fourier pattern. The dashed rectangles indicate the unit cells of real (e) and *k*-space (f) lattices. (g) Image of two domains A and B relatively rotated by 60° (h) The additional intense spots marked by 1 and 2 originate from the rotated pattern and defines the superimposed *k*-lattice (white dotted rectangles).

Fig. 4.3a shows an image created by in-situ Ultra High Vacuum Scanning Tunneling Microscopy (UHV-STM) at RT of the surface nanostructure of 1 ML 1T´ $MoTe_2$. The samples were moved to the STM (OMICRON) chamber for in-situ STM characterization after the growth of $MoTe_2$ films without breaking the vacuum. Using a Pt/Ir tip, STM pictures were captured in UHV conditions (base pressure 10^{-9} mbar) at

room temperature. The high resolution images (Figs 4.3e–h) were captured at V = 0.1 mV, I = 1 nA, while the remaining images were captured at V = 0.4 mV, I = 400 pA. The domains differ in height by about 3.5 (Fig. 4.3b), which is equal to the height of the monoatomic steps of the underlying InAs substrate. The domains have an average lateral size of around 40 nm. As a result, it is determined that the monatomic step nanostructure of the InAs surface is where the domain creation in $MoTe_2$ originates, which is in line with the data from scanning transmission electron microscopy (STEM) that are shown in the section below (Fig. 4.4). The development of 2D islands after the deposition of a second layer has a height of ~7 Å (Fig. 4.3d), which is almost equivalent to the thickness of a single layer of 1T' $MoTe_2$ when the van der Waals gap between the top and bottom layers is taken into account. The islands merge to form an entire second layer.

The symmetry of the 1T' $MoTe_2$ surface is compatible with atomic resolution STM imaging of a single domain (Fig. 4.3e). The surface reciprocal space is produced by the Fourier transform in Fig. 4.3f, which is identical to the schematic in Fig. 4.1f. Two domains A and B, imaged in a different area of the surface, are rotated by 60 degrees with respect to one another (Fig. 4.3g). This creates a more complicated reciprocal space (see the Fourier transform of Fig. 4.3h), where the additional periodicities 1 and 2 define a reciprocal lattice for domain B (indicated with white dashed rectangles) that is rotated by 60 degrees with respect to domain A. (red dashed rectangles).

4.2.3. Orthorhombic and unconventional triclinic layer stacking structure

To determine the film layer stacking, the $MoTe_2$ thin films are examined in cross-section by STEM at RT. With a Cs-corrected FEI Themis operating at 200 keV, STEM measurements have been performed. Using a convergence semiangle of 18 mrad and collecting scattering greater than 65 mrad, HAADF-STEM pictures were obtained. STEM specimens were created using an FEI dual-beam Strata 400S at 30 kV and the FIB lift-out procedure. Images of the cross-sections of the 1 ML and 3ML $MoTe_2$ are shown in Fig. 4.4. Two sections of 1 ML of 1T $MoTe_2$ are shown disrupted in Fig. 4.4a by an atomic step in the InAs, ~3.5 Å, resulting in the formation of domains of various heights, which is consistent with STM observations in Fig. 4.3a.

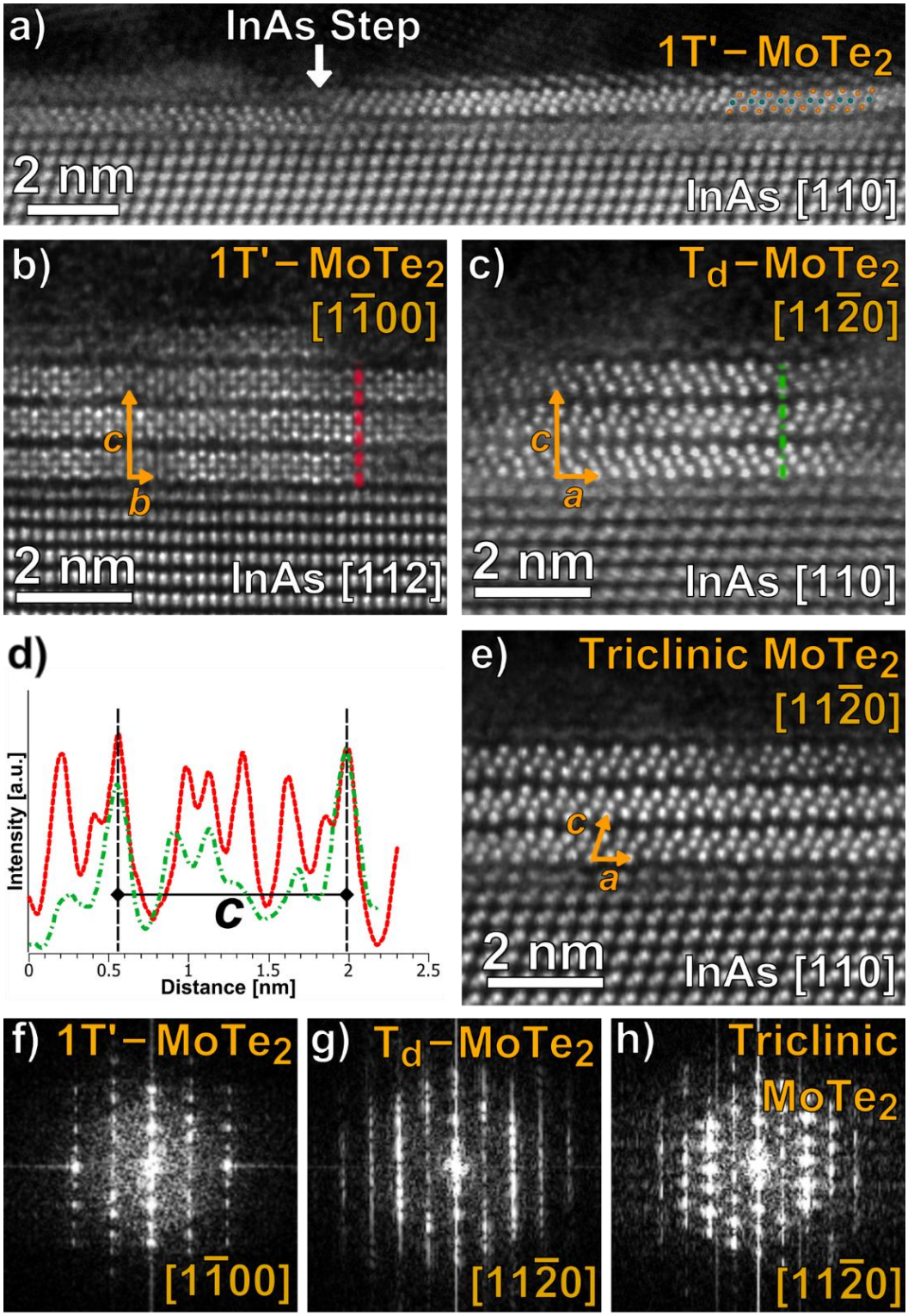

Figure 4.4. STEM images of 1 and 3 ML $MoTe_2$ films. (a) 1 ML of $MoTe_2$ indicating film interruption at the edge of an InAs step (b) 3 ML $MoTe_2$ along $[1\bar{1}00]$zone axis, (c) 3ML with orthorhombic (T_d) stacking along the $[11\bar{2}0]$ axis, (d) intensity line scan in the *c* lattice direction derived from (b) and (c) images in red and green, respectively, (e) 3 ML of an unconventional triclinic stacking along the $[11\bar{2}0]$ axis. (f-h) FFT patterns of the respective STEM images.

It is important to note that the thin films are in a pure 1T' phase because there is no indications for the 2H hexagonal phase, which is the most stable at room temperature. The orthorhombic T_d-$MoTe_2$ phase (Fig. 4.4c), which has two layers in the unit cell and typically manifests at lower temperatures (250K), and an unconventional triclinic stacking with one layer per unit cell (Fig. 4.4e), which has not yet been reported, are the two dominant phases that are seen as the growth progresses from 1 ML to 3 ML 1T' $MoTe_2$. The second layer is rotated by 180 degrees with respect to the first layer in the triclinic stacking of Fig. 4.4e as opposed to the traditional room temperature stable *β*-$MoTe_2$ monoclinic phase. In the T_d orthorhombic structure (Fig. 4.4b,c), the lattice parameter along the *c*-axis is measured to be between 14.1 and 14.2 (Fig. 4.4d), which is significantly larger than the previously reported experimental *c* values from bulk T_d-$MoTe_2$ crystals [4.6-4.9], which were found to be in the range between 13.861 Å and 13.8935 Å. Additionally, our films lack the *β*-$MoTe_2$ monoclinic stacking, which is the most stable room temperature monoclinic stacking among the various 1T' structures. The STEM images' sections containing only the $MoTe_2$ film were also used to generate fast Fourier transform (FFT) patterns, which are displayed in Fig. 4.4f–h.

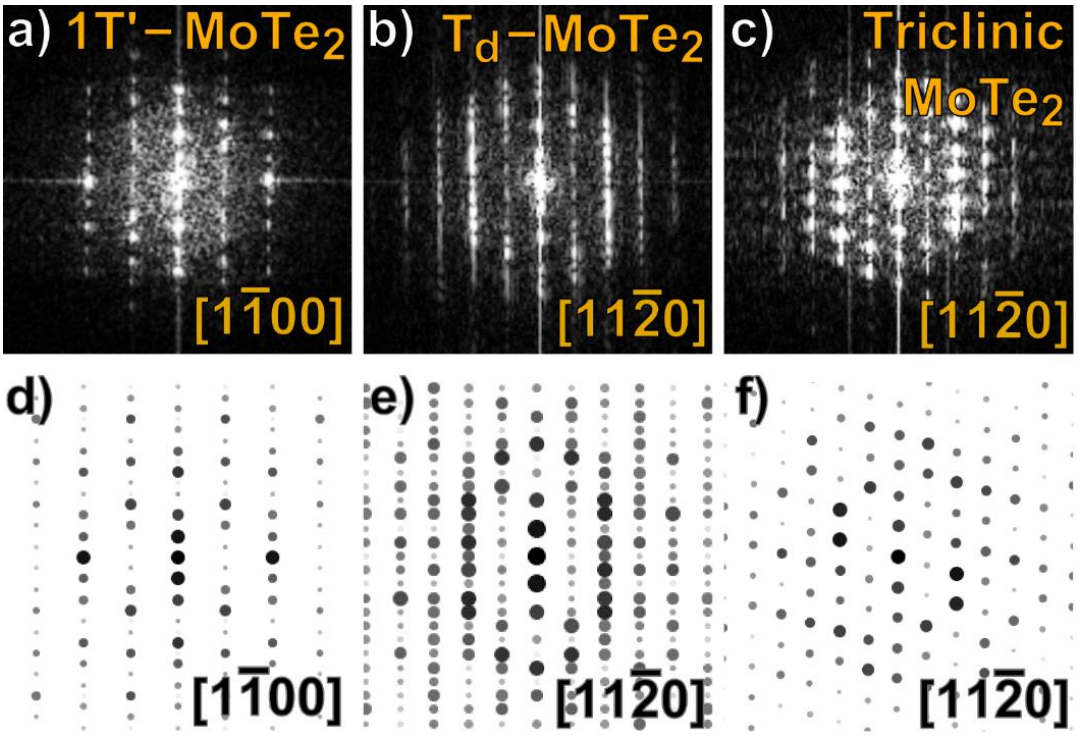

Figure 4.5 (a–c) FFT images from STEM image measurements with the corresponding (d–f) simulated electron diffraction patterns. The respective $MoTe_2$ crystal structure were used in order to simulate each of the diffraction patterns.

To confirm the various $MoTe_2$ crystal structures, the FFT patterns were examined and compared with corresponding simulated electron diffraction patterns. In Fig. 4.5, the patterns of simulated electron diffractions are shown. Only the section that contains the 3 ML of $MoTe_2$ was used to calculate the FFT patterns. When compared to an electron diffraction pattern from a bulk material, the FFT pattern is more challenging to understand because it is calculated from a small region, but it accurately depicts the local film structure. To easily distinguish between the various structures discovered, the FFT patterns are compared to simulated electron diffraction patterns. Using the predicted crystal structures (1T′-$MoTe_2$, T_d-$MoTe_2$, and triclinic $MoTe_2$) and the corresponding zone axis, the JEMS software program computed each simulated electron diffraction pattern. The newly discovered triclinic crystal structure is well represented by the FFT patterns, which also closely resemble the simulated patterns.

4.2.4. In-plane epitaxial orientation investigated by synchrotron grazing incidence X-Ray diffraction

Single-layer and three-layer $MoTe_2$ are examined by grazing incidence X-ray diffraction (GIXD), and Fig. 4.6 shows the data for three-layer ML films. At the European Synchrotron Radiation Facility (ESRF), diffraction measurements were carried out using the UHV-MBE CVD diffractometer, which was placed at the BM32 CRG/IF beamline and optimized for GIXD. In order to maximize the 2D film signal while reducing the background, the experimental setup's incidence angle and energy were set at 0.2° and 11 keV (1.13 keV), respectively. The $MoTe_2$ film is epitaxially formed on InAs in such a way that $[100]_{MoTe2}/[11\text{-}2]_{InAs}$ and $[010]_{MoTe2}/[01\text{-}1]_{InAs}$ are present in the plane, according to the in-plane Reciprocal Space Map (RSM) in Fig. 4.6a. No other polycrystallinity or rotational domains other than those resulting from the Al protective cap are visible (rings in Fig. 4.6a). The locations of the diffraction peaks in *k*-space are consistent with a complicated reciprocal space (shown as open circles in Fig. 4.6a) that is a superposition of domains that have been rotated by 0, 60, and 120°.

The triplet along $h=k$ ($[01\bar{1}]_{InAs}$) comprised of the on-axis (020) peak and the two off-axis (310) peaks both belonging to different domains rotated between each other by 60 degrees is the most distinctive configuration. It should be noted that all three closely spaced reciprocal lattice points should coincide to produce a single diffraction peak in

the ideal scenario where $b^*/a^* = \sqrt{3}$ applies to the hexagonal crystal symmetry of the undistorted 1T structure (see Fig. 4.1d).

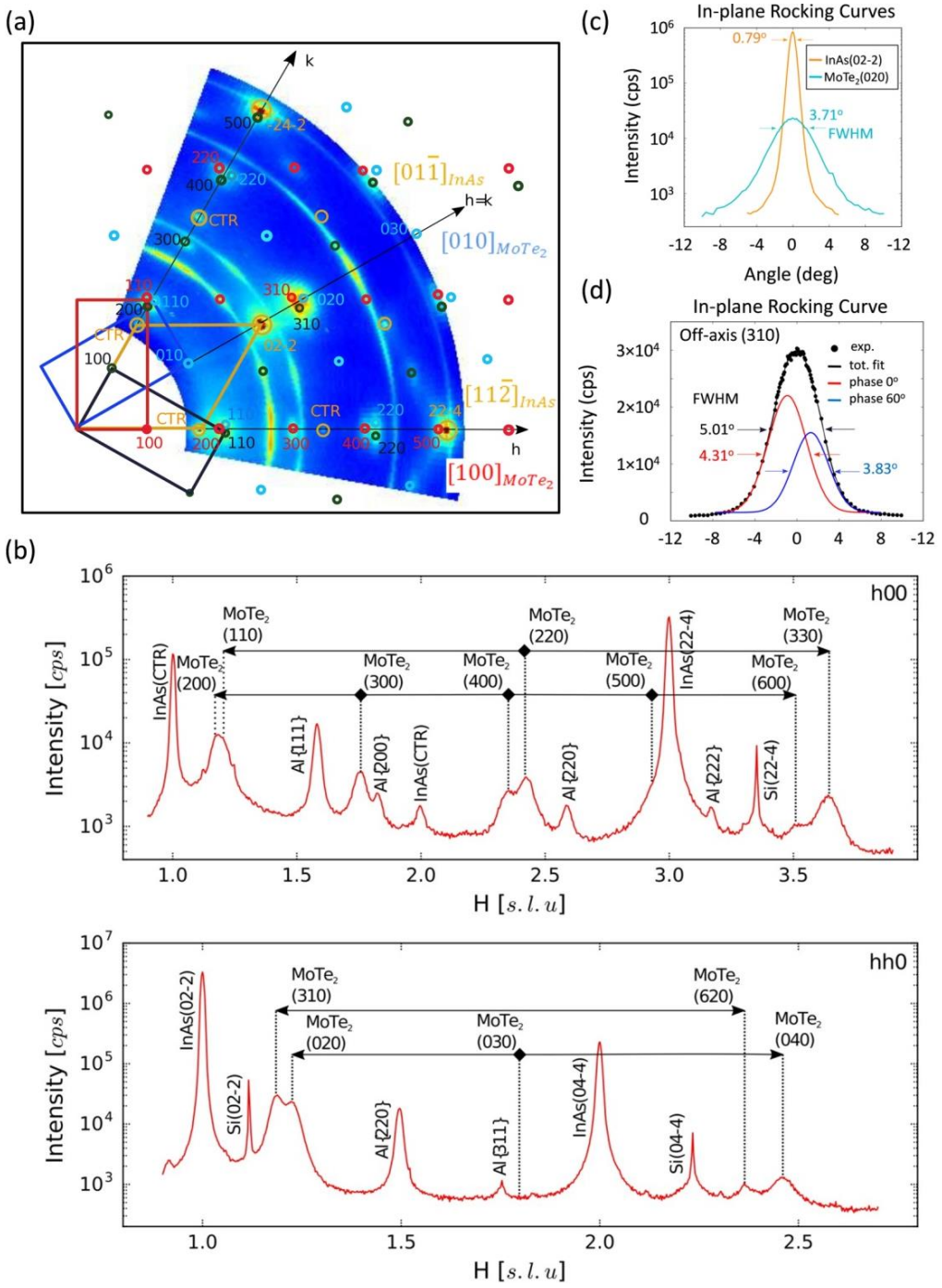

Figure 4.6. (a) Reciprocal space map obtained from Synchrotron GIXD measurement of epitaxial 3 ML $MoTe_2$ (a). The *h*, *k* and *h*=*k* axis are the high symmetry directions of the hexagonal *k*-space surface. The rectangles and open circles denote the unit cells and reciprocal lattice points, respectively, originating from the three rotated domains of 0° (red), 60° (blue), and 120° (black). (b) Radial scans along the *h* and *h*=*k* directions indicated in (a), (c) In-plane rocking curves of the (020) axis single peak and (d) the (310) axis peak, deconvoluted into two peaks (blue and red lines) created from two different domains relatively rotated by 60°.

Although the ratio in our example of a deformed 1T´ $MoTe_2$ lattice is not optimal ($b^*/a^* > \sqrt{3}$), GIXD clearly detects the peak splitting into a triplet shape (Fig. 4.6a). Shared characteristics occur along h ($[11\bar{2}]_{InAs}$) direction with the triplet including (200) and two (110) peaks as well as the triplet involving the on-axis (400) peak and two off-axis (220) peaks from rotated domains, however the latter triplet is not very well resolved. The result is that certain diffractions exhibit doublets in the radial scans along the h and $h=k$ directions of Fig. 4.6b. Since there are two off-axis diffraction peaks contributing to the doublet's peak due to the superposition of off-axis signals (see the deconvolution of the (310) diffraction peak in Fig. 4.6d, the peak's transverse breadth is bigger. An in-plane mosaicity of 3.71° is estimated from the FWHM of the on-line single peak (020) in Fig. 4.6c, which is much greater than that of the InAs substrate (0.79°) and higher than the mosaicity of 1.79° found in epitaxial $ZrTe_2$ on InAs(111) substrate [4.39]. From the RSM and the radial scans, the reciprocal (a^*, b^*) and direct (a, b) lattice parameters can be precisely calculated by taking into account just the well-resolved on-axis single peaks (020), (300), and (400). The 020 peak is located at position q=3.5894 $Å^{-1}$ in the q space, which is two times the k-space unit cell lattice constant b. (Fig. 4.6b). Due to this, $b^*=q/2$ = 1.7947 $Å^{-1}$ and $b=2/b^*$= 3.501 (±0.003) Å are obtained. Looking along the h and k directions in Fig. 4.6a, the (300) and (400) peaks are $3a^*$ and $4a^*$ respectively and by taking into consideration their location in k-space from Fig. 4.6b, a^*= 0.99105 $Å^{-1}$ (averaged over the four peaks, two in each of the h and k directions.) and $a=2\pi/a^*$ = 6.340 (±0.005) Å are obtained. It is necessary to note that the values of a, b, and c in our epitaxial thin films (determined from GIXD and STEM, respectively) are higher than those measured from bulk T_d-$MoTe_2$ crystals [4.6-4.9] . This is a result of the substrate's influence and the layer-by-layer sequential growth method used in the current work.

4.2.5. Electronic band structure of 1T′ $MoTe_2$ epitaxial thin films

A 100 mm hemispherical electron analyzer (SPECS PHOIBOS 100) and a 2D CCD detector were used to conduct in-situ ARPES experiments in a room-temperature metal analytical chamber. Utilizing 21.22 eV photons from an He discharge source (SPECS UVS35/10), the detection system's energy resolution was higher than 40 meV; however, because the measurement was made at room temperature (RT), the resolution was about 100 meV.

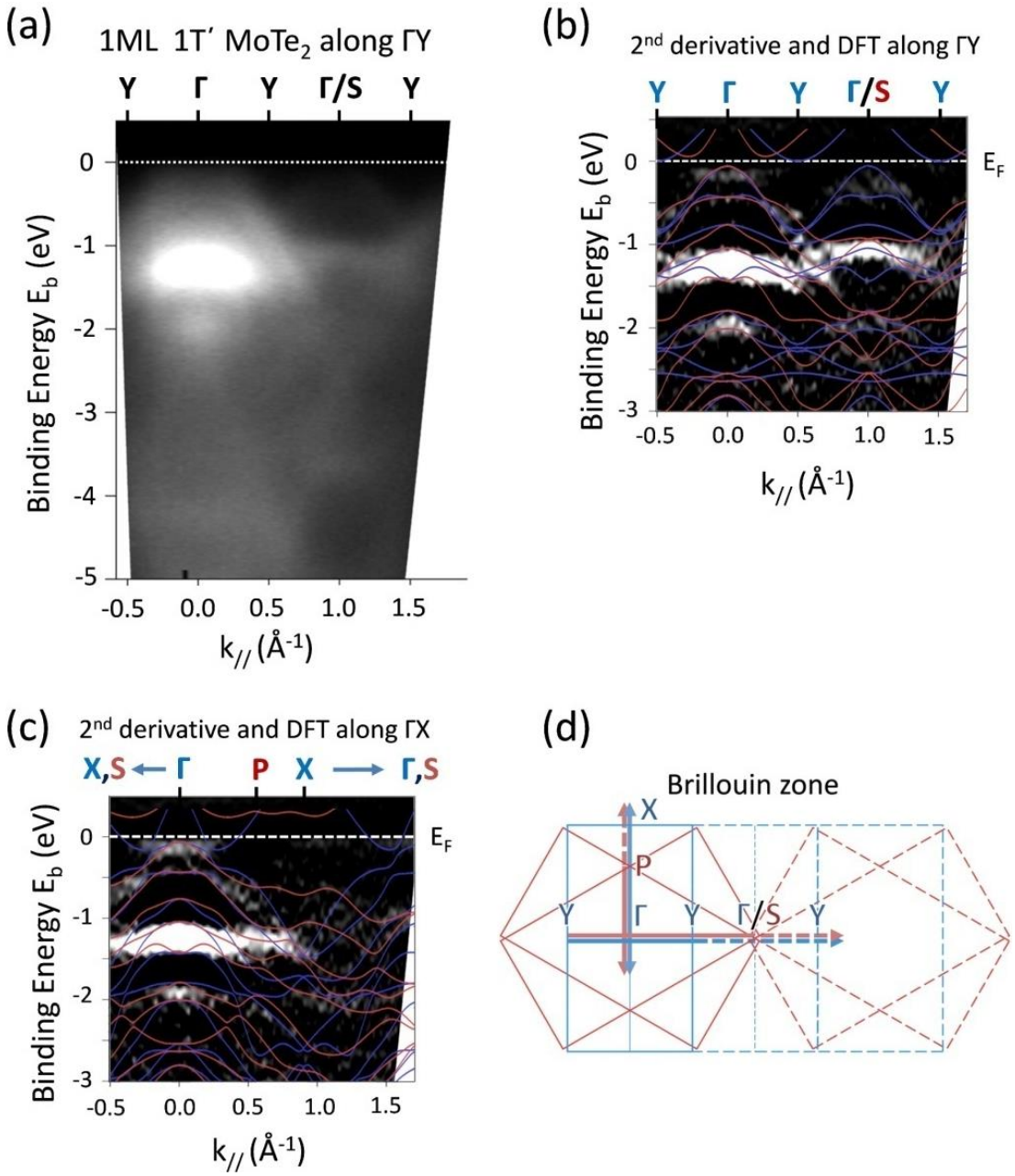

Figure 4.7. (a) In-situ electronic band structure measurement of 1 ML 1T′ $MoTe_2$ imaged by ARPES at RT (a) ARPES along the ΓY direction, (b) second derivative of ARPES spectra in (a) compared with DFT calculations for 1 ML of 1T′ $MoTe_2$. Blue line is along the ΓY direction, and the red line is along the ΓS direction, (c) second derivative of ARPES spectra along the ΓX direction compared to the DFT caclulations for 1 ML of 1T′ $MoTe_2$ (d) A schematic illustration of the *k*-space constructed by superimposing orthorhombic BZs originated from of 0^o (blue solid line), 60^o and 120^o rotated domains (red solid lines). The dashed lines indicate the neighboring BZs. The Γ point of the neighboring BZ of 0^o, almost coincides with the S point of the rotated BZs. The horizontal thick arrows indicate the directions along which the ARPES spectra in (a) and (b) are measured. Note that the ARPES images show simultaneously the bands along the ΓY (blue arrow) and the ΓS (red arrow) directions due to the overlapping of rotated domains.

Fig. 4.7 shows a direct comparison between the electronic band structure of 1 ML 1T´ $MoTe_2$ as imaged by in-situ ARPES and 1 ML from density functional theory (DFT) first principles calculations utilizing the experimental lattice parameters derived from our epitaxial thin films. Our epitaxial material, in contrast to exfoliated single crystal 1T' $MoTe_2$, has rotational domains that differ from one another by 60 degrees (see also discussion of RHEED, STM and XRD in Figs 4.2, 4.4 and 4.6, respectively). Due to the complex Brillouin zone (BZ) configuration that results from this (Fig. 4.7d), the electronic band structure in the BZ overlaps in two different directions, such as the Y and S directions in the ARPES spectrum of Fig. 4.7a. This results in a complex dispersion that adversely affects energy and momentum resolution. The resolution is increased (Fig. 4.7b, c) by using the second derivative of the energy dispersion, and this leads to a good agreement with DFT simulations along the high symmetry lines in the BZ, which are denoted by thick (blue and red) arrows in Fig. 4.7d. Notably, the band at around $k_{//}$= 0 $Å^{-1}$ in Fig. 4.7b is practically a duplication of the feature at around $k_{//}$~1 $Å^{-1}$ in Fig. 4.7b, which is located at the position of the nearby BZ (shown by the broken line in Fig. 4.7d). Additionally, Fig. 4.7c provides proof that electron pockets reside close to the point along the ΓX direction, as predicted by DFT (blue line).

In theory, it should be feasible to determine the most prevalent configuration by applying ARPES to thicker films and distinguishing between orthorhombic T_d-$MoTe_2$ phase and triclinic stacking, however the ARPES spectra for 2 and 3 ML are extremely similar to those for 1 ML (Fig. 4.7). This may be understood by considering that the surface-sensitive 21.22 eV ARPES approach probes the topmost layer, which is weakly linked to the bottom layers and exhibits the behavior of a single layer in ARPES.

In order to predict the existence of Weyl nodes and determine their location in energy and *k*-space, we performed DFT and tight-binding band structure calculations for the non-centrosymmetric orthorhombic (T_d) structure using the measured set of lattice parameters in our epitaxial thin films (*a*=6.340 Å, *b*=3.501 Å, and *c*=14.15 Å). The Vienna Ab initio Simulation Package (VASP) [4.40, 4.41] and projector-augmented waves [4.42] were used to perform the first-principles calculations. The exchange correlation functional was calculated using the generalized-gradient approximation (GGA) with Perdew-Burke-Ernzerhof (PBE) parameterization [4.43]. Using the Monkhorst-Pack technique [4.44] and a 12×10×6 *k*-point mesh for bulk calculations,

the kinetic energy cutoff was set at 450 eV. Utilizing a force threshold of 1×10^{-3}eV/Å, the atomic locations were entirely optimized by conjugate gradient using the experimental lattice constants. In order to use van der Waals corrections, the semi-empirical DFT-D3 Grimme's approach was applied [4.45]. The Wannier90 code [4.46] is used to fit the Maximally-Localized Wannier functions based on the *s* and *d* orbitals of Mo and *p* of Te, and WannierTools [4.47] is used to calculate the surface states, topological Fermi arcs, and Weyl points. Band structure simulations took spin-orbit coupling (SOC) into consideration.

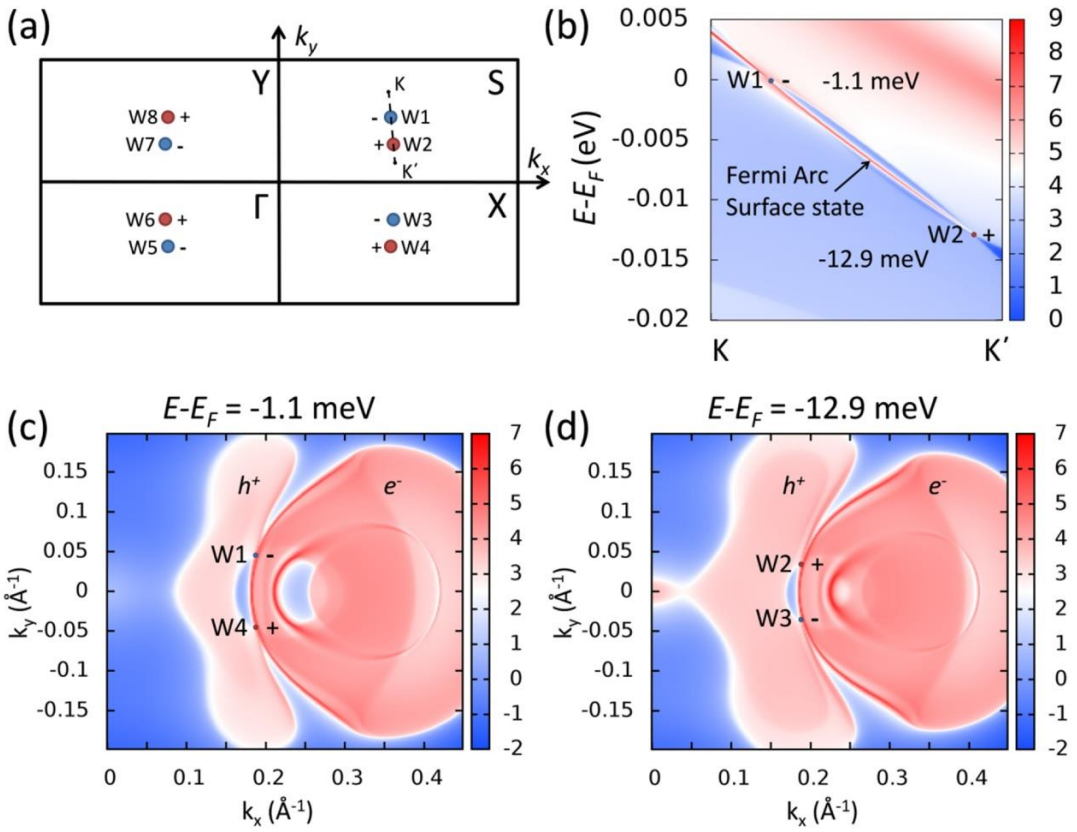

Figure 4.8. DFT and tight-binding calculations of the Weyl node configuration for the bulk orthorhombic T_d-$MoTe_2$ using the experimental lattice constants measured from our epitaxial films. (a) Schematic illustration of the positions of Weyl nodes in the first BZ. The blue and red dots demostrate pairs of Weyl nodes of opposite chirality. (b) BZ projection calculations along an KK′ path shown by broken line in subfigure (a), passing through a single pair of Weyl nodes. Theoretical Fermi surface contour plots for two different energies of E = -1.1meV (c) and -12.9meV (d) corresponding to the energy possitions of the Weyl nodes. The e^- and h^+ indicate the electron and hole pockets, respectively.

As a result of broken inversion symmetry, we can find 8 Weyl nodes by taking into account the topmost valence band and the following conduction band (Fig. 4.8). These nodes are all situated in the k_z=0 plane and according to the schematic of Fig. 4.8a, are

symmetrically positioned in *k*-space with respect to the high symmetry directions X-Γ-X and Y-Γ-Y. These are their precise positions in energy and *k*-space: $W1^-$: $E-E_F$= -1.1 meV at (k_x = 0.18707 $Å^{-1}$, k_y = 0.0456 $Å^{-1}$, k_z = 0 $Å^{-1}$), $W2^+$: $E-E_F$= -12.9 meV at (k_x = 0.1871 $Å^{-1}$, k_y = 0.0351 $Å^{-1}$, k_z = 0 $Å^{-1}$). Each pair's Weyl nodes have opposite chirality, and are found below the Fermi level, but very near it (Fig. 4.8b). Fig. 4.8b depicts the surface state that passes through the Weyl nodes with opposite chirality (+, -) and the Fermi arc linking them. It is important to note that the Weyl nodes produced by this combination of lattice parameters derived from our epitaxial thin films are closer to the Fermi level than any other Weyl nodes for $MoTe_2$ reported in the literature [8-9, 18, 20, 23–24]. The Weyl nodes are predicted in our epitaxial thin films to be slightly below the Fermi level, which makes them accessible to transport and makes them easier to see by ARPES. This makes them appropriate for electrical applications where topological features might play a crucial role.

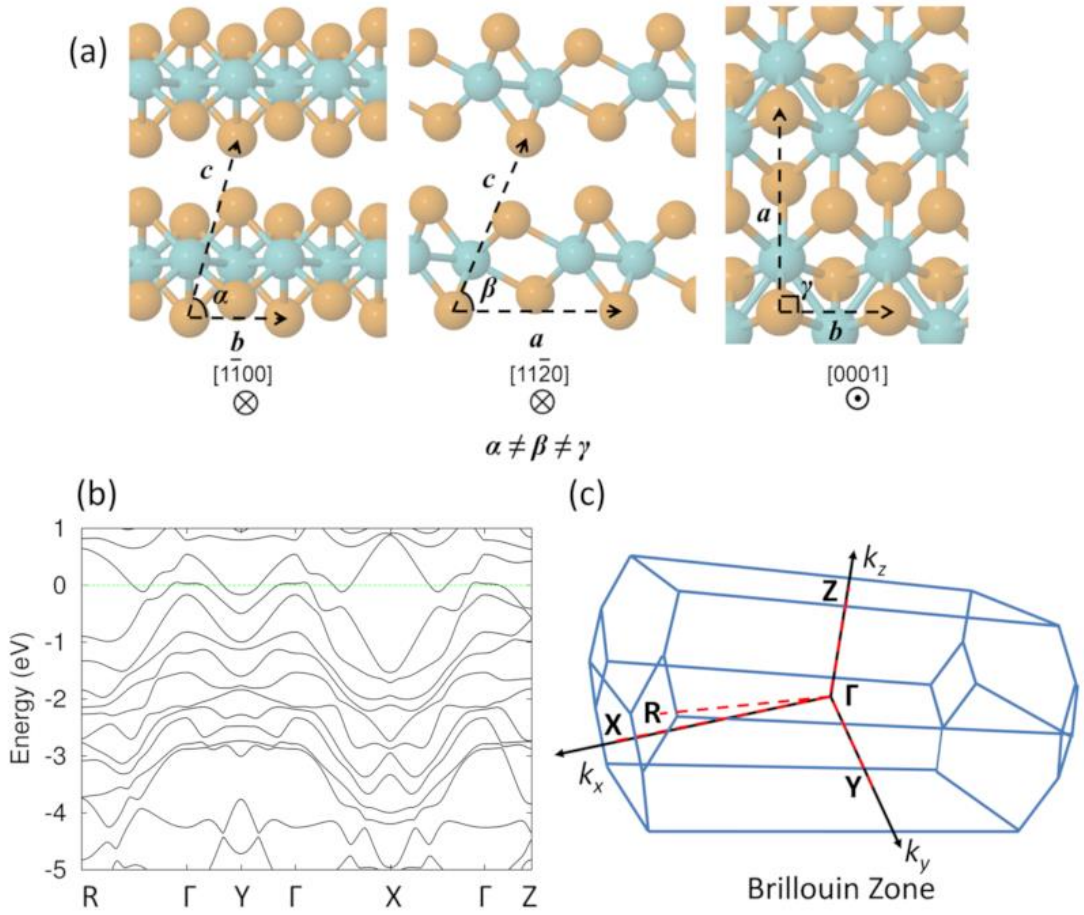

Figure 4.9. (a) Crystal structure of the unconventional triclinic stacking along the [1$\bar{1}$00], [11$\bar{2}$0] and [0001] directions, (b) the band structure by DFT calculations along the high symmetry points and (c) the first Brillouin zone of the triclinic phase.

As shown by STEM in Fig. 4.4e, the unconventional layer with triclinic stacking results in a predicted bulk band structure (Fig. 4.9) with no Weyl points, which is to be expected given that the structure is centrosymmetric. We identify the unconventional structure as triclinic using STEM measurements (Fig. 4.4e) since the lattice vectors and the angles between them are different from one another (Fig. 4.9a). We employed the experimentally (XRD) determined lattice parameters for a single layer to produce the bulk structure for the first principles calculations by DFT, which is consistent with the STEM pictures along both the $[11\bar{0}0]$ and $[112\bar{0}]$ zone axes. The optimal values of the angles between the three axes are 75.55°, 68.09°, and 90° after relaxation. The second layer is rotated by 180° with regard to the first and the third layers in the triclinic stacking, which is different from the well-known room temperature β-$MoTe_2$ monoclinic stacking.

We examine our first principles calculations that were carried out using two different sets of experimental lattice parameters (Fig. 4.10) using a similar methodology and justification as in Ref 4.21 to learn more about the potential effects of the larger lattice parameters on the stabilization of the orthorhombic T_d-phase in our epitaxial thin films at room temperature. Set #1 (a=6.3341 Å, b=3.5751 Å, c=13.8816 Å) in Fig. 4.10a is an average derived from experimentally published values for bulk, free-standing T_d-$MoTe_2$ [4.6-4.9], observed at low temperatures, while Set #2 (a=6.340 Å, b=3.501 Å, c=14.15 Å) in Fig. 4.10b is from our measured T_d-$MoTe_2$ epitaxial films at RT.

The highest valence band B1 along ΓA in both band configurations (Fig. 4.10 a, b) is made up of hybridized Te p_x and Mo d_{xz} orbitals, whereas the lower band B2 is made up of hybridized Te p_z and Mo d_{z2} orbitals. According to Figs. 4.10c,d, which illustrate the wavefunctions of B1 and B2 at for Set #2 (our experimental conditions), interlayer coupling takes place between inner Te atoms with large and opposite sign wavefunction values along the interlayer distance d. Since B2 is fully occupied in both scenarios, the likelihood of $MoTe_2$ to stabilize in the T_d phase depends on the extent to which the interlayer andibonding band B1 along ΓA and near Γ is occupied. A sizeable portion of the topmost valence band B1 near Γ point along ΓA is unoccupied for Set#1 of the experimental bulk parameters taken from the literature (Fig. 4.10a and Fig. 4.11). In contrast, the experimental parameters for Set#2 of our epitaxial thin film are enlarged.

As a result of B1's full occupancy, the interlayer antibonding state is strengthened, favoring an elongated interlayer distance *d*. (Fig. 4.10c).

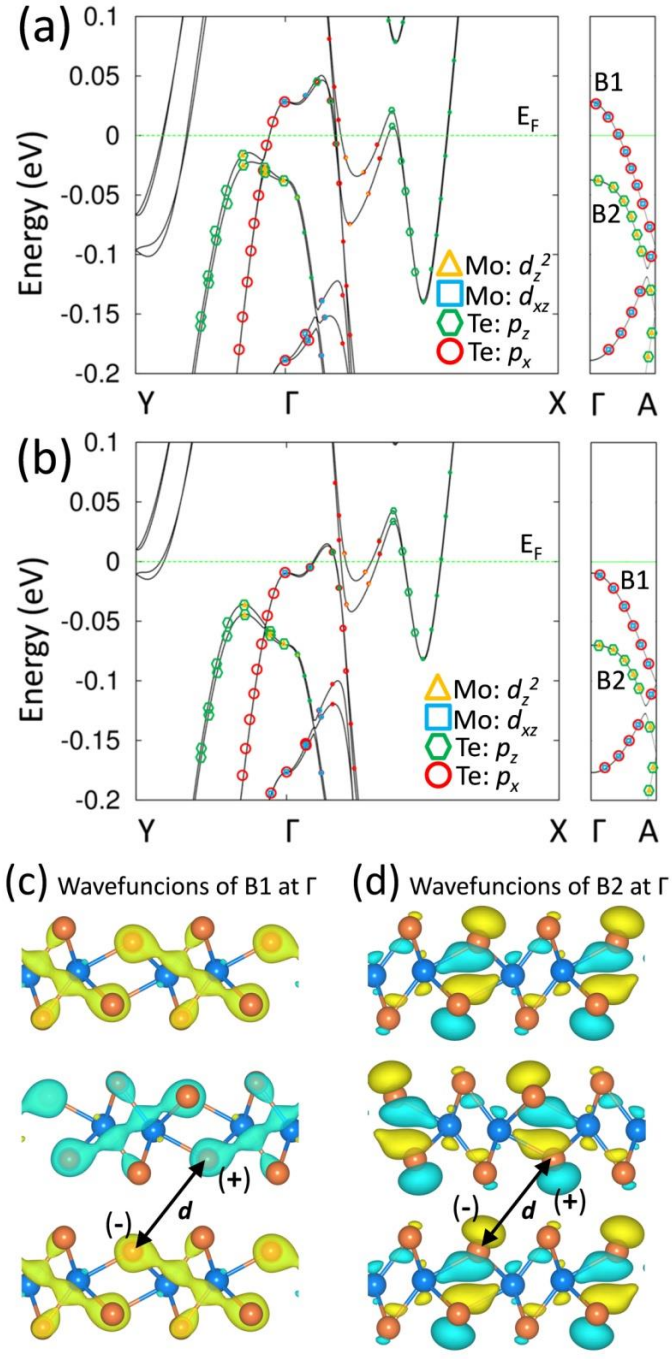

Figure 4.10. DFT calculations for bulk T_d-$MoTe_2$ using two different sets of experimental lattice parameters: (a) averaged experimental lattice parameters from bulk T_d-$MoTe_2$ collected from References 4.6–4.9; and (b) experimental lattice parameters from epitaxial thin films in this work. The bands' projections in the Te and Mo orbitals are shown by the symbols in both (a) and (b). Wavefunctions for valence bands B1 and B2 that correspond to T_d-$MoTe_2$ calculated using the experimental parameters mentioned in this study (set #2) are plotted in (c) and (d), respectively, at the point. The wavefunction (+) and (-) signs are denoted by the colors blue and green, respectively.

The band structure calculations for the four various sets of experimental lattice parameters [4.6-4.9], from which we deduced the average values for Fig. 4.10a, are presented in Fig. 4.11. In contrast to our epitaxial thin films, where the band B is fully occupied (Figure 4.10b), the uppermost valence band B along A whose orbitals are related to antibonding states [4.5] across the interlayer distance is partially unoccupied. This could be the cause of the stabilization of our T_d-$MoTe_2$ at RT. The lattice constants values used in DFT calculations in Fig. 4.11 are (a) a=3.4783 Å, b=6.3563 Å, c=13.8935 Å [4.6], (b) a=3.477 Å, b=6.335 Å, c=13.889 Å [4.7], (c) a=3.468 Å, b=6.310 Å, c=13.861 Å [4.8] and (d) a=3.477 Å, b=6.335 Å, c=13.883 Å [4.9].

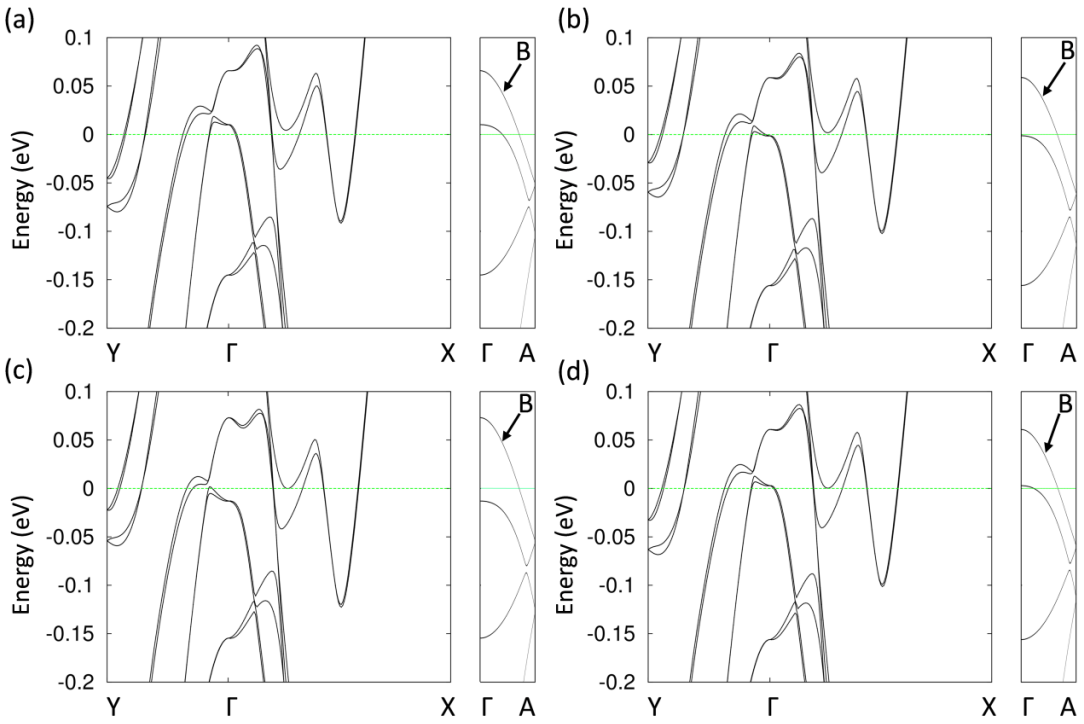

Figure 4.11. Band structure calculations of bulk T_d-$MoTe_2$ (a-d) using four different sets of experimental lattice parameters from Refs. 4.6-4.9, respectively.

4.3. Discussion

In this study, we epitaxially developed the distorted 1T phase of $MoTe_2$ on InAs(111) substrates using MBE. We demonstrate by STEM and synchrotron GIXD that a pure 1T′ $MoTe_2$ phase can be achieved with increased crystallinity following post-growth annealing at 400°C by using an layer-by-layer growth methodology at low temperatures (280°C), which was originally applied to on the MBE grown WTe_2 on HOPG and MoS_2 substrates [4.31]. Although the 2H phase of $MoTe_2$ is more stable at room temperature (RT), a pure 1T′ $MoTe_2$ phase is observed here, which is ascribed to the substrate's

influence due to tensile biaxial strain. It is believed that the shift from the stable 2H to the metastable 1T′ $MoTe_2$ phase at or near RT is caused by tensile strain of between 0.3 and 3% under uniaxial strain, as theoretically predicted [4.5] or 0.2% as experimentally demonstrated [4.11]. In our case, the in-plane *a* and *b* lattice parametersconstants of the epitaxial films are precisely measured by synchrotron GIXD (Fig. 4.6), and it is found that they are larger than those derived in free standing films exfoliated from bulk [4.6, 4.9], indicating a epitaxial tensile strain with $\varepsilon_{xx}=\delta a/a$ ~ +0.1% and $\varepsilon_{yy}=\delta b/b$ ~ +0.7%, Additionally, it has been suggested [4.17] that $MoTe_2$ 2H to 1T transition is induced by electron doping at a rate of 0.1 e^- per unit cell. In our instance, electron doping might be an option since the InAs substrate, which is known to have strong n-type semiconductor characteristics at the surface due to the formation of a dense electron gas [4.48], can provide the electronic charge.

Thin film structures that are difficult to produce under equilibrium conditions can be made via MBE, a technique that is often far from equilibrium. Beyond the impacts of the substrate (strain, doping) already mentioned, the present work's sequential layer growth method allows for a variety of stacking configurations that are not possible with films exfoliated from bulk. A triclinic layer stacking, which presents a fundamental distinction from the normal monoclinic or orthorhombic structures where two successive layers are 180 degrees out of phase, is seen here by STEM (Fig. 4.4). Although not properly emphasized, hints of such in-phase layer stacking are also present in MBE-grown WTe_2 [4.31]. The fact that the significant non-centrosymmetric orthorhombic (T_d) Weyl semimetal phase is here seen by STEM coexisting with the triclinic structure is particularly interesting, despite the fact that the triclinic structure is centrosymmetric with trivial topologyn since no Weyl nodes were found. Questions are raised about the potential cause of this orthorhombic phase's stability at RT as it was discovered in our work because it is normally documented in the literature below 250 K or 150 K. Our ultrathin (1-3 ML) films are not affected directly by the reduced dimensionality analysis that was previously put forth to explain the indirect finding [4.38] of RT T_d-$MoTe_2$ in 12-nm thick films exfoliated from bulk. Our DFT analysis for T_d-$MoTe_2$ (Fig. 4.10) demonstrates that the increased lattice constants of our epitaxial thin films produce a distinctive band structure where the uppermost valence band B along ΓA directions is fully occupied dispersing well below the Fermi level, similar to what has been observed for T_d-WTe_2 [4.21]. The full occupation of this band

in the case of T_d-WTe_2 is related to the lack of an energy barrier for the transition from β the to the T_d-phase [4.21], which explains the stability of T_d-phase at RT. The epitaxial $MoTe_2$ in this research may fall under a similar circumstance. To put it differently, if this fully occupied band B (Fig. 4.10) is associated with an antibonding state [4.21] along the interlayer distance *d* (see Fig. 4.1), the T_d-$MoTe_2$ is preferred since this phase is consistent with an increased *d* ($d_o > d_m$ in Fig. 4.1), as it would be predicted for an antibonding state. Therefore, This analysis demonstrates that the finding of the orthorhombic T_d-$MoTe_2$ phase at RT rather than the monoclinic phase may be explained by the increased lattice constants in the epitaxial thin films.

Since the RT orthorhombic $MoTe_2$ presented here lacks inversion symmetry, a topological Weyl semimetal is what is anticipated. A DFT study of the T_d-$MoTe_2$ using the increased experimental lattice parameters reported in this work predicts 8 type-II Weyl nodes that are located just below the Fermi level and very close to it, which is a major difference from earlier findings that found all Weyl points to be located above the E_F (Fig. 4.8). In order to create devices that could take advantage of the non-trivial topological properties of these films in real-world RT applications, epitaxial thin films of T_d-$MoTe_2$ on InAs substrates can be used. The Fermi level position near the Weyl nodes makes them accessible in ARPES band imaging and to transport measurements.

Future research should concentrate on enhancing these films' epitaxial quality. Although the $MoTe_2$ and InAs substrate exhibit excellent in-plane epitaxial alignment, as shown in Fig. 4.6, with $[100]_{MoTe2}//[11\bar{2}]_{InAs}$, and $[010]_{MoTe2}//[01\bar{1}]_{InAs}$, the in-plane mosaicity of 3.71° is significantly higher than the InAs one (0.79°) and higher than the 1.79° mosaicity of epitaxial $ZrTe_2$ on InAs [4.39]. Additionally, the $MoTe_2$ epilayer, like $ZrTe_2$ [4.39], adapts to the InAs surface's topography (STEM in Fig. 4.4), which displays monatomic steps of 3.5 Å. This results in a $MoTe_2$ nanostructure with domain sizes in the order of a few tens of nm, as also visible by STM in Fig. 4.3. STM, RHEED, and GIXD data clearly demonstrate the presence of 60 and 120° rotated domains, which is a distinguishing feature of our thin epitaxial films compared to single crystals derived from bulk where such domains are lacking. While these rotated domains in a hexagonally undistorted 1T or 2H $MoTe_2$ structure are equivalent, they produce a complex *k*-space and Brillouin zone in 1T $MoTe_2$, mixing the energy dispersion along different directions and adversely affecting resolution, making it difficult to observe the Weyl node configuration in ARPES clearly. At the step edges, where the continuity of

the film may also be disrupted (Fig. 4.4), domain rotation may be enhanced, which could be detrimental for electrical transport. In an effort to produce a single crystalline epitaxial film, we may be able to reduce the density of monatomic steps and increase the domain size by enhancing the surface treatment of InAs prior to development. Although the use of single crystal InAs(111) could address some of the problems associated with step and domain formation and enhance the mosaicity of $MoTe_2$, the effort should instead concentrate on improving epitaxial InAs on Si substrates because the future manufacture of $MoTe_2$ and other 2D materials will depend on the availability of large area wafers.

4.4. Conclusions

In this study, $MoTe_2$ epitaxial thin films with distorted 1T′ structures are produced on InAs(111)/Si(111) substrates using molecular beam epitaxy. Despite the presence of 60^o and 120^o rotational domains, the films are rotationally consistent with the substrate, allowing for the observation of $[100]_{MoTe2}//[11\bar{2}]_{InAs}$ and $[010]_{MoTe2}//[01\bar{1}]_{InAs}$ by RHEED, STM and synchrotron GIXD. We find two distinct phases coexisting in the layer using STEM cross sectional measurements in 3 ML $MoTe_2$. In the first phase, an orthorhombic (T_d) stacking (or γ-$MoTe_2$) can be seen, while in the second phase, a previously unreported triclinic stacking is visible. From GIXD and STEM, we measure lattice parameter values a=6.340 Å, b=3.501 Å, and out of plane parameter for the orthorhombic T_d-phase c=14.1–14.2 Å that are bigger than free standing thin films exfoliated from bulk as a result of the substrate's effect.

Because of the larger lattice constants of our epitaxial thin films, the $MoTe_2$ orthorhombic T_d-phase, which is generally seen at temperatures lower than 250 K, is detected here at room temperature. This is attributable to an interlayer antibonding state consistent with the orthorhombic T_d-phase. An orthorhombic type-II Weyl semimetal phase is obtained by the orthorhombic Td-non-centrosymmetric $MoTe_2$ structure. Eight Weyl nodes predicted by DFT that are accessible to transport are a few meV below the Fermi level, opening the door for room temperature electronic applications, where the topologically non-trivial characteristics of $MoTe_2$ epitaxial films could be beneficial.

References

[4.1] S. Manzeli, D. Ovchinnikov, D. Pasquier, O. V. Yazyev, A. Kis,Nat. Rev. Mater. 2017,2, 17033.

[4.2] W. Choi, N. Choudhary, G. H. Han, J. Park, D. Akinwande, Y. H. Lee, Mater. Today 2017, 20, 116-130.

[4.3] D. L. Duong, S. J. Yun, Y. H. Lee, ACS Nano 2017,11, 11803.

[4.4] H. Yang, S. W. Kim, M. Chhowalla, Y. H. Lee, Nat. Phys. 2017,13, 931–937.

[4.5] K.-A. N. Duerloo, Y. Li, E. J. Reed, Nat. Commun. 2014, 5, 4214.

[4.6] R. Sankar, G. N. Rao, I. P. Muthuselvam, C. Butler, N. Kumar, G. S. Murugan, C. Shekhar, T.- R. Chang, C.- Y. Wen, C.- W. Chen, W.- L. Lee, M.- T. Lin, H.- T. Jeng, C. Felser, F. C. Chou, Chem. Mater. 2017, 29, 699-707.

[4.7] Y. Qi, P. G. Naumov, M. N. Ali, C. R. Rajamathi, W. Schnelle, O. Barkalov, M. Hanfland, S.- C. Wu, C. Shekhar, Y. Sun, V. Süő, M. Schmidt, U. Schwarz, E. Pippel, P. Werner, R. Hillebrand, T. Förster, E. Kampert, S. Parkin, R. J. Cava, C. Felser, B. Yan, S. A. Medvedev, Nat. Commun. 2017, 7, 11038.

[4.8] A. Tamai, Q. S. Wu, I. Cucchi, F. Y. Bruno, S. Riccò, T. K. Kim, M. Hoesch, C. Barreteau, E. Giannini, C. Besnard, A.A. Soluyanov, F. Baumberger,Phys. Rev. X 2016, 6, 031021.

[4.9] J. Jiang, Z. K. Liu, Y. Sun, H. F. Yang, C. R. Rajamathi, Y. P. Qi, L. X. Yang, C. Chen, H. Peng, C.- C. Hwang, S. Z. Sun, S.- K. Mo, I. Vobornik, J. Fujii, S.S.P. Parkin, C. Felser, B. K. Yan, Y. L. Chen, Nat. Commun. 2017, 8, 13973.

[4.10] J. Seok, J.- H. Lee, S. Cho, B. Ji, H. W. Kim, M. Kwon, D. Kim, Y.- M. Kim, S. H. Oh, S. W. Kim, Y. L. Lee, Y.- W. Son, H. Yang, 2D Mater. 2017, 4, 025061.

[4.11] S. Song, D. H. Keum, S. Cho, D. Perello, Y. Kim, Y. Lee,Nano Lett.2015,16, 188.

[4.12] Y. Wang, J. Xiao, H. Zhu, Y. Alsaid, K. Y. Fong, Y. Zhou, S. Wang, W. Shi, Y. Wang, A. Zettl, E. J. Reed, X. Zhang, Nature 2017, 550, 487.

[4.13] X. Qian, J. Liu, L. Fu, J. Li, Science 2014, 346, 1344.

[4.14] S. Tang, C. Zhang, D. Wong, Z. Pedramrazi, H.- Z. Tsai, C. Jia, B. Moritz, M. Claassen, H. Ryu, S. Kahn, J. Jiang, H. Yan, M. Hashimoto, D. Lu, R. G. Moore, C.- C. Hwang, C. Hwang, Z. Hussain, Y. Chen, M. M. Ugeda, Z. Liu, X. Xie, T. P. Devereaux, M. F. Crommie, S.- K. Mo, Z.- X. Shen, Nat. Phys. 2017, 13, 683.

[4.15] A. A. Soluyanov, D. Gresch, Z. Wang, Q. S. Wu, M. Troyer, X. Dai, B. A. Bernevig, Nature 2015, 527, 495.

[4.16] Y. Wu, D. Mou, N. H. Jo, K. Sun, L. Huang, S. L. Bud'ko, C. Canfield, A. Kaminski, Phys. Rev B 2016, 94, 121113 (R).

[4.17] D. H. Keum, S. Cho, J. H. Kim, D.- J. Choe, H.- J. Sung, M. Kan, H. Kang, J.- Y. Hwang, S. W. Kim, H. Yang, K. J. Chang, Y. H. Lee, Nat. Phys. 2015, 11, 482.

[4.18] Y. Sun, S.-C. Wu, M. N. Ali, C. Felser, B Yan, Phys. Rev B 2015, 92, 161107 (R).

[4.19] L. Huang, T. M. McCormick, M. Ochi, Z. Zhao, M.- T. Suzuki, R. Arita, Y. Wu, D. Mou, H. Cao, J. Yan, N. Trivedi, A. Kaminski, Nat. Mater. 2016, 15, 1155.

[4.20] K. Deng, G. Wan, P. Deng, K. Zhang, S. Ding, E. Wang, M. Yan, H. Huang, H. Zhang, Z. Xu, J. Denlinger, A. F., H. Yang, W. Duan, H. Yao, Y. Wu, S., H. Zhang, X. Chen, S. Zhou, Nat. Phys. 2016, 12, 1105.

[4.21] H.- J. Kim, S.- H. Kang, I. Hamada, Y.- W. Son, Phys. Rev. B 2017, 95, 180101 (R).
[4.22] A. Crepaldi, G. Autès, G. Gatti, S. Roth, A. Sterzi, G. Manzoni, M. Zacchigna, C. Cacho, R. T. Chapman, E. Springate, E. A. Seddon, Ph. Bugnon, A. Magrez, H. Berger, I. Vobornik, M. Kalläne, A. Quer, K. Rossnagel, F. Parmigiani, O. V. Yazyev, M. Grioni, Phys. Rev. B 2017, 96241408 (R).
[4.23] Z. Wang, D. Gresch, A. A. Soluyanov, W. Xie, S. Kushwaha, X. Dai, M. Troyer, R. J. Cava, B. A. Bernevig, Phys. Rev. Lett. 2016, 117, 56805.
[4.24] F. Y. Bruno, A. Tamai, Q. S. Wu, I. Cucchi, C. Barreteau, A. de la Torre, S. M. Walker, S. Riccò, Z. Wang, T. K. Kim, M. Hoesch, M. Shi, N. C. Plumb, E. Giannini, A. A. Soluyanov, F. Baumberger, Phys. Rev. B 2016, 94, 121112 (R).
[4.25] C. Wang, Y. Zhang, J. Huang, S. Nie, G. Liu, A. Liang, Y. Zhang, B. Shen, J. Liu, C. Hu, Y. Ding, D. Liu, Y. Hu, S. He, L. Zhao,L. Yu, J. Hu, J. Wei, Z. Mao, Y. Shi, X. Jia, F. Zhang, S. Zhang, F. Yang, Z. Wang, Q. Peng, H. Weng, X. Dai, Z. Fang, Z. Xu, C. Chen, X. J. Zhou ,Phys. Rev. B 2016, 94, 241119 (R).
[4.26] Belopolski,D. S. Sanchez, Y. Ishida, X. Pan, P. Yu, S.-Y. Xu, G. Chang, T.-R. Chang, H. Zheng, N. Alidoust, G. Bian, M. Neupane, S.-M. Huang, C.-C. Lee, Y. Song, H. Bu, G. Wang, S. Li, G. Eda, H.-T. Jeng, T. Kondo, H. Lin, Z. Liu, F. Song, S. Shin, M. Z. Hasan, Nat. Commun. 2016, 7, 13643.
[4.27] Belopolski, S.-Y. Xu, Y. Ishida, X. Pan, P. Yu, D. S. Sanchez, H. Zheng, M. Neupane, N. Alidoust, G. Chang, T.-R. Chang, Y. Wu, G. Bian, S.-M. Huang, C.-C. Lee, D. Mou, L. Huang, Y. Song, B. Wang, G. Wang, Y.-W. Yeh, N. Yao, J. E. Rault, P. L. Fevre, F. Bertran, H.-T. Jeng, T. Kondo, A. Kaminski, H. Lin, Z. Liu, F. Song, S. Shin, M. Z. Hasan, Phys. Rev. B 2016, 94, 085127.
[4.28] L. Zhu, K. Xu, A. Zubair, A. D. Liao, W. Fang, F. Ouyang, Y. -H. Lee, K. Ueno, R. Saito, T. Palacios, J. Kong, M. S. Dresselhaus, J. Am. Chem. Soc. 2015, 137, 11892.
[4.29] C. H. Naylor, W. M. Parkin, J. Ping, Z. Gao, Y. R. Zhou, Y. Kim, F. Streller, R. W. Carpick, A. M. Rappe, M. Drndić, J. M. Kikkawa, A. T. C. Johnson, Nano Lett. 2016, 16, 4297.
[4.30] T. A. Empante, Y. Zhou, V. Klee, A. E. Nguyen, I.- H. Lu, M. D. Valentin, S. A. N. Alvillar, E. Preciado, A. J. Berges, C. S. Merida, M. Gomez, S. Bobek, M. Isarraraz, E. J. Reed, L. Bartels, ACS Nano 2016, 11, 900.
[4.31] L. A. Walsh, R. Yue, Q. Wang, A. T. Barton, R. Addou, C. M. Smyth, H. Zhu, J. Kim, L. Colombo, M. J. Kim, R. M. Wallace, C. L. Hinkle, 2D Mater. 2017, 4, 025044.
[4.32] H. C. Diaz, R. Chaghi, Y. Ma, M. Batzill, 2D Mater. 2015, 2, 044010.
[4.33] A. Roy, H. C. P. Movva, B. Satpati, K. Kim, R. Dey, A. Rai, T. Pramanik, S. Guchhait, E. Tutuc, S. K. Banerjee, ACS Appl. Mater. Interfaces 2016, 8, 7396–7402.
[4.34] S. Vishwanath, A. Sundar, X. Liu, A. Azcatl, E. Lochocki, A. R. Woll, S. Rouvimov, W. S. Hwang, N. Lu, X. Peng, H.-H. Lien, J. Weisenberger, S. McDonnell, M. J. Kim, M. Dobrowolska, J. K. Furdyna, K. Shen, R. M. Wallace, D. Jena, H. G. Xing, J. Cryst. Growth 2018, 482, 61 (2018).
[4.35] Y. Yu, G. Wang, S. Qin, N. Wu, Z. Wang, K. He, X. -A. Zhang, Carbon 2017, 115, 256.
[4.36] S. Tang, C. Zhang, C. Jia, H. Ryu, C. Hwang, M. Hashimoto, D. Lu, Z. Liu, T. P. Devereaux, Z.- X. Shen, S.- K. Mo, APL Mater. 2018, 6, 026601.
[4.37] D. Rhodes, D. A. Chenet, B. E. Janicek, C. Nyby, Y. Lin, W. Jin, D. Edelberg, E. Mannebach, N. Finney, A. Antony, T. Schiros, T. Klarr, A. Mazzoni, M.

Chin, Y.-C. Chiu, W. Zheng, Q. R. Zhang, F. Ernst, J. I. Dadap, X. Tong, J. Ma, R. Lou, S. Wang, T. Qian, H. Ding, R. M. Osgood Jr., D. W. Paley, A. M. Lindenberg, P. Y. Huang, A. N. Pasupathy, M. Dubey, J. Hone, L. Balicas, Nano Lett. 2017, 17, 1616.

[4.38] R. He, S. Zhong, H. H. Kim, G. Ye, Z. Ye, L. Winford, D. McHaffie, I. Rilak, F. Chen, X. Luo, Y. Sun, A. W. Tsen, Phys. Rev B 2018, 97, 041410 (R).

[4.39] P. Tsipas, D. Tsoutsou, S. Fragkos, R. Sant, C. Alvarez, H. Okuno, G. Renaud, R. Alcotte, T. Baron, A. Dimoulas, ACS Nano 2018, 12, 1696-1703.

[4.40] G. Kresse, J. Furthmuller, Comput. Mater. Sci. 1996, 6, 15–50.

[4.41] G. Kresse, J. Furthmuller, Phys. Rev. B 1996, 54, 11169–11186.

[4.42] P. E. Blöchl, Phys. Rev. B 1994, 50, 17953–17979.

[4.43] P. Perdew, K. Burke, M. Ernzerhof, Phys. Rev. Lett. 1996, 77, 3865–3868.

[4.44] H. Monkhorst, J. Pack, Phys. Rev. B 1976, 13, 5188–5192.

[4.45] S. Grimme, J. Antony, S. Ehrlich, S. A. Krieg, J. Chem. Phys. 2010, 132, 154104.

[4.46] A. A. Mostofi, J. R. Yates, Y.- S. Lee, I. Souza, D. Vanderbilt, N. Marzari, Comput. Phys. Commun. 2014, 185, 2309.

[4.47] Q. S. Wu, S. N. Zhang, H.- F. Song, M. Troyer, A. A. Soluyanov, Comput. Phys. Commun. 2018, 224, 405-416.

[4.48] L. Ö. Olsson, C. B. M. Andersson, M. C. Håkansson, J. Kanski, L. Ilver, U. O. Karlsson, Phys. Rev. Lett. 1996, 76, 3626–3629.

5. Topological Dirac semimetals in group IV transition metal ditelluride family

5.1. Introduction

Dirac-like cones with linear dispersion can be seen in all three dimensions in k-space in topological 3D Dirac semimetals (DSMs) and Weyl semimetals (WSMs), which are frequently referred to as "3D graphenes" [5.1]. DSMs are divided into two categories: type-I DSM, which has an untilted or slightly tilted Dirac cone and a Fermi surface that resembles a point, or type-II DSM [5.1]. The latter situation results in an overtilted Dirac cone and a finite Fermi surface made up of electron and hole pockets that cross at the Dirac point (DP) (Fig. 5.1). However, a type-III DSM [5.2-5.4] merges theoretically as a possibility just at the intersection of type-I and type-II, and it is distinguished by a unique Fermi surface that resembles a line and a flat energy dispersion along one direction of the Brillouin zone (BZ) (Fig. 5.1).

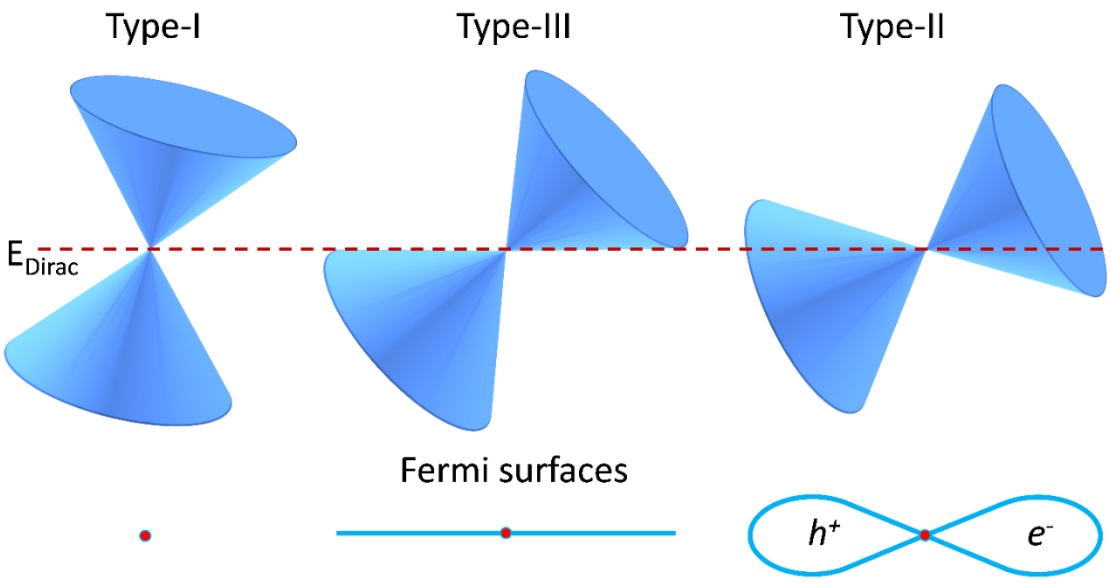

Figure 5.1. Schematic illustration of the different types of DSMs. Type-III is located at the border between type-I and type-II, characterized by a flat energy dispersion at the Fermi level and a line-like Fermi surface.

The position of the Fermi level in relation to the energy degeneracy points (Dirac Points) of the DSM/WSM has a significant impact on the Fermi surface topology. Under the effect of external stimuli, the system might experience a topological (Lifshitz) phase transition close to the Dirac point [5,6]. (e.g., temperature, pressure etc.). The Fermi surface topology can vary significantly at the critical conditions for the

transition [5.7–5.10], which has significant ramifications for electrical and thermoelectric transport. A temperature-driven Lifshitz transition from a hole-like to an electron-like Fermi surface is most frequently seen [5.7]; examples include $ZrTe_5$ [5.7, 5.8] and $HfTe_5$ [5.9], which is accompanied with resistivity and thermopower anomalies at the critical temperature. In TaP and TaAs WSMs, an anomalous Nernst effect that has been linked to a topological Lifshitz transition has also been noted [5.10]. In a type-III DSM, a very different Lifshitz transition is anticipated. The system is capable of easily switching from a type-I to type-II DSM, which is accompanied by a significant change in the Fermi surface's configuration from a point-like to a needle-like one. This transition is also likely accompanied by changes in resistivity and thermopower, as was the case with $ZrTe_5$ [5.8]. There is a significant motivation to search for type-III DSMs (and WSMs) because the latter alterations might be accessible to (thermo)electric transport studies. The extraordinary predictions [5.2, 5.3] that type-III DSMs, such as black phosphorous [5.11] and $Zn_2In_2S_5$ [5.12], may be the solid state (or fermionic) equivalent of the black hole event horizon, potentially generating "Hawking radiation" at relatively high "Hawking temperatures" [5.2], showing promise for new exotic physics and applications, are another driving force behind this search. Although a type-III Dirac crossover was previously solely a theoretical possibility, experimental evidence has recently been found in artificial photonic orbital graphene lattices [5.14] as well as in strained epitaxial SnTe [5.13], between its two highest valence bands, 1.83 eV below the Fermi level.

Standard topological Dirac semimetals are three-dimensional (3D) crystal structures that are often formed as bulk crystals [5.15, 5.16]. These materials frequently include heteroepitaxial defects that result in discontinuous films with inferior crystalline quality. By creating thin epitaxial films and devices using van der Waals epitaxy on suitable substrates, the discovery and engineering of topological semimetals from the family of two-dimensional transition metal dichalcogenides (TMDs) could pave the way for the use of their topological features. The first experimental proof that the few layer 1T-$HfTe_2$ [5.17] and 1T-$ZrTe_2$ [5.18] epitaxially formed by molecular beam epitaxy (MBE) are 3D DSMs is presented in earlier studies from our team [5.17, 5.18]. More specifically, we found that, contrary to theory, which predicts the DP to be well above the Fermi level, linearly dispersing bands along the ΓK and ΓM

directions in the plane of the film cross at the Fermi level, indicating the existence of Dirac fermions even down to the ultimate 2D limit of 1 ML.

The possibility of topological characteristics in $HfTe_2$ and $ZrTe_2$ is still an open subject. In contrast to the epitaxially grown films [5.17, 5.18], synchrotron ARPES studies on single crystals of K and Cr doped $HfTe_2$ and $ZrTe_2$ respectively show no clear signs of Dirac-like features, while others, by combining synchrotron ARPES [5.22] on 1T-$ZrTe_2$ single crystals with DFT calculations, suggest that $ZrTe_2$ is a DSM. As a result of the aforementioned debate, it is determined that doping by intercalation significantly alters both the crystal and electrical structure of these materials, and it is therefore impossible to rule out a change in the topological features of $HfTe_2$ and $ZrTe_2$. Despite the debate, there is mounting proof that these materials have non-trivial topology. $HfTe_2$ [5.23] and $ZrTe_2$ [5.24, 5.25] are both topological materials, according to magnetotransport experiments. In addition, $HfTe_2$ and $ZrTe_2$ are both predicted to be topological semimetals by a recent theoretical study [5.26], which makes use of a recently created formalism known as topological quantum chemistry [5.27]. But take note that some [5.28, 5.29] classified $ZrTe_2$ as a topological crystalline insulator while $HfTe_2$ as a DSM. $ZrTe_2$ and $HfTe_2$ are two examples of topological materials with a wide range of uses. Due to their electronic band structure and strong spin-orbit coupling, several of these materials have significant spin Berry curvature. They are therefore good candidates for charge to spin conversion in coupled topological and ferromagnet spin orbit torque (SOT) devices due to their substantial spin hall conductivity [5.30, 5.31]. This could result in the adoption of all electrically powered SOT spintronic devices for data processing and storage. It is anticipated that the energy efficiency for charge to spin conversion will increase when two-dimensional TMDs replace heavy metals like Pt or Ta that are normally employed in SOT devices [5.31]. The WTe_2/permalloy system has previously had this proven [5.32]. Similar trends may be observed in other ditellurides, such as $HfTe_2$ and $ZrTe_2$, demonstrating their applicability for spintronics applications. Similar to this, a recent study [5.24] finds an anomalous hall effect of $ZrTe_2$ in close proximity to a magnetic material, which could be interpreted as evidence that a quantum anomalous Hall effect (QAHE), as anticipated for topological/ferromagnetic material combinations, is feasible in this system. This creates the opportunity to design energy-efficient spintronic devices free of a magnetic field by utilizing the dissipationless chiral edge states of a QAHE system. According to

a different viewpoint [5.33], monolayer 1T-$HfTe_2$ nanosheets are expected to be highly selective for the detection of environmentally dangerous NO gas, which is also involved in a number of physiological processes. As a result, these nanosheets may find significant use in the fields of medicine and the environment.

$HfTe_2$ and $ZrTe_2$ are type-I and type-II DSMs, respectively, according to our first-principles calculations in this work. Therefore, there is a chance that by alloying the two materials, a new $Hf_xZr_{1-x}Te_2$ type-III DSM material will develop. A type-III Dirac cone with a line-like Fermi surface is anticipated to occur at a Hf concentration of 20% in combination with an in-plane compressive strain of 1% after a comprehensive examination of $Hf_xZr_{1-x}Te_2$ energy bands as a function of composition and strain. Furthermore, we give experimental proof that the top of the type-III Dirac cone is at - or very close to - the Fermi level by using in situ ARPES to image the electronic energy bands of this layered compound at the appropriate composition x=0.2, grown by MBE on InAs(111) substrate.

5.2. First-principles calculations

Both $HfTe_2$ and $ZrTe_2$ are members of the 2D layered 1T octahedral family with space group $P\bar{3}m1$ (No. 164). To demonstrate the topological nature of the Dirac cones in these materials, we perform ab initio calculations of electronic structure and carry out symmetry analysis. Vienna Ab-initio Simulation Package (VASP) [5.34, 5.35] was used for the first-principles calculations. As exchange-correlation functional the generalized-gradient approximation with Perdew–Burke–Ernzerhof (PBE) [5.36] parameterization was used. Instead of using the equilibrium lattice constants from DFT calculations, our analysis of the electronic band structure is based on the experimental lattice constants from References [5.17] and [5.18], which were obtained by synchrotron x-ray diffraction. The reciprocal space was sampled using the Monkhorst–Pack scheme [5.37] employing a $11 \times 11 \times 7$ *k*-point mesh and the kinetic energy cutoff was set at 500 eV. Spin-orbit coupling (SOC) was introduced in the band structure calculations. We used Hf *d* orbitals, Zr *d* orbitals, and Te *p* orbitals to construct Wannier functions using the *Wannier90* code [5.38, 5.39] and the band structures and Fermi surfaces were obtained by the *WannierTools* software [5.40].

5.2.1. Electronic band structure of $HfTe_2$ and $ZrTe_2$

The topology of the VASP wavefunctions was investigated, and irreducible representations at the high-symmetry sites were calculated using the VASP2Trace programme [5.26]. From the BANDREP program [5.27, 5.41, 5.42] of the Bilbao Crystallographic Server, it was possible to infer the decomposition of these irreducible representations for both $HfTe_2$ and $ZrTe_2$, moving in the ΓA direction. Due to the fact that the two bands are members of different irreducible representations (Fig. 5.2a,b), which prevent hybridization and gap opening, gapless crossings occur. The consequence is the generation of two fourfold degenerate Dirac nodes that are protected by C_3 rotational symmetry along the c axis [5.43] at $(0,0,\pm 0.036c^*)$ and $(0,0,\pm 0.228c^*)$, respectively, for $HfTe_2$ and $ZrTe_2$. A pair of DPs is defined by the crossings, which are produced by band inversion [5.43] at points that are symmetrically positioned with respect to Γ along Γ-A (k_z) direction of the BZ. The electronic band structures around the DPs are shown in the k_z-k_x plane in Figs. 5.2c,d.

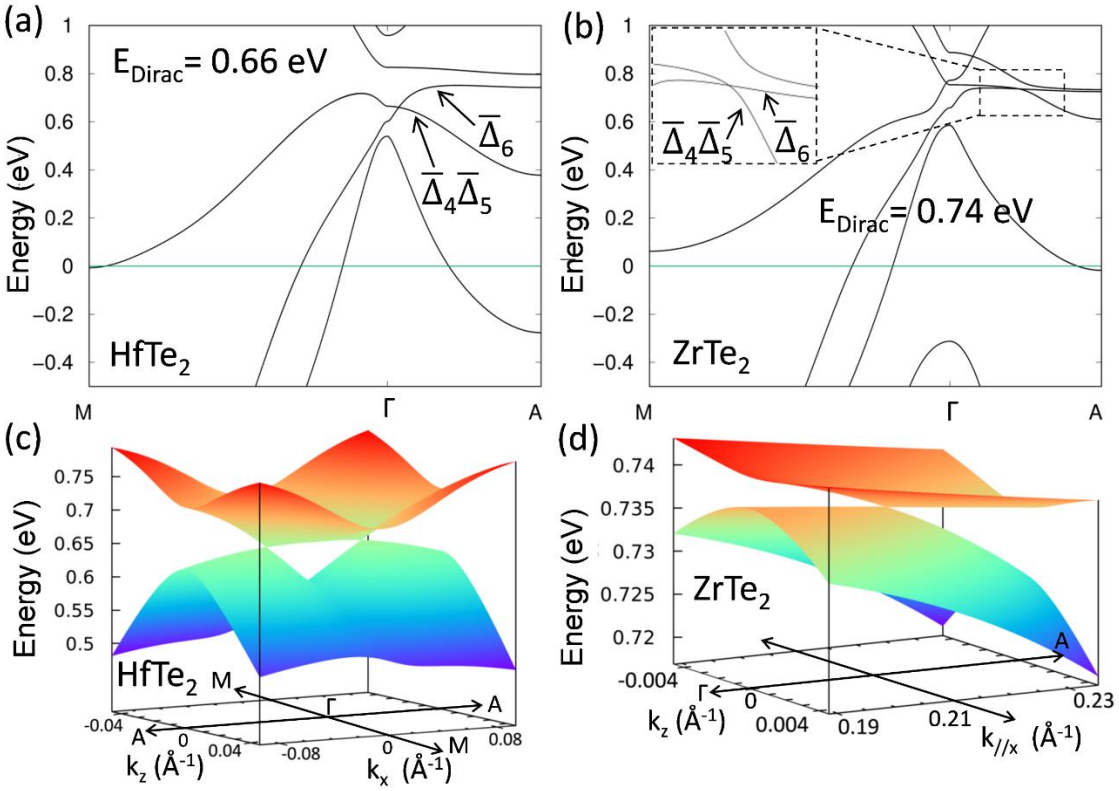

Figure 5.2. Electronic band structure of (a) $HfTe_2$ and (b) $ZrTe_2$ along the MΓA direction of the Brillouin zone, where conduction and valence bands cross each other, since they belong to different irreducible representations. (c) and (d) show the energy dispersion in the k_z-k_x plane near the crossings for $HfTe_2$ and $ZrTe_2$, respectively.

Fig. 5.3 displays additional computations of the 2D and 3D Fermi surfaces. In the case of $HfTe_2$, a point-like Fermi surface (inset in Fig. 5.3a,c) characteristic to a type-I Dirac semimetal is shown by placing the chemical potential at the position of the Dirac points. However, in the case of $ZrTe_2$ (Fig. 5.3b and 5.3d), needle-like electron and hole pockets form and meet at the DP, proving $ZrTe_2$ is a type-II DSM.

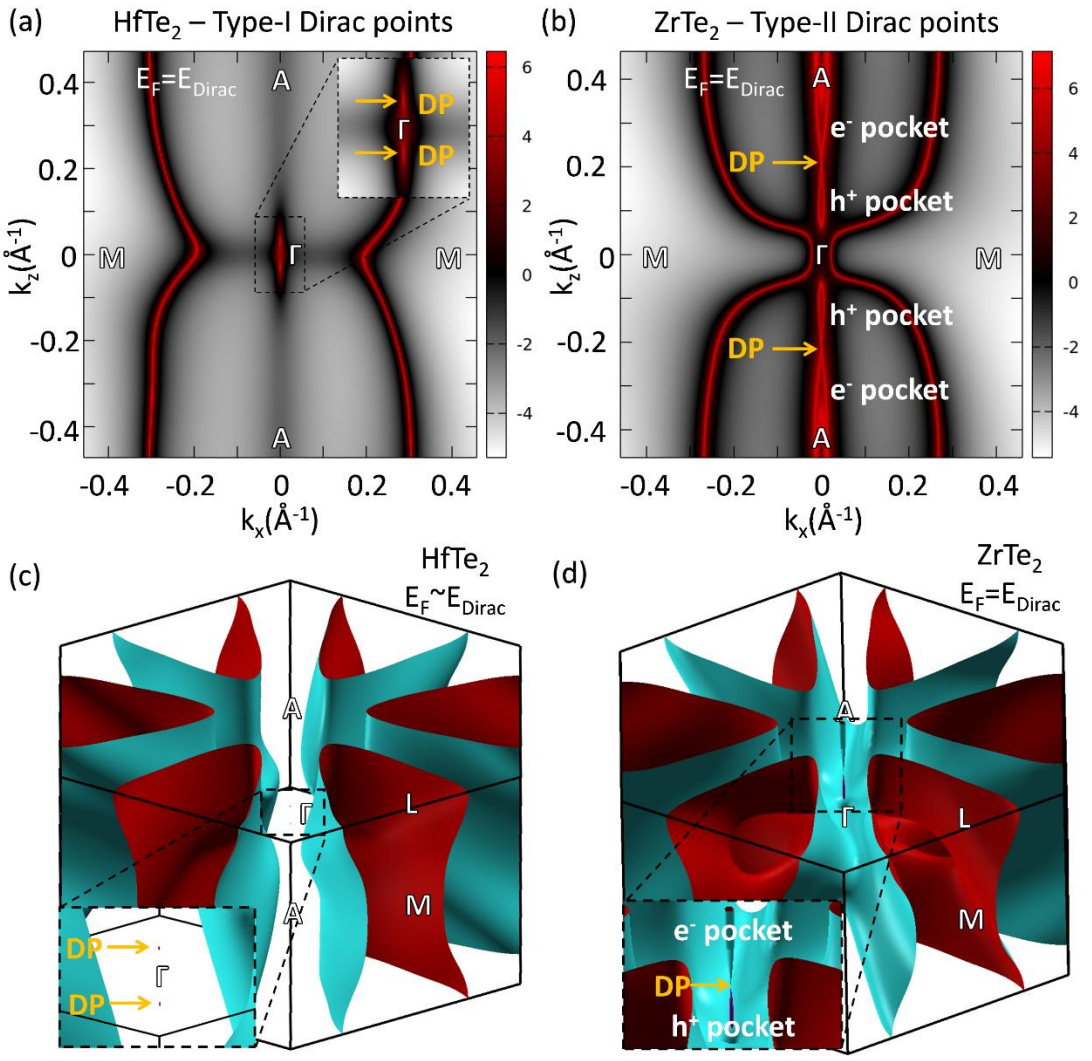

Figure 5.3. The 2D (a,b) and 3D (c,d) Fermi surface of $HfTe_2$ and $ZrTe_2$ by setting the chemical potential at the DP energy. The point-like features in the inset of (c) indicate a type-I DSM for $HfTe_2$. The needle-like e^- and h^+ pockets in $ZrTe_2$ [inset of (d)] define the DP at the touching point revealing type-II DSM behaviour.

The three-dimensional DPs are achiral since they are the sum of two Weyl nodes with opposite chirality at the same energy and momentum, hence unlike Weyl semimetals, they do not possess Berry phase nor Berry curvature. In the Brillouin zone, the topological charge is therefore zero all across momentum space. Dirac semimetals, in contrast to Weyl semimetals, are additionally only protected by underlying

crystallographic symmetries, or else, they become gapped. In our situation, the C_3 rotational symmetry fulfills this purpose.

5.2.2. The $Hf_{0.2}Zr_{0.8}Te_2$ type-III Dirac semimetal state

A new $Hf_xZr_{1-x}Te_2$ material with a type-III Dirac cone and a line-like Fermi surface could be formed by alloying the two materials ($HfTe_2$ and $ZrTe_2$). The electronic band structure of the $Hf_xZr_{1-x}Te_2$ alloy was calculated by a linear interpolation of tight-binding model matrix elements [5.44-5.46] of $HfTe_2$ and $ZrTe_2$ of the form $t_{ij,Hf_xZr_{1-x}Te_2} = x \cdot t_{ij,HfTe_2} + (1-x) \cdot t_{ij,ZrTe_2}$, generated by the *Wannier90* code [5.38, 5.39], where x is the Hf concentration, and since the crystal structures of the two materials are substantially similar, the experimental lattice constants from Ref. [5.18] were applied. The suggested method might be sensitive to a potential asymmetry in the radii of Zr and Hf. However, as Hf and Zr have van der Waals radii [5.47] of 2.53 and 2.52 Å, respectively, their difference is insignificant. In addition, Hf and Zr have the same value of 1.614 Å if we take into account the Wigner-Seitz radii offered by the PBE pseudopotentials [5.36]. The empirical atomic radii with a value of 1.55 Å [5.48] also support this. As a result, the radii of Hf and Zr are very similar, and we don't anticipate any significant size asymmetries that would have a negative impact on our calculations. Everything necessary for an interpolation to account for all changes in the electronic structure between the two end point materials is contained in tight-binding elements [5.44–5.46]. This method is appropriate and reliable for computing the alloys of topological materials since Wannier functions are crucial for the study and identification of topological materials [5.26, 5.27, 5.49-5.52]. The electronic band structure of the transition metal dichalcogenide $Mo_xW_{1-x}Te_2$ topological WSM [5.46] and the topological insulator $BiTlSe_{1-x}S_x$ was previously studied using the same method, and the results were in excellent agreement with their ARPES measurements.

A comprehensive examination of $Hf_xZr_{1-x}Te_2$ energy bands in relation to composition was conducted (Fig. 5.4a). The valence band surrounding the crossing point cannot be entirely flattened by Hf doping. The slope dE/dk = -0.001 eV/ $Å^{-1}$ that is produced by the optimum value of x = 0.2 is quite close to the ideal slope for a type-III crossing. As a result, we applied an in-plane compressive strain (Fig. 5.4b), which caused the film to expand out of plane, weakening the interaction between the layers and flattening the bands in the Γ-A direction.

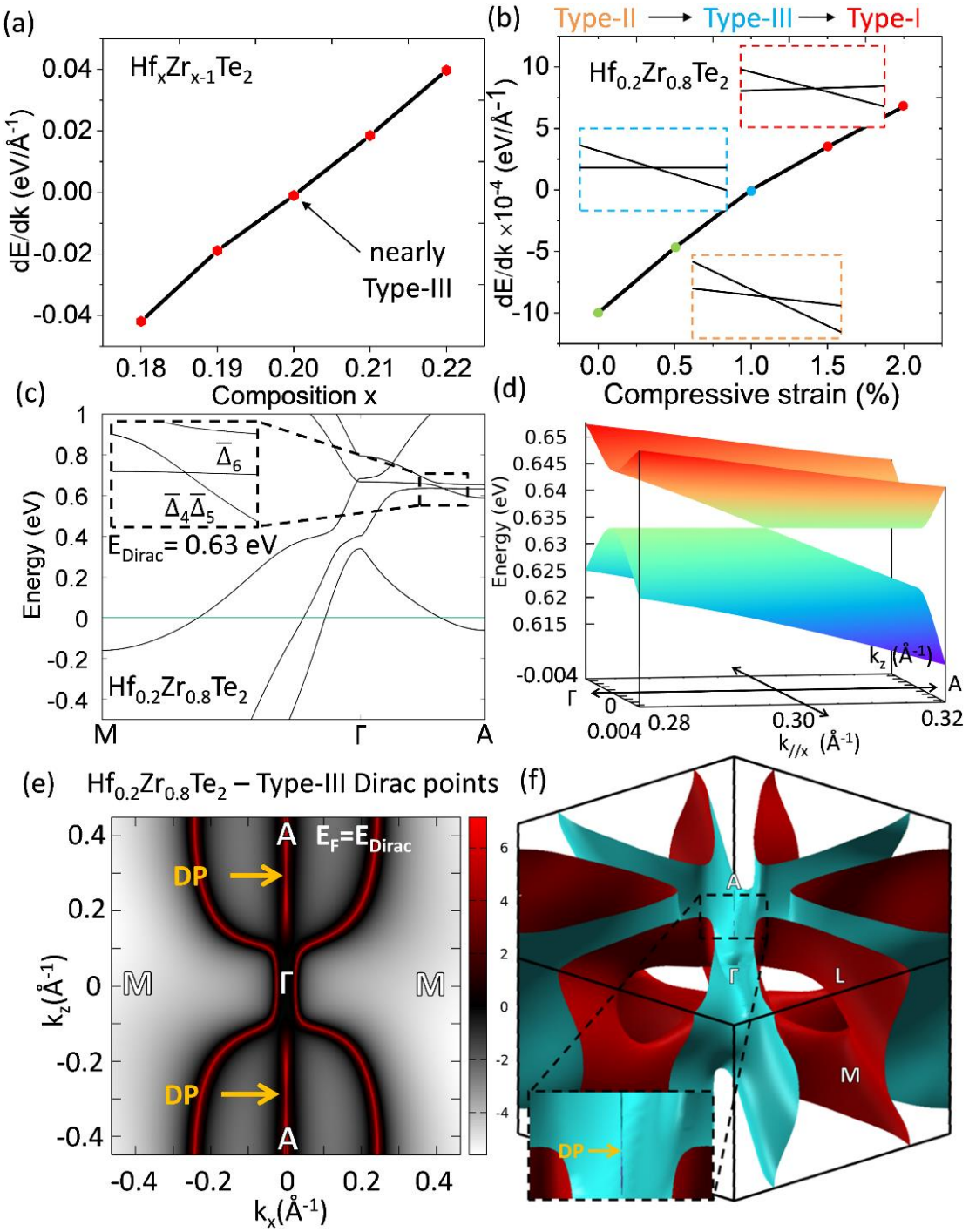

Figure 5.4. (a) Systematic investigation of $Hf_xZr_{1-x}Te_2$ energy bands as a function of composition *x* and (b) of compressive strain, where the red, blue and orange insets show the evolution of the Dirac cone. (c) Electronic band structure of $Hf_{0.2}Zr_{0.8}Te_2$ with 1% in-plane compressive strain along the MΓA direction. The inset shows the type-III band crossing between conduction and valence bands forming a line-like Fermi surface. (d) The 3D band structure near the type-III DP. (e) and (f) the 2D and 3D Fermi surfaces of $Hf_{0.2}Zr_{0.8}Te_2$, respectively.

More specifically, by applying 1% in-plane compressive strain, the $\bar{\Delta}_6$ valence band is dispersionless near the crossing point while the $\bar{\Delta}_4\bar{\Delta}_5$ conduction band disperses

downwards crossing the $\bar{\Delta}_6$ flat-band (Fig. 5.4 c and d). Plotting the 2D and 3D Fermi surfaces (Fig. 5.4e,f), the presence of line-like electron and hole pockets, which cross at (0,0, ±0.332c*) satisfies the requirement for the emergence of type-III Dirac cones. As seen in Fig. 4.4b, the in-plane strain might be thought of as a switching mechanism for going from type-I to type-II DSM. It is vital to remember that this alteration is highly desirable because it represents an electronic topological Lifshitz phase transition with significant implications for thermoelectric and electronic transport (see introduction).

Fig. 5.5 shows the crystal structures of 1T $HfTe_2$, $ZrTe_2$, and $Hf_{0.2}Zr_{0.8}Te_2$, where the Hf atomic positions in $Hf_{0.2}Zr_{0.8}Te_2$ are selected at random.

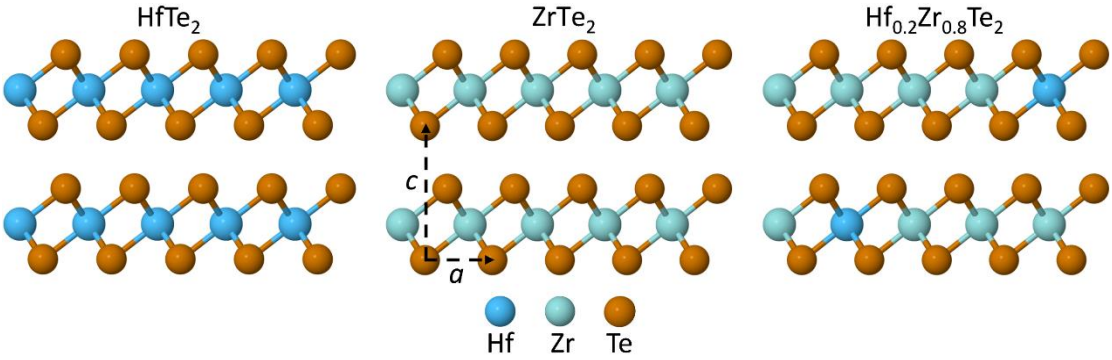

Figure 5.5. Schematic illustration of $HfTe_2$, $ZrTe_2$ and $Hf_{0.2}Zr_{0.8}Te_2$ crystal structures. The Hf atoms are randomly placed inside the $Hf_{0.2}Zr_{0.8}Te_2$ crystal.

5.3. Growth and electronic band imaging of $Hf_{0.2}Zr_{0.8}Te_2$ alloy

In this section, we present experimental proof that the few layer $Hf_xZr_{1-x}Te_2$ compound can be produced using MBE on InAs(111) substrates with the appropriate composition x=0.2. The chemically cleaned InAs(111)/Si(111) substrates were prepared in a 5N HF solution in isopropyl alcohol for 5 min to etch (remore) the surface oxide and then washed in isopropyl alcohol for 30 seconds to prevent the substrate from reoxidizing. To obtain a clean and flat InAs(111) (In-terminated) surface, an annealing step at 400° C in UHV is then performed, as shown by RHEED. A 2 × 2 reconstruction in RHEED pattern attributable to In surface vacancies shows that appropriate, mild Ar+ sputtering (E ≈ 1.5 keV, p ≈ 2×10^{-5} mbar, t ≈ 30 s) was used to create a clean surface before the annealing process [5.53]. It should be noted that starting with a clean 2 × 2 InAs(111) reconstructed surface is an important requirement in order to obtain a good registry of the epitaxial film with the substrate with an in-plane orientation. The exact process has already been applied in $ZrTe_2$ [5.18], $MoTe_2$ [5.54] and $TiTe_2$ [5.55] 2D TMDs. The films are developed in a UHV MBE (DCA) vertical chamber under Te-rich conditions.

The system's base pressure is $\sim 5\times10^{-10}$ Torr. Te (99.999%) evaporates from the Knudsen cell. Co-evaporation occurs between Hf 99.9% (metal basis excluding Zr, Zr nominal 2%), and Zr 99.8% (metal basis excluding Hf, Hf nominal 4%). A 100 mm hemispherical electron analyzer (SPECS) with a 2D CCD detector was used to conduct ARPES experiments at ambient temperature without compromising the vacuum. Photoelectrons are excited using the resonance line of the He I atom (21.22 eV). With a polar angle step of 1°, the system's energy resolution is better than 40 meV.

As anticipated for a clean oxygen-free In-terminated InAs(111) surface, a 2×2 reconstruction of the InAs(111) surface is shown by RHEED after the cleaning process (Fig. 5.6a). The 17 monolayer $Hf_{0.2}Zr_{0.8}Te_2$ films exhibit streaky patterns along the $[1\bar{1}0]$ and $[11\bar{2}]$ InAs azimuths, indicating smooth, well-ordered surfaces, that are aligned in-plane with the InAs(111) substrate, which is characteristic of vdW epitaxial growth. Scanning tunneling microscopy (STM) is used to analyze the surface morphology of a 17-monolayer $Hf_{0.2}Zr_{0.8}Te_2$ film on InAs(111) in situ at room temperature and ultra-high vacuum. The scanning conditions are V = 200 mV and I = 400 pA. Fig. 5.6b shows a 500 × 500 nm^2 area scan of the sample. With an average surface roughness of about 3.5 Å, it can be deduced that $Hf_{0.2}Zr_{0.8}Te_2$ is developed as two-dimensional islands, which is compatible with the InAs atomic step previously shown in epitaxial $ZrTe_2$ [5.18] and $MoTe_2$ [5.54].

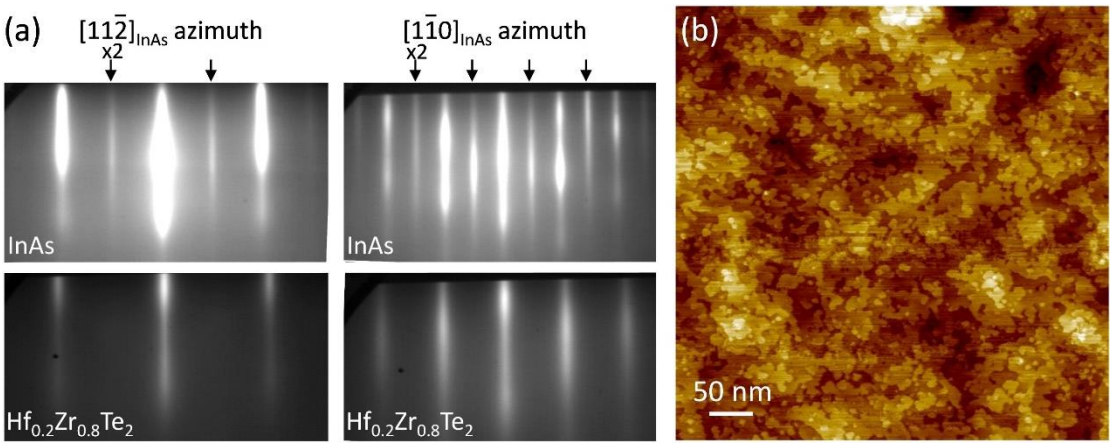

Figure 5.6. (a) RHEED patterns of InAs(111) substrate and 17 monolayers $Hf_{0.2}Zr_{0.8}Te_2$ films along the InAs$[1\bar{1}0]$ and $[11\bar{2}]$ azimuths. (b) 500 nm × 500 nm STM image of 17 monolayers $Hf_{0.2}Zr_{0.8}Te_2$ on InAs(111).

In Fig. 5.7, the band structure of 17 layers of $Hf_{0.2}Zr_{0.8}Te_2$ is shown along the BZ's ΓM direction. Similar to the Dirac-like cone dispersion seen in epitaxial $HfTe_2$ and $ZrTe_2$

[5.17, 5.18], the valence band in this material exhibits a Fermi level touching at the cone tip. However, these observations significantly deviate from the theoretical predictions that the DP is located at a distance of 0.63 eV above the E_F.

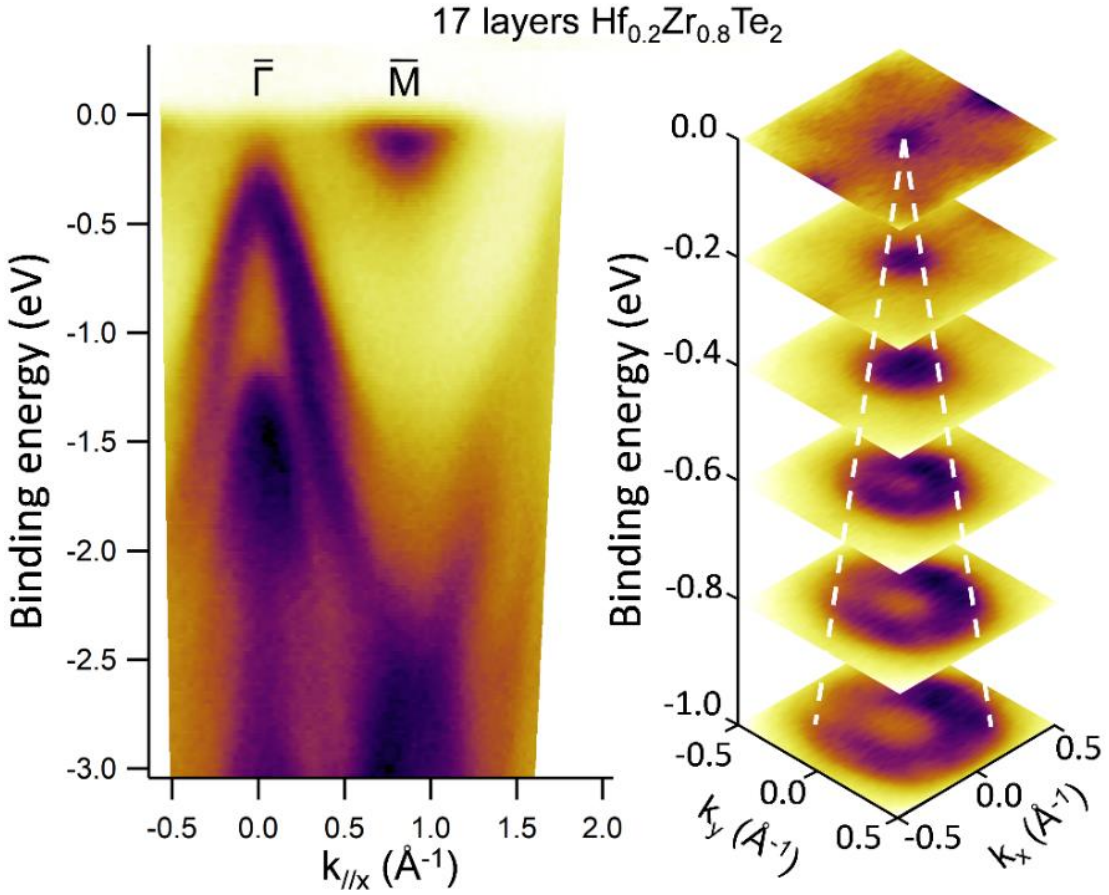

Figure 5.7. ARPES spectra and k_x–k_y Fermi surface plots at various binding energies of 17 layers $Hf_{0.2}Zr_{0.8}Te_2$ along the ΓM direction of the Brillouin zone using the He-I resonance line at 22.21 eV. The valence bands cone-like dispersion, which intersects at the Dirac point, is shown visually by the white dashed lines.

Additionally, this is in contrast to what has been seen in the band structure of bulk single crystals of $ZrTe_2$ and $HfTe_2$ as observed by synchrotron ARPES [5.19-5.22]. An influence on the epitaxial few-layer film caused by the substrate may be responsible for this variation. The Fermi level might be raised by a potential doping of the epitaxial films emerging from the InAs(111) substrate, enabling the observation of the linear band dispersions up to the Dirac cone's tip. A parabolic band at the M point overlaps with the cone-shaped band, indicating semimetalic nature. The Fermi surface at various binding energies below the Fermi level is imaged using the k_x-k_y constant energy contours. White dashed lines that cross at the Dirac point at the Fermi level are used to depict the conical band surrounding the zone centre. Using $E = \hbar v_F k$, the Fermi velocity

v_F can be calculated to be 0.6×10^6 m/s, which is comparable to the results found for epitaxial films of $HfTe_2$ and $ZrTe_2$ [5.17, 5.18].

5.4. Conclusions

The ab initio calculations in this study show that $HfTe_2$ is a type-I DSM with a point-like Fermi surface, whereas $ZrTe_2$ is a type-II DSM with needle-like electron and hole pockets touching at the DP. It is expected that the new alloy $Hf_xZr_{1-x}Te_2$ will produce a type-III Dirac cone with a line-like Fermi surface at x=0.2. To obtain the type-III phase, an in-plane compressive strain is additionally applied. This strain may be used to alternate between the two types of DSMs. By using MBE, epitaxial $Hf_{0.2}Zr_{0.8}Te_2$ films are successfully grown on InAs(111) substrates. According to ARPES measurements, $Hf_{0.2}Zr_{0.8}Te_2$ films display topological Dirac semimetal behavior, with the valence bands exhibiting a linear dispersion in k-space. Contrary to theory, which expects the DP at an energy considerably above the Fermi level, the top of the Dirac cone actually touches the Fermi level. These data show that the type-III topological DP, anticipated by theoretical calculations, naturally lies at -or very close to- the Fermi level, even though further research with synchrotron ARPES is required to see the k_z dispersion of the energy bands by adjusting the photon energy.

References

[5.1] N. P. Armitage, E. J. Mele, and A. Vishwanath, Rev. Mod. Phys. **90,** 015001 (2018); *and references therein.*

[5.2] G. E. Volovik, JETP Letters **104**, 645 (2016).

[5.3] G. E. Volovik and K. Zhang, J. Low Temp. Phys. **189**, 276 (2017).

[5.4] T. Mizoguchi and Y. Hatsugai, J. Phys. Soc. Jpn. **89**, 103704 (2020).

[5.5] I. M. Lifshitz, Sov. Phys. JETP **11**, 1130 (1960).

[5.6] G. E. Volovik, Phys.-Usp. **61**, 89 (2018).

[5.7] Y. Zhang, C. Wang, L. Yu, G. Liu, A. Liang, J. Huang, S. Nie, X. Sun, Y. Zhang, B. Shen, J. Liu, H. Weng, L. Zhao, G. Chen, X. Jia, C. Hu, Y. Ding, W. Zhao, Q. Gao, C. Li, S. He, L. Zhao, F. Zhang, S. Zhang, F. Yang, Z. Wang, Q. Peng, X. Dai, Z. Fang, Z. Xu, C. Chen, and X. J. Zhou, Nat. Commun. **8**, 15512 (2017).

[5.8] H. Chi, C. Zhang, G. Gu, D. E. Kharzeev, Xi Dai, and Q. Li, New J. Phys. **9**, 015005 (2017).

[5.9] Y. Zhang, C. Wang, G. Liu, A. Liang, L. Zhao, J. Huang, Q. Gao, B. Shen, J. Liu, C. Hu, W. Zhao, G. Chen, X. Jia, L. Yu, L. Zhao, S. He, F. Zhang, S. Zhang, F. Yang, Z. Wang, Q. Peng, Z. Xu, C. Chen, and X. Zhou, Sci. Bull. **62**, 950 (2017).

[5.10] F. Caglieris, C. Wuttke, S. Sykora, V. Süss, C. Shekhar, C. Felser, B. Büchner, and C. Hess, Phys. Rev. B **98**, 201107(R) (2018).

[5.11] H. Liu, J.-T. Sun, C. Song, H. Huang, F. Liu. S. Meng, Chin. Phys. Lett. **27**, 067101 (2020).

[5.12] H. Huang, K.-H. Jin, and F. Liu, Phys. Rev B **98**, 121110 (2018).

[5.13] S. Fragkos, R. Sant, C. Alvarez, E. Golias, J. Marquez-Velasco, P. Tsipas, D. Tsoutsou, S. Aminalragia-Giamini, E. Xenogiannopoulou, H. Okuno, G. Renaud, O. Rader, and A. Dimoulas, Phys. Rev. Mater. **3**, 104201 (2019).

[5.14] M. Milićević, G. Montambaux, T. Ozawa, O. Jamadi, B. Real, I. Sagnes, A. Lemaître, L. Le Gratiet, A. Harouri, J. Bloch, and A. Amo, Phys. Rev. X **9**, 031010 (2019).

[5.15] Z. K. Liu, B. Zhou, Y. Zhang, Z. J. Wang, H. M. Weng, D. Prabhakaran, S.-K. Mo, Z. X. Shen, Z. Fang, X. Dai, Z. Hussain, and Y. L. Chen, Science **343**, 864 (2014).

[5.16] Z. K. Liu, J. Jiang, B. Zhou, Z. J. Wang, Y. Zhang, H. M. Weng, D. Prabhakaran, S-K. Mo, H. Peng, P. Dudin, T. Kim, M. Hoesch, Z. Fang, X. Dai, Z. X. Shen, D. L. Feng, Z. Hussain and Y. L. Chen, Nat. Mater. **13**, 677 (2014).

[5.17] S. Aminalragia-Giamini, J. Marquez-Velasco, P. Tsipas, D. Tsoutsou, G. Renaud, and A. Dimoulas, 2D Mater. **4**, 015001 (2017).

[5.18] P. Tsipas, D. Tsoutsou, S. Fragkos, R. Sant, C. Alvarez, H. Okuno, G. Renaud, R. Alcotte, T. Baron, and A. Dimoulas, ACS Nano **12**, 1696 (2018).

[5.19] Y. Nakata, K. Sugawara, A. Chainani, K. Yamauchi, K. Nakayama, S. Souma, P.-Y. Chuang, C.-M. Cheng, T. Oguchi, K. Ueno, T. Takahashi, and T. Sato, Phys. Rev. Mater. **3**, 071001 (2019).

[5.20] Z. E. Youbi, S. W. Jung, S. Mukherjee, M. Fanciulli, J. Schusser, O. Heckmann, C. Richter, J. Minár, K. Hricovini, M. D. Watson, and C. Cacho, Phys. Rev. B **101**, 235431 (2020).

[5.21] B. Zhang, Z. Muhammad, P. Wang, S. Cui, Y. Li, S. Wang, Y. Wu, Z. Liu, H. Zhu, Y. Liu, G. Zhang, D. Liu, L. Song, and Z. Sun, J. Phys. Chem. C **124**, 16561 (2020).

[5.22] I. Kar, J. Chatterjee, L. Harnagea, Y. Kushnirenko, A. V. Fedorov, D. Shrivastava, B. Büchner, P. Mahadevan, and S. Thirupathaiah, Phys. Rev. B **101**, 165122 (2020).

[5.23] S. Mangelsen, P. G. Naumov, O. I. Barkalov, S. A. Medvedev, W. Schnelle, M. Bobnar, S. Mankovsky, S. Polesya, C. Näther, H. Ebert, and W. Bensch, Phys. Rev. B **96**, 205148 (2017).
[5.24] S. M. Ng, H. Wang, Y. Liu, H. F. Wong, H. M. Yau, C. H. Suen, Z. H. Wu, C. W. Leung, and J.-Y. Dai, ACS Nano **14**, 7077 (2020).
[5.25] H. Wang, C. H. Chan, C. H. Suen, S. P. Lau, and J.-Y. Dai, ACS Nano **13**, 6008 (2019).
[5.26] M. G. Vergniory, L. Elcoro, C. Felser, N. Regnault, B. A. Bernevig, and Z. Wang, Nature **566**, 480 (2019).
[5.27] B. Bradlyn, L. Elcoro, J. Cano, M. G. Vergniory, Z. Wang, C. Felser, M. I. Aroyo, and B. A. Bernevig, Nature **547**, 298 (2017).
[5.28] T. Zhang, Y. Jiang, Z. Song, H. Huang, Y. He, Z. Fang, H. Weng, and C. Fang, Nature **566**, 475 (2019).
[5.29] F. Tang, H. C. Po, A. Vishwanath, and X. Wan, Nature **566**, 486 (2019).
[5.30] N. H. D. Khang, Y. Ueda, and P. N. Hai, Nat. Mater. **17**, 808 (2018).
[5.31] Y. Wang, R. Ramaswamy, and H. Yang, J. Phys. D: Appl. Phys. **51**, 273002 (2018).
[5.32] S. Shi, S. Liang, Z. Zhu, K. Cai, S. D. Pollard, Y. Wang, J. Wang, Q. Wang, P. He, J. Yu, G. Eda, G. Liang, and H. Yang, Nat. Nanotechnol. **14**, 945 (2019).
[5.33] D. Chakraborty and P. Johari, ACS Appl. Nano Mater **3**, 5160 (2020).
[5.34] G. Kresse and J. Furthmüller, Comput. Mater. Sci. **6**, 15 (1996).
[5.35] G. Kresse and J. Furthmüller, Phys. Rev. B **54**, 11169 (1996).
[5.36] J. P. Perdew, K. Burke, and M. Ernzerhof, Phys. Rev. Lett. **77**, 3865 (1996).
[5.37] H. J. Monkhorst and J. D. Pack, Phys. Rev. B **13**, 5188 (1976).
[5.38] A. A. Mostofi, J. R. Yates, Y.-S. Lee, I. Souza, D. Vanderbilt, and N. Marzari, Comput. Phys. Commun. **185**, 2309 (2014).
[5.39] G. Pizzi, V. Vitale, R. Arita, S. Blügel, F. Freimuth, G. Géranton, M. Gibertini, D. Gresch, C. Johnson, T. Koretsune, J. Ibañez-Azpiroz, H. Lee, J.-M. Lihm, D. Marchand, A. Marrazzo, Y. Mokrousov, J. I. Mustafa, Y. Nohara, Y. Nomura, L. Paulatto, S. Poncé, T. Ponweiser, J. Qiao, F. Thöle, S. S. Tsirkin, M. Wierzbowska, N. Marzari, D. Vanderbilt, I. Souza, A. A Mostofi, and J. R. Yate, J. Phys. Cond. Matt. **32**, 165902 (2020).
[5.40] Q. S. Wu, S. N. Zhang, H.-F. Song, M. Troyer, and A. A. Soluyanov, Comput. Phys. Commun. **224**, 405 (2018).
[5.41] M. G. Vergniory, L. Elcoro, Z. Wang, J. Cano, C. Felser, M. I. Aroyo, B. A. Bernevig, and B. Bradlyn, Phys. Rev. E **96**, 023310 (2017).
[5.42] L. Elcoro, B. Bradlyn, Z. Wang, M. G. Vergniory, J. Cano, C. Felser, B. A. Bernevig, D. Orobengoa, G. de la Flor, and M. I. Aroyo, J. Appl. Crystallogr. **50,** 1457 (2017).
[5.43] B.-J. Yang and N. Nagaosa, Nat. Commun. **5**, 4898 (2014).
[5.44] S.-Y. Xu, Y. Xia, L. A. Wray, S. Jia, F. Meier, J. H. Dil, J. Osterwalder, B. Slomski, A. Bansil, H. Lin, R. J. Cava, M. Z. Hasan, Science **332**, 560 (2011).
[5.45] T.-R. Chang, S.-Y. Xu, G. Chang, C.-C. Lee, S.-M. Huang, B.-K. Wang, G. Bian, H. Zheng, D. S. Sanchez, I. Belopolski, N. Alidoust, M. Neupane, A. Bansil, H.-T. Jeng, H. Lin & M. Z. Hasan, Nat. Commun. **7**, 10639 (2016).
[5.46] I. Belopolski, D. S. Sanchez, Y. Ishida, X. Pan, P. Yu, S.-Y. Xu, G. Chang, T.-R. Chang, H. Zheng, N. Alidoust, G. Bian, M. Neupane, S.-M. Huang, C.-C. Lee, Y. Song, H. Bu, G. Wang, S. Li, G. Eda, H.-T. Jeng, T. Kondo, H. Lin, Z. Liu, F. Song, S. Shin, and M. Z. Hasan, Nat. Commun. **7**, 13643 (2016).
[5.47] S. Avarez, Dalton Trans. **42**, 8617 (2013).
[5.48] J. C. Slater, J. Chem. Phys. **41**, 3199 (1964).

[5.49] N. Marzari, A. A. Mostofi, J. R. Yates, I. Souza, and D. Vanderbilt, Rev. Mod. Phys. **84**, 1419 (2012).
[5.50] G. W. Winkler, A. A. Soluyanov, and M. Troyer, Phys. Rev. B **93**, 035453 (2016).
[5.51] M. Nakagawa, R.-J. Slager, S. Higashikawa, and T. Oka, Phys. Rev. B **101**, 075108 (2020).
[5.52] A. A. Soluyanov and D. Vanderbilt, Phys. Rev. B **83**, 035108 (2011).
[5.53] A. Taguchi and K. Kanisawa, Appl. Surf. Sci. **252**, 5263 (2006).
[5.54] P. Tsipas, S. Fragkos, D. Tsoutsou, C. Alvarez, R. Sant, G. Renaud, H. Okuno, and A. Dimoulas, Adv. Funct. Mater. **28**, 1802084 (2019).
[5.55] S. Fragkos, R. Sant, C. Alvarez, A. Bosak, P. Tsipas, D. Tsoutsou, H. Okuno, G. Renaud, and A. Dimoulas, Adv. Mater. Interfaces **6**, 1801850 (2019).

6. Magnetic skyrmion manipulation in $CrTe_2/WTe_2$ 2D van der Waals heterostructure

6.1. Introduction

In magnetic materials, magnetic skyrmions are swirling spin textures (Fig. 6.1a) [6.1]. The Dzyaloshinskii-Moriya interaction (DMI) controls the formation and stabilization of skyrmions in the majority of systems [6.2]. These systems produce five different kinds of magnetic skyrmions that are related to their symmetries [6.3-6.5]. Theoretically, isolated magnetic skyrmions and their lattices have been studied in terms of magnetic field-driven evolution [6.3-6.5]. According to these observations, the global minimum of the system is represented by the magnetic skyrmion lattices at high fields, and their formation is frequently interpreted as a first-order magnetic field-induced phase transition from the helical phase. Additionally, the skyrmion lattice undergoes a second-order phase transition into an ensemble of isolated skyrmions that exist in the saturated state and provides two cases of evolution with a lowering in the applied magnetic field. Either they stay as localized states in the metastable saturated phase and transform into helical states, or they condense into skyrmion lattices below a critical applied field. Magnetic skyrmions might present a special opportunity to include topology into electronic devices for communications and information storage. The most promising implementations are: (i) Skyrmion racetrack memory [6.6–6.8], which takes advantage of the solitonic nature of skyrmions and allows for the encoding of information by a series of individual skyrmions along a magnetic track. (ii) There have been numerous skyrmion-based logic devices proposed, which rely on the idea that a skyrmion can be thought of as an independent particle [6.9, 6.10]. (iii) Skyrmion radio-frequency devices [6.11–6.14], where it has been suggested that a radio-frequency signal can be produced by using the skyrmion breathing mode brought on by spin-torques.

The discovery of magnetic skyrmions in single crystals of non-inversion symmetric magnetic compounds [6.15, 6.16] supported the existence of DMI caused by spin-orbit coupling (SOC). Then, skyrmions were discovered in inversion-symmetric ultrathin magnetic films that were epitaxially grown on heavy metals (HMs). These films were

created as a result of significant DMIs that were caused by the interface's breaking of inversion symmetry as well as the strong SOC of the nearby HM [6.17–6.19].

Building heterostructures with spin ordering and strong SOC is a feasible technique to generate DMI since the presence of skyrmions depends on the strength of the DMI. To produce DMI, inversion symmetry must always be broken at the interface of two different materials in a heterostructure [6.20–6.22]. The research of magnetic skyrmions is being pushed towards the 2D limit, and two-dimensional (2D) van der Waals (vdW) magnets are a new and mostly unexplored class of magnets that possess numerous benefits over ordinary magnetic materials [6.22-6.30]. In mechanically exfoliated heterostructures of Fe_3GeTe_2 with WTe_2 topological material, Néel-type skyrmions have been observed [6.22]. Additionally, by building heterostructures with topological insulators, and compounds related to Cr_xTe_y 2D vdW ferromagnetic materials have been extensively investigated [6.31–6.33]. Topological Hall effect, which is thought to be evidence for magnetic skyrmions at the interfaces, has been seen in Cr_2Te_3/Bi-bilayer, Cr_2Te_3/Bi_2Te_3, and $CrTe_2/Bi_2Te_3$ vdW heterostructures [6.31–6.33]. However, there hasn't been any direct detection of them to yet. Atomic-scale spin simulations contributed to these results, which, however, are not supported by first-principles calculations.

Using first-principles calculations and atomic-scale spin simulations, we demonstrate in this work that bilayer vdW heterostructures made of $CrTe_2/WTe_2$ and, to a lesser extent, $CrTe_2/MoTe_2$ produce an interfacial DMI strong enough to maintain magnetic skyrmion lattice. A magnetic field-controlled Néel-type skyrmion lattice - ferromagnet transition cycle is also suggested by our simulations. Our findings further show that at temperatures near the Curie temperature, the skyrmion lattice is resistant to thermal fluctuations. Additionally, to analyze the motion of a skyrmion on a racetrack, a spin-torque caused by ultra-low spin-polarized current densities was simulated. This effect can be observed experimentally at liquid nitrogen temperatures, where a higher skyrmion Hall angle is shown at 80 K compared to 0 K. As a result, our research demonstrates that we can regulate the generation and destruction of skyrmions using a magnetic field or temperature, as well as the velocity and direction of Néel-type skyrmions using temperature and ultra-low spin-current densities.

6.2. Results

In Figs. 6.1b-d the side and top views of the $CrTe_2/WTe_2$ 2D van der Waals heterostructure are shown, calculated by first-principles calculations. $CrTe_2$ 2D ferromagnet is a member the layered 1T octahedral family of transition metal dichalcogenides (TMDs) with space group $P\bar{3}m1$ (No. 164), where two Te sublayers sandwich a Cr sublayer. The magnetic moment m of $CrTe_2$ is 3.0 μ_B/Cr [6.31-6.33]. On the other hand, bulk WTe_2 adopts the orthorhombic T_d structure with space group $Pmn2_1$. In the limit of a single layer, WTe_2 has been theoretically predicted and experimentally confirmed to be a 2D topological insulator (or quantum spin Hall insulator) and to possess one of the largest SOCs among other TMDs [6.34, 6.35], whereas the bulk WTe_2 material transforms into a topological type-II Weyl semimetal as first predicted [6.36] and subsequently experimentally verified [6.37]. We may safely ignore the impact of interfacial strain since the lattice mismatch value between $CrTe_2$ and WTe_2 (<1%) is relatively low to other heterostructures, which report values around 3-4% [6.29, 6.30]. So, as shown in Fig. 6.1, we stacked WTe_2 directly on top of $CrTe_2$ in a supercell with lattice constants a = 3.797 Å and b = 6.576 Å. (b).

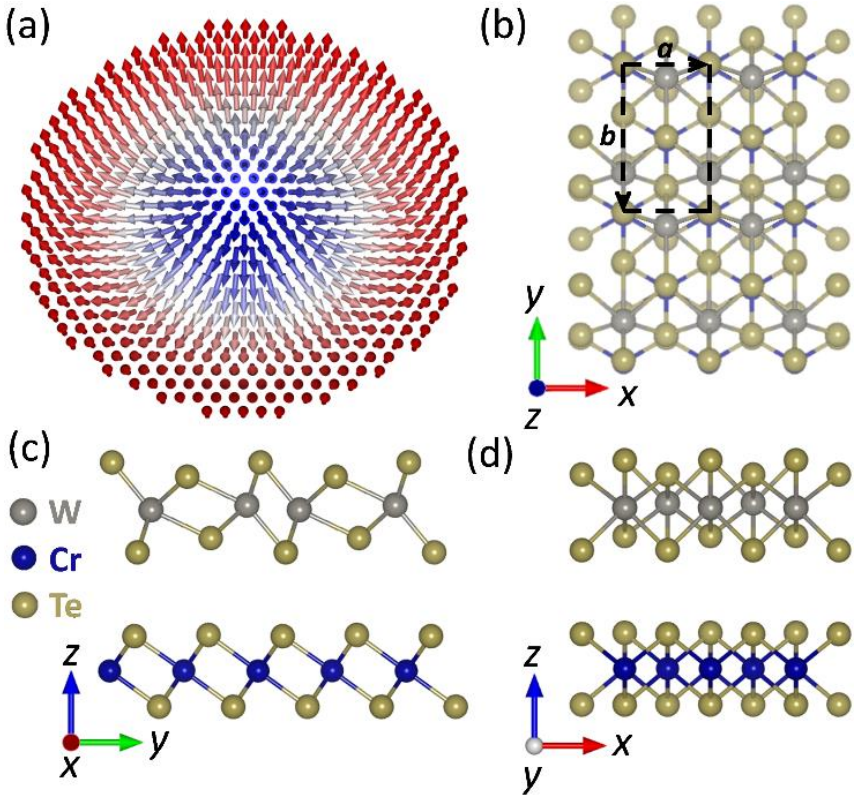

Figure 6.1. (a) Schematic illustration of a magnetic skyrmion. (b-d) Side and top views of $CrTe_2/WTe_2$ vdW heterostructure.

Large DMI has been found to cause skyrmion formation in Fe_3GeTe_2/WTe_2 heterostructures [6.22]. Additionally, WTe_2 has been theoretically predicted to have a high efficiency of charge to spin conversion with a spin Hall angle of $\theta_{SH} = 0.17$ to 1.0 [6.38–6.41], making it a viable candidate for current-driven, low-energy skyrmion manipulation [6.1]. However, few studies on the related compound $MoTe_2$ metastable topological T_d phase [6.42] reveal spin all angle values that are smaller than those of WTe_2 [6.38, 6.43], making it less investigated and examined for spintronic applications [6.22, 6.30, 6.39-6.41].

Due to the presence of inversion symmetry, the DMI is absent in a free-standing $CrTe_2$. Nevertheless, at the interface of a heterostructure, inversion symmetry is broken (Fig. 6.2) and an interfacial DMI emerges, increasing the potential for the generation of skyrmions. For the $CrTe_2/WTe_2$ heterostructure, top and hollow stacking types were taken into consideration. Both hollow and top stackings relaxed to the same configuration after relaxation, as shown in Fig. 6.2. Additionally, the inversion symmetry of $CrTe_2$ is broken since Cr-Te bonds ceased to be equivalent (as opposed to free-standing $CrTe_2$, where all Cr-Te bonds are equal). The Cr-Te bonds of the relaxed heterostructure as index in Fig. S5.1 are summarized as $d_{1,3} = 2.680$ Å, $d_{1,4} = 2.712$ Å, $d_{1,5} = 2.706$ Å, $d_{1,6} = 2.708$ Å, $d_{2,3} = 2.674$ Å, $d_{2,4} = 2.706$ Å, $d_{2,5} = 2.711$ Å, $d_{2,6} = 2.713$ Å.

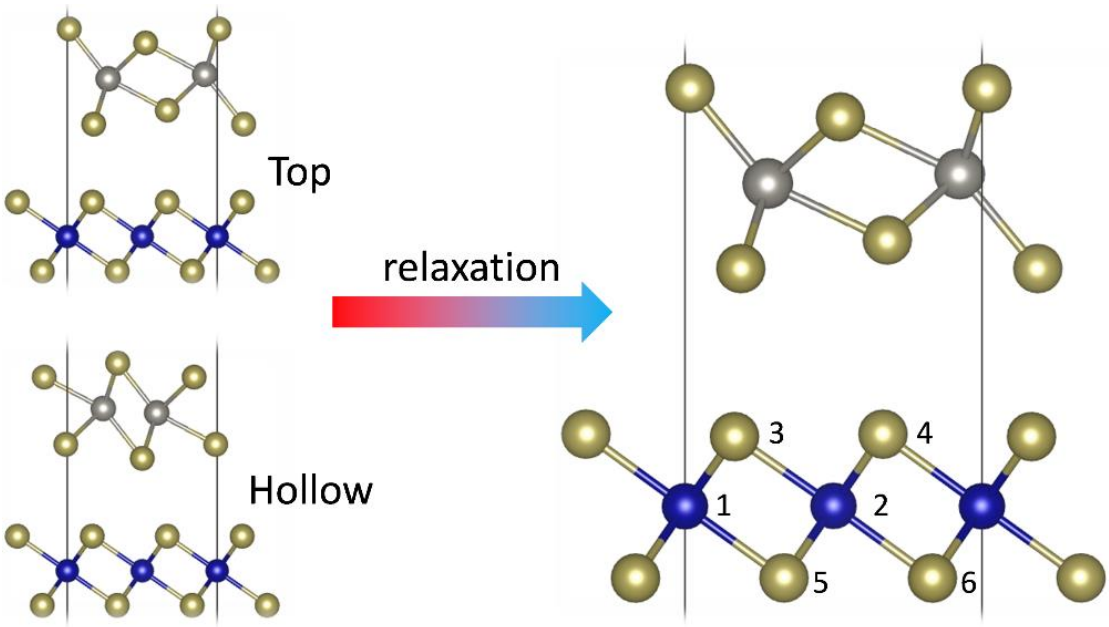

Figure 6.2. The side view of top, hollow and relaxed stacking.

Atomistic spin simulations using the *Spirit* package [6.44] have been carried out to determine whether the generation of skyrmions is feasible in the $CrTe_2/WTe_2$ heterostructure. The following atomically resolved Hamiltonian is taken into consideration to describe the magnetic interactions of Cr atoms:

$$H = -\sum_i m_i B \cdot n_i - \sum_i \sum_j K_i \left(\widehat{K}_j \cdot n_i\right)^2 - \sum_{\langle ij \rangle} J_{ij} n_i \cdot n_j - \sum_{\langle ij \rangle} D_{ij} \cdot \left(n_i \times n_j\right) \tag{6.1}$$

here the spin direction is denoted by n_i at each lattice site i, such that the magnetic moment is expressed as $m_i = \mu_i n_i$, where B is the applied magnetic field, K the magnetic anisotropy constant, J the exchange coupling constant and D the DMI. The Landau–Lifshitz–Gilbert (LLG) equation [6.45, 6.46] is used to describe the spin dynamics:

$$\frac{\partial n_i}{\partial t} = -\frac{\gamma}{(1+a^2)\mu_i} n_i \times B_i^{eff} - \frac{\gamma a}{(1+a^2)\mu_i} n_i \times \left(n_i \times B_i^{eff}\right) - \frac{\gamma a}{(1+a^2)\mu_B} u n_i \times (\hat{j}_e \cdot \nabla_r) n_i + \frac{\gamma}{(1+a^2)\mu_B} u n_i \times [n_i \times (\hat{j}_e \cdot \nabla_r) n_i] \tag{6.2}$$

where $\alpha = 0.05$ is the damping parameter, γ is the electron gyrometric ratio, the effective field is $B_i^{eff} = -\partial H / \partial n_i$ and u is spin-torque defined as:

$$u = j_e P \hbar \mu_B / (2 e M_s) \tag{6.3}$$

with j_e the spin-polarized current density, ħ is Planck's reduced constant, e the electron charge, P is the current polarization and M_s the magnetization saturation. The effective field containing a stochastic thermal field $B_i^{eff} \rightarrow B_i^{eff} + B_i^{th}$ is given by:

$$B_i^{th}(t) = \sqrt{2D_i}\eta_i(t) = \sqrt{2ak_B T \frac{\mu_i}{\gamma}}\eta_i(t) \tag{6.4}$$

where η_i is white noise [6.44].

Density functional theory (DFT) calculations are used to obtain the Hamiltonian parameters K, J and D. The DFT were performed using the Vienna Ab Initio Simulation Package (VASP) [6.47, 6.48]. The generalized-gradient approximation (GGA) with Perdew-Burke-Ernzerhof (PBE) parametrization was used as the exchange correlation functional [6.49]. The kinetic cutoff energy was set at 500 eV, employing a Gamma-centered 18 × 10 × 1 k-point mesh. Using the Dudarev approach [6.50], a Hubbard parameter U_{eff} = 3 eV has been applied on Cr d orbitals, in order to obtain the desired magnetic moment of 3.0 μ_B/Cr [6.31-6.33]. The lattice parameters and atomic positions were fully optimized by conjugate gradient, until energy and force converge to 10^{-8} eV and 10^{-3} eV $Å^{-1}$, respectively. DFT-D3 Grimme's method [6.51] was included in order to apply vdW corrections and a vacuum of 20 Å was used, to avoid interaction between the periodically repeated layers. Spin-orbit coupling was included in all calculations.

The magnetic anisotropy K can be obtained by $K = E_{100} - E_{001}$, where E_{100} and E_{001} are the total energies of configurations with the magnetization directions parallel and perpendicular to the plane of $CrTe_2$, respectively. The magnetic exchange interaction J is proportional to the energy difference between antiferromagnetic (AFM) and ferromagnetic (FM) spin configurations, and is defined by $J = (E_{AFM} - E_{FM})/12$ [6.28, 6.30, 6.52]. The DMI strength D is established by mapping the total energies of artificially placed spin configurations to the Hamiltonian $H = \sum_{\langle ij \rangle} D_{ij} \cdot (n_i \times n_j)$ [6.28, 6.30, 6.53, 6.54]. The D_{12}^x in-plane component between the spin site 1 and 2 (n_1 and n_2), perpendicular to Cr-Cr bonds, can be obtained by setting the following four spin configurations: (i) $n_1 = (0,n,0)$, $n_2 = (0,0,n)$, (ii) $n_1 = (0,n,0)$, $n_2 = (0,0,-n)$, (iii) $n_1 = (0,-n,0)$, $n_2 = (0,0,n)$, (iv) $n_1 = (0,-n,0)$, $n_2 = (0,0,-n)$. The energies of the four spin configurations are denoted as E_1, E_2, E_3, and E_4, where the D_{12}^x can be obtained by $D_{12}^x = (E_1 + E_4 - E_2 - E_3)/4$. The values of the Hamiltonian parameters determined from the DFT calculations are summarized as K = 19 μeV, J = 11.53 meV and D = 0.64 meV. The positive values of K, J and D suggest out-of-plane magnetic anisotropy, ferromagnetic spin order and anticlockwise magnetization rotation from spin site 1 to 2, respectively. The DMI value that is calculated from the first-principles calculations is comparable to the values reported in the literature for other 2D vdW materials and heterostructures which range from 0.2 up to 2 meV [6.23-6.30].

An external stimulus has a significant impact on a magnet's properties and spin texture. Few intriguing transitions have been extensively investigated, such as skyrmion-(bi)meron or skyrmion-antiskyrmion transitions that are influenced by temperature or an applied magnetic field [6.28, 6,30, 6.55, 6.56]. We propose a field-controlled skyrmion lattice - ferromagnet transition cycle (Fig. 6.3) after conducting a systematic analysis of the impact of applied magnetic field and temperature on the spin texture of Cr atoms of $CrTe_2/WTe_2$ 2D vdW heterostructure.

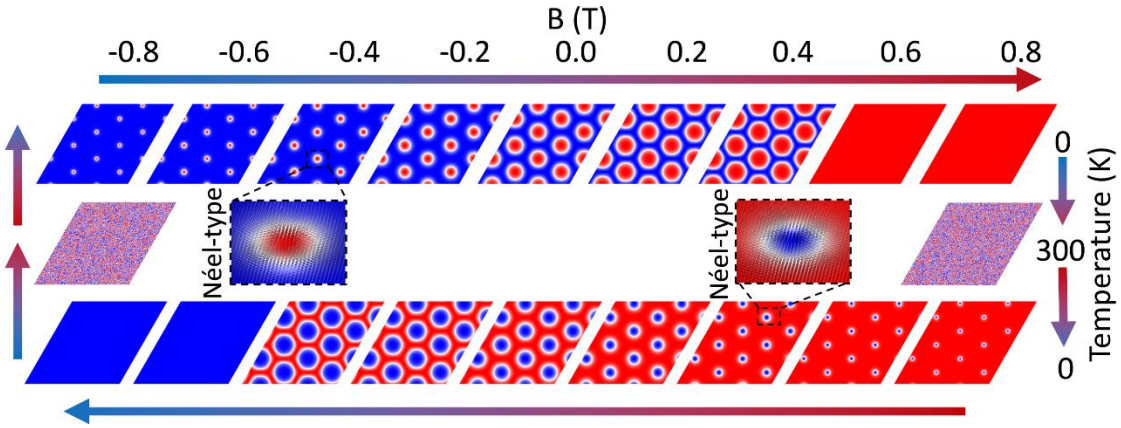

Figure 6.3. A complete transition cycle of spin texture from -0.8 T to 0.8 T.

Fig. 6.3 depicts a complete cycle on a 300×300 supercell with an external applied field along the z axis from -0.8 to 0.8 T. An Néel-type skyrmion lattice configuration becomes the system's ground state when an applied field perpendicular to it of -0.8 T is applied. When the applied magnetic field exceeds 0.6 T, the nearest neighboring skyrmions merge and the configuration changes to a ferromagnetic state as the applied magnetic field moves toward larger positive values. In order to stimulate skyrmions from the ferromagnetic state, we increased the temperature to 300 K and subsequently decreased it. This created a reversed, compared to the initial, Néel-type skyrmion lattice, which further transformed into a ferromagnetic state at -0.6 T. The method of heating followed by rapid cooling has been extensively employed both theoretically and experimentally to produce skyrmions [6.30, 6.57–6.59].

It is expected that isolated skyrmions are allowed to exist at zero applied magnetic field [6.1, 6.3] when the DMI becomes smaller than a critical value $D_c = 2\sqrt{2JK}/\pi$ [6.3, 6.60, 6.61], while for DMI higher than D_c, isolated skyrmions arise at applied fields higher than the transition field between skyrmion lattice and saturated phase [6.4]. However, in our case, where the interfacial DMI D = 0.64 meV of the $CrTe_2/WTe_2$

vdW bilayer is larger than the critical value D_c = 0.42 meV, no isolated skyrmions were observed in the ferromagnetic state as anticipated.

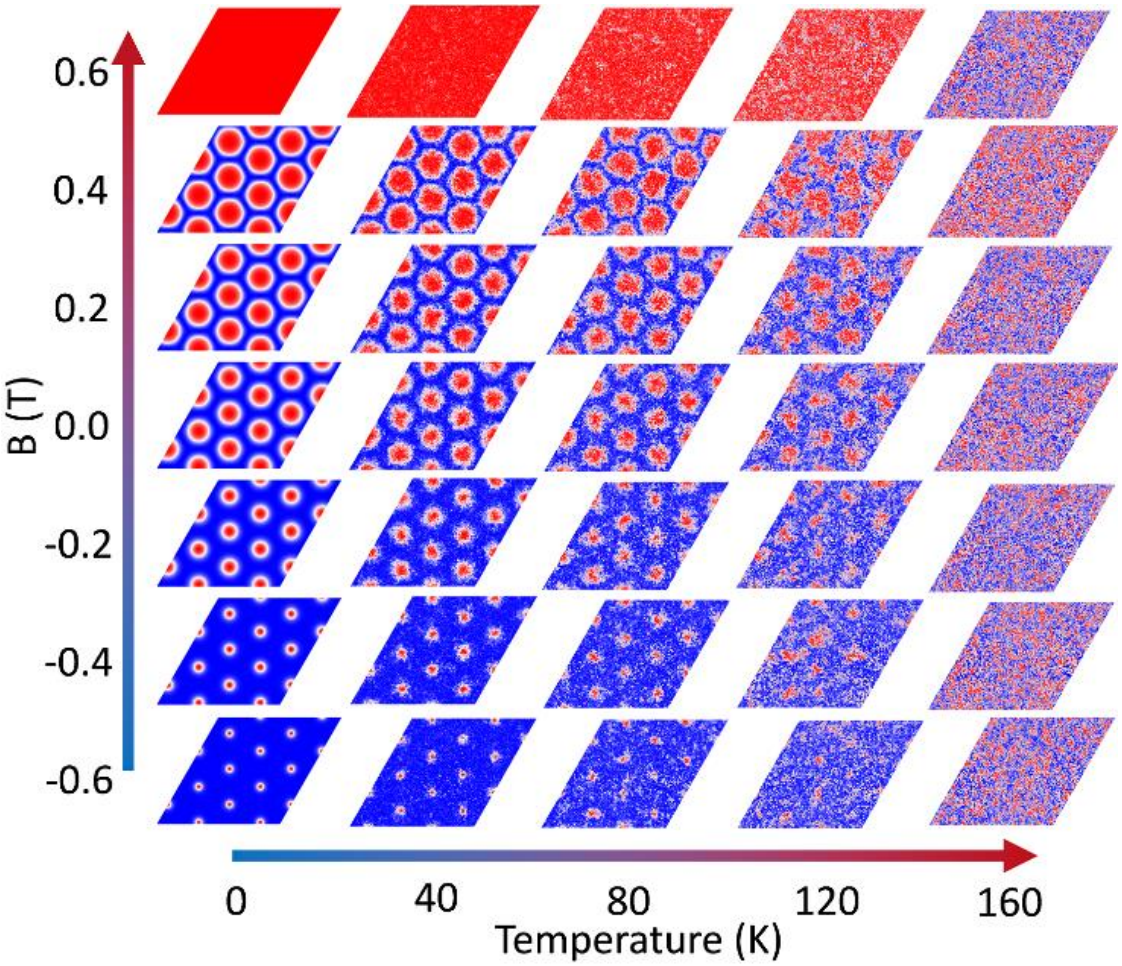

Figure 6.4. Skyrmion phase diagram as a function of temperature and magnetic field.

A phase diagram of spin texture as a function of temperature and an applied out-of-plane magnetic field, B, is shown in Fig. 6.4. Thermal noise causes the well-rounded skyrmions at zero degrees Celsius to substantially deform as the temperature rises. Due to the increase in skyrmion diameter, skyrmions exhibit robustness against thermal fluctuations even when the applied magnetic field approaches positive values. When the Curie temperature T_c = 163 K is reached, the skyrmion lattice arrangement dissolves and $CrTe_2$ becomes paramagnetic for the whole magnetic field range. Therefore, it can be inferred from Figs. 6.3 and 6.4 that the temperature and applied field can both function as processes for writing and deleting skyrmions on the $CrTe_2/WTe_2$ 2D vdW heterostructure.

Despite the focus of the research being on the more efficient $CrTe_2/WTe_2$ bilayer, as discussed in the Introduction section, the $CrTe_2/MoTe_2$ 2D vdW heterostructure also underwent the aforementioned DFT calculations and atomic scale spin simulations. A Néel-type skyrmion lattice, which is less resistant to applied magnetic field and temperature, was formed with a smaller DMI value of 0.48 meV.

As already mentioned above, both first-principles calculations and atomic scale spin simulations were also performed for the $CrTe_2/MoTe_2$ heterostructure, were a DMI value of 0.48 meV was obtained. On a 300×300 supercell, a field-controlled Néel-type skyrmion lattice - ferromagnet transition cycle is seen (Fig. 6.5) with an externally applied field along the z axis from -0.6 to 0.6 T. This is similar to the $CrTe_2/WTe_2$ heterostructure, however, the transition cycle is smaller in the applied field range compared to $CrTe_2/WTe_2$ heterostructure due to the decreased DMI.

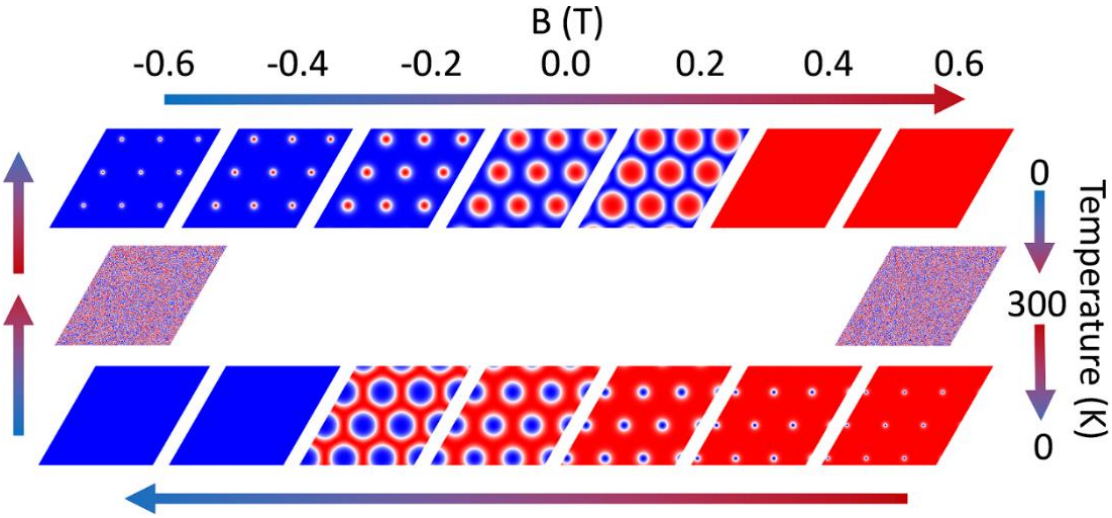

Figure 6.5. A complete transition cycle of spin texture from -0.6 T to 0.6 T in $CrTe_2/MoTe_2$ heterostructure.

A phase diagram of spin texturing in a $CrTe_2/MoTe_2$ heterostructure as a function of temperature and applied out-of-plane magnetic field *B* is shown in Fig. 6.6. Again, due to thermal noise, the well-rounded skyrmions at 0 K experience considerable deformation as the temperature rises. The skyrmions appear to be less resistant to thermal noise than the $CrTe_2/WTe_2$ heterostructure, and they only essentially survive up to 120 K because of the reduced DMI.

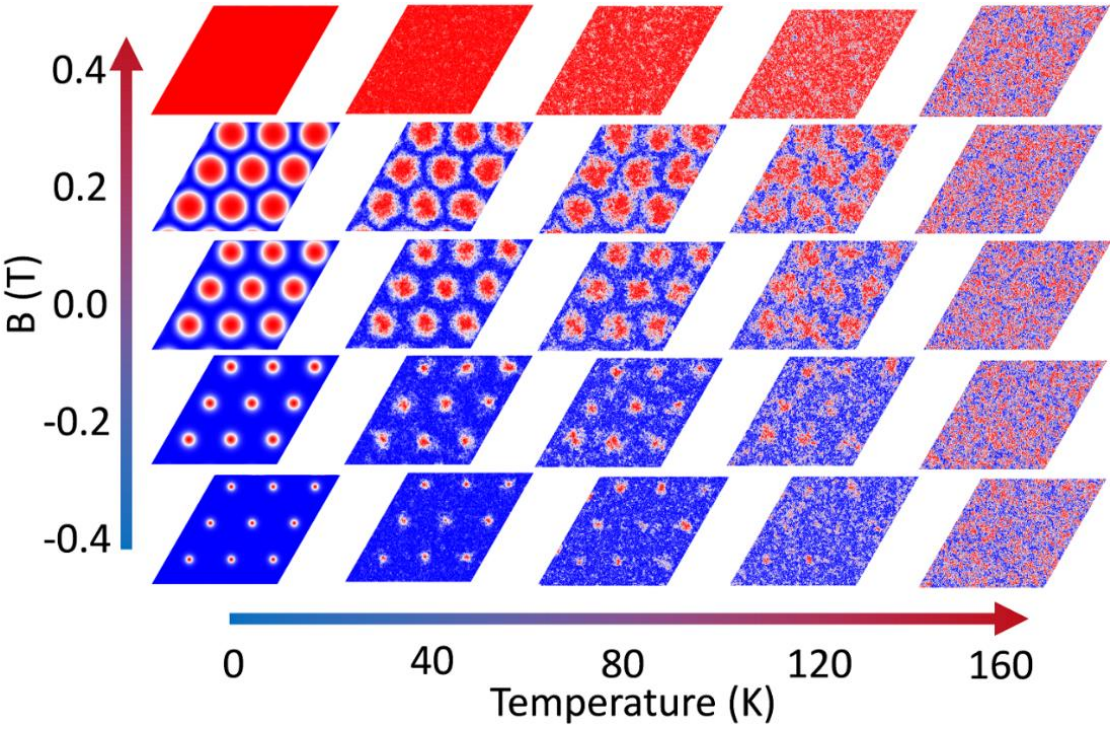

Figure 6.6. Skyrmion phase diagram as a function of temperature and magnetic field in $CrTe_2/MoTe_2$ heterostructure.

Low current densities can move magnetic skyrmions [6.30, 6.62-6.68]. Skyrmions can avoid impurities during current-driven motions due to the topological protection's flexible deformation of their shape. To investigate the spin-polarized current-induced motion of skyrmions, we placed a Néel-type skyrmion on a $CrTe_2/WTe_2$ racetrack under a 0.2 T applied out-of-plane magnetic field. The Eq. (6.3) was used to simulate the spin-torque caused by the injection of spin current. A modified Thiele equation can be used to explain the skyrmion motion caused by the spin-torque [6.1, 6.30, 6.62, 6.65]:

$$G \times v - a\boldsymbol{\mathcal{D}} \cdot v + 4\pi\boldsymbol{\mathcal{B}} \cdot j_e = 0 \tag{6.5}$$

where $G = (0, 0, -4\pi Q)$ is the gyromagnetic coupling vector with topological charge $Q = 1/4\pi \int m \cdot (\partial_x n \times \partial_y n) d_x d_y$, $\boldsymbol{\mathcal{D}}$ is the dissipative force tensor, which depends on the width of the skyrmion domain wall, $v = (v_x, v_y)$ is the skyrmion drift velocity along the x and y direction axis, respectively, and $\boldsymbol{\mathcal{B}}$ is the tensor related to the spin-torque driving force. The first term corresponds to a Magnus force that is similar to the Lorentz force for charge carriers and causes skyrmions to behave in a way that is similar to the Hall effect. A moving skyrmion intrinsic magnetic damping is represented by the

second term as a dissipative force, while the spin-torque driving force is represented by the third term.

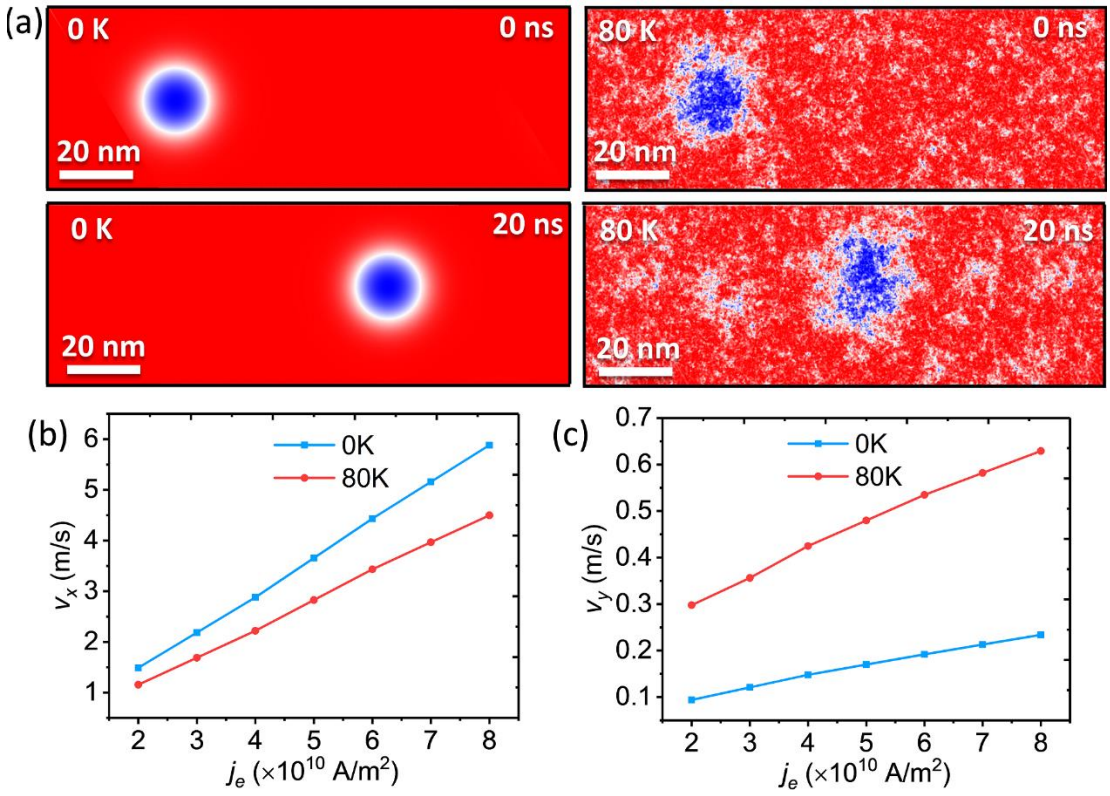

Figure 6.7. (a) Screenshots of Néel-type skyrmion motion at 0 and 80 K, under the same spin-polarized current density $j_e = 4\times10^{10}$ A/m^2. (b) and (c) v_x and v_y as a function of j_e, respectively.

Screenshots of a Néel-type skyrmion moving under the same spin current density $j_e = 4\times10^{10}$ A/m^2 polarized along the x direction are shown in Fig. 6.7a. At 0 and 80 K, the velocities are $v_x = 2.88$ m/s, $v_y = 0.15$ m/s, and $v_x = 2.22$ m/s, $v_y = 0.42$ m/s, respectively. Figs 6.7b and c show the skyrmion velocity as a function of the spin current density j_e. While the v_x of the Néel-type skyrmion velocity decreases at 80 K, the v_y component increases, which is a phenomenon that can be seen at liquid nitrogen temperature. According to a prior study, the skyrmion Hall angle increases with temperature as a result of the side-jump motion that skyrmions undergo as a result of the Magnus force that pushes them out of equilibrium while they continuously move over thermal fluctuations. This results in a finite value of the skyrmion hall angle, whose magnitude increases with larger driving forces and temperatures [6.68]. The critical current density to move a skyrmion is found to be ~0.9 ×10^{10} A/m^2. The $CrTe_2/WTe_2$ 2D vdW heterostructure is a promising system for current-driven skyrmion manipulation with low energy consumption since the applied spin-polarized current densities to generate

skyrmion motion are up to two orders of magnitude lower than those required to drive skyrmionic bubbles in synthetic multilayer films [6.1].

6.3. Conclusions

In conclusion, the perpendicular anisotropy constant *K*, the exchange coupling constant J, and the DMI *D*, were determined using DFT calculations in the $CrTe_2/WTe_2$ bilayer vdW heterostructure and introduced to atomic-scale spin simulations. We discovered that the heterostructure's interfacial DMI is powerful enough to stabilize magnetic skyrmions. Additionally, we developed a field-controlled Néel-type skyrmion lattice-ferromagnet transition cycle in which the skyrmion lattice is resistant to thermal fluctuations in the vicinity of Tc. In order to investigate the spin-polarized current-induced motion of skyrmions, we set up a Néel-type skyrmion on a racetrack. The skyrmion velocity as a function of spin-polarized current density suggests a greater skyrmion Hall angle at 80 K compared to 0 K, an effect that can be seen at liquid nitrogen temperature. Our research demonstrates that the applied field or temperature can be controlled to generate or annihilate skyrmions in the $CrTe_2/WTe_2$ bilayer vdW heterostructure, and that temperature control and ultra-low spin-polarized currents may be used to alter the skyrmions' velocity and direction.

References

[6.1] A. Fert, N. Reyren, and V. Cros, Nat. Rev. Mater. **2**, 17031 (2017).
[6.2] I. E. Dzyaloshinskii, Sov. Phys. JETP **19**, 960 (1964).
[6.3] A. Bogdanov and A. Hubert, J. Magn. Magn. Mater. **138**, 255 (1994).
[6.4] A. O. Leonov, T. L. Monchesky, N. Romming, A. Kubetzka, A. N. Bogdanov, and R. Wiesendanger. N. J. Phys. **18**, 065003 (2016).
[6.5] A. N. Bogdanov and C. Panagopoulos, Nat. Rev. Phys. **2**, 492–498 (2020).
[6.6] J. Sampaio, V. Cros, S. Rohart, A. Thiaville, and A. Fert, Nat. Nanotechnol. **8**, 839–844 (2013).
[6.7] R. Tomasello, E. Martinez, R. Zivieri, L. Torres, M. Carpentieri, and G. Finocchio, Sci. Rep. **4**, 6784 (2014).
[6.8] W. Kang, Y. Huang, C. Zheng, W. Lv, N. Lei, Y. Zhang, X. Zhang, Y. Zhou, and W. Zhao, Sci. Rep. **6**, 23164 (2016).
[6.9] Y. Zhou and M. Ezawa, Nat. Commun. **5**, 8 (2014).
[6.10] X. Zhang, M. Ezawa, and Y. Zhou, Sci. Rep. **5**, 9400 (2015).
[6.11] J.-V. Kim, F. Garcia-Sanchez, J. Sampaio, C. Moreau-Luchaire, V. Cros, and A. Fert, Phys. Rev. B **90**, 064410 (2014).
[6.12] M. Carpentieri, R. Tomasello, R. Zivieri, and G Finocchio, Sci. Rep. **5**, 16184 (2015).
[6.13] G. Finocchio, M. Ricci, R. Tomasello, A. Giordano, M. Lanuzza, V. Puliafito, P. Burrascano, B. Azzerboni, and M. Carpentieri, *Appl. Phys. Lett.* **107**, 262401 (2015).
[6.14] F. Garcia-Sanchez, N. Reyren, J. Sampaio, V. Cros, and J.-V. Kim, New J. Phys. **18**, 075011 (2016).
[6.15] A. Fert and P. M, Levy, Phys. Rev. Lett. **44**, 1538–1541 (1980).
[6.16] A. Fert, Mater. Sci. Forum 59–60, 439–480 (1990).
[6.17] S. Heinze, K. von Bergmann, M. Menzel, J. Brede, A. Kubetzka, R. Wiesendanger, G. Bihlmayer, and S. Blügel, Nat. Phys. **7**, 713 (2011).
[6.18] N. Romming, C. Hanneken, M. Menzel, J. E. Bickel, B. Wolter, K. von Bergmann, A. Kubetzka, and R. Wiesendanger, Science **341**, 636 (2013).
[6.19] H. Yang, A. Thiaville, S. Rohart, A. Fert, and M. Chshiev, Phys. Rev. Lett. **115**, 267210 (2015).
[6.20] A. N. Bogdanov and U. K. Rößler, Phys. Rev. Lett. **87**, 037203 (2001).
[6.21] M. Bode, M. Heide, K. von Bergmann, P. Ferriani, S. Heinze, G. Bihlmayer, A. Kubetzka, O. Pietzsch, S. Blügel, and R. Wiesendanger, Nature **447**, 190 (2007).
[6.22] Y. Wu, S. Zhang, J. Zhang, W. Wang, Y. L. Zhu, J. Hu, G. Yin, K. Wong, C. Fang, and C. Wan, Nat. Commun. **11**, 3860 (2020).
[6.23] Q. Cui, J. Liang, Z. Shao, P. Cui, and H. Yang, Phys. Rev. B **102**, 094425 (2020).
[6.24] C. Xu, P. Chen, H. Tan, Y. Yang, H. Xiang, and L. Bellaiche, Phys. Rev. Lett. **125**, 037203 (2020).
[6.25] M. J. Meijer, J. Lucassen, R. A. Duine, H. J. Swagten, B. Koopmans, R. Lavrijsen, and M. H. Guimarães, Nano Lett. **20**, 8563 (2020).
[6.26] M.-G. Han, J. A. Garlow, Y. Liu, H. Zhang, J. Li, D. DiMarzio, M. W. Knight, C. Petrovic, D. Jariwala, and Y. Zhu, Nano Lett. **19**, 7859 (2019).
[6.27] D. Amoroso, P. Barone, and S. Picozzi, Nat. Commun. **11**, 5784 (2020).
[6.28] W. Sun, W. Wang, H. Li, G. Zhang, D. Chen, J. Wang, and Z. Cheng, Nat. Commun. **11**, 5930 (2020).
[6.29] C.-K. Li, X.-P. Yao, and G. Chen, G. Phys. Rev. Res. 3, L012026 (2021).

[6.30] W. Sun, W. Wang, J. Zang, H. Li, G. Zhang, J. Wang, and Z. Cheng, Adv. Funct. Mater. **31**, 2104452 (2021).
[6.31] J. Chen, L. Wang, M. Zhang, L. Zhou, R. Zhang, L. Jin, X. Wang, H. Qin, Y. Qiu, J. Mei, F. Ye, B. Xi, H. He, B. Li, and G. Wang, Nano Lett. **19**, 6144 (2019).
[6.32] L. Zhou, J. Chen, X. Chen, B. Xi, Y. Qiu, J. Zhang, L. Wang, R. Zhang, B. Ye, P. Chen, X. Zhang, G. Guo, D. Yu, J.-W. Mei, F. Ye, G. Wang, and H. He, ACS Appl. Mater. Interfaces **12**, 25135 (2020).
[6.33] X. Zhang, S. C. Ambhire, Q. Lu, W. Niu, J. Cook, J. S. Jiang, D. Hong, L. Alahmed, L. He, R. Zhang, Y. Xu, S. S.-L. Zhang, P. Li, and G. Bian, ACS Nano **15**, 15710 (2021).
[6.34] X. Qian, J. Liu, L. Fu, and J. Li, Science **346**, 1344 (2014).
[6.35] S. Tang, C. Zhang, D. Wong, Z. Pedramrazi, H.-Z. Tsai, C. Jia, B. Moritz, M. Claassen, H. Ryu, S. Kahn, J. Jiang, H. Yan, M. Hashimoto, D. Lu, R. G. Moore, C.-C. Hwang, C. Hwang, Z. Hussain, Y. Chen, M. M. Ugeda, Z. Liu, X. Xie, T. P. Devereaux, M. F. Crommie, S.-K. Mo, and Z.-X. Shen, Nat. Phys. **13**, 683 (2017).
[6.36] A. Soluyanov, D. Gresch, Z. Wang, Q. S. Wu, M. Troyer, X. Dai, and B. A. Bernevig, Nature **527**, 495 (2015).
[6.37] Y. Wu, D. Mou, N. H. Jo, K. Sun, L. Huang, S. L. Bud'ko, C. Canfield, and A. Kaminski, Phys. Rev. B **94**, 121113 (2016).
[6.38] J. Zhou, J. Qiao, A. Bournel, and W. Zhao, Phys. Rev. B **99**, 060408(R) (2019).
[6.39] B. Zhao, D. Khokhriakov, Y. Zhang, H. Fu, B. Karpiak, A. M. Hoque, X. Xu, Y. Jiang, B. Yan, and S. P. Dash, Phys. Rev. Res. **2**, 013286 (2020).
[6.40] Y. Fan, H. Li, DC. Mahendra, T. Peterson, J. Held, P. Sahu, J. Chen, D. Zhang, A. Mkhoyan, and J.-P. Wang, APL Mater. **8**, 041102 (2020).
[6.41] I. Shin, W. J. Cho, E.-S. An, S. Park, H.-W. Jeong, S. Jang, W. J. Baek, S. Y. Park, D.-H. Yang, J. H. Seo, G.-Y. Kim, M. N. Ali, S.-Y. Choi, H.-W. Lee, J. S. Kim, S. D. Kim, and G.-H. Lee, *Adv. Mater*. 2101730 (2021).
[6.42] K.-A. N. Duerloo, Y. Li, and E. J. Reed, Nat. Commun. **5**, 4214 (2014).
[6.43] C. K. Safeer, N. Ontoso, J. Ingla-Aynés, F. Herling, V. T. Pham, A. Kurzmann, K. Ensslin, A. Chuvilin, I. Robredo, M. G. Vergniory, F. de Juan, L. E. Hueso, M. R. Calvo, and F. Casanova, Nano Lett. **19** (12), 8758-8766 (2019).
[6.44] G. P. Müller, M. Hoffmann, C. Dißelkamp, D. Schürhoff, S. Mavros, M. Sallermann, N. S. Kiselev, H. Jónsson, and S. Blügel, Phys. Rev. B **99**, 224414 (2019).
[6.45] L. Landau and E. Lifshitz, Phys. Z. Sowjet. **8**, 153 (1935).
[6.46] T. L. Gilbert, IEEE Trans. Magn. **40**, 3443 (2004).
[6.47] G. Kresse and J. Furthmüller, Comput. Mater. Sci. **6**, 15 (1996).
[6.48] G. Kresse and J. Furthmüller, Phys. Rev. B **54**, 11169 (1996).
[6.49] J. P. Perdew, K. Burke, and M. Ernzerhof, Phys. Rev. Lett. **77**, 3865 (1996).
[6.50] S. L. Dudarev, G. A. Botton, S. Y. Savrasov, C. J. Humphreys, and A. P. Sutton, Phys. Rev. B **57**, 1505 (1998).
[6.51] S. Grimme, J. Antony, S. Ehrlich, and H. Krieg, Chem. Phys. **132**, 154104 (2010).
[6.52] M. T. Hutchings and E. J. Samuelsen, Phys. Rev. B **6**, 3447 (1972).
[6.53] H. J. Xiang, E. J. Kan, S.-H. Wei, M.-H. Whangbo, and X. G. Gong, Phys. Rev. B **84**, 224429 (2011).
[6.54] C. Xu, J. Feng, S. Prokhorenko, Y. Nahas, H. Xiang, L. Bellaiche, Phys. Rev. B **101**, 060404(R) (2020).
[6.55] H. Jani, J.-C. Lin, J. Chen, J. Harrison, F. Maccherozzi, J. Schad, S. Prakash, C.-B. Eom, A. Ariando, and T. Venkatesan, Nature **590**, 74 (2021).

[6.56] L. Peng, R. Takagi, W. Koshibae, K. Shibata, K. Nakajima, T.-H. Arima, N. Nagaosa, S. Seki, X. Yu, and Y. Tokura, Nat. Nanotechnol. **15**, 181 (2020).
[6.57] H. Oike, A. Kikkawa, N. Kanazawa, Y. Taguchi, M. Kawasaki, Y. Tokura, and F. Kagawa, Nat. Phys. **12**, 62 (2016).
[6.58] C. Jin, Z.-A. Li, A. Kovács, J. Caron, F. Zheng, F. N. Rybakov, N. S. Kiselev, H. Du, S. Blügel, and M. Tian, Nat. Commun. **8**, 15569 (2017).
[6.59] A. Chacon, L. Heinen, M. Halder, A. Bauer, W. Simeth, S. Mühlbauer, H. Berger, M. Garst, A. Rosch, and C. Pfleiderer, Nat. Phys. **14**, 936 (2018).
[6.60] A. N. Bogdanov and D. A. Yablonsky, Sov. Phys. JETP **68**, 101 (1989).
[6.61] A. N. Bogdanov, U. K. Rössler, and C. Pfleiderer, Physica B: Condensed Matter **359**–**361**, 1162–1164 (2005).
[6.62] J. Iwasaki, M. Mochizuki, and N. Nagaosa, Nat. Commun. **4**, 1463 (2013).
[6.63] W. Koshibae and N. Nagaosa, Sci. Rep. **8**, 6328 (2018).
[6.64] J. Iwasaki, M. Mochizuki, and N. Nagaosa, Nat. Nanotechnol. **8**, 742 (2013).
[6.65] W. Jiang, X. Zhang, G. Yu, W. Zhang, X. Wang, M. B. Jungfleisch, J. E. Pearson, X. Cheng, O. Heinonen, K. L. Wang, Y. Zhou, A. Hoffmann, and S. G. E. te Velthuis, Nat. Phys. **13**, 162 (2017).
[6.66] D. Maccariello, W. Legrand, N. Reyren, K. Garcia, K. Bouzehouane, S. Collin, V. Cros, and A. Fert, Nat. Nanotechnol. **13**, 233 (2018).
[6.67] L. Peng, K. Karube, Y. Taguchi, N. Nagaosa, Y. Tokura, X. Yu, Nat. Commun. **12**, 6797 (2021).
[6.68] C. Reichhardt and C. J. O. Reichhardt, J. Phys.: Condens. Matter **31**, 07LT01 (2018).

7. Summary of conclusions and proposed future research

7.1 Summary of conclusions

In summary, in this doctoral dissertation we investigated structural, electronic and transport properties for a large number of topological materials, by combining experimental methods and various theoretical tools. More specifically, we focus on 2D vdW topological insulators, Weyl and Dirac semimetals. The theoretical and experimental results is this study contributes to the more than ten years of research on topological materials by investigating electronic and transport properties, topological phase transitions and the possibility of incorporating topological with magnetic materials for next generation devices.

Firstly, we fabricated by MBE epitaxial $(SnBi_2Te_4)_n(Bi_2Te_3)_m$ natural van der Waals superlattices. Theoretical calculations with DFT and Wannier functions show that these materials possess TSS. $SnBi_2Te_4$ is confirmed by TEM and XRD to create septuplet layers separated by vdW gaps. On the other hand, $SnBi_4Te_7$ creates an ordered natural vdW superlattice of alternating SL/QL. On both materials BCB barely overlaps with TSS on the Fermi level, where $SnBi_2Te_4$, which contains the largest Sn concentration, acquires the least overlap, as observed by ARPES measurements. Magnetotransport experiments on $SnBi_2Te_4$ show two different electron-like carriers, where one of them has high electron mobility, attributed to the presence of TSS. Longitudinal magnetoresistance exhibits a resistance dip at zero magnetic field for both parallel and perpendicular configurations. These findings point towards the presence of WAL effect due to the presence of TSS. Further analysis of the prefactor values of the HLN formula suggests that the entire film, which consists of two interfaces and one bulk contribution, acts as one 2D channel.

In addition, $MoTe_2$ epitaxial thin films with distorted 1T′ structures are produced on InAs substrates using MBE. Despite the presence of 60^o and 120^o rotational domains, the films are rotationally consistent with the substrate, allowing for the observation by RHEED, STM and synchrotron GIXD. We find two distinct phases coexisting in the layer using STEM cross sectional measurements in 3 ML $MoTe_2$. In the first phase, an orthorhombic (T_d) stacking can be seen, while in the second

phase, a previously unreported triclinic stacking is visible. From GIXD and STEM, we measure the lattice parameter values for the orthorhombic T_d-phase that are found to be bigger than free standing thin films exfoliated from bulk as a result of the substrate's effect. Because of the larger lattice parameters of our epitaxial thin films, the $MoTe_2$ orthorhombic T_d-phase, which is generally seen at temperatures lower than 250 K, is detected here at room temperature. This is attributable to an interlayer antibonding state compatible with the orthorhombic T_d-phase. An orthorhombic type-II Weyl semimetal phase is obtained by the orthorhombic T_d-non-centrosymmetric $MoTe_2$ structure. Eight Weyl nodes predicted by first-principles, that are accessible to transport, are a few meV below the Fermi level, opening the door for room temperature electronic applications where the topologically non-trivial characteristics of $MoTe_2$ epitaxial layers could be beneficial.

Moreover, the family of group IV transition metal ditellurides is studied with theoretical calculations by using DFT, Wannier functions and tight-binding model. Both $HfTe_2$ and $ZrTe_2$ possess two topologically protected fourfold degenerate Dirac nodes caused by band inversion. In the case of $HfTe_2$, a point-like Fermi surface characteristic to a type-I Dirac semimetal is shown by placing the chemical potential at the position of the Dirac points. However, in the case of $ZrTe_2$, needle-like electron and hole pockets form and meet at the DP, proving $ZrTe_2$ is a type-II DSM. A new $Hf_xZr_{1-x}Te_2$ material with a type-III Dirac cone and a line-like Fermi surface was formed by alloying the two materials ($HfTe_2$ and $ZrTe_2$). The electronic band structure of the $Hf_xZr_{1-x}Te_2$ alloy was calculated by a linear interpolation of tight-binding model matrix elements. The new alloy $Hf_xZr_{1-x}Te_2$ will produce a type-III Dirac cone with a line-like Fermi surface at $x = 0.2$. To obtain the type-III phase, an in-plane compressive strain is additionally applied. This strain may be used to alternate between the two types of DSMs in order to achieve a topological phase transition. By using MBE, epitaxial $Hf_{0.2}Zr_{0.8}Te_2$ films are successfully grown on. According to ARPES measurements, $Hf_{0.2}Zr_{0.8}Te_2$ film displays topological DSM behavior, where the valence bands exhibiting a linear dispersion in *k*-space.

Finally, we report theoretical results of the $CrTe_2/WTe_2$ bilayer, and to a lesser extend $CrTe_2/MoTe_2$. By performing DFT calculations, we obtained the

perpendicular anisotropy constant *K*, the exchange coupling constant *J*, and the DMI *D*, and introduced them to the spin Hamiltonian of atomic-scale spin simulations. The interfacial DMI of these heterostructures in strong enough to stabilize a lattice of magnetic skyrmions. A field-controlled Néel-type skyrmion lattice-ferromagnet transition cycle is developed in which the skyrmion lattice is resistant to thermal fluctuations in the vicinity of T_c. Moreover, we set up a Néel-type skyrmion on a racetrack in order to investigate the spin-polarized current-induced motion of these skyrmions. The results demonstrated that the skyrmion velocity as a function of spin-polarized current density acquires a greater skyrmion Hall angle at 80 K compared to 0 K. Our research demonstrates that the applied field or temperature can be controlled to generate or annihilate skyrmions in the $CrTe_2/WTe_2$ bilayer vdW heterostructure, and that temperature control and ultra-low spin-polarized currents may be used to alter the skyrmions' velocity and direction.

7.2 Proposed future research

The results of this doctoral dissertation could also trigger for further research on the field of 2D topological materials:

1) Charge to spin interconversion and magnetization switching of $SnBi_2Te_4$ in combination with a 2D ferromagnet, should be investigated. The presence of TSS and the small contribution from bulk states suggests that $SnBi_2Te_4$ could be a very promising candidate for SOT-MRAM and MTJ applications.
2) Future research should concentrate on enhancing $MoTe_2$/InAs film epitaxial quality. Although the $MoTe_2$ and InAs substrate exhibit excellent in-plane epitaxial alignment, the in-plane mosaicity of $MoTe_2$ is significantly higher than the InAs
3) The fact that the eight Weyl nodes of T_d-$MoTe_2$ (on InAs substrates) predicted by first-principles are a few meV below the Fermi level, practically makes them accessible to transport, opening the door for room temperature electronic and spintronics applications where the topologically non-trivial characteristics of $MoTe_2$ epitaxial layers could be beneficial.

4) Electronic band structure measurements on $HfTe_2$ and $ZrTe_2$ should be performed by synchrotron ARPES in order to establish whether they are type-I and type-II DSMs, respectively, as predicted by the DFT calculations.
5) In the future more experimental studies should be performed in the unknown field of type-III TSMs, since their thermoelectric transport properties could be related to new exotic physics and promise new applications, and the $Hf_{0.2}Zr_{0.8}Te_2$ type-II DSM could be an excellent platform for such research.
6) In the future, it could be appealing to fabricate such the $CrTe_2/WTe_2$ (or even $MoTe_2$ as discussed previously) 2D vdW bilayer and propose mechanisms to enhance the T_c above room temperature. The possibility of incorporating topology into electronic devices for communications and information storage, is particularly promising is these systems, by realizing an all-2D skyrmion racetrack memory, where skyrmions can be manipulated by ultra-low powered currents.